21-CM SIGNAL FROM THE COSMIC DAWN AND EPOCH OF REIONIZATION

A Thesis

Submitted to the

Tata Institute of Fundamental Research
(A Deemed University)

for the degree of Doctor of Philosophy
in Physics

by

Raghunath Ghara

National Centre for Radio Astrophysics
Tata Institute of Fundamental Research
2016

Dedication

I would like to dedicate my thesis to my beloved parents.

Acknowledgements

The thesis presented here is not only my work, many people have contributed in some way to it. I could not cover this long journey without their help and I would like to thank them all.

First and foremost, I would like to thank my Ph.D. supervisor Tirthankar Roy Choudhury for his guidance over last four years. Thanks for keeping patience on me even when I delayed the research projects unnecessarily. He gave me lots of freedom in the workplace which gave me the opportunity to open my mind and explore various things related to the research work. He encouraged me to attend many conferences and present my works there. This created a good opportunity for me to meet many people related to this field and discuss various research projects with them. His support and encouragements were essential for successfully completing my Ph.D.

Secondly, I would like to thank Kanan K. Datta who is one of my collaborators and a close friend. He was a post-doctoral fellow at NCRA for some time during the initial stage of my Ph.D. I gained a lot from his vast knowledge. His advice was essential for me on many occasions over the years.

Additionally, I would like to thank my review committee members Nissim Kanekar and Poonam Chandra for keeping eyes on me during last few years. Their suggestions, encouragements, friendly chats helped me to improve myself.

All the faculty members in NCRA are very friendly and happily helped me on many occasions. I would like to pay my sincere gratitude to them. I would like to thank Subhashis Roy and Divya Oberoi from

NCRA for useful academic discussions. In addition, I would like to thank Raghunathan Srianand, Aseem Paranjape from our neighbor institute IUCAA for organizing weekly Astroph discussion, regular workshops and keeping me updated with the recent works in these fields. Their friendly chats really inspire me to do good research.

I would like to thank Somnath Bharadwaj, Prasun Dutta, Suman Majumdar, Sourav Mitra, Samir, Rajesh, Vikram , Prakash for useful discussion and providing feedbacks, comments on my works which helped me to improve the quality of the thesis. I had the opportunity to discuss many research projects with them over Skype and during conferences which improve my understanding on this subject.

Beside NCRA academic members, other stuff including the administrative, scientific, technical etc were very helpful during these years and saved lots of my times on many occasions. I would like to thank them all. Especially, I would like to thank Mr. V.VenkataSubramani and Amol for solving various computation related problems in NCRA servers as quickly as possible.

My Ph.D. was impossible without the support from my friends. I would like to thank all my friends for maintaining a friendly atmosphere in NCRA. I would like to thank Naren Da, Arun, Rohit, Dharmadas, Avirup, Sushma, Biny, Nayana for making my Ph.D. days eventful. I would like to thank Prakash for teaching me the skill of laughing without any reason. I am thankful to Naren Da, Jotirmoy Da, Alka for sharing their delicious cooking with me on many occasions. I want to thank Sushan Konar (wife of my guide) for giving us many parties and adding many good memories in my life.

Finally, I am grateful to my family members who always believed in me even when I lost belief in myself. Without their supports and inspirations, it was impossible to complete my Ph.D.

Declaration

This thesis is a presentation of my original research work. Wherever contributions of others are involved, every effort is made to indicate this clearly, with due reference to the literature, and acknowledgement of collaborative research and discussions. The work was done under the guidance of Dr. Tirthankar Roy Choudhury, at the Tata Institute of Fundamental Research, Mumbai.

Raghunath Ghara

(Raghunath Ghara)
October 28, 2016

In my capacity as supervisor of the candidate's thesis, I certify that the above statements are true to the best of my knowledge.

T. Roy Choudhury

(Dr. Tirthankar Roy Choudhury)

Date: October 25, 2016

Abstract

The 21-cm brightness temperature ($\delta T_{\rm b}$) fluctuations from the cosmic dawn and the epoch of reionization promise to provide information on the physical processes during these epochs. In this thesis, we present a formalism for generating $\delta T_{\rm b}$ distribution using dark matter simulations and a one-dimensional radiative transfer code. Our analysis is able to account for the spin temperature ($T_{\rm S}$) fluctuations arising from inhomogeneous X-ray heating and Lyα coupling during the cosmic dawn. Main findings of the thesis are as follows.

1. The $\delta T_{\rm b}$ power spectrum amplitude at large scales ($k \sim 0.1$ Mpc^{-1}) is maximum when $\sim 10\%$ of the gas (by volume) is heated above the CMBR temperature. The power spectrum shows a "bump"-like feature during cosmic dawn and its location measures the typical sizes of heated regions. We find that the effect of peculiar velocities on the power spectrum is negligible at large scales for the most part of the reionization history. During early stages (when the volume averaged ionization fraction $\lesssim 0.2$) this is because the signal is dominated by fluctuations in $T_{\rm S}$. For reionization models that are solely driven by stars within high-mass ($\gtrsim 10^9$ M$_\odot$) haloes, the peculiar velocity effects are prominent only at smaller scales ($k \gtrsim 0.4$ Mpc^{-1}) where patchiness in the neutral hydrogen density dominates the signal. The conclusions are unaffected by changes in the amplitude or steepness in the X-ray spectra of the sources.
2. Details of various unknown physical processes during the cosmic dawn and the epoch of reionization can be extracted from observations of the redshifted 21-cm signal. These observations,

however, will be affected by the evolution of the signal along the line of sight which is known as the "light-cone effect". We model this effect by post-processing a dark matter N-body simulation with a 1D radiative transfer code. We find that the effect is much stronger and dramatic in the presence of inhomogeneous heating and Lyα coupling compared to the case where these processes are not accounted for. One finds an increase (decrease) in the spherically averaged power spectrum up to a factor of 3 (0.6) at large scales ($k \sim 0.05\,\mathrm{Mpc}^{-1}$) when the light-cone effect is included, though these numbers are highly dependent on the source model. The effect is particularly significant near the peak and dip-like features seen in the power spectrum. The peaks and dips are suppressed and thus the power spectrum can be smoothed out to a large extent if the width of the frequency band used in the experiment is large. We argue that it is important to account for the light-cone effect for any 21-cm signal prediction during cosmic dawn.

3. Currently several low-frequency experiments are being planned to study the nature of the first stars using the redshifted 21-cm signal from the cosmic dawn and epoch of reionization. Using a one-dimensional radiative transfer code, we model the 21-cm signal pattern around the early sources for different source models, i.e., the metal-free Population III (PopIII) stars, primordial galaxies consisting of Population II (PopII) stars, mini-QSOs and high-mass X-ray binaries (HMXBs). We investigate the detectability of these sources by comparing the 21-cm visibility signal with the system noise appropriate for a telescope like the SKA1-low. Upon integrating the visibility around a typical source over all baselines and over a frequency interval of 16 MHz, we find that it will be possible to make a $\sim 9-\sigma$ detection of the isolated sources like PopII galaxies, mini-QSOs and HMXBs at $z \sim 15$ with the SKA1-low in 1000 hours. The exact value of the signal to noise ratio (SNR) will depend on the source

properties, in particular on the mass and age of the source and the escape fraction of ionizing photons. The predicted SNR decreases with increasing redshift. We provide simple scaling laws to estimate the SNR for different values of the parameters which characterize the source and the surrounding medium. We also argue that it will be possible to achieve an SNR ~ 9 even in the presence of the astrophysical foregrounds by subtracting out the frequency-independent component of the observed signal. These calculations will be useful in planning 21-cm observations to detect the first sources.

4. Understanding properties of the first sources in the Universe using the redshifted H I 21-cm signal is one of the major aims of present and upcoming low-frequency experiments. We investigate the possibility of imaging the redshifted 21-cm pattern around the first sources during the cosmic dawn using the SKA1-low. We model the H I 21-cm image maps, appropriate for the SKA1-low, around the first sources consisting of stars and X-ray sources within galaxies. In addition to the system noise, we account also for the astrophysical foregrounds by adding them to the signal maps. We find that after subtracting the foregrounds using a polynomial fit and suppressing the noise by smoothing the maps over $10' - 30'$ angular scale, the isolated sources at $z \sim 15$ are detectable with $\sim 4 - 9\,\sigma$ confidence level in 2000 h of observation with the SKA1-low. Although the 21-cm profiles around the sources get altered because of the Gaussian smoothing, the images can still be used to extract some of the source properties. We account for overlaps in the patterns of the individual sources by generating realistic H I 21-cm maps of the cosmic dawn that are based on N-body simulations and a one-dimensional radiative transfer code. We find that these sources should be detectable in the SKA1-low images at $z = 15$ with an SNR of $\sim 14(4)$ in 2000 (200) h of observations. One possible observational strategy thus could be to observe multiple fields

for shorter observation times, identify fields with SNR $\gtrsim 3$ and observe these fields for much longer duration. Such observations are expected to be useful in constraining the parameters related to the first sources.

Synopsis

Name : Raghunath Ghara
Title of the thesis : 21-cm signal from the cosmic dawn and epoch of reionization
Supervisor : Dr. Tirthankar Roy Choudhury

1 Introduction

The birth of the first stars a few hundred million years after the Big Bang is one of the landmark events in the history of the Universe. It is believed that the radiation produced by these sources spread through the intergalactic medium (IGM) and significantly affected its thermal and ionization state. The onset of the first sources of light which marked the end of the 'dark ages' and modified the thermal state of the IGM is often termed as the 'cosmic dawn'. The subsequent period when the neutral hydrogen (H I) was ionized by the radiation from the first stars is popularly known as the epoch of reionization (EoR).

Understanding the physical processes during this epoch is one of the major goals of present-day observational astronomy. Unfortunately, we have very little knowledge about these processes. Many important questions such as, the redshift at which the first sources in the Universe formed, the nature of the radiating sources that drove the reionization process, the exact duration of reionization, the evolution of the thermal and ionization state of the IGM during reionization, the impact of the reionization process on the structure formation in the Universe, are not understood in full detail. A huge effort has been placed to find answers of some of these questions from both observational and theoretical sides. Observations of $z \gtrsim 6$ quasars absorption spectra (Becker et al. 2001; Fan et al. 2006b,

2003; Goto et al. 2011; Gunn and Peterson 1965) and the cosmic microwave background radiation (CMBR) (Komatsu et al. 2011; Planck Collaboration et al. 2016) suggest that the reionization probably occurred around $6 \lesssim z \lesssim 15$ (Choudhury and Ferrara 2006; Fan et al. 2006b; Goto et al. 2011; Mitra et al. 2011, 2012, 2015). These observations provide limited but very useful information about the epoch, however, they are unable to provide the details of the physical processes.

Observations of the redshifted H I 21-cm signal from the IGM is a powerful probe and is expected to provide us with an enormous amount of information about the EoR (Furlanetto et al. 2006; Morales and Wyithe 2010; Pritchard and Loeb 2012). A number of experiments have been designed to measure the redshifted 21-cm signal both from the cosmic dawn and EoR. Low frequency observations with the present-day radio telescopes like the Low Frequency Array (LOFAR)[1] (van Haarlem et al. 2013), the Precision Array for Probing the Epoch of Reionization (PAPER)[2] (Parsons et al. 2014), the Murchison Widefield Array (MWA)[3] (Bowman et al. 2013; Tingay et al. 2013), and the Giant Metrewave Radio Telescope (GMRT)[4](Ghosh et al. 2012; Paciga et al. 2013) and future telescopes like Square Kilometre Array (SKA)[5] and the Hydrogen Epoch of Reionization Array (HERA)[6] (Pober et al. 2014) would probably contain information on many of the unknown processes during the EoR and cosmic dawn. In addition, future space infra-red telescope like the James Webb Space Telescope (JWST)[7] and ground-based optical telescopes like the European Extremely Large Telescope (ELT)[8] and the Thirty Meter Telescope (TMT)[9] should be able to reveal the properties of the very early sources responsible for reionizing the Universe by directly imaging them.

In parallel, many theoretical studies are ongoing to explore the effects of all possible parameters. Different approaches such as analytical (e.g., Furlanetto et al. 2004a; Paranjape and Choudhury 2014), semi-numerical (Choudhury et al.

[1]http://www.lofar.org/
[2]http://eor.berkeley.edu/
[3]http://www.mwatelescope.org/
[4]http://www.gmrt.tifr.res.in
[5]http://www.skatelescope.org/
[6]http://reionization.org/
[7]http://jwst.nasa.gov
[8]http://www.eso.org/facilities/eelt/
[9]http://www.tmt.org/

2009; Ghara et al. 2015a; La Plante et al. 2014; Mesinger and Furlanetto 2007; Santos et al. 2008; Thomas et al. 2009; Zahn et al. 2007), and numerical (Baek et al. 2009; Iliev et al. 2006; McQuinn et al. 2007b; Mellema et al. 2006; Shin et al. 2008) have been attempted in modelling the signal. These studies are useful for interpreting the observational results and also for designing observational strategies.

2 Outline of the thesis

The thesis mainly focuses on developing a new semi-numerical method to model the redshifted 21-cm signal self-consistently using a one-dimensional radiative transfer code. The code is applied to study various physical processes during the EoR. The thesis also aims to predict the detectability of different types of very early sources like the population III stars, normal stars within galaxies, mini-quasars and high-mass X-ray binaries using radio observations like the SKA1-low. The outline of the thesis is given below.

2.1 Semi-numerical one-dimensional radiative transfer code

The expected 21-cm signal not only depends on the amount of neutral hydrogen but also on the spin temperature ($T_{\rm S}$) of H I. The spin temperature, in turn, depends on the kinetic temperature $T_{\rm K}$ of the gas and various coupling processes like the Lyα coupling, collisional coupling and coupling with the CMBR photons. Many reionization models (Battaglia et al. 2013; Choudhury et al. 2009; Datta et al. 2012a; Furlanetto et al. 2004a; Iliev et al. 2014; McQuinn et al. 2006; Mesinger and Furlanetto 2007) simply ignore the effect of the spin temperature and deal only with the amount of neutral hydrogen in the medium. Under these assumptions, it is relatively easier to build models for the redshifted 21-cm maps. However, these models may not be entirely realistic at the cosmic dawn and the first stages of reionization when the contribution of the spin temperature to the signal could be significant.

Usually the redshifted 21-cm signal from neutral hydrogen is measured in terms of the deviation of 21-cm brightness temperature from the brightness temperature of background CMBR along a line of sight. The differential brightness

temperature observed at a frequency $\nu_{\rm obs}$ along a direction $\hat{\mathbf{n}}$ is given by (Furlanetto et al. 2006; Madau et al. 1997)

$$\delta T_{\rm b}(\nu_{\rm obs}, \hat{\mathbf{n}}) \equiv \delta T_{\rm b}(\mathbf{x}) = 27\ x_{\rm HI}(z, \mathbf{x})[1 + \delta_{\rm B}(z, \mathbf{x})] \left(\frac{\Omega_B h^2}{0.023}\right) \times \left(\frac{0.15}{\Omega_m h^2} \frac{1+z}{10}\right)^{1/2} \left[1 - \frac{T_\gamma(z)}{T_{\rm S}(z, \mathbf{x})}\right] \ {\rm mK}, \tag{1}$$

where $\mathbf{x} = r_z \hat{\mathbf{n}}$ and $1 + z = 1420\ {\rm MHz}/\nu_{\rm obs}$, with r_z being the comoving radial distance to redshift z. The quantities $x_{\rm HI}(z, \mathbf{x})$ and $\delta_{\rm B}(z, \mathbf{x})$ denote the neutral hydrogen fraction and the density contrast in baryons respectively at point $\mathbf{x}$ at a redshift z. The CMBR temperature at a redshift z is denoted by $T_\gamma(z) = 2.73 \times (1 + z)$ K and $T_{\rm S}$ is the spin temperature of neutral hydrogen. The quantities h, Ω_m and Ω_B are the usual cosmological parameters (Planck Collaboration et al. 2014a).

We have developed a semi-numerical method for generating the brightness temperature ($\delta T_{\rm b}$) distribution of the redshifted 21-cm signal from the cosmic dawn and EoR using dark matter N-body simulations and a one-dimensional radiative transfer code. The formalism is primarily based on the algorithm presented in Thomas and Zaroubi (2008) and Thomas et al. (2009) except that we use slightly different methods for the Lyα coupling and heating calculation. The radiative transfer code tracks the time evolution of the ionization fraction of different ionization states of hydrogen and helium and the kinetic temperature of gas in the IGM around individual sources. Our analysis is also able to account for the spin temperature fluctuations arising from inhomogeneous X-ray heating and Lyα coupling during cosmic dawn and the EoR. Although it is necessary to carry out full three-dimensional radiative transfer simulations to generate the ionization and heating maps, such simulations require huge computational power and long run time. We rather prefer an alternative method based on the one-dimensional radiative transfer which is faster and hence more efficient for exploring the unknown parameter space (Thomas and Zaroubi 2011; Thomas et al. 2009). The basic steps of the method are briefly described here.

1. The ionization and heating profile around a galaxy depend on the luminosity and the surrounding neutral hydrogen distribution. We generate the

ionization and heating profiles around sources for different galaxy masses, redshifts and background gas densities.

2. The density and velocity fields at different redshifts are generated using the publicly available dark matter N-body code CUBEP^{3}M[1]. The dark matter haloes in the simulation box are identified using the spherical overdensity method. In case the mass resolution of the simulation is not high enough to identify dark matter haloes down to $M_{\rm halo} \sim 10^8\,{\rm M}_\odot$, we use a sub-grid recipe to identify the low mass haloes. This sub-grid method uses the extended Press-Schechter model of Bond et al. (1991) and hybrid prescription of Barkana and Loeb (2004). After identifying all the dark matter haloes in the simulation box, we assign the stellar mass to each halo. The relation between the stellar mass of a galaxy and the hosting dark-matter halo mass $M_{\rm halo}$ is assumed to be

$$M_\star = f_\star \left(\frac{\Omega_B}{\Omega_m}\right) M_{\rm halo}, \tag{2}$$

where $f_\star$ is the fraction of the baryon residing in stellar form in the galaxy. We assume that no star formation occurs within low mass haloes ($< 10^8\,{\rm M}_\odot$). In order to incorporate radiative feedback, we suppress the galaxy formation within newly formed haloes having mass $M_{\rm halo} < 10^9\,{\rm M}_\odot$ if they form in already ionized regions, i.e., regions of the IGM with $x_{\rm HII}$ larger than 0.5.

3. Depending on the mass, background gas distribution and redshift of the galaxies, we estimate the ionizing photons from the galaxies from the pre-generated ionization profiles. In the case of overlap between the bubbles, we estimate the unused ionizing photons and distribute them equally among the overlapping ionized bubbles.

4. The X-rays can penetrate into and partially ionize the neutral IGM. Beyond the highly ionized regions around the sources, the ionization fraction is estimated using the pre-generated profiles. Once the ionization maps are generated, the kinetic temperature maps are generated using a correlation of kinetic temperature and ionization fraction in the partially ionized regions.

[1] `http://wiki.cita.utoronto.ca/mediawiki/index.php/CubePM`

5. As far as the radiative transfer of the Lyα photons are concerned, we simply assume the escape fraction of the Lyα photons to be unity and the number density of Lyα photons from the galaxies to decrease as $1/d^2$, where d be the distance from the source [1]. The Lyα coupling coefficient is calculated from the Lyα flux. Subsequently, the brightness temperature maps are generated in the simulation box using equation (1).

6. The effect of the peculiar velocity of the gas in the IGM is incorporated into the $\delta T_{\rm b}$ maps using the particle moving method or the cell movement method (Mesh-to-Mesh (MM)-RRM scheme) described in Mao et al. (2012).

The details of the method are described in Chapter 2 of the thesis.

2.2 Imprints of spin temperature fluctuations and peculiar velocities on the 21-cm signal from cosmic dawn

One of the major goals of the thesis is to understand the effect of inhomogeneous Lyα coupling and IGM heating and the peculiar velocities of the gas, popularly known as the redshift-space distortion (RSD), in the IGM on the H I 21-cm signal from the cosmic dawn. The peculiar velocity has a significant impact on the reionization and pre-reionization H I 21-cm signal (Bharadwaj and Ali 2004). This makes the 21-cm power spectrum anisotropic (Barkana and Loeb 2005a; Majumdar et al. 2013). It has already been shown that the peculiar velocity can boost the H I power spectrum by a factor of ~ 5 at large scales during the initial stages of reionization when $x_{\rm HII} \lesssim 0.2$ (Jensen et al. 2013; Mao et al. 2012). During the same period, power spectrum becomes highly anisotropic which is detectable with LOFAR 2000 h of observations. It has also been suggested that such observations could tell us whether reionization occurred inside-out or outside-in (Jensen et al. 2013; Majumdar et al. 2013). However, all the results mentioned above is based on the assumption that the spin temperature is much higher than the CMBR

[1] Several works (e.g., Pritchard and Furlanetto 2006) suggest that the Lyα profile is steeper than simple $1/d^2$ form due to the conversion of photons from Lyn to Lyα. Lyn photons ($n > 2$) are generated during the decay of excited hydrogen from nP state to the ground state. The detail radiative transfer including the conversion of Lyn photons to Lyα is beyond the scope of this thesis and will be addressed later.

temperature, thus making the signal independent of the exact value of $T_{\rm S}$. Here we investigate how the above results change once the heating and Lyα coupling, and hence the spin temperature, are calculated self-consistently. The implementation of the peculiar velocity effects on the signal during this epoch is slightly different compared to the case when the spin temperature is much higher than the CMBR temperature. Apart from that, we investigate how the peaks in the evolution of the large-scale power spectrum can be used to extract information about the ionization state and size of the 'heated bubbles'.

We have studied the impact of different sources like the stars in galaxies and mini-quasars on the expected spherically averaged power spectrum of the brightness temperature fluctuations. For the reionization models driven by stars, the size of the emission regions in the IGM is small throughout the EoR. However, in the presence of the mini-quasars, there will be a mixture of emission and absorption regions in the IGM at cosmic dawn and the initial stage of reionization. The power spectrum in such model shows a "bump"-like feature during the cosmic dawn and its location measures the typical sizes of heated regions. The presence of inhomogeneous Lyα coupling, X-ray heating, and ionization produce separate peaks in the large-scale power spectrum while plotted as a function of redshift. In the case of stellar driven reionization models, the heating in the neutral region is not present and thus the second peak (heating peak) will be absent when the large-scale power spectrum is plotted as a function of redshift (Ghara et al. 2015a).

The effect of the RSD will be different for different source models, for example, the effect will be significant for most of the period for a reionization model driven by stars in galaxies, where inhomogeneous heating is not present. We find that in the presence of inhomogeneous Lyα coupling and heating, the effect of RSD at large scales will be smaller than expected earlier, while the effect will be prominent at small scales. The effect of RSD, at large scales, will be significant at the trough regions in the power spectrum when plotted as a function of redshift. This work is described in Chapter 3 of the thesis.

2.3 Imprints of the light-cone effects on the 21-cm signal from the cosmic dawn

We have investigated one of the important line of sight effects i.e, the 'light-cone effect' on the 21-cm signal from the cosmic dawn and EoR. While simulating the signal, it is generally assumed that every part of a simulation box has the same redshift. We call each such simulation snapshot as 'coeval box'. In reality, regions which are nearer to the observer along a line of sight will have lower redshifts than the regions which are far away. As a result, the observed signal will have effects of redshift evolution imprinted on it. Studies using analytical modelling and simulations have been done to understand this light-cone effect on the two-point correlation function (Barkana and Loeb 2006; Zawada et al. 2014) and power spectrum (Datta et al. 2014, 2012b; La Plante et al. 2014). Datta et al. (2014) found that, depending on the observational bandwidth, the effect could enhance the power spectrum by a factor of up to ~ 5 at the initial stages of the EoR and suppress by a significant amount at the last stages of the EoR. Interestingly, no significant light-cone anisotropy has been found in Datta et al. (2014). It has also been noticed that the light-cone effect on the power spectrum will be significant when it evolves non-linearly with redshift as the linear evolution is smoothed out (Datta et al. 2012b). However, these studies assume that the entire IGM is always heated significantly higher than the CMBR brightness temperature and that the Lyα coupling is very strong. These assumptions may hold during the later stages of reionization but may not be true at the cosmic dawn and the initial phase of reionization. It is believed that the inhomogeneities in heating and Lyα coupling will significantly influence the signal during cosmic dawn and early phase of the EoR (when the mass averaged ionization fraction $x_{\rm HII} \lesssim 0.2$). These make the evolution of the H I power spectrum with redshift more dramatic and thus we expect a very strong light-cone effect on the signal. Zawada et al. (2014) too have studied this using numerical simulations focussing mainly on the two-point correlation functions.

We self-consistently calculate the Lyα coupling, heating of the IGM for various source models and reionization histories and study the light-cone effect on the H I power spectrum. We find that the effect is much stronger and dramatic in the presence of inhomogeneous heating and Lyα coupling compared to the case

where these processes are not accounted for. One finds an increase (decrease) in the spherically averaged power spectrum up to a factor of 3 (0.6) at large scales ($k \sim 0.05\,\mathrm{Mpc}^{-1}$) when the light-cone effect is included, though these numbers are highly dependent on the source model. The effect is particularly significant near the peak and dip-like features seen in the power spectrum. The peaks and dips are suppressed and thus the power spectrum can be smoothed out to a large extent if the width of the frequency band used in the experiment is large. We refer Ghara et al. (2015b) to the reader for details of the work. This work is presented in Chapter 4 of the thesis.

2.4 21-cm signature of the first sources in the Universe: Prospects of detection with SKA

We predict the detectability of different types of very early sources in radio observations like the SKA1-low. Though the high redshift 21-cm signal is expected to carry information about the first sources, it is quite challenging to detect the signal and extract this information. The main difficulty is that the strength of the cosmological signal is very weak compared to the typical system noise and the foregrounds. The system noise increases at low frequencies and hence one requires optimal baseline design and large observation times to keep the noise below the expected signal.

Given that the signal from the first sources is very weak, the first task would be to simply make a detection of the signatures of these early sources in low-frequency observations. Once the detection is confirmed, one can follow it up and make further progress by constraining various properties of these sources. It would thus be interesting to explore the detectability of these first sources with telescopes like the SKA1-low within reasonable observation time. Keeping this in mind, we have modelled the 21-cm signal around the first sources with the source properties and the properties of the surrounding medium being characterized by a number of parameters. The main goal of this study is to characterize the detectability of the 21-cm signal as a function of these parameters. This would help in planning observations using the SKA1-low so as to make the detection of the signal around the first sources. Similar studies have been done, e.g., by Datta et al. (2007a, 2012b); Geil and Wyithe (2008), who showed that the large

ionized bubbles around individual sources can be detected using telescopes like the GMRT, LOFAR and the MWA within reasonable integration time around redshift ~ 8. In our case, however, the situation is much more complex as we are interested in the very early stages of reionization (i.e., the cosmic dawn) where the IGM contains both emission and absorption regions.

Using our one-dimensional radiative transfer code, we model the 21-cm signal pattern around the early sources for different source models, i.e., the metal-free Population III (PopIII) stars, primordial galaxies consisting of Population II (PopII) stars, mini-QSOs and high-mass X-ray binaries (HMXBs). We investigate the detectability of these sources by comparing the 21-cm visibility signal with the system noise appropriate for a telescope like the SKA1-low. Upon integrating the visibility around a typical source over all baselines and over a frequency interval of 16 MHz, we find that it will be possible to make a $\sim 9-\sigma$ detection of the isolated sources like PopII galaxies, mini-QSOs and HMXBs at $z \sim 15$ with the SKA1-low in 1000 hours. The exact value of the signal to noise ratio (SNR) will depend on the source properties, in particular on the mass and age of the source and the escape fraction of ionizing photons. The predicted SNR decreases with increasing redshift. We provide simple scaling laws to estimate the SNR for different values of the parameters which characterize the source and the surrounding medium. We also argue that it will be possible to achieve an SNR ~ 9 even in the presence of the astrophysical foregrounds by subtracting out the frequency-independent component of the observed signal. These calculations will be useful in planning 21-cm observations to detect the first sources. The details on the method and the results are presented in Chapter 5 of the thesis.

2.5 Imaging the first sources during the cosmic dawn using SKA

We have also studied the detectability of the first sources with the SKA1-low using image-based techniques in the presence of the system noise and astrophysical foregrounds. Most of the studies related to the cosmic dawn and EoR have been done in terms of statistical quantities like the rms and power spectrum of the signal. It will be interesting to study the what kind of information does the image of the signal carry. Some recent attempts have been made to understand

the detection possibility of the large ionized bubbles in the image with LOFAR (Datta et al. 2012b). Zaroubi et al. (2012) showed that the redshifted 21-cm signal from the epoch of reionization can be detected in low-resolution images with LOFAR. Studies have also been done to detect the signal in post-reionization epochs with the SKA (Villaescusa-Navarro et al. 2014).

It is expected that the sources may not be detectable in very high-resolution images within observation time $\sim$ 2000 hours, mainly because the signal will be contaminated by the foregrounds and the system noise. These sources, however, can be detected in lower resolution images within reasonable observation time where the signal per beam is expected to be higher than the rms noise. We use the models we built earlier to calculate the signal expected from the early sources. In addition, we also model the astrophysical foregrounds to contaminate the signal similar to what is expected in observations. We find that, after subtracting the foreground sufficiently and suppressing the rms noise by smoothing using a Gaussian filter, the sources are detectable with $\sim 9-\sigma$ confidence level over 2000 hours of observation with the SKA1-low in images of resolution $2'$. Though the recovered brightness temperature profiles around the sources get modified because of the Gaussian smoothing, they can still be used to extract the source parameters. As the signal to noise ratio increases for low-resolution images, the first attempt of the low-frequency radio experiments should probably be to observe multiple fields and detect the signal in low-resolution images within short observation time like 200 hours. Once there is a detection of the signal in some field, one should attempt for longer observation in that particular field and try to recover the $\delta T_{\rm b}$ profiles around the isolated sources which can be used for parameter estimation. These calculations are presented in Chapter 6 of the thesis.

List of publications

- **Accepted manuscripts**

  1. *21 cm signal from cosmic dawn: imprints of spin temperature fluctuations and peculiar velocities*, Ghara, R., Choudhury, T. R., & Datta, K. K. 2015, MNRAS, 447, 1806
  2. *21-cm signal from cosmic dawn : Imprints of the light-cone effects*, Ghara, R., Datta, K. K., & Choudhury, T. R. 2015, MNRAS, 453, 3143
  3. *21-cm signature of the first sources in the Universe: Prospects of detection with SKA*, Ghara, R., Choudhury, T. R., & Datta, K. K. 2016, MNRAS, 460, 827
  4. *Imaging the redshifted 21-cm pattern around the first sources during the cosmic dawn using the SKA*, Ghara, R., Choudhury, T. R., Datta, K. K. & Choudhuri, S., arXiv:1607.02779

Contents

List of Figures

LIST OF FIGURES

List of Tables

1 | Introduction

1.1 The cosmic dawn and epoch of reionization

The birth of the first stars during few hundred million years after the Big Bang is one of the landmark events in the history of the Universe. It is believed that the radiation produced by these sources spread through the intergalactic medium (IGM) and significantly affected its thermal and ionization state. The onset of the first sources of light which marked the end of the 'dark ages' and changed the thermal state of the IGM is often termed as the 'cosmic dawn'. The subsequent period when the neutral hydrogen (H I) was ionized by the radiation from the first stars is popularly known as the epoch of reionization (EoR). We refer the reader to Barkana and Loeb (2001a); Furlanetto et al. (2006); Loeb (2006); Mesinger (2016); Morales and Wyithe (2010); Pritchard and Loeb (2012); Zaroubi (2013) for excellent reviews on these subjects.

Understanding the physical processes during these epochs are some of the major goals of present-day observational astronomy. Unfortunately, we have very little knowledge about these processes. Many important questions such as, the redshift at which the first sources in the Universe formed, the nature of the radiating sources that drove the reionization process, the exact duration of reionization, the evolution of the thermal and ionization state of the IGM during reionization, the impact of the reionization process on the structure formation in the Universe, are not understood in full detail. A huge effort has been placed to find answers to some of these questions from both observational and theoretical sides. Observations of redshift $z \gtrsim 6$ quasars absorption spectra (Becker et al. 2001; Fan et al. 2006b, 2003; Goto et al. 2011; Gunn and Peterson 1965) and the cosmic microwave background radiation (CMBR) (Komatsu et al. 2011; Planck Collabo-

1. INTRODUCTION

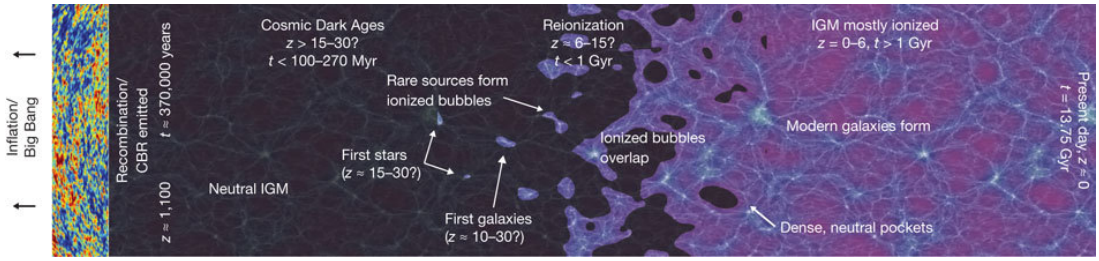

Figure 1.1: The figure shows the schematic view of the evolution of the neutral hydrogen from the cosmic recombination at redshift $\sim$ 1100 to the present day. The figure is taken from Robertson et al. (2010).

ration et al. 2016) suggest that the event probably took place around $6 \lesssim z \lesssim 15$ (Choudhury and Ferrara 2006; Fan et al. 2006b; Goto et al. 2011; Mitra et al. 2011, 2012, 2015). These observations provide limited but very useful information about the epoch. However, they are unable to provide the details of the physical processes. Figure 1.1 show a schematic view of the evolution of the neutral hydrogen during the EoR as a part of the history of the Universe.

Observations of the redshifted H I 21-cm signal from the IGM is a powerful probe and is expected to provide us with an enormous amount of information about the epoch of reionization (Furlanetto et al. 2006; Morales and Wyithe 2010; Pritchard and Loeb 2012). A number of experiments have been designed to measure the redshifted 21-cm signal from the cosmic dawn and EoR. Low-frequency observations with the present-day radio telescopes like the Low-Frequency Array (LOFAR)[1] (van Haarlem et al. 2013), the Precision Array for Probing the Epoch of Reionization (PAPER)[2] (Parsons et al. 2014), the Murchison Widefield Array (MWA)[3] (Bowman et al. 2013; Tingay et al. 2013), and the Giant Metrewave Radio Telescope (GMRT)[4](Ghosh et al. 2012; Paciga et al. 2013) and future telescopes like Square Kilometre Array (SKA)[5] and the Hydrogen Epoch of Reionization Array (HERA)[6] (Pober et al. 2014) should reveal many of the unknowns during the EoR and cosmic dawn. In addition, future space infra-red

[1]http://www.lofar.org/
[2]http://eor.berkeley.edu/
[3]http://www.mwatelescope.org/
[4]http://www.gmrt.tifr.res.in
[5]http://www.skatelescope.org/
[6]http://reionization.org/

telescope like the James Webb Space Telescope (JWST)[1] and ground-based optical telescopes like the European Extremely Large Telescope (ELT)[2] and the Thirty Meter Telescope (TMT)[3] should disclose the unknown properties of the very early sources responsible for reionizing the Universe by directly imaging them.

In parallel, many theoretical studies are going on to explore the effects of all possible parameters. Different approaches such as analytical (e.g., Furlanetto et al. 2004a; Paranjape and Choudhury 2014), semi-numerical (Choudhury et al. 2009; Ghara et al. 2015a; La Plante et al. 2014; Mesinger and Furlanetto 2007; Santos et al. 2008; Thomas et al. 2009; Zahn et al. 2007), and numerical (Baek et al. 2009; Iliev et al. 2006; McQuinn et al. 2007b; Mellema et al. 2006; Shin et al. 2008) have been attempted in modeling the redshifted 21-cm signal from the EoR and cosmic dawn. These studies are useful for interpreting the observational results and also designing observational strategies.

The thesis mainly focuses on developing a new semi-numerical method to model the redshifted 21-cm signal self-consistently using the outputs of a N-body simulation and a one-dimensional radiative transfer code. The code is applied to study the impact of various physical processes during the EoR. The thesis also aims to predict the detectability of different types of very early sources like population III stars, galaxies, mini-quasars (mini-QSOs) and high-mass X-ray binaries (HMXBs) in radio observations like the SKA1-low.

This chapter is organized as follows. In Section 1.2, we give a brief overview of the formation and evolution of the first sources and discuss their impact in ionizing the universe. The current observational constraints on reionization epoch are discussed in Section 1.3. We discuss the evolution of the 21-cm signal and main challenges in detecting the signal in Section 1.4 and 1.5 respectively. We discuss the motivation and main challenges of various simulation techniques for the EoR science in Section 1.6. We discuss the current observational constraints from the 21-cm experiments on the epoch of reionization in Section 1.7 before we state the outlines of the rest of the thesis in Section 1.8.

[1] http://jwst.nasa.gov
[2] http://www.eso.org/facilities/eelt/
[3] http://www.tmt.org/

1.2 Formation of the first sources of light and reionization

Observations show that the present state of the Universe consists of high-density objects like the galaxies, clusters etc and a highly ionized IGM. Galaxy surveys like the 2-degree Field Galaxy Redshift Survey[1] (2dFGRS) and the Sloan Digital Sky Survey[2] (SDSS) are able to quantify the distribution of the galaxies in the local Universe. According to the most favorable model for the evolution of the Universe, our Universe started with a Big Bang about 13.799 ± 0.021 billion years ago (Planck Collaboration et al. 2015b) and went through various phases of evolution until reaching the present state. In this section, we briefly review the evolution of the Universe. We discuss only the main physical elements which will be required to understand the thesis, without going into too much of details. For details, the reader is referred to Mo et al. (2010); Padmanabhan (1993); Peacock (1999); Peebles (1993) books.

1.2.1 The history of the expanding Universe

The modern cosmology is mainly based on the mathematical description of the large-scale properties and the observational evidence of the expanding Universe. The evolution of the Universe was first described by Einstein's General theory of relativity (Einstein 1916) and the observational evidence of expanding Universe was provided by Hubble and Humason (1931). It is believed that right after the Big Bang, the Universe was very dense and hot. The frequent collisions between the elements like the electrons, protons and photons prevented the formation of neutral atoms. Eventually, the Universe expanded adiabatically and the temperature of the primordial plasma decreased to ~ 3000 K at redshift ~ 1100, which then allowed the formation of neutral atoms. This event is called the '*Cosmic recombination*'.

Before the epoch of recombination, the photons were trapped due to repeated Thomson scattering with the free electrons in the medium. This scattering stopped as soon as the neutral elements formed in the Universe and the pho-

[1] http://www.2dfgrs.net/
[2] http://www.sdss.org/

tons could free stream. These photons got redshifted due to the expansion of the Universe and we observe these in the form of the Cosmic Microwave Background radiation (CMBR). From the observations of the CMBR, we also know that there were tiny fluctuations, of the order 10^{-5} (Fixsen 2009; Mather et al. 1990; Planck Collaboration et al. 2015a), in the radiation and matter field at the Cosmic recombination. These tiny fluctuations in matter density eventually grew and formed the large-scale structures which we observe at the present time.

In the Big Bang model, around 68% of Universe's energy is in the form of '*dark energy*', which is the reason for the late-time acceleration of the Universe. Around 32% of the energy is in the form of non-relativistic matter, out of which only 5% is in the form of baryons. Rest of the invisible matter is non-baryonic, named as '*dark matter*'. It is believed that the dark matter is pressure-less and interact only through gravity, which is the main driver of structure formation in the Universe. The contribution of the radiation to the total energy density of the Universe at present is very small compared to the other components.

The observations by Hubble and Humason (1931) implied that the far away galaxies are moving far away from us and the recessional velocity (v) is proportional to their distance (r) from us. This fact is expressed as $v = Hr$, which is known as the Hubble Law. The quantity H is known as the *Hubble parameter*, whose value at the present epoch is commonly defined in terms of the dimensionless Hubble parameter h as $H_0 = h \times 100$ km s^{-1} Mpc^{-1}. The Hubble parameter can also be expressed as $H \equiv \dot{a}/a$, where $a = (1+z)^{-1}$ is the expansion factor (commonly known as the *scale factor*) at redshift z and $\dot{a}$ is the time derivative of a. The scale factor is related to the physical separation (Δl_p) of two points in the Universe and its comoving separation (Δl_c) as $\Delta l_p = \Delta l_c \times a$. The mathematical description of the expanding Universe is obtained from the Einstein's field equations (Friedmann 1922) and given by

$$H^2(a) \equiv \left(\frac{\dot{a}}{a}\right)^2 = \frac{8\pi G}{3}\rho - \frac{kc^2}{a^2}, \tag{1.1}$$

where G is the gravitational constant, ρ is the total energy density of the University, k is the geometric curvature and c is the speed of light. From equation 1.1, one can see that the curvature $k = 0$ or the Universe is flat for a density $\rho_c = 3H^2/(8\pi G)$, which is called the *critical density* of the Universe. In case the density of the Universe is larger than ρ_c or $k > 0$, the gravitational pull will

eventually cause re-collapse of the Universe. In the other situation, when $\rho < \rho_c$ or $k < 0$, the Universe will expand very rapidly to infinity.

As described previously, there are mainly three components in the total energy budget of the Universe. Thus the total energy density of the Universe can be expressed as $\rho = \rho_r + \rho_m + \rho_\Lambda$, where ρ_r, ρ_m and ρ_Λ are the energy densities of the radiation, matter and the dark energy respectively. All of these three components follow different evolution relation with time

$$\begin{aligned} \rho_r &\propto a^{-4}, \\ \rho_m &\propto a^{-3}, \\ \rho_\Lambda &\equiv \frac{\Lambda c^2}{8\pi G}, \end{aligned} \tag{1.2}$$

where we assume that the dark energy density is constant in time as is usually done in the ΛCDM paradigm (CDM stands for cold dark matter and Λ is the *cosmological constant*). Generally, the individual contributions of the different components of energy densities are expressed in terms of the *density parameters*, which are the ratios of the respective energy densities and the critical density. The density parameters for the radiation, matter and the dark energy at present day are $\Omega_r = \frac{\rho_{r,0}}{\rho_{c,0}}$, $\Omega_m = \frac{\rho_{m,0}}{\rho_{c,0}}$ and $\Omega_\Lambda = \frac{\rho_{\Lambda,0}}{\rho_{c,0}}$ respectively, where the subscript '0' represents the present day ($a = 1$) quantities. The observational evidences show that the preferred geometry of the Universe is flat, which means $\Omega_r + \Omega_m + \Omega_\Lambda = 1$ with $\Omega_r = 5 \times 10^{-5}, \Omega_m = 0.32$ and $\Omega_\Lambda = 0.68$ (Planck Collaboration et al. 2015b). In such an Universe, equation 1.1 can be written in terms of the density parameters as follows,

$$H^2(a) = H_0^2 \left(\Omega_r a^{-4} + \Omega_m a^{-3} + \Omega_\Lambda \right), \tag{1.3}$$

where H_0 is the Hubble constant at present time with $h = 0.67$ (Planck Collaboration et al. 2014a).

From the Friedmann equation, it is clear that the expansion rate of the Universe is dominated by different components at different epochs. The dynamics of the Universe was mainly driven by the radiation density during the period with redshift $\geq z_{\rm eq}$, where $1 + z_{\rm eq} = \Omega_m/\Omega_r \approx 6 \times 10^3$. Subsequently, the Universe went through an epoch where the expansion was dominated by the matter density

until redshift $z_\Lambda = (\Omega_\Lambda/\Omega_m)^{1/3} - 1 \approx 0.3$ when the matter density and the dark energy density were equal. At present, the expansion of the Universe is primarily driven by the dark energy.

1.2.2 Structure formation

Till now, we have not discussed the formation of structures and radiating sources in the Universe. The radiating sources like the galaxies formed in dark matter haloes which evolved from the tiny fluctuations in matter density formed at the very beginning of the Universe. These tiny ripples in matter density grow with time due to gravitational instability and form the large scale structures that we observe today.

The most convenient way to study the growth of the density fluctuations is in terms of the density contrast, which can be defined as $\delta(\mathbf{r}) = \rho_m(\mathbf{r})/\bar{\rho}_m - 1$, where $\rho_m(\mathbf{r})$ is the matter density at spatial location $\mathbf{r}$ and $\bar{\rho}_m$ is the average matter density in the Universe. Initially $\delta(\mathbf{r}) \ll 1$ and the growth of density perturbation can be described by the linear theory (see Padmanabhan (1993); Peacock (1999) for detail). Generally, it is easier to study the equations in the Fourier space rather than the real space. Lets $\delta(\mathbf{k})$ denote the Fourier component of the density fluctuation in a scale λ which is related to the wave number $\mathbf{k}$ as $|\mathbf{k}| = 2\pi/\lambda$. It is believed that the primordial density fluctuations are scale-invariant Gaussian random fields with independent Fourier modes.

The growth of the fluctuations depends on the length scale of the fluctuation with respect to the size of the particle horizon $\lambda_H \sim cH^{-1}$, which is the physical distance travelled by photons since the Big Bang. Initial fluctuations in the dark matter density on super-horizon scales grow as $\delta \propto a^2$ and $\delta \propto a$ during the radiation dominated and matter dominated epochs respectively. On the other hand, the fluctuations on sub-horizon scales grow as $\delta \propto a$. Eventually, the fluctuations on the super-horizon scales will enter the horizon and evolve as sub-horizon fluctuations.

Linear theory of the density growth starts to break down once the density contrast δ approaches unity. It is not straightforward to mathematically solve the density growth in the non-linear regime. The most commonly used tool to understand the non-linear growth is the spherical collapse model, which assumes

spherical symmetry. In this model, the dynamics of the high-density regions decouple from the Hubble flow due to the self-gravity, and the regions turn around and collapse to form dark matter haloes. The virial theorem relates the kinetic and potential energies of the haloes and provides the condition to halt the collapse of the halo. According to the spherical collapse model, the density contrast of the halo $\Delta_c \approx 179$ (for $\Omega_m = 1$) is independent of the halo mass and the collapse redshift. However, in a universe with $\Omega_m + \Omega_\Lambda = 1$, this is modified to the following (Bryan and Norman 1998).

$$\Delta_c \approx 18\pi^2 + 82x - 39x^2, \tag{1.4}$$

where $x = \Omega_m^z - 1$ with

$$\Omega_m^z = \frac{\Omega_m(1+z)^3}{\Omega_m(1+z)^3 + \Omega_\Lambda}. \tag{1.5}$$

The mass of the halo of radius $r_{\rm vir}$ will be $M_{\rm vir} = 4\pi/3(1+\Delta_c)\bar{\rho}_m r_{\rm vir}^3$. The temperature of the baryonic gas, collapsing into the dark matter halo, increases due to shock-heating to the virial temperature $T_{\rm vir} = \mu m_H v_{\rm vir}^2/(2k_B)$ of the halo, where μ is the mean molecular weight, m_H is the mass of atomic hydrogen, $v_{\rm vir} = \sqrt{GM_{\rm vir}/r_{\rm vir}}$ is the velocity dispersion and k_B is the Boltzmann constant. The virial mass of the halo is related to the virial temperature as follows.

$$M_{\rm vir} \approx 2 \times 10^6\ {\rm M}_\odot \left(\frac{T_{\rm vir}}{10^3\ {\rm K}}\right)^{3/2} \left(\frac{1+z}{10}\right)^{-3/2} \left(\frac{\mu}{1.22}\right)^{-3/2} \left(\frac{\Omega_m}{\Omega_m^z}\frac{\Delta_c}{18\pi^2}\right)^{-1/2}. \tag{1.6}$$

The dark matter haloes are ideal locations for the formation of the radiating sources like the galaxies, which produce ultraviolet (UV) photons that ionize the neutral medium. While the dark matter is assumed to be pressure-less and evolution of its density depends solely on the gravitational pull, the baryonic gas has thermal pressure which opposes the growth of small-scale fluctuations. The thermal pressure prevents the growth of the baryonic density fluctuations if the free fall time is larger than the sound crossing time λ/c_s, where $c_s = \sqrt{\gamma k_B T_{\rm K}/(\mu m_H)}$ is the sound speed and γ is the ratio of specific heats (for ideal, mono-atomic gas, $\gamma = 5/3$). The condition for the growth to be suppressed can be simplified by introducing a length scale, called the Jeans scale λ_J, as

$\lambda \leq \lambda_J \equiv c_s\sqrt{\pi/(G\rho_m)}$. The associated Jeans mass is $M_J \equiv (4\pi/3)\rho_m(\lambda_J/2)^3$, which also can be written as,

$$M_J \approx 6 \times 10^7 \ \mathrm{M}_\odot \ \Delta^{-1/2} \left(\frac{T_\mathrm{K}}{10^3 \ \mathrm{K}}\right)^{3/2} \left(\frac{1+z}{10}\right)^{-3/2} \left(\frac{\mu}{1.22}\right)^{-3/2} \left(\frac{\Omega_m h^2}{0.13}\right)^{-1/2}, \tag{1.7}$$

where $\Delta \equiv \rho_m/\bar{\rho_m}$ is the over-density in total Jeans mass (dark matter and baryons).

From equation 1.7, one can see that the Jeans mass is strongly dependent on the gas temperature. To have an idea about the Jeans mass at different epochs, let us discuss the evolution of the gas temperature and CMBR brightness temperature. Following the recombination around redshift 1100, the CMBR temperature decreases due to the expansion of the Universe. Evolution of the CMBR temperature can be written as $T_\gamma(z) = T_{\gamma 0} \times (1+z)$ K, where $T_{\gamma 0}$ =2.73 K is the brightness temperature of the observed CMBR at the present day. On the other hand, the gas expands adiabatically and thus, the temperature is expected to evolve as $T_\mathrm{K}(z) \propto (1+z)^2$. However, after recombination, the gas temperature follows the CMBR temperature up to a redshift (often called as the redshift of decoupling) $1 + z_\mathrm{dec} \approx 150\,(\Omega_B h^2/0.023)^{2/5}$ (Furlanetto et al. 2006) due to the scattering of the CMBR photons with the residual electrons in the medium. After z_dec, the gas temperature evolves as $T_\mathrm{K}(z) = T_{\gamma 0}(1+z)^2/(1+z_\mathrm{dec})$, until the first stars form and change the ionization and heating history significantly.

The mass function of haloes in the universe is best obtained using N-body simulations and using different halo finding algorithms like the friends-of-friends (FOF) (Davis et al. 1985) or the spherical over-density (SO) (Lacey and Cole 1994) etc. In addition, there are analytical formalisms, like that of Press and Schechter (1974), which match quite well with the numerical simulations. Though these analytical formalisms are unable to provide the three-dimensional spatial distribution of the haloes, they are very useful to study the parameter space in relatively shorter run times. The comoving number density of the haloes per logarithmic mass interval is given by (Press and Schechter 1974),

$$M\frac{dn}{dM} = \left(\frac{2}{\pi}\right)^{1/2} \frac{d(ln\sigma)}{d(lnM)} \ \frac{\rho_{m,0}}{M} \ \nu_\mathrm{crit} \ \exp\left[-\frac{\nu_\mathrm{crit}^2}{2}\right] \tag{1.8}$$

where dn is the number of haloes with mass between M and $M+dM$, $\sigma(M)$ is the standard deviation of the density contrast smoothed over a scale containing mass M, $\rho_{m,0}$ is the average mass density of the present day, and $\nu_{\rm crit} = \delta_c(z)/\sigma(M)$. Here, $\delta_c(z) = 1.686/D(z)$ where $D(z)$ is the linear density growth factor.

1.2.3 Reionizing the Universe

The first major phase change in the baryonic component of the Universe, namely hydrogen and helium, occurred during the epoch of recombination around redshift ~ 1100 when the neutral hydrogen formed in the Universe. The Universe remained neutral until very first sources of radiation formed in the high-density regions and started ionizing the surrounding medium. The exact time of the formation of the first sources and the nature of reionization is still poorly understood. Many models of the EoR have been developed, though these models depend crucially on the various assumptions and simplifications.

Reionizing sources have always been a source of uncertainty in the EoR models. It is believed that the dark matter haloes are the cradles for the formation of radiating sources like the population III stars and the first galaxies which provide a significant number of ionizing photons. Besides these, quasars too can contribute a significant amount of ionizing photons to reionize the Universe (Khaire et al. 2015). It is believed that these sources create highly ionized bubbles around themselves which eventually merge and complete the reionization by redshift $\sim$ 6 (Choudhury and Ferrara 2006; Fan et al. 2006b; Malhotra and Rhoads 2006; Mitra et al. 2011, 2012). All these models of reionization are dependent on many parameters. One of these parameters is the escape fraction ($f_{\rm esc}$), which is the fraction of the intrinsic UV photons that are able to escape into the IGM. The mechanism of these UV photons to escape from the interstellar medium (ISM) is highly controversial. It is believed that these photons can escape through the various holes created in the ISM by processes like supernova feedback, radiative transfer through superbubbles etc (e.g., Dove et al. 2000; Ferrara and Loeb 2013; Fujita et al. 2003; Roy et al. 2015).

However, the value of $f_{\rm esc}$ is highly uncertain for these high-redshift galaxies. $f_{\rm esc}$ depends on the structure of the ISM, nature of star formation, feedbacks etc. Recently, there are many attempts to measure the $f_{\rm esc}$ at low redshifts. The

escape fraction is estimated as 10-20% using the Lyman break galaxies at redshift ~ 3 (Adelberger and Steidel 2000; Cooke et al. 2014). However, estimating $f_{\rm esc}$ at higher redshift $z \sim 6$ is very difficult as the Lyman continuum photons are absorbed in intervening H I. There are many theoretical predictions of the value of $f_{\rm esc}$. These predictions use the constraints of reionization, e.g., the observations of high-redshift quasars and CMBR. Studies like Ferrara and Loeb (2013) predicted the escape fraction to increase with the redshift during the EoR. Recently, Mitra et al. (2015) showed that a non-evolving $f_{\rm esc}$ of $\sim 10\%$ between redshift 6 to 9 is consistent with the recent observational constraint of *Planck* mission (Planck Collaboration et al. 2015b).

Though the first stars are believed to have formed in a metal-free environment, they eventually enrich the ISM with metals. In the presence of the metals, not only the star formation rate is modified, but also the properties of the galaxies themselves (see, e.g., Mannucci et al. 2010). Incorporating the detailed evolution of the spectral energy distribution in reionization models is a challenging task. Thus, most of the reionization models ignore such difficulties and work under simple assumptions. The galaxies can form in the dark matter haloes only if the gas can cool via the atomic (or molecular) cooling. As a result, the small dark matter haloes may not contain sources of ionization. As molecular cooling is more efficient process than atomic cooling, the minimum halo mass which can contain sources is much smaller (typically $\sim 10^6\,{\rm M}_\odot$) for the molecular cooling than that for atomic cooling provides (typically $\sim 10^8\,{\rm M}_\odot$). It is believed that the formation of first-star occurred in the Universe around redshift 20-30 due to the molecular hydrogen cooling (see e.g., Loeb 2006). However, molecular hydrogen is very fragile and can be easily dissociated by the UV and Lyman-Werner photons from the sources, which prevents the star formation in mini-haloes of mass $\sim 10^6\,{\rm M}_\odot$. In addition, the gas is heated due to the formation of the sources, which suppressed the further star formation in those mini-haloes. In our study, we only considered the contributions from the haloes with mass larger than $\sim 10^8\,{\rm M}_\odot$. Another complexity comes from the radiative feedback of the ionizing sources. The temperature of the highly ionized region during the EoR is $\sim 10^4$ K due to photo-heating. In addition, the X-rays from the sources can penetrate long distances to the neutral IGM and heat up the medium. In addition, the radiative feedback can influence the population of sources. We

assume a suppression of star formation in haloes lighter than $\sim 10^9\,\mathrm{M}_\odot$ in the regions with $T_\mathrm{K} > 10^4$ K.

Another important component of modeling the EoR is the method to create ionized bubbles around the sources. In principle, one needs a full 3D radiative transfer to accurately implement the ionization from both the UV and X-rays. Studies like Baek et al. (2009); McQuinn et al. (2007b); Mellema et al. (2006); Shin et al. (2008); Trac and Cen (2007) use a 3D radiative transfer to generate the ionization maps from the outputs of a N-body simulation. However, these radiative transfer codes are computationally very expensive and thus, cannot be used to explore large parameter space. On the other hand, there are many studies like Geil and Wyithe (2008); Hassan et al. (2016); Mesinger and Furlanetto (2007); Santos et al. (2010) etc which avoid the N-body simulations and use excursion set based methods to generate the ionization fields. While these codes are relatively faster and computationally less expensive than the full 3D radiative transfer codes, one has to make simplifying assumptions about the physical processes. There are other schemes like Ghara et al. (2015a); Thomas et al. (2009) which uses intermediate method between these two. These codes use a N-body simulation and a 1D radiative transfer method to generate the ionization maps in the simulation box. On the other hand, studies like Choudhury et al. (2009); Santos et al. (2008) use a N-body simulation and excursion set based formalism for generating the ionization bubbles around the sources without using any radiative transfer code.

It is expected that the process of reionization of the neutral hydrogen consists of several stages. The process must have started as soon as the first sources (like galaxies) formed in the Universe. At first, the number density of the ionizing sources is small and thus the IGM is expected to consist of individual H II bubbles around the sources. This stage is known as the "pre-overlap" stage. At a later time, the neighboring H II bubbles start to overlap. This phase is named as the "overlap" phase. Generally, the analytical and semi-analytical models of the EoR focus on the evolution of the global averaged quantities like the volume filling factor of ionized regions Q_HII. As the mean free path of the ionizing photons is expected to be smaller than the horizon size, the evolution of the volume filling factor can be written as (see, e.g, Choudhury 2009),

$$\frac{dQ_{\rm HII}}{dt} = \frac{\dot{n}_\gamma}{n_H} - Q_{\rm HII}\ C\ \alpha(T_{\rm K})\ n_H \tag{1.9}$$

The term C is the clumping factor which can be defined as $C \equiv \frac{<n_{\rm HII}\ n_e>}{<n_{\rm HII}><n_e>}$ where n_e and $n_{\rm HII}$ are the mean number density of free electrons and the ionized hydrogen respectively. The clumping factor accounts for the recombination rate in a clumpy IGM. The quantity $\alpha(T_{\rm K})$ represents the recombination coefficient at a temperature $T_{\rm K}$. The term $\dot{n}_\gamma$ represents the number of ionizing photons in the IGM per unit time per unit comoving volume and can be expressed as,

$$\dot{n}_\gamma = \zeta\ n_H\ \frac{df_{\rm coll}}{dt} \tag{1.10}$$

where n_H is the comoving number density of hydrogen and ζ is a parameter which combines the effect of star-formation efficiency, the number of ionizing photons produced by the stars per unit time and the escape fraction. The term $f_{\rm coll}$ is the collapse fraction which can be expressed as,

$$f_{\rm coll} = \frac{1}{\bar{\rho_m}} \int_{M_{\rm min}}^{\infty} dM\ M\ \frac{dn(M,z)}{dM} \tag{1.11}$$

where $M_{\rm min}$ is the minimum mass of the halo that can forms stars.

Mitra et al. (2015) considers ζ as a free parameter in their model. The study brings strong constraints on ζ using a Principle Component Analysis (PCA) technique by comparing with the existing observations of the Thomson scattering optical depth of the CMBR from *Planck* and the observations of high-redshift quasar absorption spectra. Figure 1.2 shows the predicted evolution of $Q_{\rm HII}$ from their model. One can see that the existing observational data sets prefer a reionization model which starts around redshift ~ 15 and ends around redshift ~ 6. However, uncertainty about the ionization fraction around redshift $\sim 7-8$ is quite significant as shown by the shaded region in the figure. Thus, one can expect other probes like the 21-cm observation from the EoR will play an important role to reduce the uncertainties.

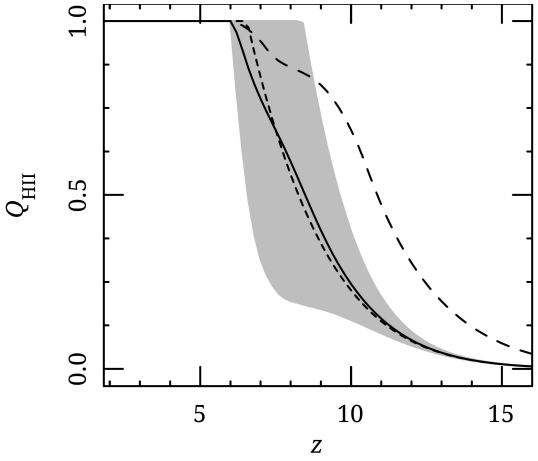

Figure 1.2: The figure is taken from Mitra et al. (2015). The figure shows the evolution of the volume filling factor as a function of redshift. The evolution of $Q_{\rm HII}$ (solid line) is consistent with the observations of Planck electron scattering optical depth and the high-redshift quasar absorption spectra blueward to the Lyα line. Shaded region represent $2-\sigma$ limits. The short-dashed curve represents the fiducial model of Mitra et al. (2015), while the long-dashed curve represents constraint from WMAP9 data.

1.3 Different probes of the EoR and observational constraints

Currently, there are a number of observations which provide constraints on this epoch. However, these constraints on the EoR are limited and unable to provide the details of the epoch. Also, most of these constraints from the observations related to the reionization epoch are model dependent. Here, we provide a brief description of different probes of the EoR.

- *Observations of the high-redshift quasars :*

  Observations of redshift $z \gtrsim 6$ quasar absorption spectra (Becker et al. 2001; Fan et al. 2006b, 2003; Goto et al. 2011; Gunn and Peterson 1965) provide strong constraints on the ionization state of the Universe during the final phase of the EoR. Absorption of the Lyα photons by the residual neutral hydrogen in the medium give rise to absorption features in the spectra of the background quasars. Even when the IGM neutral fraction $\gtrsim 10^{-4}$,

one expects complete absorption of photons blue-ward of the Lyα emission line in the quasar spectrum, which shows up as a trough-like feature in the observed SED of the quasar (Gunn and Peterson 1965). The first confirmed Gunn-Peterson trough was reported in Becker et al. (2001) in the SDSS sample. Till now, hundreds of quasars have been detected at redshift ~ 6 (Fan et al. 2006a; Mortlock et al. 2011a; Venemans et al. 2015), which makes it easy to identify the difference in the spectral features of the quasars above and below redshift 6. While there are pieces of evidence of the Gunn-Peterson trough in a quasar spectrum at $z > 6$, it is not clear whether that indicates a neutral IGM.

Though all these observations agree with the fact that the IGM is most likely be ionized to at $z \sim 6$ and there is a trend of increasing the neutral fraction at $z \gtrsim 6$, the controversy is related to the value of the neutral fraction. Fan et al. (2006a) studied the evolution of the ionization state of the IGM around $z \sim 6$ using the moderate resolution spectra of 19 quasars at redshift $5.74 < z < 6.42$ from the SDSS. The study suggested an increase of the mass averaged neutral fraction $\sim 10^{-3}$ at $z = 5.7$ to $\sim 10^{-2}$ at redshift $z \sim 6.2$. In addition, spectroscopic analysis of high-redshift bright quasars suggests a volume averaged neutral fraction $0.06 \pm 0.05(1\sigma)$ at redshift $z = 5.9$ (McGreer et al. 2015), which provide very strong evidence that reionization completed by redshift 6.

The observation of the quasar ULAS J1120+0641 at $z = 7.085$ shows the presence of Gunn-Peterson trough and a damping wing extending red-ward the Lyα line (Mortlock et al. 2011b). The expected near zone H II region around the quasar is expected to be smaller than similar quasars at redshift 6 (Bolton et al. 2011). These studies suggest a neutral fraction of the IGM to be $\gtrsim 0.1$. However, one should keep in mind that the predicted neutral fraction from this observation is a single data point and not necessarily represent the global mean neutral fraction at that redshift.

- *Observations of the cosmic microwave background radiation :*

  Another important constraint comes from the observations of the cosmic microwave background radiation (Komatsu et al. 2011; Planck Collaboration et al. 2014a). The CMBR photons, generated during the epoch of

recombination, scatter off the free electrons produced during the EoR. This scattering smooths the fluctuations in the CMBR temperature anisotropies and generates a polarized radiation on angular scales larger than 10°, which corresponds to the scale of the horizon at reionization (Komatsu et al. 2011; Zaldarriaga and Seljak 1997). In addition, the gravitational lensing of the CMBR too can be used to indirectly constrain reionization (Planck Collaboration et al. 2014b, 2015c).

The measurement of the large-scale CMBR polarization power spectrum provide the Thomson scattering optical depth τ. The optical depth is defined as,

$$\tau(z) = c\sigma_T \int_0^z n_e(z')dz'(dt/dz') \tag{1.12}$$

where σ_T is the Thompson scattering cross section, n_e is the free electron density. As the measured value of τ represents the integrated density of the electron, it can only provide limited information about the reionization history. Different reionization histories can produce same optical depth.

However, the observation of CMBR polarization can provide interesting constraints on reionization. The recently analyzed *Planck* data suggests the value of the measured optical depth as 0.066 ± 0.016 (Planck Collaboration et al. 2015b). For an instantaneous reionization model, the redshift of reionization is $8.8^{1.7}_{-1.4}$ (Planck Collaboration et al. 2015b). Thus, the observations of CMBR, alone with the quasar observation, suggest that the reionization process must be an extended process which starts at redshift ~ 15 and ends around redshift ~ 6 (Choudhury and Ferrara 2006; Fan et al. 2006b; Malhotra and Rhoads 2006; Mitra et al. 2011, 2012). In addition, CMBR may also contain the signature of patchy reionization at small angular scales ($< 0.1°$) (Santos et al. 2003).

- *Galaxies at high redshift :*

  One of the major uncertainties in the EoR is the sources of reionization. Among the various possible sources during the EoR, galaxies are assumed to provide the dominant contribution to the ionizing photons during the EoR. This assumption is motivated by the fact that the number of other possible

sources of ionizing photons, e.g., the QSOs, are known to be declining at $z > 6$. One must keep in mind that such an assumption can be quite uncertain at high redshifts because of lack of observational data and understanding of the physical processes. Thus, observation of the high-redshift galaxies gives the direct information of the reionization sources.

The main problem with the observation of $z > 6$ galaxies is that these are very faint and thus only galaxies with very high luminosity can be detected. By detecting a large number of galaxies at $z > 6$ using broad-band colour (Bouwens et al. 2015; Ellis et al. 2013) and narrow-band Lyα emission (e.g., Hu et al. 2010; Kashikawa et al. 2011), one can have a rough estimate of the production of the ionizing photons at that time. Using these estimations, one can predict ionization histories using analytical models like Mitra et al. (2015). However, as these models rely on many assumptions like the value of escape fraction and the clumpiness of the IGM, the predicted reionization histories are highly uncertain.

- Lyα *emitters :*

  Lyα emitters (LAE) are star-forming galaxies with a large fraction of flux in Lyα line. Studies like Raiter et al. (2010) show that the Lyα luminosity could be as large as 30-40% of the bolometric luminosity of the first generations of galaxies as they formed in low-metallicity environments. Although the Lyα flux from the LAEs are relatively weaker than the quasars, studies of the LAEs can still provide interesting constraints on the EoR as the number observed LAEs are quite large and thus can be used as a statistical probe of the EoR.

  The observation of 207 Lyα emitters at redshift 6.6 using the Subaru Telescope shows a clear evidence of the redshift evolution of the LAEs at $z > 6$ (Ouchi et al. 2010a). The decrease in Lyα luminosity by 30% from redshift 5.7 to 6.6 could be due to the change in the duty cycle, an increase in the halo mass or due to the reionization etc. However, to use LAEs as a reliable probe of the EoR, one has to understand the population of the LAEs and the evolution of the metallicity at lower redshifts. Ouchi et al. (2010a) claim the global neutral fraction to be less than 0.2 at redshift 6.6. The decrease in the Lyα luminosity at high redshift also provide a tentative evidence of

rapid evolution of the ionization fraction at $6 < z < 8$ (Choudhury et al. 2015; Dijkstra et al. 2011).

Studies like McQuinn et al. (2007a) consider clustering of LAEs in their reionization models and show that the detection of clustering can be used to constrain reionization. The study shows that 10 Mpc H II regions during EoR modulate the observed distribution of the emitters and enhance the measured clustering of LAEs. Such enhancement can not be connected to something other than reionization. The enhancement of clustering depends on the neutral fraction and also on the morphology of the H II bubbles. The detection of clustering signature in the LAEs survey and the observations of Lyman-break or Hα in the same field can confirm the reionization hypothesis.

In addition to these probes, there are a quite few other observations which can provide valuable inputs to constrain the EoR. A list of such probes could be, (1) observation of high-resolution Lyα forest at $z < 6$ (Hui and Haiman 2003; Raskutti et al. 2012; Theuns et al. 2002), (2) gamma-ray bursts (GRBs) (see, e.g., Bromm and Loeb 2006), (3) cosmic infrared and soft x-ray backgrounds (Dijkstra et al. 2004) etc.

1.4 Redshifted 21-cm signal as a probe of the EoR

While probes like the observations of $z > 6$ quasars, galaxies and the CMBR provide different types of information on the EoR, the redshifted H I 21-cm signal from the EoR is able to provide more details related to this epoch. We will refer the reader to reviews like Furlanetto et al. (2006); Morales and Wyithe (2010); Pritchard and Loeb (2012) for details. As this signal originates from the neutral hydrogen, it can probe the morphology of H I during reionization epoch and one can, in principle, directly image the neutral hydrogen during this time.

The global and statistical properties of the signal depend on various quantities like the ionization fraction, kinetic temperature, Lyα coupling, collisional and radiative coupling. The observed quantity in the 21-cm signal is the differential brightness temperature ($\delta T_{\rm b}$), which is the difference between the brightness

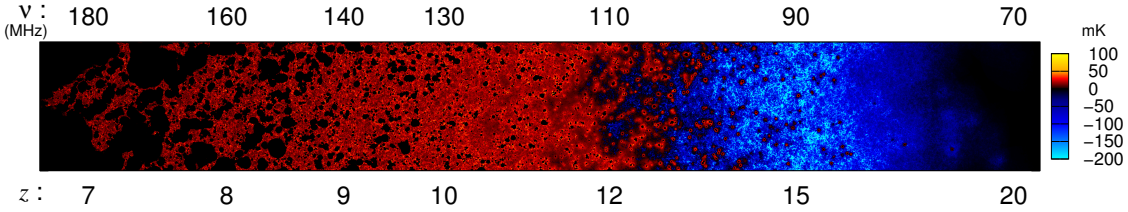

Figure 1.3: Differential brightness temperature slice along the frequency or redshift axis. This slice is generated from a simulation with box 200 cMpc/h for source model mini-QSO.

temperatures of the signal and the CMBR. Figure 1.3 shows the evolution of the brightness temperature maps along the frequency direction for a model of EoR developed later in the thesis. This light-cone slice is taken from a simulation with 200 cMpc/h box where the ionization is driven by stars within galaxies and the heating is driven by mini-quasar type sources. Just before cosmic dawn, the $\delta T_{\rm b}$ is zero due to the dominance of the radiative coupling over the collisional coupling. When the first sources formed in the Universe, $\delta T_{\rm b}$ deviates from zero due to strong Lyα coupling. Studies like Furlanetto et al. (2004a); Mesinger et al. (2014); Pritchard and Loeb (2012) show that the global averaged $< \delta T_{\rm b} >$ remains negative during the cosmic dawn and the first phase of reionization, as these sources are not able to heat up the IGM above the CMBR temperature. Eventually, the IGM gets heated above T_γ, which transforms the negative $< \delta T_{\rm b} >$ into a positive value. Around redshift 6, when the Universe got sufficiently ionized, $< \delta T_{\rm b} >$ vanishes again as the residual neutral hydrogen (in galaxies and very high-density regions) is negligible.

1.5 Main challenges of the 21-cm observations

While the redshifted 21-cm signal carries enormous information about the EoR, the signal itself is very difficult to deal with. As the signal is generated by the hyperfine transition of the neutral hydrogen atom, the strength is very weak compared to the other components like the astrophysical foregrounds, system noise, radio frequency interference (RFI) (Ghosh et al. 2015, 2012; Patil et al. 2014a). Thus, it is a challenging task to detect the cosmological 21-cm signal at

low frequencies.

While the signal is expected to be few $\sim 10-100$ mK, different astrophysical foregrounds could be four to five order larger than the signal (Bernardi et al. 2009, 2010; Choudhuri et al. 2014). Thus, foreground removal is one of the most challenging tasks for detecting the signal. Foreground contributions can be broadly divided into two components : (1) galactic synchrotron radiation, (2) extragalactic point sources. Among these two, the most dominating component is the galactic foreground which can contribute $\sim 70\%$ of the total foregrounds. On the other hand, extragalactic foregrounds can be dominating at angular scales less than few arcmin (Di Matteo et al. 2004).

The galactic diffuse synchrotron radiation (Shaver et al. 1999) is mainly contributed by two processes : (1) synchrotron emission due to the interaction of the galactic cosmic ray electrons and the magnetic field, (2) synchrotron emission from the supernova remnants in our galaxy. In addition, free-free emission (bremsstrahlung radiation) from the galactic diffused ionized gas can also contribute to the galactic foregrounds, however, the contribution is relatively small. A substantial contribution to the total foregrounds also comes from the unresolved extragalactic point sources like the radio galaxies, clusters etc.

In general, two approaches are followed to deal with the foregrounds: foreground removal and foreground avoidance. In foreground removal technique, the foreground is modeled very accurately and then subtracted from the total signal. However, it is often not possible to model the foreground sufficiently accurately such that one can detect the signal. The second approach is the foreground avoidance, where the main idea is to avoid the part of the signal in Fourier space which is contaminated by the foreground. This method works mainly because the foregrounds are confined in a "wedge" shape region in the Fourier space (Datta et al. 2010; Dillon et al. 2014; Pober et al. 2014; Trott et al. 2012). However, one has to keep in mind that the foreground avoidance technique could lead to discarding a substantial amount of data, which in turn can increase the variance.

In addition to the foregrounds, the system noise can also be significantly larger than the signal (e.g., Labropoulos et al. 2009). To reduce the system noise, one requires long integration times and a good baseline coverage of the interferometer. In addition, man-made radio frequency interference (RFI) from different communication devices like the cell phones can also significantly contribute to

the total signal. For interferometer like the GMRT, the RFI may be a serious difficulty for detecting the signal from the EoR (Paciga et al. 2011) and one needs a good model for the RFI to subtract it. Propagation of the signal through the ionosphere of the Earth can also introduce a stochastic error which can create additional complexity in 21-cm observations (Sokolowski et al. 2015b).

1.6 Modelling the 21-cm signal

Theoretical models, using analytical calculations (e.g., Furlanetto et al. 2004a; Paranjape and Choudhury 2014), semi-numerical simulations (Choudhury et al. 2009; Mesinger and Furlanetto 2007; Santos et al. 2008; Zahn et al. 2007), and numerical simulations involving radiative transfer (Baek et al. 2009; Ghara et al. 2015a; Iliev et al. 2006; McQuinn et al. 2007b; Mellema et al. 2006; Shin et al. 2008; Thomas et al. 2009) , are very useful to study the cosmic dawn and epoch of reionization. These simulations are useful for a detailed understanding of the redshifted 21-cm signal and the impact of various physical processes on the signal. These simulations generally combine prescriptions for the evolution of the matter distribution, star formation in the over-dense regions and recipe for the propagation of ionizing photos into the IGM. In other words, one requires information like, the evolution of the cosmic gas distribution, distribution of the radiating sources, their feedback on the star formation in subsequential times, enrichment of metals in the IGM that can modify the star formation history, propagation of the ionizing photons in the IGM. In the context of studying the epoch using the redshifted 21-cm signal, one also needs to have some idea about the Lyα emissivity and kinetic temperature of the IGM. Dealing with this huge parameter space makes the problem very challenging.

However, it is difficult to follow all the details of galaxy formation and evolution and their impact on the surrounding medium. The details of the star formation, metal enrichment, radiative feedback are difficult to implement in the simulations. It not only takes huge computational time, the parameters too are very uncertain. Thus, simulations are usually simplified by ignoring or simplifying many such complicated physical processes. One has to interpret the results from such simulations keeping these issues in mind.

1.6.1 Analytical models

Analytical models of the EoR are the simplest among the existing models of the EoR. These models are based on creating ionized bubbles around the sources like the galaxies. Studies like Bharadwaj and Ali (2005); Datta et al. (2007b) consider the IGM to be consist of many non-overlapping H II bubbles and thus these models are valid at the very beginning of the reionization when the ionized bubbles do not overlap with each other. However, models like Furlanetto et al. (2004b) account the overlaps between the individual H II bubbles using the excursion set formalism. This approach decides if a spherical region of radius R is ionized or not using the condition

$$\langle f_{\rm coll} \rangle_{\delta_L,R} \geq \zeta^{-1} \tag{1.13}$$

where δ_L is the linearly extrapolated desity contrast to present epoch.

These ionized bubbles can be used to obtain the power spectrum of the 21-cm signal. Paranjape and Choudhury (2014) improve this excursion set approach by using the fact that the haloes preferably form in high-density regions. This improved method is called the excursion sets peak (ESP) model.

Although these analytical models are very fast to explore the huge parameter space and also provide reasonable accuracy in the growth of the ionized regions, these methods have many drawbacks. For examples, these methods can not incorporate non-sphericity of the H II regions during the overlap phase, not able to account the effects of peculiar velocities of the gas in the IGM etc. These models also do not incorporate the calculations of the gas temperature and thus are not able to construct realistic 21-cm signal maps. Thus, one should use more realistic simulations to predict the 21-cm signal from the EoR using N-body simulations and radiative transfers.

1.6.2 Semi-numerical models

Semi-numerical models are one level of improvement on the analytical models of the EoR. Models like Geil and Wyithe (2008); Mesinger and Furlanetto (2007); Santos et al. (2010) are based on generating dark matter density field within a large simulation box using the perturbation theory, calculating the collapse

fraction at each grid points of the simulation box using methods like extended Press-Schechter model (Bond et al. 1991) and then generating ionization fields using the excursion set formalism. Other semi-numerical models like Choudhury et al. (2009); Zahn et al. (2007) use N-body simulations and find the haloes inside the simulation box using halo finding algorithm like FOF or SO and then create the ionization field using the excursion set formalism.

All these methods calculate the spherically averaged collapse fraction $\langle f_{\rm coll} \rangle_R$ at each grid points of the simulation box for a wide range of radius R. If equation 1.13 holds for any value of R, then the corresponding grid point is set as completely ionized. Otherwise, the grid point is associated with a neutral fraction of $\zeta \langle f_{\rm coll} \rangle_{R_{\rm cell}}$ where $R_{\rm cell}$ is the size of the grid cell. In addition, studies like Choudhury et al. (2009); Sobacchi and Mesinger (2014) also account for the recombination process which may change the H I topology significantly.

Although these semi-numerical simulations use some assumptions to simplify the scenarios, these are fast enough to explore the parameter space of the EoR with many realizations. Studies like Majumdar et al. (2014) shows that the semi-numerical calculations are quite similar to the full radiative transfer calculations. This suggests that one can use the fast semi-numerical schemes to constrain the EoR parameters using sophisticated parameter estimation methods like the Markov chain Monte Carlo (MCMC) (Greig and Mesinger 2015).

1.6.3 Numerical simulations

Most numerical simulations use the density and velocity fields from a N-body simulation and use a radiative transfer to generate the ionization field in the simulation box. Algorithm like the C2-RAY (Mellema et al. 2006), FLASH (Fryxell et al. 2000), TRAPHIC (Pawlik and Schaye 2008), START (Hasegawa and Umemura 2010), SimpleX2 (Paardekooper et al. 2010), McQuinn et al. (2007b); Razoumov and Cardall (2005); Trac and Cen (2007) track photons from different sources and iteratively solve the time evolution of the neutral fraction at different grid points in the simulation box. On the other hand, codes like CRASH (Maselli et al. 2003), LICORICE (Baek et al. 2009) are based on a Monte Carlo technique. The method developed by Gnedin and Abel (2001) use optically thin variable Eddington tensor (OTVET) approximation to implement the radiative

transfer. In general, reionization models require large simulation boxes with size at least few hundred comoving megaparsecs to avoid any difficulties related to the cosmic variance. Running of a N-body simulation and the full radiative transfer algorithm is computationally very expensive and thus, it is very difficult to explore huge parameter space of the EoR with such methods.

However, there are other radiative transfer methods which work under a number of approximations like spherical symmetry in the photon propagation. Methods like Ghara et al. (2015a); Thomas et al. (2009) use a 1D radiative transfer to create the ionization bubbles around the sources formed in the dark matter haloes. While these methods create a spherically symmetric 21-cm pattern around the sources, these can also take care the overlap between the individual regions properly. These codes are relatively faster than the full radiative transfer codes and thus have the potential to be used for parameter estimation.

One of the drawbacks of these numerical schemes is finding the low-mass haloes in large simulation boxes. While simulating the epoch of reionization, it is very important to resolve the lowest mass haloes which are likely to be the site of first stars like population III stars and small galaxies. In the presence of molecular hydrogen, source formation is possible in haloes with mass as small as $\sim 10^6$ $M_\odot$. However, the molecular hydrogen can be destroyed easily by the Lyman-Werner photons from the very first sources in the Universe. In that case source formation is dominant in haloes with mass $\gtrsim 10^8$ $M_\odot$ due to atomic cooling. Spatially resolving such low-mass haloes in a simulation box with the size of few hundreds of cMpc is computationally a very expensive task. Thus, most of the studies avoid the small mass haloes or use some simple prescriptions to find the small mass haloes.

1.7 Current constrains from the 21-cm observations

Till now, there have been mainly two approaches to detect the redshifted 21-cm signal from the cosmic dawn and EoR. The first one measures the average brightness temperature of the signal or so-called "global" signal. Experiments like EDGES (Bowman and Rogers 2010), SARAS (Patra et al. 2015), BigHorns

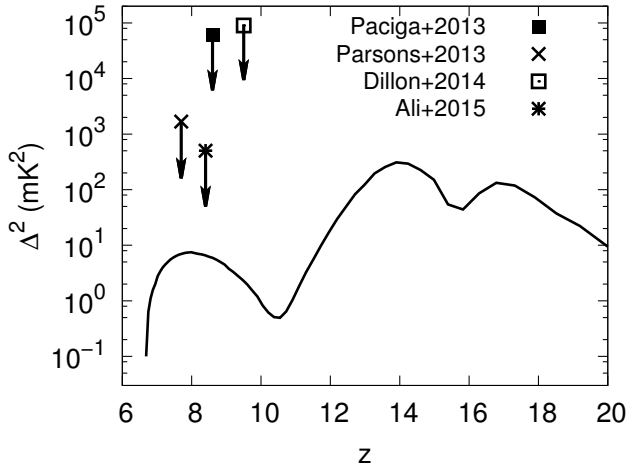

Figure 1.4: The figure shows the current constrains from the redshifted 21-cm observations with various radio telescopes. The solid curve represent the dimensionless power spectrum of the differential brightness temperature at scale $k = 0.1$ Mpc^{-1} as a function of redshift. The power spectrum is generated using a mini-QSO source model within a simulation of size box 200 cMpc/h.

(Sokolowski et al. 2015a), SciHi (Voytek et al. 2014) and LEDA (Greenhill and Bernardi 2012) have been designed to detect the global averaged 21-cm signal with single antenna elements. These observations generally rely on the auto-correlation of a small number of dipoles, although recent works like Presley et al. (2015); Vedantham et al. (2015) have claimed that interferometric cross-correlation may also work to detect the sky-averaged 21-cm signal. While the signal is expected to be ~ 10 mK, it is contaminated by huge galactic and extragalactic foregrounds with strength > 100 K. Till date, the best constraints come from the observation of EDGES (Bowman and Rogers 2010), which report an all-sky spectrum between redshift $6 < z < 13$. This experiment excludes rapid reionization with the redshift extent $\Delta z < 0.06$ with 95% confidence level.

The second approach is to detect the signal in terms of the statistical quantities like the power spectrum of the signal using bigger interferometers. Experiments like GMRT, LOFAR, PAPER, 21CMA, MWA are engaged in detecting the signal in terms of the statistical quantities. So far the achievements can be listed as:

- Observations with the GMRT were one of the first to be reported (Paciga

et al. 2013, 2011). It used a band width coverage of 139.3 to 156 MHz. The experiment calculated a $2-\sigma$ upper limit of the signal power spectrum at redshift 8.6 as $(248 \text{ mk})^2$ at mode $k = 0.5\ h\ \text{Mpc}^{-1}$.

- Parsons et al. (2013) presented limits on the 21-cm power spectrum from three month long observations with the interferometer PAPER using 32 antennae. They provided a $2-\sigma$ upper limit of $(41 \text{ mK})^2$ for $k = 0.27\ h\ \text{Mpc}^{-1}$ at redshift 7.7. This study claimed to be inconsistent with the cold reionization scenario and predicted an X-ray heated IGM at redshift 7.7.

- So far the best upper limit on the redshifted 21-cm signal power spectrum is 502 mK^2 at redshift ~ 8.4 (Ali et al. 2015) at scales $0.15 < k < 0.5\ h\ \text{Mpc}^{-1}$ using a 135 days observation with the 64 element PAPER instrument. Similar to Parsons et al. (2013), this observation also ruled out little or no heating scenario of the neutral IGM at $z \sim 8.4$ (Pober et al. 2015).

- In addition to these measurements at the lower end of the epoch of reionization, several efforts have been put to measure the power spectrum from relatively higher redshifts. Dillon et al. (2014) put the upper limit of $(300 \text{ mK})^2$ at scale $k = 0.046\ \text{Mpc}^{-1}$ at redshift 9.5 using the 32-tile MWA pathfinder for 22 hours of observation.

- Ewall-Wice et al. (2016) have done even deep observation at redshift range of 11.6 to 17.9 with the 128-tile MWA. After 3 hours of integration, they present a upper limit of $(10^4 \text{ mK})^2$ at scale $k < 0.5\ h\ \text{Mpc}^{-1}$, though it is limited by calibration errors.

Figure 1.4 shows the current constraints on the 21-cm power spectrum from different observations. The solid curve represents the expected power spectrum of the 21-cm signal at scale $k = 0.1\ \text{Mpc}^{-1}$. The power spectrum corresponds to a mini-QSO source model within a simulation of size box 200 cMpc/h. One can see that the current best constraint is still 1-2 order larger than the expected signal. One needs a better understanding of the systematics, better methods to deal with the foregrounds etc to put better constraints on the EoR 21-cm signal.

1.8 Thesis outline

In this section, we briefly describe the summaries of Chapters 2-7 of this thesis. The main scientific contribution of the thesis is modeling the redshifted 21-cm signal from the cosmic dawn and EoR using semi-numerical simulations. In particular, we have developed a semi-numerical code to generate the brightness temperature distribution of the redshifted 21-cm signal using dark matter simulations and a 1D radiative transfer (RT) code. The RT code tracks the time evolution of the ionization fraction of different ionization states of hydrogen and helium and the kinetic temperature of gas in the IGM around individual sources. Our analysis is able to account for the spin temperature fluctuations arising from inhomogeneous X-ray heating and Lyα coupling during the cosmic dawn and EoR. A brief summary of Chapters 2-7 is given below.

Chapter 2 : In Chapter 2, we briefly describe the redshifted 21-cm signal from the neutral hydrogen from the IGM before we describe our semi-numerical formalism to generate the brightness temperature maps self-consistently. We describe the one-dimensional radiative transfer method which is used to produce the temperature and ionization profiles of hydrogen and helium around the isolated sources. Then we discuss the method to use this one-dimensional radiative transfer for generating the brightness temperature maps from the outputs of the N-body dark matter simulations.

Chapter 3 : In Chapter 3, we have considered different source models like galaxies, mini-QSO and used the semi-numerical method, described in Chapter 2, to generate the brightness temperature maps. The chapter mainly focuses on two topics: (i) study the effect of spin temperature fluctuation due to the inhomogeneous X-ray heating and Lyα coupling, (ii) effect of redshift-space distortion on the H I 21-cm signal. The studies are mainly done in terms of the spherically averaged power spectrum of the brightness temperature distribution.

Chapter 4 : In this chapter, we have considered another important line of sight effect (the "light-cone effect") and studied its impact on the spherically averaged power spectrum of the 21-cm signal. The study is done for different models and observational bandwidth.

Chapter 5 : The chapter mainly focuses on the detectability of very early sources in 21-cm observation in the presence of system noise and astrophysical

foregrounds with radio telescope like the SKA1-low. In particular, we have considered various sources like population III stars, galaxies, mini-QSOs and HMXBs and studied their detectability using the visibilities.

Chapter 6 : In this chapter, we simulate the expected signal for different kind of sources, system noise and foregrounds appropriately. The chapter mainly focuses on the detectability of these sources using imaging techniques and predict new observational strategies for future 21-cm observations.

Chapter 7 : Finally in Chapter 7 we briefly summarize the thesis and describe the possible future extensions of the works presented in the thesis.

2 | Semi-numerical method using a 1D radiative transfer

A major part of this chapter is based on Ghara et al. (2015a).

2.1 Introduction

The expected 21-cm signal depends not only on the amount of neutral hydrogen but also on the spin temperature $T_{\rm S}$ of H I which in turn depends on the kinetic temperature $T_{\rm K}$ of the gas and Lyα photon flux. Many reionization models (Battaglia et al. 2013; Choudhury et al. 2009; Datta et al. 2012a; Furlanetto et al. 2004a; Iliev et al. 2014; McQuinn et al. 2006; Mesinger and Furlanetto 2007) simply ignore the effect of the spin temperature fluctuation by assuming $T_{\rm S} \gg T_{\gamma}$ and deal with the amount of neutral hydrogen in the IGM. Under these assumptions, it is easier to build the models for the redshifted 21-cm maps. However, these models may not be appropriate at the cosmic dawn and the first phase of reionization, when the contribution from the spin temperature fluctuation is non-negligible.

The 21-cm signal from H I is sensitive to various quantities such as the number density and clustering of sources, their ionizing, heating and coupling efficiencies, the escape fraction of photons at various frequency bands, various feedback effects etc. These quantities are eventually parametrized in terms of the collapse fraction of dark matter haloes, the fraction of baryons converted into stars, the stellar initial mass function, Lyα, UV and X-ray luminosities, X-ray spectral index etc (Mesinger et al. 2014; Morales and Wyithe 2010; Pritchard and Loeb 2012). In addition, the line of sight effects such as the peculiar velocities and evolution of

the 21-cm signal could also affect the signal significantly. It is thus very important to model the expected H I 21-cm signal properly in order to interpret the observations. A large amount of theoretical modelling and simulations is needed to explore all possible scenarios and such analyses are expected to play a major part in designing 21-cm experiments.

In this chapter, we will describe the method to generate the brightness temperature maps self-consistently from the output of a N-body simulation and using a one-dimensional radiative transfer code. We briefly describe the basics of 21-cm signal in Section 2.2. We then discuss the detailed methodology for modelling the signal including the N-body simulation (Section 2.3.1), the method to incorporate small mass haloes (Section 2.3.2), the source model (Section 2.4), radiative transfer code for generating the maps around isolated sources (Section 2.5), signal profile around isolated sources (Section 2.6) and the generation of global maps (Section 2.7).

2.2 Basics of the 21-cm signal

The $1s$ ground state of a neutral hydrogen atom exhibits hyperfine splitting into singlet and triplet states due to the interaction of the magnetic moments of electrons and protons in the atoms. The energy difference between these two states is 5.87433 μeV and transition from the triplet to singlet state gives rise to a photon with wavelength $\lambda = 21$ cm. If n_0 and n_1 be the number density of H I in singlet and triplet levels with the degeneracy factors g_0 and g_1 respectively, then the spin temperature $T_{\rm S}$ of the neutral hydrogen gas can be defined as,

$$\frac{n_1}{n_0} = \frac{g_1}{g_0}\ \exp\left(-\frac{T_\star}{T_{\rm S}}\right) \tag{2.1}$$

where $T_\star = h\nu_{21\rm cm}/k_B = 0.0681$ K and k_B is the Boltzmann constant.

The spin temperature $T_{\rm S}$ is determined by the coupling of neutral hydrogen gas with CMBR photons by Thomson scattering, Lyα coupling and collisional coupling. Considering all these coupling effects, the spin temperature can be written in the following form (Field 1958; Furlanetto and Oh 2006)

$$T_{\rm S}^{-1} = \frac{T_\gamma^{-1} + x_\alpha T_\alpha^{-1} + x_c T_{\rm K}^{-1}}{1 + x_\alpha + x_c}, \tag{2.2}$$

where $T_{\rm K}$ is the kinetic temperature of the gas and T_α is the colour temperature of the Lyα photons which, in most cases of interest, is coupled to $T_{\rm K}$ by recoil during repeated scattering. The quantities x_c and x_α are the coupling coefficients due to collisions and Lyα scattering respectively. The collision efficiency x_c includes both the collisions between neutral hydrogen atoms (H − H) and hydrogen atom with free electrons in the medium (H − e) and can be written as (Hirata and Sigurdson 2007),

$$x_c = \frac{4T_\star}{3A_{10}T_\gamma}\left[\kappa^{\rm HH}(T_{\rm K})n_{\rm H} + \kappa^{\rm eH}(T_{\rm K})n_e\right], \tag{2.3}$$

where $A_{10} = 2.85 \times 10^{-15}$ s^{-1} is the spontaneous Einstein A-coefficient, $n_{\rm H}$ and n_e be the local number densities of neutral hydrogen and electrons respectively. The table of $\kappa^{\rm eH}$ as a function of $T_{\rm K}$ is taken from Furlanetto and Furlanetto (2007) and table of $\kappa^{\rm HH}$ is taken from Allison and Dalgarno (1969); Zygelman (2005).

The most important process which couples $T_{\rm S}$ to $T_{\rm K}$ during reionization is the Wouthysen-Field effect (Chuzhoy et al. 2006a; Field 1958; Hirata 2006; Madau et al. 1997; Wouthuysen 1952). The Lyα coupling coefficient in this case is given by

$$x_\alpha = \frac{16\pi^2 T_\star e^2 f_\alpha}{27A_{10}T_\gamma m_e c}J_\alpha, \tag{2.4}$$

where J_α is the Lyα flux density, $f_\alpha = 0.4162$ is the oscillator strength for the Lyα transition, m_e and e are the mass and charge of the electron respectively.

Usually the redshifted 21-cm signal from neutral hydrogen is measured in terms of the deviation of 21-cm brightness temperature from the brightness temperature of background CMBR along a line of sight. The differential brightness temperature observed at a frequency $\nu_{\rm obs}$ along a direction $\hat{\mathbf{n}}$ is given by (Furlanetto et al. 2006; Madau et al. 1997)

$$\begin{aligned}\delta T_{\rm b}(\nu_{\rm obs}, \hat{\mathbf{n}}) \equiv \delta T_{\rm b}(\mathbf{x}) = 27\ x_{\rm HI}(z,\mathbf{x})[1+\delta_{\rm B}(z,\mathbf{x})]\left(\frac{H}{dv_r/dr + H}\right) \\ \times \left(\frac{\Omega_B h^2}{0.023}\right)\ \left(\frac{0.15}{\Omega_m h^2}\frac{1+z}{10}\right)^{1/2}\left[1 - \frac{T_\gamma(z)}{T_{\rm S}(z,\mathbf{x})}\right]\ {\rm mK},\end{aligned} \tag{2.5}$$

where $\mathbf{x} = r_z\hat{\mathbf{n}}$ and $1 + z = 1420\ {\rm MHz}/\nu_{\rm obs}$, with r_z being the comoving radial distance to redshift z. The quantities $x_{\rm HI}(z,\mathbf{x})$ and $\delta_{\rm B}(z,\mathbf{x})$ denote the neutral

hydrogen fraction and the density contrast in baryons respectively at point $\mathbf{x}$ at a redshift z. The CMBR temperature at a redshift z is denoted by $T_\gamma(z) = 2.73 \times(1+z)$ K and $T_{\rm S}$ is the spin temperature of neutral hydrogen. The third term in the right-hand side expression represents the effect of line of sight peculiar velocities (Barkana and Loeb 2005a; Bharadwaj and Ali 2004) which essentially maps the point $\mathbf{x}$ in real-space to a point $\mathbf{s}$ in the redshift-space, the mapping being determined by the velocity gradient along the line of sight dv_r/dr . We will discuss how to account for this effect in Section 3.2 of Chapter 3.

The primary goal of the first generation radio telescopes is to measure the fluctuations in $\delta T_{\rm b}$ using the spherically averaged power spectrum $P(k)$ which is defined as

$$\langle \delta\hat{T}_{\rm b}(\mathbf{k}) \delta\hat{T}_{\rm b}^{\star}(\mathbf{k}') \rangle = (2\pi)^3 \delta_D(\mathbf{k}-\mathbf{k}') P(k), \tag{2.6}$$

where $\delta\hat{T}_{\rm b}(\mathbf{k})$ is the Fourier transform of $\delta T_{\rm b}(\mathbf{x})$ defined in equation (2.5). The dimensionless power spectrum is defined as $\Delta^2(k) = k^3 P(k)/2\pi^2$ which also represents the power per unit logarithmic interval in k.

In many studies of reionization, particularly those dealing with later stages (Battaglia et al. 2013; Choudhury et al. 2009; Datta et al. 2012a; Furlanetto et al. 2004a; Iliev et al. 2014; McQuinn et al. 2006; Mesinger and Furlanetto 2007), one assumes the Lyα coupling to be highly efficient and uses the approximation $T_{\rm S} \approx T_{\rm K}$. In addition, if the IGM is assumed to be heated substantially compared to the CMBR ($T_{\rm K} \gg T_\gamma$), then the term $(T_{\rm S} - T_\gamma)/T_{\rm S} \to 1$ in equation (2.5) and hence one obtains the simple expression where $\delta T_{\rm b}$ tracks the neutral hydrogen distribution $x_{\rm HI}(1+\delta_{\rm B})$. These assumptions, however, have been shown not to hold in early stages of reionization where the Lyα coupling may not be uniformly strong in all locations and not all regions of the IGM will be heated uniformly (Baek et al. 2010; Santos et al. 2008). This would lead to variations in $T_{\rm S}$ and hence would affect the fluctuations in the 21-cm signal. In our semi-numerical method, we take all these effects into account using a combination of N-body simulations and a one-dimensional radiative transfer code.

2.3 Numerical simulations

The method we have used for simulating the 21-cm brightness temperature signal is essentially based on (i) obtaining the dark matter density field and the distri-

bution of collapsed haloes from a N-body simulation, (ii) assigning luminosities to sources in these dark matter haloes and (iii) using a one-dimensional radiative transfer code to obtain the neutral hydrogen and spin temperature maps.

2.3.1 N-body simulation

We have performed dark matter N-body simulations using the publicly available CUBEP^{3}M[1] (Harnois-Déraps et al. 2013) which is essentially a massively parallel particle-particle-particle-mesh (P^{3}M) code. This code is fortran90 based and is the successor to the N-body simulation code PMFAST (Merz et al. 2005). CUBEP^{3}M incorporate the particle-particle interaction at the sub-grid level and solved Poisson's equations on a two level mesh. While the long range gravity force is computed on a coarse grid, the short range and the particle-particle interaction are solved on fine grids (called *tiles*). Initialization of the particle positions and velocities at redshift $z = 200$ was done by using CAMB transfer function[2] (Lewis et al. 2000) and employing Zel'dovich approximation. For example, the fiducial simulation used in Chapter 3 (for the study of the effect of redshift-space distortion on the signal) contains 768^3 particles in a box of size 100 h^{-1} cMpc with 1536^3 grid points. The mass resolution of the dark matter particles in the simulation is $M_{\rm part} = 1.945 \times 10^8\, h^{-1}\, {\rm M}_\odot$. The simulation generates snapshots at $25 \geq z \geq 6$ in equal time gap of 10^7 years. The output at each snapshot consists of the density and velocity fields in a grid which is 8 times coarser than the simulation grid (along the side). The code is also equipped with a run time halo finder which identifies haloes within the simulation volume using spherical overdensity algorithm. We assume that the smallest halo at least contains 20 dark matter particles. As far as the baryonic density field is concerned, we simply assume that the baryons trace the dark matter, i.e., each dark matter particle is accompanied by a baryonic particle of mass $(\Omega_B/\Omega_m) \times M_{\rm part}$. Though this assumption is not valid in very small scales, i.e., scales comparable to or smaller than the local jeans scale, it probably works fine at large scales which are of our interest.

The main difficulty with our simulation is that the volume does not contain small mass haloes (e.g., those with $M_{\rm halo} \sim 10^8\, {\rm M}_\odot$) which are believed to be

[1] `http://wiki.cita.utoronto.ca/mediawiki/index.php/CubePM`
[2] `http://camb.info/`

driving the reionization at early stages. Resolving such small haloes requires simulations of very high dynamic range which are beyond the computing power we have access to. In order to address this issue, we have used a sub-grid model to include the small mass haloes in our simulation box, as described in Section 2.3.2. The minimum halo mass resolution achieved in this case is $\sim 10^8\,\mathrm{M}_\odot$, which is helpful in probing the effects of small mass haloes at early stages.

2.3.2 Small mass haloes using sub-grid model

In this section, we describe the method used to obtain small mass haloes (i.e., smaller than that allowed by the dark matter particle mass of the simulation) using a sub-grid recipe. This is mainly done using the extended Press-Schechter model of Bond et al. (1991) and hybrid prescription of Barkana and Loeb (2004). The steps are following,

(1) First, the non-linear overdensity at each grid point is calculated from the mass density distribution, obtained from the N-body simulation,

$$\delta_{\rm NL}(z,\mathbf{x}) = \rho(z,\mathbf{x})/\bar{\rho}(z) - 1, \tag{2.7}$$

where $\rho(z,\mathbf{x})$ is the mass density at comoving position $\mathbf{x}$ at redshift z and $\bar{\rho}(z)$ is the mean mass density at that redshift.

(2) If the comoving volume and non-linear overdensity of a cell are $V_{\rm cell}$ and $\delta_{\rm NL}$ respectively, then the Lagrangian cell size $R_{\rm cell}$ corresponding to that cell is given by the relation

$$\frac{4\pi}{3}R_{\rm cell}^3 \times \bar{\rho}(z) = (1+\delta_{\rm NL})V_{\rm cell} \times \bar{\rho}(z). \tag{2.8}$$

(3) The linearly extrapolated overdensity δ_L, corresponding to $\delta_{\rm NL}$, is calculated by solving the following parametric equations (e.g., Ahn et al. 2015)

$$\delta_{\rm NL} = \left(\frac{10\delta_L}{3(1-\cos\theta)}\right)^3 - 1, \;\; \delta_L = \frac{3\times 6^{2/3}}{20}\left(\theta - \sin\theta\right)^{2/3}, \tag{2.9}$$

when $\delta_{\rm NL}(z,\mathbf{x}) > 0$, and

$$\delta_{\rm NL} = \left(\frac{10\delta_L}{3(\cosh\theta-1)}\right)^3 - 1, \;\; \delta_L = \frac{3\times 6^{2/3}}{20}\left(\sinh\theta - \theta\right)^{2/3}, \tag{2.10}$$

when $\delta_{\rm NL}(z,\mathbf{x}) < 0$.

(4) According to the extended Press-Schechter model (Bond et al. 1991), the collapse fraction (i.e. the fraction of mass in collapsed objects) at $\mathbf{x}$ is given by,

$$f_{\rm coll}^{\rm PS}(z,\mathbf{x};M_{\rm min}) = {\rm erfc}\left(\frac{\delta_c(z)-\delta_L(z,\mathbf{x})}{\sqrt{2(\sigma^2_{R_{\rm min}}-\sigma^2_{R_{\rm cell}})}}\right), \tag{2.11}$$

where $\sigma^2_{R_{\rm cell}}$ is the variance of the mass $M_{\rm cell}$, enclosed in a sphere of comoving radius $R_{\rm cell}$ and $\sigma^2_{R_{\rm min}}$ is variance to the minimum halo mass $M_{\rm min}$ that can host a galaxy. The parameter $\delta_c(z)$ is the critical overdensity for halo collapse at redshift z. The minimum mass in our study is taken to be (e.g., Barkana and Loeb 2001b)

$$M_{\rm min} = 3\times10^9(1+z)^{-1.5}{\rm M}_\odot. \tag{2.12}$$

This implies a threshold mass of $\sim 10^8$ $\rm M_\odot$ at $z\sim 10$, appropriate for studying haloes which can cool via atomic hydrogen transitions.

(5) While $f_{\rm coll}^{\rm PS}(M_{\rm min})$ can be worked out analytically in a straightforward manner, the mass function of Sheth and Tormen (1999) provides a much better match with simulations. Thus we follow hybrid prescription of Barkana and Loeb (2004) and normalize the collapse fraction to match with the simulation result:

$$f_{\rm coll}(z,\mathbf{x};M_{\rm min}) = \frac{\bar{f}^{\rm ST}(z)}{\bar{f}^{\rm PS}(z)}{\rm erfc}\left(\frac{\delta_c(z)-\delta_L(z,\mathbf{x})}{\sqrt{2(\sigma^2_{R_{\rm min}}-\sigma^2_{R_{\rm cell}})}}\right), \tag{2.13}$$

where $\bar{f}^{\rm PS}$ and $\bar{f}^{\rm ST}$ are the mean collapse fraction according to Press-Schechter and Sheth-Tormen prescriptions respectively.

(6) As we have the collapse fraction at each cell inside the simulation box, the total mass within haloes with mass above $M_{\rm min}$ in each cell can be obtained from

$$M_{\rm halo}(z,\mathbf{x}) = f_{\rm coll}(z,\mathbf{x};M_{\rm min})\times(1+\delta_{NL}(z,\mathbf{x}))V_{\rm cell}\times\bar{\rho}(z). \tag{2.14}$$

For example, in the fiducial simulation used in Chapter 3, we prepare a new halo list, where small mass haloes (smaller than the smallest halo identified in the box, i.e., $3.89\times10^9\,h^{-1}\,{\rm M}_\odot$) are obtained from this subgrid prescription and haloes heavier than $3.89\times10^9\,h^{-1}\,{\rm M}_\odot$ are obtained directly from the simulations using spherical overdensity method.

2.4 Source selection

The stars residing in the galaxies are believed to be the major source of ionizing photons that completes the hydrogen reionization process of the universe. The dark matter haloes are the most suitable place to form galaxies but not all of them will contain luminous sources. For galaxy formation to proceed, the gas is required to be cooled below their virial temperature by atomic (or molecular) cooling which may not be possible in the smallest mass haloes. Typically, the minimum mass of haloes which can cool via atomic hydrogen is $\sim 10^8\,\mathrm{M}_\odot$ while the same value can be much smaller $\sim 10^6\,\mathrm{M}_\odot$ in the presence of hydrogen molecules. In addition, there could be further suppression of star formation in haloes lighter than $\sim 10^9\,\mathrm{M}_\odot$ which are residing in ionized regions because of radiative feedback.

The relation between the dark matter halo mass and the galaxy luminosity of these early galaxies are all very uncertain. The fraction of baryons $f_\star$ residing within the stars in a galaxy depends on the metallicity and mass of the galaxy. There is no well-known relation between the stellar mass and total mass of the galaxies at very high redshifts. For simplicity, here we have assumed $f_\star$ to be constant throughout the reionization epoch and its value is chosen such that the resulting reionization history is consistent with the constraints obtained from CMBR polarization measurements. In case we work with varying $f_\star$ in some of the simulation models, we will state that explicitly. The stellar mass of a galaxy corresponding to a dark matter halo of mass $M_{\rm halo}$ is

$$M_\star = f_\star \left(\frac{\Omega_B}{\Omega_m}\right) M_{\rm halo}. \tag{2.15}$$

Given $M_\star$, one can calculate the spectral energy distribution (SED) of stellar sources in a galaxy using stellar population synthesis codes. However, the SED will depend upon the initial metallicity and the stellar IMF, both of which evolve with time. For example, stars in very first galaxies are expected to be metal-poor (Finkelstein et al. 2009; Lai et al. 2007) and short-lived (Meynet and Maeder 2005). Eventually, they enrich the ISM with metals which changes the nature of subsequent star formation. Since tracking the evolution of metallicity self-consistently is not straightforward, we have taken the best fit mass-metallicity

relation from Dayal et al. (2009) and Dayal et al. (2010)

$$\frac{Z}{Z_\odot} = (0.25 - 0.05\delta z)\ \log_{10}\left(\frac{M_\star}{\mathrm{M}_\odot}\right) - (2.0 - 0.3\delta z), \tag{2.16}$$

where $\delta z = (z - 5.7)$. The evolution of stellar IMF of high-redshift galaxies too is not well constrained. For our study, we assume that the stars follow a Salpeter IMF with mass range 1 to 100 $\mathrm{M}_\odot$.

The UV and NIR spectral energy distributions of the stellar sources in galaxies are generated using the code PEGASE2[1] (Fioc and Rocca-Volmerange 1997) which computes the galactic SED using standard star formation scenarios for different initial metallicities, IMF and star formation history at different epochs. The lifetime of the stars in the galaxy may vary with metallicity and mass (Meynet and Maeder 2005). For convenience, we set the stellar lifetime to be 10^7 years which is the time difference between two simulation snapshots.

The dotted blue curve in Figure 2.1 shows the intrinsic SED of the stellar component in a galaxy with stellar mass 10^8 $\mathrm{M}_\odot$ with metallicity 0.1 $Z_\odot$. The SED peaks around hydrogen ionization wavelength and falls sharply for higher energies ($\gtrsim$ 50 eV). Thus, in the absence of any other processes, these galaxies can only ionize H I and He I, however, they are unlikely to be efficient sources of He II ionization and heating of the IGM.

These galaxies can produce photons of higher energies if they harbour accreting (supermassive or intermediate mass) black holes at the centre. In that case, these galaxies will behave as mini-quasars and will produce X-rays with power-law SED $E^{-\alpha}$ (Elvis et al. 1994; Laor et al. 1997; Vanden Berk et al. 2001; Vignali et al. 2003). There could be other sources of X-rays in galaxies like the HMXBs. These have a very different SED in the X-ray band (Fragos et al. 2013a,b) and thus show very different effects on heating and ionization (Fialkov et al. 2014). Another major source of X-ray photons could be the hot interstellar medium within early galaxies (Pacucci et al. 2014). The impact of X-rays from the hot interstellar medium is similar to those from the mini-quasar like sources, as we will see later in Chapter 3. This is because of the fact that the hot interstellar medium produces a significant number of soft X-ray photons similar to mini-quasar like sources. The HMXBs, on the other hand, show very different signatures since they do not contain any significant amount of soft X-rays.

[1] `http://www2.iap.fr/pegase/`

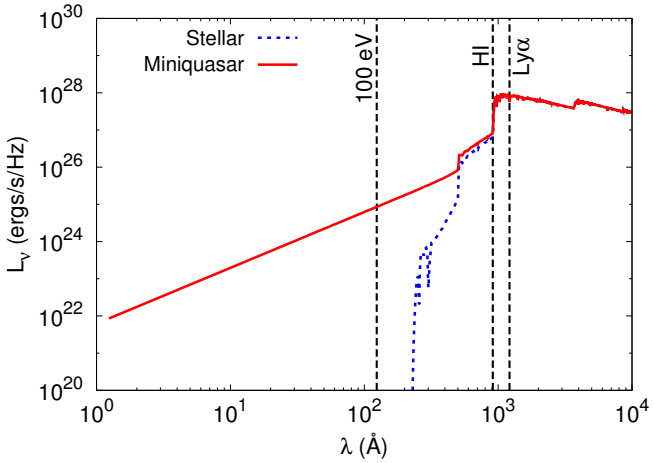

Figure 2.1: The SED of a galaxy of mass 10^8 $M_\odot$ and metallicity 0.1 $Z_\odot$. The dotted blue curve shows the stellar-like component, while the solid red curve shows the SED of the mini-quasar like component. We have assumed the mini-quasar to emit 5% of the UV energy in X-ray band with a power law SED (in this case the power law index α is 1.5). The vertical dashed lines correspond to energies 10.2 eV, 13.6 eV and 100 eV respectively.

Let us assume the UV spectrum to be spanning from 10.2 eV to 100 eV in energy band, and the X-ray spectrum to span from 100 eV to 10 keV. Let f_X be the ratio of X-ray to UV luminosity from the sources

$$f_X = \frac{\int_{100\ \mathrm{eV}}^{10\ \mathrm{keV}} I(E)dE}{\int_{10.2\ \mathrm{eV}}^{100\ \mathrm{eV}} I(E)dE}, \tag{2.17}$$

where $I(E)$ is the SED of the galaxy. Let us denote the SED of the stellar component by $I_\star(E)$, which in our case is computed using the stellar population synthesis code PEGASE2. We have seen from Figure 2.1 that this component does not contribute significantly to the X-rays, i.e., to the numerator of the above equation. The SED of the mini-quasar like component is assumed to have a power law form with spectral index α,

$$I_q(E) = A\ E^{-\alpha}, \tag{2.18}$$

where A is a normalisation constant to be determined in terms of f_X and α. The

parameter f_X in our model can be related to the black hole (BH) to galaxy mass ratio. Recent observations of high-redshift quasars show that accretion rate of black holes are close to the Eddington limit (e.g., Willott et al. 2010). In addition observations of local galaxies show that the mass ratio of the BH and galaxy is $\sim 10^{-3}$ (e.g., Rix et al. 2004). If we fix $\alpha = 1.5$ in our model, we find that for a metal-free source the BH to galaxy mass ratio is $\sim 2 \times 10^{-3}$ for $f_X = 0.1$. Thus we choose $f_X = 0.1$ as a upper bound for our study.

Let $L_\star$ be the luminosity of the stellar component in the UV band, i.e., $L_\star = \int_{10.2\ \mathrm{eV}}^{100\ \mathrm{eV}} I_\star(E)\ \mathrm{d}E$. Then, it is straightforward to show that the constant A is determined by the relation

$$A = \frac{f_X L_\star}{\left(\int_{100\ \mathrm{eV}}^{10\ \mathrm{keV}} E^{-\alpha} dE - f_X \int_{10.2\ \mathrm{eV}}^{100\ \mathrm{eV}} E^{-\alpha} dE\right)}. \tag{2.19}$$

We have varied the X-ray properties (i.e., the parameters f_X and α) of the sources to study the effects on various quantities of interest. However, while choosing the values for f_X and α it should be kept in mind that the normalization coefficient A must be positive.

2.5 Radiative transfer around an isolated source

As the first sources of light appear in the universe, they start to ionize the surrounding IGM and create ionized bubbles around them. In addition, the UV and X-ray radiation from these sources would heat up the medium. In order to simulate the ionization and heating patterns around ionizing sources, we have developed a code which closely follows the treatment of Thomas and Zaroubi (2008, 2011). Essentially, the global ionization and temperature distributions are simulated in two steps: in the first step, we generate the ionization and temperature patterns as a function of time and distance around isolated sources surrounded by a uniform density field, and in the second step, we account for possible overlaps between these individual patterns around all the sources in the simulation box. Here we highlight some of the important features of the method.

- Let us consider a galaxy of stellar mass $M_\star$ surrounded by a uniform IGM. Following the procedures outlined in the previous section, we can estimate

the photons production rate at every energy band of interest. We then assume that the ionization and heating pattern around this isolated galaxy would be spherical in nature, and hence a one-dimensional radiative transfer setup is sufficient to solve the problem. The motivation for this assumption comes from the fact that at early stages of reionization the number density of the sources are low and the bubbles are believed to be separated from each other. Radiative transfer simulations studying the impact of the sources on the surrounding IGM indicate that the ionized bubbles around galaxies were probably almost spherical in nature before the overlap started (Alvarez et al. 2010; Kuhlen and Madau 2005; Thomas and Zaroubi 2008).

- **Ionization of H and He :**
  We assume that the IGM is uniformly distributed around the source and contains only the primordial neutral hydrogen and helium when the source form in the host dark matter halo. The average number density of hydrogen and helium at redshift z is,

$$n_{\rm H}(z) = 1.9 \times 10^{-7}(1+z)^3 \times (1+\delta)\ {\rm cm}^{-3} \quad (2.20)$$

$$n_{\rm He}(z) = 1.5 \times 10^{-8}(1+z)^3 \times (1+\delta)\ {\rm cm}^{-3} \quad (2.21)$$

  where δ is the density contrast.

  As soon as the first sources form in the high-density regions, the process of photo-ionization of the neutral hydrogen and helium begins. As far as hydrogen reionization is concerned, the following processes are the most important.

  - Photo-ionization : The most efficient process for ionizing H I in the IGM is the photo-ionization by the UV light from the sources with energy larger than the ionization energy of H I (i.e., $E_{\rm HI} = 13.6$ eV). For helium reionization, higher energy UV photons and X-rays are the most effective as the ionization energy of helium is larger than the ionization energy of H I (24.6 eV for He I and 54.4 eV for He II).
  - In addition, there will be secondary ionization due to the collision of high-energy electrons and the neutral hydrogen and helium.

– Collisions of the electrons in the medium with the neutral hydrogen and helium atoms.

– Recombination process.

The UV and X-ray radiation flux from the central source are calculated self-consistently accounting for the d^{-2} dilution and also the effects of optical depth along the photon path. The number densities of H I and H II along with those of He I, He II and He III are calculated as a function of distance d from the source by solving the relevant rate equations:

$$\frac{dx_{\rm HII}}{dt} = \Gamma_{\rm HI}(1 - x_{\rm HII}) - \alpha_{\rm HII} n_e x_{\rm HII}, \tag{2.22}$$

$$\begin{aligned}\frac{dx_{\rm HeII}}{dt} = & (\Gamma_{\rm HeI} + \beta_{\rm HeI} n_e)(1 - x_{\rm HeII} - x_{\rm HeIII}) \\ & -(\beta_{\rm HeII} + \alpha_{\rm HeII} + \xi_{\rm HeII}) n_e x_{\rm HeII} \\ & +\alpha_{\rm HeIII} n_e x_{\rm HeIII} - \Gamma_{\rm HeII} x_{\rm HeII},\end{aligned} \tag{2.23}$$

$$\begin{aligned}\frac{dx_{\rm HeIII}}{dt} = & (\Gamma_{\rm HeII} + \beta_{\rm HeII} n_e) x_{\rm HeII} \\ & -\alpha_{\rm HeIII} n_e x_{\rm HeIII},\end{aligned} \tag{2.24}$$

where $x_{\rm HII}$, $x_{\rm HeII}$ and $x_{\rm HeIII}$ are the fraction of ionized hydrogen and singly and doubly ionized helium respectively and n_e is the electron number density. α, β and ξ represent the case B recombination coefficients, collisional ionization coefficients and dielectronic recombination coefficient respectively.

The photo-ionization rate for hydrogen ($\Gamma_{\rm HI}$), neutral helium ($\Gamma_{\rm HeI}$) and singly ionized helium ($\Gamma_{\rm HeII}$) are given by,

$$\Gamma_{\rm HI} = \int_{\rm E_{HI}}^{\infty} \sigma_{\rm HI} N(E,d,t)\frac{dE}{E} + f_H\left[\int_{\rm E_{HI}}^{\infty} \sigma_{\rm HI}\left(\frac{E-E_{\rm HI}}{E_{\rm HI}}\right) N(E,d,t)\frac{dE}{E}\right] + f_H\left[\frac{n_{\rm HeI}}{n_{\rm HI}}\int_{\rm E_{HeI}}^{\infty} \sigma_{\rm HeI}\left(\frac{E-E_{\rm HeI}}{E_{\rm HI}}\right) N(E,d,t)\frac{dE}{E}\right], \quad (2.25)$$

$$\Gamma_{\rm HeI} = \int_{\rm E_{HeI}}^{\infty} \sigma_{\rm HeI} N(E,d,t)\frac{dE}{E} + f_{\rm He}\left[\int_{\rm E_{HeI}}^{\infty} \sigma_{\rm HeI}\left(\frac{E-E_{\rm HeI}}{E_{\rm HeI}}\right) N(E,d,t)\frac{dE}{E}\right] + f_{\rm He}\left[\frac{n_{\rm HI}}{n_{\rm HeI}}\int_{\rm E_{HeI}}^{\infty} \sigma_{\rm HI}\left(\frac{E-E_{\rm HI}}{E_{\rm HeI}}\right) N(E,d,t)\frac{dE}{E}\right], \quad (2.26)$$

$$\Gamma_{\rm HeII} = \int_{\rm E_{HeII}} \sigma_{\rm HeII} N(E,d,t)\frac{dE}{E}, \quad (2.27)$$

where σ are the bound-free photo-ionization cross-sections (Verner et al. 1996), while $E_{\rm HI}$, $E_{\rm HeI}$ and $E_{\rm HeII}$ represent the ionization energy of H I, He I and He II respectively.

The term $N(E,d,t)$ is the radiation flux at a distance d from the centre of the source and can be written as

$$N(E,d,t) = e^{-\tau(E,d,t)}\frac{A_{\rm norm}}{(d/{\rm Mpc})^2} I(E), \quad (2.28)$$

where $\tau(E,d,t)$ is the optical depth

$$\tau(E,d,t) = \sum_i \int_0^d \sigma_i(E) n_i(r,t) dr, \quad (2.29)$$

where the sum is over all species. The normalization coefficient $A_{\rm norm}$ is given by

$$A_{\rm norm} = \frac{E_{\rm total}}{\int I(E)dE \times 4\pi({\rm Mpc})^2}, \tag{2.30}$$

where $E_{\rm total}$ is the total energy output from the source. The above form of radiation flux assumes spherical symmetry in gas distribution around a single source and ionization-recombination equilibrium.

The terms f_H and $f_{\rm He}$ represent the effects of secondary ionizations and can be expressed in terms of the ionized fraction of hydrogen $x_{\rm ion}$ (Shull and van Steenberg 1985),

$$f_H = 0.3908(1 - x_{\rm ion}^{0.4092})^{1.7592} \tag{2.31}$$

$$f_{\rm He} = 0.0554(1 - x_{\rm ion}^{0.4614})^{1.6660}. \tag{2.32}$$

- **Temperature evolution :**
The initial temperature is assumed to be uniform with a value $T_{\rm K}^i(z_i) = 2.73\ {\rm K} \times (1+z_i)^2/(1+z_{\rm dec})$, i.e., we assume that the gas temperature was coupled to the CMBR temperature till redshift $z_{\rm dec}$ and then evolved as $(1+z)^2$ due to adiabatic expansion of the gas. In this study, we have fixed $z_{\rm dec}$ to be 150 (e.g., Furlanetto et al. 2006). The most prominent heating processes are the photo-heating due to UV and X-ray flux. The UV-heating is most prominent near the boundary of the ionized and neutral regions, while X-ray heating is substantial within the partially ionized and neutral regions because of the large mean free path of high-energy photons. In addition, X-rays can increase the kinetic temperature by sufficient Compton scattering with the free electrons in the medium. Among the various cooling processes described e.g., in Thomas and Zaroubi (2008), the main cooling of the IGM comes from the expansion of the universe. The rate equation of the gas temperature $T_{\rm K}$ is given by

$$\frac{3}{2}\frac{d}{dt}\left(\frac{k_B T_{\rm K} n_B}{\mu}\right) = H_{\rm heating} - C_{\rm cooling}, \tag{2.33}$$

where the terms $H_{\rm heating}$ and $C_{\rm cooling}$ represent heating and cooling rate respectively. Photoelectric heating of hydrogen and helium atoms and Compton heating are the major heating processes that increase the kinetic temperature of the gas. There will be several cooling processes like cooling due to collisional excitation, collisional ionization, recombination, Free-free emission and Hubble expansion. Accounting all such processes, one can write the heating and cooling rate as,

$$\begin{aligned} H_{\rm heating} =& f_{\rm Heat} \sum_{\rm i=HI,HeI,HeII} n(i) \int \sigma_i(E-E_i) N(E,d,t)\ \frac{dE}{E} \\ &+ \frac{\sigma_s n_e}{m_e c^2} \int N(E,d,t)(E-4k_B T_{\rm K})\ dE \end{aligned} \tag{2.34}$$

$$\begin{aligned} C_{\rm cooling} =& \sum_{\rm i=HI,HeI,HeII} \zeta_i n_e n(i) && [{\rm collisional-ionization}] \\ &+ \sum_{\rm i=HII,HeII,HeIII} \eta_i n_e n(i) && [{\rm recombination}] \\ &+ \omega_{\rm HeII} n_e n_{\rm HeIII} && [{\rm dielectronic-recombination}] \\ &+ \sum_{\rm i=HI,HeI,HeII} \psi_i n_e n(i) && [{\rm collisional-excitation}] \\ &+ \theta_{\rm ff}[n_{\rm HII} + n_{\rm HeII} + 4n_{\rm HeIII}] n_e && [{\rm free-free}] \\ &+ 2\frac{\dot{a}}{a}\left(\frac{k_B T_{\rm K} n_B}{\mu}\right) && [{\rm Hubble\ expansion}] \end{aligned} \tag{2.35}$$

where k_B is the Boltzmann constant, $n_{\rm B}$ is the baryonic number density, μ is the average molecular weight. ζ_i and η_i are the collisional-ionization cooling and recombination cooling coefficients respectively. $\omega_{\rm He\ ii}$ is the dielectronic recombination cooling coefficient due to He II. ψ_i is the collisional excitation cooling coefficient and $\theta_{\rm ff}$ the free-free cooling coefficient. The last term of equation 2.35 represents cooling due to Hubble expansion. The factor $f_{\rm Heat}$ is the amount of heat deposited by secondary electrons and is given by (Shull and van Steenberg 1985),

$$f_{\rm Heat} = \begin{cases} 0.9971(1-(1-x_{\rm ion}^{0.2663})^{1.3163}). & \text{if } x_{\rm ion} > 10^{-4} \\ 0.15 & \text{if } x_{\rm ion} \leq 10^{-4} \end{cases}$$

The second term of equation 2.34 is the Compton heating term. σ_s is the Thompson scattering cross-section of an electron ($\sigma_s = 6.6524 \times 10^{-25}$ cm^2).

- In addition to the ionizing flux, we also keep track of the Lyα flux J_α around the source. The Lyα flux is assumed to decrease as d^{-2} with the radial distance d from the source. In addition to the continuum Lyα photons from the stellar sources, another source of Lyα photons is the X-rays from the source. In this case, a fraction of energy from the primary electrons is spent in exciting the H I, which then generate Lyα photons on relaxation. Since the Lyα photons travel large distances without being absorbed, we account for the redshift of photons having energies larger than the Lyα frequency produced in the source. We have also restricted the Lyα photons to propagate with the speed of light for a time equal to the age of the hosting halo.

- We store profiles of the fraction of different species, the kinetic temperature and the Lyα flux for a wide range of galaxy stellar masses, redshifts, density contrast, X-ray to UV luminosity ratio and X-ray SED spectral index. These catalogues are used later to generate global maps of the 21-cm brightness temperature.

2.6 Signal around individual sources

Before proceeding to the construction of global maps, we validate our code by studying the behaviour of some basic quantities for an isolated source surrounded by a uniform IGM. Figure 2.2 shows the ionization, heating and Lyα coupling patterns around a source which is taken to be a galaxy with stellar mass 10^8 M$_\odot$ at $z = 10$. The results are shown at a time 10^7 years after the sources began to radiate. The uniform IGM around the source is assumed to have a density equal to the mean density of the universe. The different curves in each panel represent different X-ray properties for the galaxy.

The top left-hand panel of the figure shows the ionization fraction of hydrogen along the radial direction for different values of f_X. One can see that the size of the H II region created around the galaxy is as large as $\sim$ 150 pkpc. In the

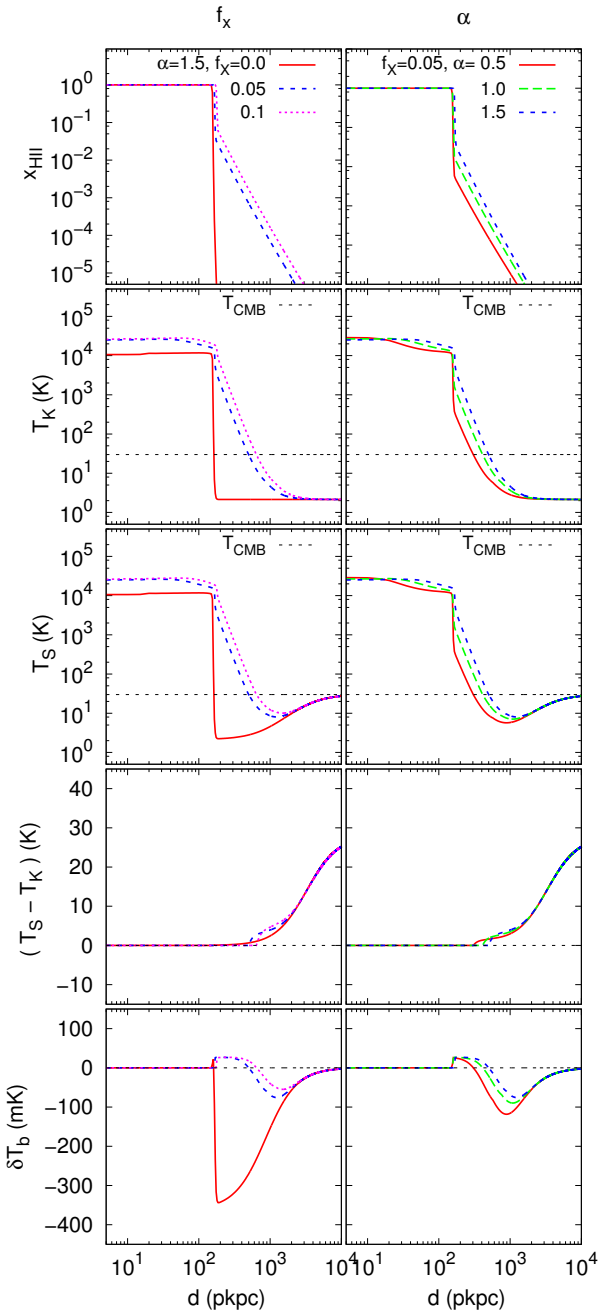

Figure 2.2: The top to bottom rows show the ionization fraction ($x_{\rm HII}$), kinetic temperature ($T_{\rm K}$), spin temperature ($T_{\rm S}$), the difference between spin and kinetic temperatures ($T_{\rm S} - T_{\rm K}$) and differential brightness temperature ($\delta T_{\rm b}$) distribution around a galaxy with stellar mass 10^8 $M_\odot$ at a time 10 Myr after the source starts radiating. The surrounding IGM is taken to be uniform with mean density of the universe at redshift 10. In first column, the three curves represent three different level of X-rays from the source (X-ray to UV luminosity fractions f_X=0.0 (solid red), 0.05 (long dashed blue) and 0.1 (dotted magenta curve)), while the power law spectral index α is kept fixed (1.5). The three curves in second column represent three different values of α (0.5, 1.0, 1.5 respectively) while $f_X = 0.05$ is kept fixed.

absence of X-rays ($f_X = 0$) the ionization front shows a sharp transition, while in the presence of X-rays the transition between ionized to neutral medium is relatively smooth. The reason behind this is the presence of high-energy photons in the spectrum, which have longer mean free paths and are efficient in partially ionizing the gas. Note that the increase in the X-ray luminosity does not increase the size of the fully ionized H II region, but creates a partially ionized region of larger size beyond the H II region. The top right-hand panel of Figure 2.2 shows the H II fraction for different values of the X-ray spectral index α. A larger α implies a steeper spectrum, which in turn implies an increase in the number of soft X-ray photons for a fixed f_X. As a result, the size of the partially ionized region is larger for a higher value of α.

Panels in the second row of Figure 2.2 show the kinetic temperature $T_{\rm K}$ pattern around the isolated source. It is clear from the left-hand panel that the presence of X-rays affects the temperature profile quite drastically. Firstly, there is a rise in $T_{\rm K}$ in the ionized region when f_X is increased; this is mainly due to the Compton scattering of X-ray photons with free electrons. The size of the heated region is larger than the H II region in the presence of X-rays, with the size increasing with increasing values of f_X. Because of the larger mean free paths of high-energy photons, $T_{\rm K}$ shows a very smooth transition from the central highly heated ($\sim$ few 10^4 K) region to far away cold region ($\sim$ few K) in the presence of X-rays, while the transition is sharp in the absence of X-rays. Even when the ratio of X-ray to UV luminosity is as small as 5%, regions as far as few hundreds of pkpc from the source have temperatures larger than the CMBR temperature. With sufficient Lyα coupling, this heated region will show the signal in emission. An increase in α results in a larger number of soft X-ray photons, hence the temperature of the ionized region increases and so does the size of the heated regions as is seen from the right-hand panel of the second row.

The pattern of the spin temperature $T_{\rm S}$ as calculated using equation 2.2 is shown in the third row from the top. It is clear from the plots that $T_{\rm S}$ closely follows $T_{\rm K}$ at distances close to the source, while it tends to follow T_γ at larger distances. This behaviour can be explained by the d^{-2} decline in the Lyα flux J_α from the source, which makes the Lyα coupling stronger closer to the source and weaker at larger distances.

In order to show the differences between $T_{\rm S}$ and $T_{\rm K}$, we plot the function

$T_S - T_K$ as a function of distance from the source in the fourth row from the top. As expected, $T_S = T_K$ close to the source because of strong Lyα coupling, and this relation holds for distances $\sim 300 - 400$ pkpc which are much larger than the H II region. If we look at larger distances, the Lyα coupling weakens and T_S gradually tends towards T_γ. Hence one cannot work with the simple assumption that T_S follows T_K at early stages of reionization. Since the value of $T_S - T_K$ is essentially determined by the Lyα coupling, which in turn is mainly determined by J_α from the central source, we find that the curves are almost independent of the X-ray properties of the source.

The bottom row shows the 21-cm signal δT_b profile around the source. As is already known (Alvarez et al. 2010; Thomas and Zaroubi 2008; Yajima and Li 2014), there are four main regions in the profile starting from the centre going outward: (i) the signal vanishes completely in the H II region, (ii) there is an emission region just beyond the H II region arising from X-ray heating in the partially ionized medium, (iii) the signal decreases and turns into an absorption feature because of the decrease in the value of T_K and finally (iv) the absorption signal decreases and gradually vanishes as the Lyα coupling becomes weaker. When $f_X = 0$, the heating due to X-rays is absent. Hence the second region with emission signal is obviously absent, and the absorption signal is much stronger. As the value of f_X is increased, the size of the region with emission signal increases, however, the amplitude of the signal remains almost the same. The amplitude of the absorption signal in the third region decreases with increasing f_X. Similarly, increasing the value of α shows a similar effect on the emission and absorption signal.

2.7 Global maps

Having discussed the generation of ionization and temperature maps around an isolated galaxy, we now discuss the method for generating such maps in the full simulation box. Our treatment closely follows that of Thomas et al. (2009) to account for overlap between the individual patterns, though we have introduced some modifications in the method which are discussed below.

The method starts by listing the location and mass of all the sources in the box. One then determines the radius R_{HII} of the H II region, defined as the

distance at which $x_{\rm HII}$ falls to $x_{\rm HII}^{\rm th} = 0.5$, for each source. Since the ionization profile shows a sharp drop from $x_{\rm HII} = 1$ to $x_{\rm HII} \sim 0.1$ for the values of f_X and α considered in this chapter, varying the threshold value in the range $0.1 < x_{\rm HII}^{\rm th} < 1$ should not affect our results. For a given source the average H I number density is measured within a sphere of radius R_0 around the source. Initially, R_0 is taken to have a small value. Having found the overdensity within R_0, we find out the radius of the ionization front R_1 for the source from the 1D catalogue as obtained in Section 2.5. If R_0 is taken to be sufficiently small, we usually end up with $R_1 > R_0$. Since the sources form preferentially at high-density peaks, we expect the average density within the sphere to decrease with increasing radius. Hence we take R_1 to be the next guess for R_0 and iterate the process till $R_1 \approx R_0$. We then assign the radius of the H II region to be $R_{\rm HII} = R_1$. Let us denote the radius of the H II region and the mean hydrogen number density within the H II region for i^{th} source to be $R_{\rm HII}^i$ and $n_{\rm H-1D}^i$, respectively.

Having found the quantities $R_{\rm HII}^i$ and $n_{\rm H-1D}^i$, the correct ionization and heating profile around the source can be selected from the previously generated catalogue of 1D profiles. While assigning the ionization profile within the H II region is straightforward, one needs to be slightly careful while assigning the ionization fraction in the partially ionized regions. If one assigns the same profile corresponding to $n_{\rm H-1D}^i$ in the partially ionized region, as is done by Thomas et al. (2009), then there will be an underestimation in the value of ionization fraction. This is due to the fact that the average density decreases with distance from the source. In order to account for this effect, we assume that the number of photons from the i^{th} source at a point $\mathbf{x}$ in the partially ionized region is given by $x_{\rm HII-1D}^i(\mathbf{x}) \times n_{\rm H-1D}^i$, where $x_{\rm HII-1D}^i(\mathbf{x})$ is the ionization fraction as obtained from our catalogue of 1D profiles. If the number density of hydrogen in that particular pixel is $n_{\rm H}(\mathbf{x})$, then the ionization fraction will be modified to $x_{\rm HII-1D}^i(\mathbf{x}) \times n_{\rm H-1D}^i/n_{\rm H}(\mathbf{x})$. Note that we do not account for the fact that the number of recombinations will also be less for lower densities as that would involve modelling of sub-grid physics.

When the individual H II regions overlap there will be excess photons residing at the overlapped regions which need to be accounted for. Following Thomas et al. (2009) we use an iterative process to estimate the total number of excess photons in the overlapping regions and distribute them among the contributing

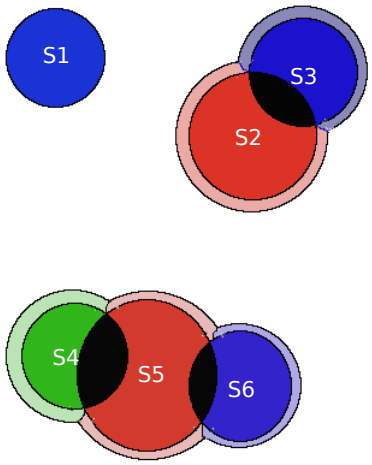

Figure 2.3: The cartoon depicts the overlap of H II bubbles in the simulation box. While the bubble around source S1 does not encounter any overlap with other bubbles, the overlap occurs for sources like S2 and S3. The unused ionizing photons for sources S2 and S3 (in the black regions) are distributed equally to the sources S2 and S3. The increase in the H II bubble radius is shown by the light colour region, while the isolated H II bubbles are shown by deep colour regions. In the case of S4, S5 and S6 group, the excess photon corresponding to source S4 is half of unused photons in the overlap regions between S4 and S5 bubbles. The excess photon for S6 is also calculated in the same way. However, the excess photon for S5 comes from the overlap regions (S4, S5) and (S5, S6).

ionizing sources. Figure 2.3 shows a cartoon of the overlap between H II bubbles. The main difference between our approach and that of Thomas et al. (2009) arises while assigning the ionization profile in the partially ionized regions. In the presence of X-rays, these regions are larger than the H II region and hence their overlap begins much earlier. The ionization fraction in overlapping partially ionized regions is given by

$$x_{\rm HII}(\mathbf{x}) = \frac{\sum_i x^i_{\rm HII-1D}(\mathbf{x}) \times n^i_{\rm H-1D} \times \left(1 - x^{i-1}_{\rm HII}(\mathbf{x})\right)}{n_{\rm H}(\mathbf{x})}, \tag{2.36}$$

where the index i is summed over all overlapping sources. Here $x^{i-1}_{\rm HII}(\mathbf{x})$ denote the ionization fraction obtained after overlapping $i-1$ number of sources. We use $x^0_{\rm HII}(\mathbf{x}) = 0$. The term $\left(1 - x^{i-1}_{\rm HII}(\mathbf{x})\right)$ takes care of the fact that the ith source encounters an already partially ionized IGM, due to overlap between previous $i-1$ number of sources, before contributing the ionizing photons.

The heated regions too extend well beyond the H II regions, and hence they start overlapping very early during reionization. Let a point be heated up by photons from n sources. Let $\{T_1, T_2, .., T_n\}$ be the set of temperatures at that point obtained from the catalogue of 1D profiles for these sources. In such a situation, a possible approach could be to assign the temperature in the overlap region by invoking the conservation of energy (Thomas et al. 2009). This approach embeds the 1D $T_{\rm K}$ profiles around the sources and calculates energy deposited from each source in each pixel within the sphere of influence in the simulation box. In the case of overlapping between different $T_{\rm K}$ profiles, the total energy at each location is calculated and the energy is distributed among all the overlapping sources. Thomas et al. (2009) change the normalization constant of the SED of the sources accordingly to account for the excess energy due to overlap. Then, the study used modified $T_{\rm K}$ profiles with new normalization constant to generate $T_{\rm K}$ maps. In our study, however, we have used a different approach which is more straightforward to implement.

Our approach is based on the correlation between $T_{\rm K}$ and $x_{\rm HII}$ in the heated regions for isolated sources. Figure 2.4 shows the plot of $T_{\rm K}$ as a function of $x_{\rm HII}$ for different types of source properties. The top left-hand panel shows the plot for different stellar masses in the galaxy, the bottom left-hand panel shows the same for different values of the density contrast, the top-right is for different

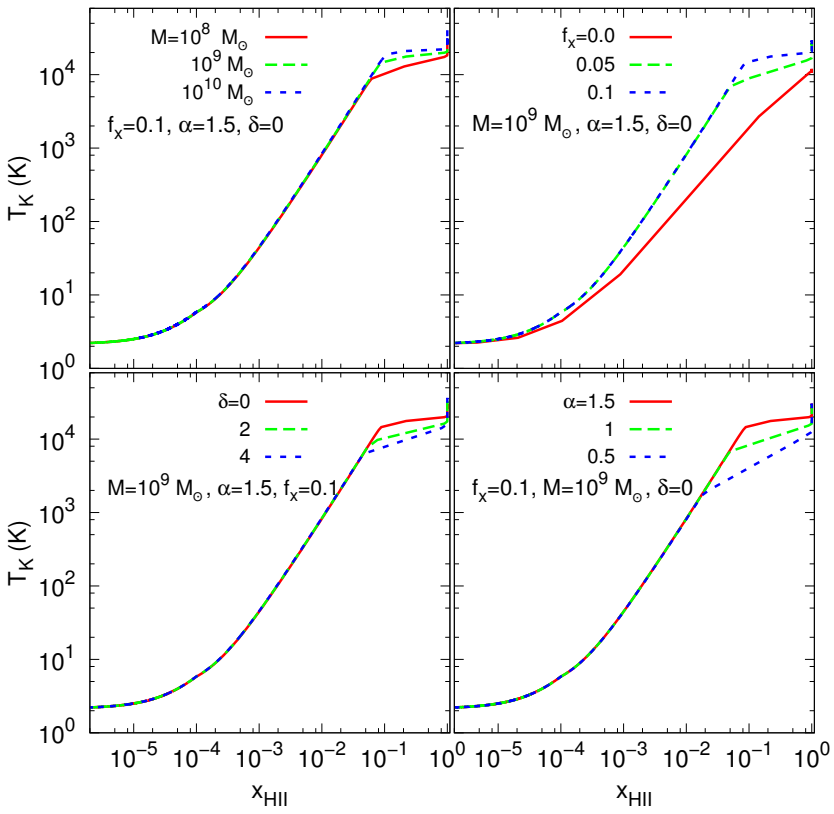

Figure 2.4: The kinetic temperature as a function of ionization fraction for an isolated source for different source masses (top left), X-ray to UV luminosity ratios (top right), IGM density contrasts (bottom left) and X-ray power law spectral indices (bottom right) at $z = 10$ at a time 10 Myr after the source starts radiating.

values of f_X and the bottom right-hand panel shows the plots for different values of α. Clearly a strong correlation exists between $T_{\rm K}$ and $x_{\rm HII}$ for $x_{\rm HII} < 0.1$ and this correlation is completely independent of the source properties and densities for $f_X > 0$. Thus we can use this correlation for determining the temperature in the overlapped regions given that we already know how to estimate the ionized fraction. This method is expected to be inaccurate for $0.1 < x_{\rm HII} < 1$, however, the fraction of such points is negligible as can be seen from the top panel of Figure 2.2. In addition, these points are highly heated and have strong Lyα coupling, thus making the signal almost independent of $T_{\rm K}$. The correlation is somewhat different when $f_X = 0$. In such cases, however, we find that the temperature falls sharply beyond the H II regions and hence the IGM can be treated as a two-phase medium characterized by the complete ionized and neutral regions. Thus we can still estimate the $T_{\rm K}$ from the correlation without introducing any significant error.

Finally, we discuss how to deal with points which receive Lyα radiation from more than one source. In this case, accounting for overlap is almost trivial as J_α essentially measures the number of Lyα photons and hence one just has to add the fluxes from different sources (Thomas and Zaroubi 2011). The brightness temperature maps from the simulation are described in Chapter 3.

3 | 21-cm signal from cosmic dawn: Imprints of spin temperature fluctuations and peculiar velocities

This chapter contains material that has been published in Ghara et al. (2015a).

3.1 Introduction

The H I 21-cm signal will be observed against the CMBR. The signal will be observed in either emission or absorption depending on whether the H I spin temperature is higher or lower than the background CMBR temperature. It is often assumed that the spin temperature is highly coupled with the IGM kinetic temperature and much higher compared to the CMBR temperature right from the birth of first light sources i.e, when reionization process starts (Battaglia et al. 2013; Choudhury et al. 2009; Datta et al. 2012a; Furlanetto et al. 2004a; Iliev et al. 2014; McQuinn et al. 2006; Mesinger and Furlanetto 2007). This leads to a situation in which the 21-cm signal is independent of the exact value of the spin temperature. However, these assumptions may not hold during the initial stages of reionization or the cosmic dawn. Although a small amount of Lyα photons is enough for establishing the coupling, it is possible that even that small number of Lyα photons is not available at every location in the IGM. The heating of the IGM is also highly dependent on nature, total number and spectra of X-ray sources at cosmic dawn which are all unknown. In a situation where the

collisions (between H I atoms or H I atoms and free electrons) become inefficient and Lyα photons are only confined near the sources, the coupling between the IGM kinetic temperature and H I spin temperature becomes inhomogeneous. Even if the coupling is strong and complete, the heating could be incomplete and inhomogeneous due to lack of X-ray photons. This would lead to fluctuations in the spin temperature and consequently additional features in the 21-cm signal. Recently there has been several attempts in order to understand the effect of spin temperature fluctuations on the observed H I 21-cm signal during the cosmic dawn (Baek et al. 2009; Barkana and Loeb 2005b; Chuzhoy and Zheng 2007; McQuinn 2012; Santos et al. 2008; Semelin et al. 2007; Thomas and Zaroubi 2011). Models with complete Lyα coupling and heating predict the variance of H I brightness temperature fluctuations to be a few 10 mK^2, while the same quantity for inhomogeneous Lyα coupling and heating model could exceed few 100 mK^2.

Efforts are also in place to understand the heating from different kind of X-ray sources such a mini-quasars (Thomas and Zaroubi 2011), X-ray binaries (Ahn et al. 2015; Fialkov et al. 2014), and thermal emission from hot interstellar medium (Pacucci et al. 2014). Because of their large mean free path, the hard X-ray photons can penetrate a few tens of Mpcs in the IGM (Shull and van Steenberg 1985), while soft X-ray photons will be absorbed within a smaller distance from the sources and as a result, the heating will be very patchy. The heating pattern will be very different in the case of high-mass X-ray binaries when compared to mini-quasars or hot interstellar medium as they do not contain a very large amount of soft X-rays (Fialkov et al. 2014; Pacucci et al. 2014). It has also proposed that measurements of H I 21-cm power spectrum from the cosmic dawn will reveal the amount of X-ray background (Christian and Loeb 2013) and the spectral energy distribution of X-ray sources (Pacucci et al. 2014).

In this chapter, we present the effects of inhomogeneous Lyα coupling and IGM heating on the H I 21-cm signal from the reionization epoch and cosmic dawn using a semi-numerical code which is described in Chapter 2. We consider mini-quasar like objects (defined as galaxies with intermediate mass black holes in the range of $10^3 - 10^6$ $M_\odot$) as X-ray heating sources and focus on statistical quantities such as the variance and power spectrum of the H I brightness temperature fluctuations which are among the primary goals of instruments like LOFAR

and SKA.

Our major effort, in this Chapter, has gone into understanding the effect of the peculiar velocity on the H I 21-cm signal from the cosmic dawn. The peculiar velocity has a significant impact on the reionization and pre-reionization H I 21-cm signal (Bharadwaj and Ali 2004). This also makes 21-cm power spectrum anisotropic (Barkana and Loeb 2005a; Majumdar et al. 2013). Recently, it has been shown that the peculiar velocity can boost the H I power spectrum by a factor of $\sim$ 5 at large scales during the initial stages of reionization when $x_{\rm HII} \lesssim 0.2$ (Jensen et al. 2013; Mao et al. 2012). During the same period, power spectrum becomes highly anisotropic which is detectable with LOFAR 2000 hrs of observations. It was also suggested that such observations could tell us whether reionization occurred inside-out or outside-in (Jensen et al. 2013; Majumdar et al. 2013). However, all results described above is based on the assumption that the spin temperature is much higher than the CMBR temperature. Here we investigate how the above results change once the heating and Lyα coupling is calculated self-consistently. As we see later, implementing the peculiar velocity effect on the signal during this epoch is slightly different compared to the case when the spin temperature is much higher than the CMBR temperature. Apart from that, we investigate how peaks in the power spectrum can be used to extract information about the ionization state and size of the 'heated bubbles'.

The plan of this chapter is as follows: In Section 3.2 we have briefly described the method to incorporate the peculiar velocities (or commonly known as the redshift-space distortion) into the calculation of $\delta T_{\rm b}$. In Section 3.3 we discuss the main results of our analyses. Results related to reionization models containing only high-mass sources have been described in Section 3.3.1. The globally averaged ionization and heating properties of our models are discussed in Section 3.3.1.1 while the fluctuations in the 21-cm signal is described in Section 3.3.1.2. The main results of this chapter, i.e., the effects of the peculiar velocities on the 21-cm signal are discussed in Section 3.3.1.3. In Section 3.3.1.4, we see whether our conclusions are unchanged when the X-ray properties of the sources are varied. In Section 3.3.2, we have described the effect of small-mass haloes on the results, and we have checked the robustness of our results with respect to the resolution of the simulation box in Section 3.3.3. We summarize and discuss our main results in Section 3.4. Throughout the chapter, we have used the cosmo-

logical parameters $\Omega_m = 0.32$, $\Omega_\Lambda = 0.68$, $\Omega_B = 0.049$, $h = 0.67$, $n_{\rm s} = 0.96$, and $\sigma_8 = 0.83$ which are consistent with the recent results of Planck mission (Planck Collaboration et al. 2014a).

3.2 Redshift-space distortion

As the 21-cm signal is a line emission at a rest frequency of 1420 MHz, observation of this redshifted signal at a particular frequency ($\nu_{\rm obs}$) can be mapped to a redshift given by $1 + z = 1420\,{\rm MHz}/\nu_{\rm obs}$. Thus the observations of the redshifted signal map the redshift-space, instead of the real-space. As the line of sight velocity component of the gas modifies the cosmological redshift, real-space distribution of the gas will be different from the redshift-space distribution. If the peculiar velocities of the gas are taken into account, the over/under dense regions in the real-space will appear as more over/under dense in the redshift-space. Thus in principle, the redshift-space distortion (RSD) can introduce anisotropies in the 21-cm power spectrum (see Barkana and Loeb 2005a; Bharadwaj and Ali 2005; Mao et al. 2012, for detailed reviews of the theory).

The method for implementing the effect of peculiar velocities on the reionization 21-cm signal during the 'emission' phase (i.e, $T_{\rm S} \gg T_\gamma$) is reasonably well-studied (Jensen et al. 2013; Majumdar et al. 2013; Mao et al. 2012; Mellema et al. 2006). The situation is different in our case because at high redshift there are regions where Lyα coupling is not sufficiently strong and regions which may not be highly heated. We follow a method outlined in Mao et al. (2012) with certain modifications to account for the fluctuations in the spin temperature. Here we explain the methods (used in this thesis) to incorporate the redshift-space distortion effect to the signal.

We will now describe two separate methods to incorporate the effect of peculiar velocities of the gas in the IGM. The first method is based on the particle movement along the line of sight and the second method is based on the movement of the simulation cells along the line of sight. While the first method is more accurate compared to the second, it is computationally very expensive. The details of the methods can be found in Mao et al. (2012). Please note that we have used the particle movement method in Ghara et al. (2015a) which is also described in this chapter, while we use the cell movement method in Ghara et al.

(2015b) (described in Chapter 4).

3.2.1 Particle movement method

We know the positions and peculiar velocities of all the dark matter particles at a certain redshift in our simulation box. Let the i^{th} dark matter particle have position (x^i, y^i, z^i) and velocity (v_x^i, v_y^i, v_z^i) and have an associated hydrogen mass $M_{\rm H}^i$. We also know the neutral fraction of hydrogen and spin temperature at the grid point that contains the particle. For the scenario where $T_{\rm S} \gg T_\gamma$, the mass of the neutral hydrogen associated with the i^{th} particle can be written as

$$M_{\rm HI}^i = M_{\rm H}^i x_{\rm HI}^i, \tag{3.1}$$

where $x_{\rm HI}^i$ is the neutral fraction of hydrogen associated to the particle. This is sufficient in case the only fluctuations in $\delta T_{\rm b}$ arise from the neutral hydrogen field. If we want to account for the spin temperature fluctuations, we need to modify the above relation suitably. Since the fluctuations in $\delta T_{\rm b}$ arises from the combination $x_{\rm HI}\,(1 - T_\gamma/T_{\rm S})$, we define an effective H I mass associated with the particle as

$$\tilde{M}_{\rm HI}^i = M_{\rm H}^i x_{\rm HI}^i \left(1 - \frac{T_\gamma}{T_{\rm S}}\right). \tag{3.2}$$

If the line of sight is taken to be along the x-axis, the position of the particle $\mathbf{s}$ in redshift-space coordinate will be given by,

$$s_x^i = x^i + \frac{v_x^i (1 + z_{\rm obs})}{H(z_{\rm obs})}, s_y^i = y^i, s_z^i = z^i, \tag{3.3}$$

where $z_{\rm obs} = (1 + z_{\rm cos})(1 - v_x^i/c)^{-1} - 1$ is the observed redshift and $z_{\rm cos}$ is the cosmological redshift. Once this mapping from $\mathbf{x} \rightarrow \mathbf{s}$ is established, we interpolate the H I contributions $\tilde{M}_{\rm HI}^i$ of each particle to an uniform grid in the redshift-space. The resultant $\delta T_{\rm b}$ map will contain the effects of redshift-space distortions which would correspond to the observed signal.

3.2.2 Cell movement method

Though it is recommended to use the particle movement method to incorporate the effect of peculiar velocities, the cell movement method (or Mesh-to-Mesh

(MM)-RRM scheme) of Mao et al. (2012) is time efficient and computationally easy to implement the redshift-space distortion. The steps to include the peculiar velocity effects into the $\delta T_{\rm b}$ maps using the cell movement method are given below.

(i) The steps to generate $\delta T_{\rm b}$ maps without RSD are described in Section 2.7. The velocity fields in the radiative transfer grids are generated from the N-body simulation using $SPH-$like smoothing. We assume that the line of sight velocity components of the cells correspond to the velocity at the middle of the respective cells and calculate the line of sight velocities at the cell boundaries using linear interpolation. Let us denote the real-space position and velocity components of a cell boundary as (x, y, z) and (v_x, v_y, v_z) respectively. If the line of sight is $x-$axes, then the redshift-space position (s_x, s_y, s_z) of the cell boundary can be written as

$$s_x = x + \frac{v_x(1+z_{\rm obs})}{H(z_{\rm obs})}, s_y = y, s_z = z, \tag{3.4}$$

where $z_{\rm obs} = (1+z_{\rm cos})(1-v_x/c)^{-1} - 1$ is the observed redshift and $z_{\rm cos}$ is the cosmological redshift. The cells will appear elongated or shrunk along the line of sight direction depending on the line of sight velocities at the boundaries.

(ii) There will be sufficient overlap between the cells in redshift-space along the line of sight. Also, there may be situations like the $fingers\,of\,God$, where the two nearby cell boundaries along the line of sight can cross each other. In that case, we have to switch the cell boundaries to keep the length of the cell positive. We re-grid the brightness temperature from the real-space to the redshift-space grid with the same resolution, where the overlaps between the cells are taken into account. The differential brightness temperature in the re-gridded cell (i', j, k) is given by,

$$\delta T_{\rm b}^s(i', j, k) = \sum_i \frac{\Delta L_{i,i'}^s}{\Delta s_i'} \delta T_{\rm b}(i, j, k), \tag{3.5}$$

where $\Delta s_i'$ is the length of the i th cell in the redshift-space along the line of sight and $\Delta L_{i,i'}^s$ be the length of the cell that belongs to i' cell in the real-space.

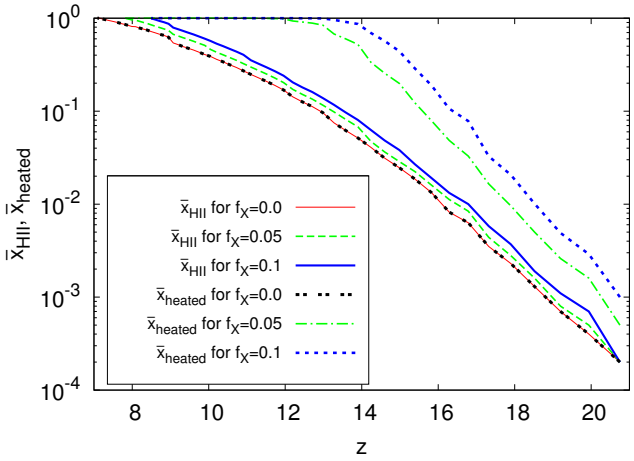

Figure 3.1: Evolution of volume weighted ionization fraction of hydrogen and heated fractions of the IGM for different X-ray luminosities of the source. The thin solid red, dashed green and thick solid blue curves represent the evolution of $x_{\rm HII}$ for $f_X = 0$, 0.05 and 0.1 respectively. The value of α is taken to be 1.5. The fractional volume occupied by heated regions (defined as those with $T_{\rm K} > T_\gamma$) are represented by the other three curves. These models are for the scenario where reionization is driven by haloes identified using spherical overdensity halo-finder in the simulation box.

3.3 Results

We present the results of our analysis of the 21-cm signal in this section. As mentioned in Section 2.2, the signal depends on the neutral hydrogen fraction, kinetic temperature, the Lyα coupling and the line of sight velocity of the neutral gas. The model we have used accounts for all these effects. However, it is important to note that there exist studies which simply assume $T_{\rm S} \gg T_\gamma$, which is obtained when the medium is highly heated ($T_{\rm K} \gg T_\gamma$) and Lyα coupling is very strong ($T_{\rm S} = T_{\rm K}$). In such cases, the effect of fluctuations in $T_{\rm S}$ on the signal can be ignored. Similarly, many studies ignore the effect of redshift-space distortion. While presenting our results using the model where all the effects are accounted for, we will also look into the effects of not accounting for the fluctuations in $T_{\rm S}$.

The details of the N-body simulation used in this chapter is described in Section 2.3.1 of Chapter 2. In this chapter, we have considered galaxy and mini-quasar type sources. The details of these sources are given in Section 2.4 of Chapter 2.

3.3.1 Reionization driven by only high-mass sources

In this section, we present the nature of signal if reionization is driven solely by high-mass sources. These sources are identified using spherical overdensity method from the N-body simulation. The minimum mass for this study is $3.89 \times 10^9\, h^{-1}\, \mathrm{M}_\odot$. We will discuss the effect of small sources on the signal later in a separate section.

3.3.1.1 Global ionization and heating history

Before carrying out any analysis, we need to fix the value of the star-forming efficiency $f_\star$. As mentioned earlier, the value of $f_\star$ would determine the global reionization history. Hence, we fix its value by demanding that it matches the electron scattering optical depth τ as observed by the CMBR observations. We find that, in the absence of X-rays ($f_X = 0$), the choice $f_\star = 0.03$ gives $\tau = 0.08$ which is consistent with the observed constraints (Hinshaw et al. 2009). Adding X-ray photons to the luminosity increases the value of τ, however, the effect is quite small. For example, using $f_X = 0.1$ with $\alpha = 1.5$ increases τ to 0.089 which still is consistent with the CMBR constraints. Hence, we fix the value $f_\star = 0.03$ and concentrate on studying the effects of changing the values of f_X and α. The evolution of the ionized hydrogen fraction x_{HII} is shown in Figure 3.1. Most of the reionization process occurs between redshifts 16 and 8 during which the ionization fraction grows from 0.01 to 1. Since our simulation boxes are not equipped for treating small-mass haloes, the reionization occurs faster than what would be allowed by quasar spectra constraints at $z \approx 6$ (Bolton and Haehnelt 2007; Choudhury and Ferrara 2006; Fan et al. 2006b, 2003; Gunn and Peterson 1965; Malhotra and Rhoads 2006). However, since the main purpose of this chapter is to study the effects of peculiar velocities on the 21-cm signal, we did not concern ourselves too much on reproducing the reionization constraints. As mentioned earlier, we have also checked whether ignoring the small-mass haloes at early stages has any effect on our conclusions, which we will discuss later in Section 3.3.2.

We can see from Figure 3.1 that increasing the value of f_X causes reionization to occur earlier, though the effect is not that drastic (at least for $f_X < 0.1$, the highest value of f_X considered in this chapter). However, the heating pattern

Model	Lyα coupling	Heating
A	coupled	heated
B	coupled	self-consistent
C	self-consistent	self-consistent

Table 3.1: Different kinds of models considered in this chapter. The terms 'coupled' and 'heated' represent the scenarios $x_\alpha \gg 1$ and $T_{\rm K} \gg T_\gamma$ respectively.

is very sensitive to the value of f_X. As can be seen from the figure, the volume fraction in which the kinetic temperature is above the CMBR temperature reaches unity only at $z \approx 8$ (at the same time when reionization is complete) for $f_X = 0$, while the same happens much earlier, at $z \approx 12(14)$ for $f_X = 0.05(0.1)$.

We have considered a number of models in this chapter which depending on the how various effects have been accounted for. These models are summarised in Table 3.1. Unless otherwise specified, the parameters related to the X-ray sources are fixed to be $f_X = 0.05$ and $\alpha = 1.5$. For model A, we have assumed the IGM to be uniformly heated and the Lyα coupling to be highly efficient, thus making the signal independent of $T_{\rm S}$. Model B accounts for the fact that the IGM may not be uniformly heated, i.e., the pattern of $T_{\rm K}$ is calculated self-consistently, however, the Lyα coupling is still taken to be highly efficient, thus making $T_{\rm S} = T_{\rm K}$. In model C, the Lyα coupling too is calculated self-consistently accounting for the inhomogeneities in the Lyα flux J_α. These models are similar to those considered by, e.g., Baek et al. (2009).

The evolution of the volume averaged brightness temperature $\delta T_{\rm b}$ is shown in Figure 3.2. For model A, the IGM is assumed to be heated and Lyα coupled, thus the brightness temperature is always positive and essentially traces the neutral hydrogen distribution. Once the non-uniform heating is accounted for (model B), the signal shows absorption at earlier times. This represents colder regions in the IGM where the X-ray flux may not have percolated as yet. As the fraction of regions with X-ray heating increases, the signal shows up in emission and follows model A at later stages. Since the Lyα coupling is assumed to be strong, $T_{\rm S} = T_{\rm K}$, and hence the signal is always non-zero (except for the point where $T_{\rm K} = T_\gamma$). When the effects of Lyα coupling are treated self-consistently (model C), the

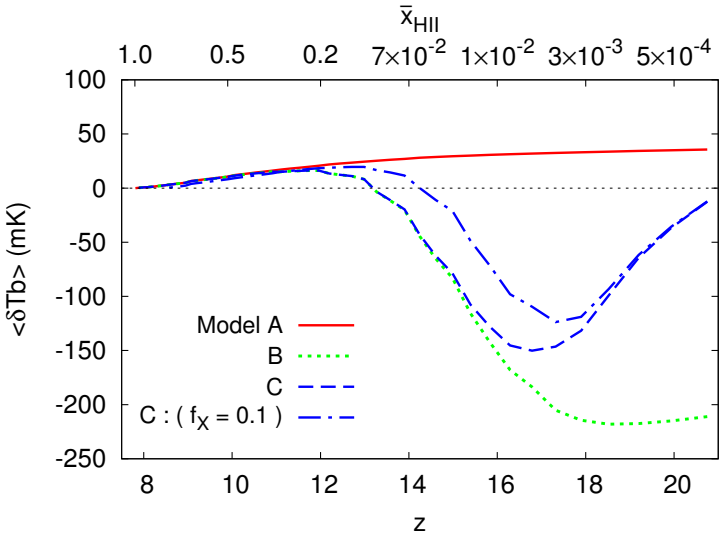

Figure 3.2: Evolution of volume weighted brightness temperature for model A (solid red curve), B (dotted green curve) and C (dashed blue curve) with redshift. The X-ray properties are chosen such that $f_X = 0.05$ and $\alpha = 1.5$. The dash-dot blue curve represents model C with a higher value of $f_X = 0.1$. These models are for the scenario where reionization is driven by haloes identified using spherical overdensity halo-finder in the simulation box.

$T_{\rm S}$ can depart from $T_{\rm K}$ towards T_γ at earlier stages when the coupling is not efficient enough, and hence $\delta T_{\rm b}$ tends to vanish. As soon as the ionized fraction $x_{\rm HII} \sim 0.05$, the Lyα coupling seems to be sufficiently strong so that model C and B becomes identical. We also show in the figure the $\delta T_{\rm b}$ evolution when the fraction of X-rays is increased $f_X = 0.1$ in model C. Clearly, the effects of heating are visible relatively early in reionization history. It is interesting to note that all the models A, B and C are identical when $x_{\rm HII} \gtrsim 0.2$ and the assumption of $T_{\rm S} = T_{\rm K} \gg T_\gamma$ works extremely well in these stages. It is only at very early stages that we need to account for the fluctuations in the spin temperature (Baek et al. 2009; Mesinger et al. 2013; Pritchard and Loeb 2012; Santos et al. 2008; Thomas and Zaroubi 2011).

3.3.1.2 Fluctuations in the brightness temperature

Since the main target of the radio interferometers is to measure the fluctuations in the 21-cm signal, we discuss how different effects impact the fluctuations. The

maps of $\delta T_{\rm b}$ obtained from a random slice through our simulation box is shown in Figure 3.3. The left-hand panels show the maps for model A for three different redshifts $z = 19.2, 15.4, 9.6$ respectively. Since this model corresponds to the case $T_{\rm S} \approx T_{\rm K} \gg T_{\gamma}$, the brightness temperature essentially follows the neutral hydrogen distribution. In the absence of any significant sources at $z = 19.2$, the IGM is neutral and the fluctuations are mainly those corresponding to underlying dark matter density field. One can see spherical ionized bubbles appearing in the slice at $z = 15.4$, where the signal drops to zero. These bubbles percolate in the IGM and gives the patchy reionization map at $z = 9.6$ as is expected.

The middle panels of Figure 3.3 show the brightness temperature maps for model B where it is assumed that $T_{\rm S} \approx T_{\rm K}$ but the temperature $T_{\rm K}$ is estimated self-consistently. At early stages $z = 19.2$, the map for model B is very different from that for model A because the effect of X-ray heating is not that strong. In fact, most of the IGM shows up in absorption because it is colder than the CMBR. Once the sources form, the signal shows a number of features. One can identify the spherically-shaped regions around the sources where the signal vanishes as expected. However, there is a "ring" of emission which corresponds to the regions which are heated by X-ray from the sources. As the effect of X-rays decreases away from the sources, the emission signal drops, changes sign and shows up in absorption. At this stage, the maps have both emission and absorption features (Baek et al. 2010; Mesinger et al. 2013; Santos et al. 2008; Thomas and Zaroubi 2011). As we come to lower redshifts $z = 9.6$, the X-ray heating is dominant all over the IGM and model B is almost identical to model A.

The right-hand panels of Figure 3.3 show the maps of $\delta T_{\rm b}$ for the model C. The main difference between this model and B is at very early stages $z = 19.2$. Since the Lyα coupling is calculated self-consistently using the value of J_{α}, the map shows effects of inefficient coupling when sources are sparse. As a result, the magnitude of the absorption signal is less than that in model B. However, since one requires only a small amount of Lyα radiation for efficient coupling, we find that the differences between model B and C go away by $z = 15.4$.

The same conclusions can be drawn if we plot the power spectrum of $\delta T_{\rm b}$ for the three models, which is done in Figure 3.4. It is clear that at relatively later stages of reionization $z = 9.6$, all the models overlap with each other when the signal traces the H I distribution. At $z = 15.4$, model B and C differ from A

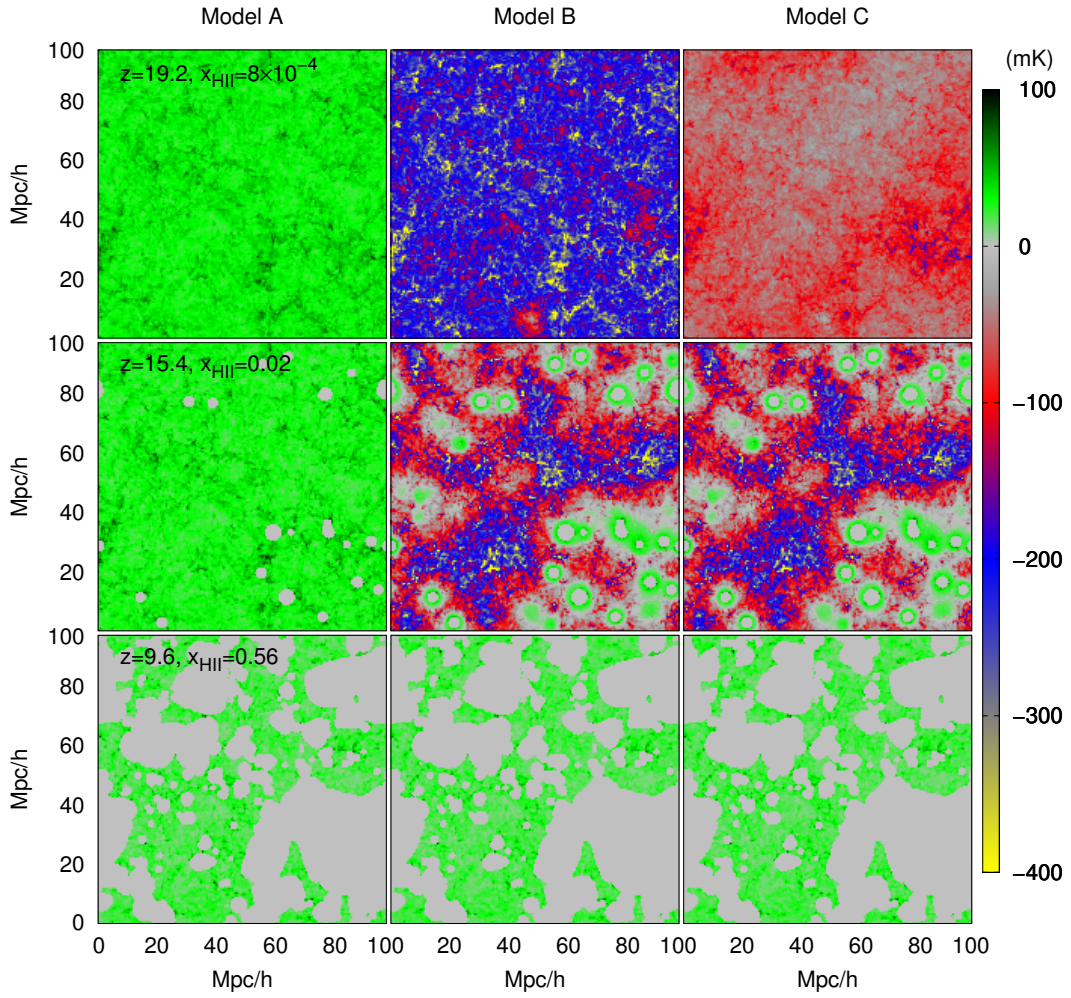

Figure 3.3: The brightness temperature maps for three different redshifts 19.2, 15.4 and 9.6 for model A,B and C for the reionization scenario driven by haloes identified using spherical overdensity halo-finder. Model A assumes the IGM to be Lyα coupled and highly heated ($T_{\rm S} \gg T_\gamma$). Model B assumes the IGM to be strongly Lyα coupled but self-consistently heated with X-ray source properties $f_X = 0.05$ and $\alpha = 1.5$ ($T_{\rm S} \approx T_{\rm K}$), while model C considers Lyα coupling and X-ray heating self-consistently.

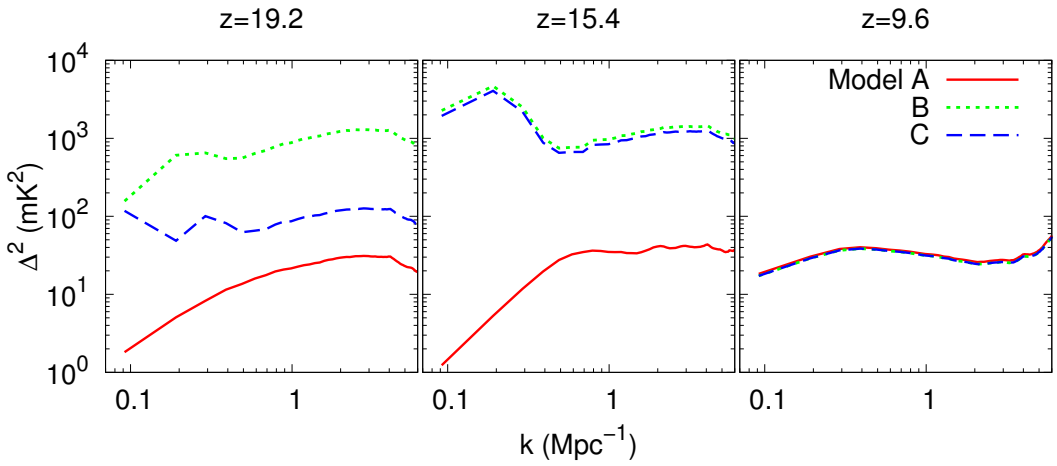

Figure 3.4: The power spectrum of brightness temperature for models A (solid red), B (dotted green) and C (dashed blue) for the scenario where reionization is driven by haloes identified using spherical overdensity method. Left-hand to right-hand panels represent previously considered three redshifts $z = 19.2, 15.4, 9.6$ respectively.

because of the inhomogeneities in the X-ray heating which is not accounted for in A. Since there are regions showing strong absorption signals in models B and C, it leads to a stronger contrast in the maps, and hence the amplitude of the power spectrum is much larger (almost $\sim$ 30 times). Interestingly, the power spectra for these models show a "bump" or a peak around $k_{\rm peak} \approx 0.2$ Mpc^{-1}. This scale corresponds to the typical sizes of regions which are heated by the sources, i.e., the sizes of the heated bubbles. In fact, one can estimate the typical radius of heated regions as $R_{\rm heat} = 2.46/k_{\rm peak}$ (Friedrich et al. 2011), which in our case turns out to be $\sim$ 12 Mpc. The amplitude of this peak is determined by the contrast in the signal between heated (i.e., emission) and colder (i.e., absorption) regions. This feature was noted in simulations of Baek et al. (2009) too. Since the peak has a relatively high amplitude ($\sim 5000\,{\rm mK}^2$) it can easily be detected by an instrument like the SKA. The size of a typical heated region is an important parameter which can help in constraining the nature of X-ray sources such as the SED and the total X-ray flux. At the earliest stages ($z = 19.2$), the effects of inhomogeneous Lyα coupling makes model B different from C. As is clear,

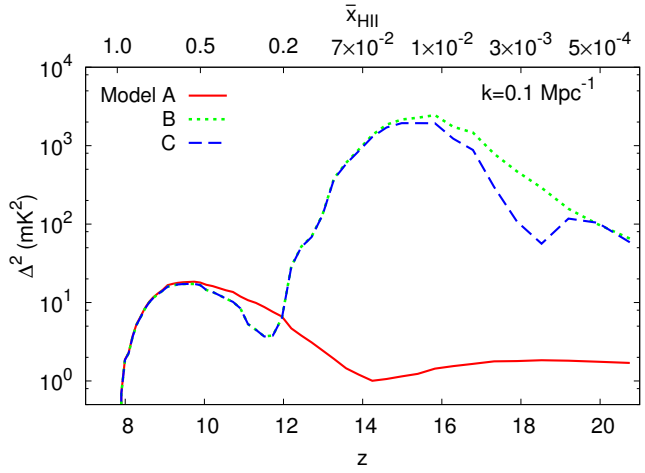

Figure 3.5: Evolution of $\delta T_{\rm b}$ power spectrum at scale $k = 0.1$ Mpc^{-1} for model A (solid red), B (dotted green) and C (dashed blue) respectively. These results are for the scenario where reionization is driven by haloes identified using spherical overdensity method.

because of inefficient Lyα coupling in regions away from sources, the brightness temperature amplitude becomes smaller in model C compared to B. This leads to a decrease in the power spectrum amplitude.

The evolution of the power spectra for different models for a typical scale $k = 0.1$ Mpc^{-1} accessible to first generation low-frequency telescopes is shown in Figure 3.5. For model A, the amplitude decreases with increase in ionization fraction during initial stages of reionization. However as the characteristic size of the ionized bubbles increase with time, Δ^2 starts to increase. This leads to a prominent trough-like feature at $z \approx 14.2$ when the ionization fraction is ~ 0.05. The rise in Δ^2 at $z < 14$ is halted when the bubbles start overlapping and the patchiness in the ionization fraction decreases. At this point, the amplitude is determined by $x_{\rm HII}$ and hence starts falling as reionization enters its last stages. Thus a prominent peak at $z \sim 10$ is created in the evolution curve of the power spectrum when the IGM is around 50 % ionized.

At early stages of reionization the power spectra for models B and C are $\sim$ 100-1000 times larger than predicted by model A. This is simply due to the fact that the signal is in absorption for models B and C while for model A it

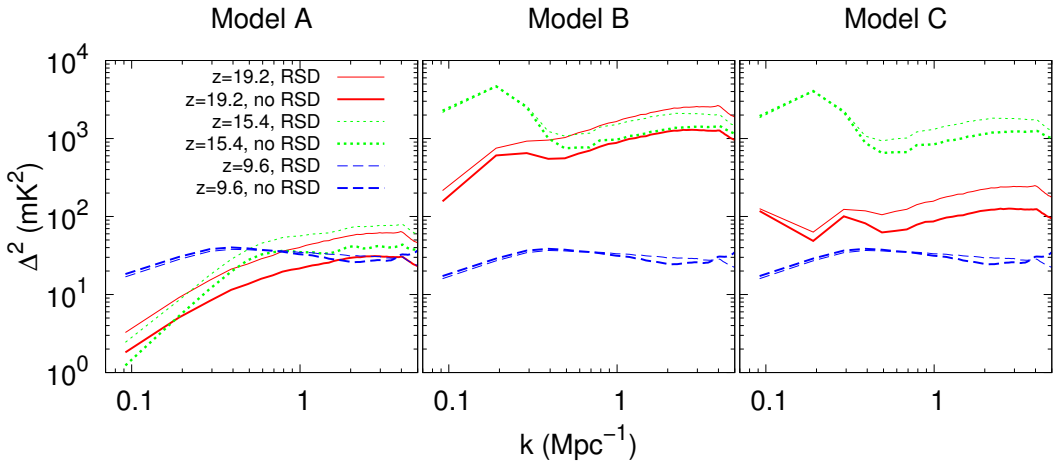

Figure 3.6: Effects of redshift-space distortion on $\delta T_{\rm b}$ power spectra for models A, B and C where reionization is driven by haloes identified using spherical overdensity method. The thick curves represent the power spctrum without redshift-space distortion at three redshifts 19.2 (solid red), 15.4 (dotted green) and 9.6 (dashed blue) respectively. The thin curves represent the corresponding power spectrum with redshift-space distortion.

is in emission. This difference reduces over time and almost vanishes when the universe is half ionized around redshift 10.

In addition to the peak arising from $x_{\rm HII}$ fluctuations, there is another peak at $z \sim 16$ for model B. This peak arises because of $T_{\rm K}$ fluctuations due to inhomogeneous X-ray heating. Since the heating is not efficient at high redshifts, the signal is in absorption and hence larger than that in model A. As sources heat up the IGM, the amplitude of the signal decreases and tends towards model A. Once sufficient heating is completed in the IGM, the signal follows model A. Model C is quite similar to B except that there is another peak in the amplitude at $z \sim 19$. This peak corresponds to inhomogeneities in Lyα coupling which is not accounted for in the other models. Once the Lyα coupling becomes efficient at $z \sim 16$, the signal for model C follows B.

3.3.1.3 Effects of redshift-space distortion

As is well known, the effects of including the peculiar velocities in the brightness temperature calculation are two-fold: one is to introduce anisotropies in the signal, and the other is to modify the amplitude of the spherically averaged power

spectrum. In this chapter, we will mostly study the second effect, i.e., the change in the amplitude because of redshift-space effects. We will also comment on the anisotropies wherever appropriate.

Before proceeding into presenting our results, let us briefly discuss a quasi-linear model (Mao et al. 2012) for studying the effects of redshift-space distortion. In order to see this, let us write equation (2.5) as

$$\delta T_{\rm b}(z,\mathbf{x}) = \widehat{\delta T_{\rm b}}(z)\bar{\eta}(z)[1+\delta_{\rho_{\rm HI}}(z,\mathbf{x})][1+\delta_{\eta}(z,\mathbf{x})], \tag{3.6}$$

where

$$\widehat{\delta T_{\rm b}}(z) = 27\ \bar{x}_{\rm HI}(z)\left(\frac{\Omega_B h^2}{0.023}\right)\left(\frac{0.15}{\Omega_m h^2}\frac{1+z}{10}\right)^{1/2}\ {\rm mK}, \tag{3.7}$$

is the average brightness temperature at z and

$$\eta(z,\mathbf{x}) = 1 - \frac{T_\gamma(z)}{T_{\rm S}(z,\mathbf{x})}. \tag{3.8}$$

The average value of η is denoted as $\bar{\eta}$ while the corresponding contrast is given by $\delta_\eta = \eta/\bar{\eta} - 1$. The power spectrum in the redshift-space can be decomposed as

$$P^s(\mathbf{k}) = P_0(k) + P_2(k)\ \mu^2 + P_4(k)\ \mu^4, \tag{3.9}$$

where $\mu = k_\parallel/|\mathbf{k}|$, $k_\parallel$ being the component of $\mathbf{k}$ along the line of sight. In the quasi-linear approximation, the different components appearing in the above equation are given in terms of the real-space power spectra as

$$\begin{aligned}
P_0(k) &= \left(\widehat{\delta T_{\rm b}}\bar{\eta}\right)^2\left[P_{\delta_{\rho_{\rm HI}}\delta_{\rho_{\rm HI}}}(k) + P_{\delta_\eta\delta_\eta}(k) + 2P_{\delta_{\rho_{\rm HI}}\delta_\eta}(k)\right],\\
P_2(k) &= 2\left(\widehat{\delta T_{\rm b}}\bar{\eta}\right)^2\left[P_{\delta_{\rho_{\rm B}}\delta_{\rho_{\rm HI}}}(k) + P_{\delta_{\rho_{\rm B}}\delta_\eta}(k)\right],\\
P_4(k) &= \left(\widehat{\delta T_{\rm b}}\bar{\eta}\right)^2 P_{\delta_{\rho_{\rm B}}\delta_{\rho_{\rm B}}}(k),
\end{aligned} \tag{3.10}$$

where $\delta_x = x/\bar{x} - 1$ is the contrast of the quantity x. The quantities $\rho_{\rm B}$ and $\rho_{\rm HI}$ represent the density of baryons and neutral hydrogen respectively. The quantities of the form $P_{\delta_x\delta_x}$ denote the real-space auto-power spectrum of the quantity x, while $P_{\delta_x\delta_y}$ are the real-space cross-power spectrum between fields x and y. The spherically-averaged power spectrum in redshift-space is simply given by

$$P^s_{\rm ave}(k) = P_0(k) + \frac{1}{3}P_2(k) + \frac{1}{5}P_4(k). \tag{3.11}$$

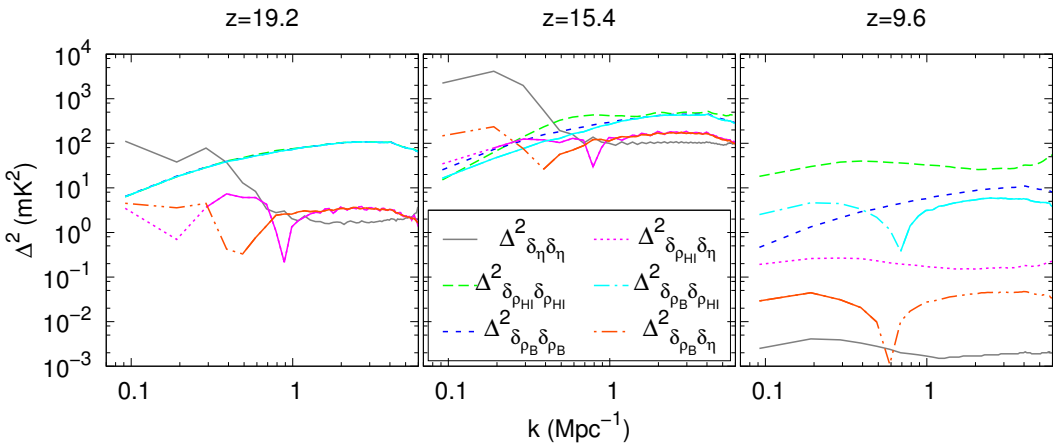

Figure 3.7: The auto and cross-power spectra of baryonic density contrast $\delta_{\rho_{\rm B}}$, neutral hydrogen density contrast $\delta_{\rho_{\rm HI}}$ and the contrast δ_η in the term $\eta = 1 - T_\gamma/T_{\rm S}$ at three different redshifts. The solid parts in the cross-power spectra curves represent positive values, while the other parts represent negative values. The reionization is assumed to be driven by haloes identified using spherical overdensity method.

We should mention here that we have *not* used this quasi-linear model to calculate any of our results, nor have we verified its validity for our work. The model is introduced so as to help understand the various properties of the redshift-space power spectrum in a simple way.

We now present our results incorporating the effects of line of sight peculiar velocities on the $\delta T_{\rm b}$ fluctuations. The resulting power spectra for the three models are shown in Figure 3.6. The left-hand panel shows the results for model A for three different redshifts and for the cases with and without the redshift-space distortion. At higher redshifts, the effect of including the redshift-space effects is to increase the amplitude of the power spectra, without affecting the shape significantly. For example, the increase in amplitude is about a factor of 1.87 at $z = 19.2$ and 15.4 at scales probed by our simulation when the redshift-space distortion is accounted for. This is expected from the quasi-linear model when there are no fluctuations in $T_{\rm S}$, i.e., $\delta_\eta = 0$ and the H I density follows the baryonic density field $\delta_{\rho_{\rm HI}} = \delta_{\rho_{\rm B}}$. The effect decreases as the neutral hydrogen fraction decreases further and we find that the effect is negligible for model A

at $z = 9.6$. Since the difference between real-space and redshift-space power spectra for model A is essentially determined by the cross term $P_{\delta_{\rho_{\rm B}}\delta_{\rho_{\rm HI}}}(k)$, it is obvious that the correlation between the underlying baryonic field and the H I field vanishes when the ionization fronts propagate into the low-density regions at later stages of reionization.

The situation is clearly different for models B and C at higher redshifts. We find that the redshift-space power spectra are higher than the real-space ones by a factor ~ 1.87 at smaller scales $k \gtrsim 0.4$ Mpc^{-1} at $z = 19.2, 15.4$, implying that the fluctuations in $T_{\rm S}$ are negligible at these scales. At larger scales, however, the $T_{\rm S}$ fluctuations dominate the brightness temperature power spectrum, and in addition, these fluctuations are not correlated with the baryonic density field. This makes the effect of redshift-space distortion negligible at scales $k \lesssim 0.4$ Mpc^{-1}. The models B and C are identical to A at $z = 9.6$, and hence the effect of redshift-space is not visible.

In order to bring more clarity to these arguments, we plot the various terms which contribute to the redshift-space power spectrum in Figure 3.7. We show the plots only for model C. At $z = 19.2$ and 15.4, the power spectra will be dominated by the terms $P_{\delta_{\rho_{\rm B}}\delta_{\rho_{\rm B}}}$, $P_{\delta_{\rho_{\rm B}}\delta_{\rho_{\rm HI}}}$ and $P_{\delta_{\rho_{\rm HI}}\delta_{\rho_{\rm HI}}}$ at smaller scales, all of which are almost identical because of very little ionization. At larger scales, the fluctuations are dominated by the $P_{\delta_\eta\delta_\eta}$ term. Clearly the spin temperature fluctuations δ_η are not correlated with the other fields as is shown by the smallness of the terms $P_{\delta_{\rho_{\rm HI}}\delta_\eta}$ and $P_{\delta_{\rho_{\rm B}}\delta_\eta}$, hence we find that the difference between redshift-space and real-space power spectra are negligible. The fluctuations in η decrease as the IGM is heated, however, because the ionization fronts have propagated into low-density regions by then, the effects of redshift-space distortions are negligible. This can also be seen in Figure 3.8, where we have plotted the amplitude of the different components of $P^s(\mathbf{k})$ as defined in equation 3.11. It is clear that the second and fourth order anisotropic terms, due to RSD, are quite small compared to the μ-independent term throughout the reionization history at large scales. Hence overall we find that the effects of redshift-space distortion are negligible at large scales $k \lesssim 0.4$ Mpc^{-1}, though the reasons differ over the history of reionization. At smaller scales, however, the redshift-space power spectrum is ~ 2 times higher in amplitude that the real-space counterpart at early stages of reionization, mainly because the signal is dominated by the H I fluctuations at these scales. These

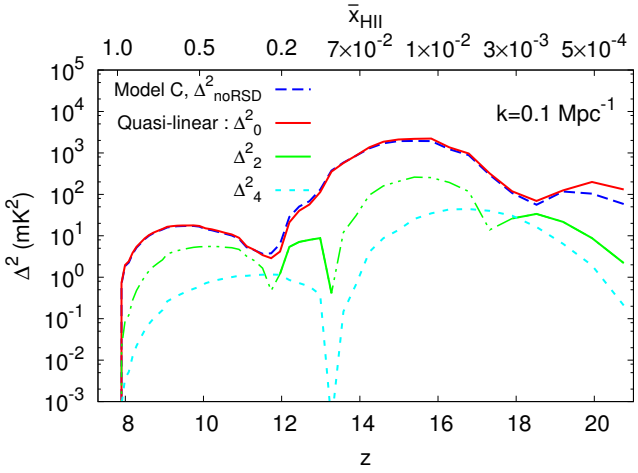

Figure 3.8: Evolution of different components of redshift-space power spectrum (in linear theory) with redshift in model C for the reionization scenario driven by haloes identified by spherical overdensity halo-finder. Solid part in the green curve represent positive value, whereas the dotted dashed part represent negative value.

fluctuations, in turn, are strongly correlated with the density field because of formation of sources at preferentially high-density peaks.

The evolution of the ratio of the redshift-space and real-space power spectra for a typical scale $k = 0.1$ Mpc^{-1} accessible to first-generation low-frequency telescopes is shown in Figure 3.9. One obvious conclusion is that the effects of redshift-space distortion are only visible for model A and that too at early stages of reionization $\bar{x}_{\rm HII} \lesssim 0.1$. Unfortunately, this model is not appropriate at early stages of reionization because it does not account for fluctuations in $T_{\rm S}$. Once these fluctuations are taken into account, the power at large scales is dominated by δ_η contribution which does not correlate with the underlying density field. Hence the effects of peculiar velocities are negligible at large scales throughout the reionization history.

We should mention here that the results obtained using our model A are somewhat in disagreement with results obtained using radiative transfer simulations (Jensen et al. 2013; Mao et al. 2012). For example, the maximum value of the ratio of redshift and real-space power spectra is ~ 1.9 in our model A, while the same rises to ~ 5 in the case of Mao et al. (2012). The main reason is that there

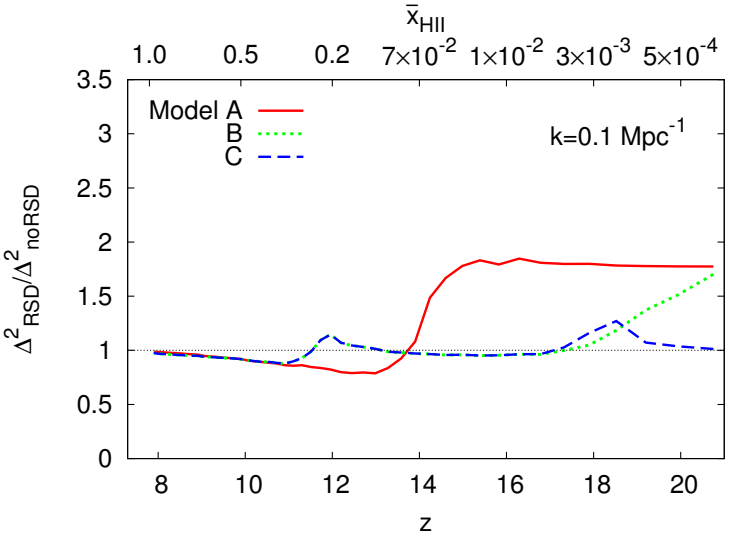

Figure 3.9: Ratio of power spectra with and with-out redshift-space distortion as a function of redshift for models A, B and C at a scale $k = 0.1$ Mpc^{-1}. The plot is for the reionization scenario driven by haloes identified by spherical overdensity halo-finder.

are no small-mass sources (say with halo mass $\sim 10^8 M_\odot$) in our simulation box. As a result, the ionization field is not strongly coupled to the density field. As a result, the trough in the evolution of the real-space power spectrum around $\bar{x}_{\rm HII} \sim 0.2$ at large scales for model A (see Figure 3.5) is not sufficiently deep (compared to, e.g., Jensen et al. 2013; Mao et al. 2012). We note that the trough, which is very prominent in earlier works, is the main reason for the RSD power spectrum getting enhanced by a factor 5 for $\bar{x}_{\rm HII} \sim 0.2$ on large scales. To address this issue, we have studied the contribution from small-mass sources using a sub-grid model which is discussed in Section 3.3.3.

It has been suggested that for scenarios similar to our model A, the anisotropies in the power spectrum produced by the redshift-space distortion effect is detectable in 2000 hrs of observations with LOFAR (Jensen et al. 2013). It was also suggested that such observations could tell us whether reionization occurred inside-out or outside-in (Jensen et al. 2013; Majumdar et al. 2013). However, we find that the amplitude of the isotropic component $P_0(k)$ of the power spectrum is much larger (~ 10 times, see Figure 3.8) than the anisotropic terms $P_2(k)$ and

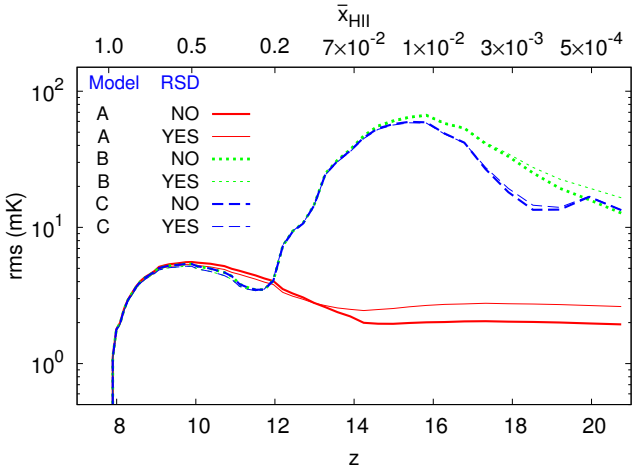

Figure 3.10: Evolution of the RMS of brightness temperature fluctuations (smoothed over scales of 15 cMpc) as a function of redshift for models A, B and C with and without the effects of redshift-space distortion. The plot is for the reionization scenario driven by haloes identified by spherical overdensity halo-finder.

$P_4(k)$ at large scales ($k \lesssim 0.4$ Mpc^{-1}) in a scenario where the spin temperature fluctuations δ_η dominate the power spectrum. Although the inclusion of T_S fluctuations does not affect the amplitude of the anisotropic terms, it still may have interesting consequences for the detectability of the anisotropic signal . For example, it has been shown that the cosmic variance/sample variance is an important factor in extracting the anisotropic term from the total power spectrum (Shapiro et al. 2013). The errors arising from cosmic variance would be proportional to $P_0(k)$ in our case, which can affect the detectability of the anisotropic components. Though extraction of anisotropy in the μ-decomposition formalism could be difficult because of the sample variance and the possibility of leaking one μ-term into other (Jensen et al. 2013; Shapiro et al. 2013), there may be other ways to extract the anisotropy such as using an orthogonal basis like the Legendre polynomial formalism (Majumdar et al. 2013). It could be interesting to explore the possibility for the case where the fluctuations in the spin temperature dominate the H I 21-cm signal. It could also be interesting to explore the possibility of detecting this anisotropy in intermediate scales ($k \sim 1$ Mpc^{-1}) where the effects of redshift-space distortion are much more significant.

The root mean square (RMS) of H I brightness temperature fluctuations $\delta T_{\rm b}$ is another major statistical quantity that will also be targeted by the first generation instruments (Bittner and Loeb 2011; Jelić et al. 2008; Mellema et al. 2006; Patil et al. 2014b). It is defined as,

$$\mathrm{RMS}(\delta T_{\rm b}) = \sqrt{\frac{1}{N}\sum_{i=1}^{N}(\delta T_{\rm b}{}^{i} - \overline{\delta T_{\rm b}})^2}, \tag{3.12}$$

where N is the number of $\delta T_{\rm b}$ data cube pixels after smoothing over a scale of 15 cMpc and $\overline{\delta T_{\rm b}}$ is the average value of $\delta T_{\rm b}$. The plot of RMS deviation as a function of z is shown in Figure 3.10. The behaviour of this quantity, as expected, is very similar to the evolution of $\Delta^2(k)$ at large scales (Figure 3.5). It shows three peaks at different locations corresponding to different physical processes discussed earlier. Recently, it was proposed that a function having a single peak (e.g., $\propto (z/z_R)^{\beta}\,(1+\tanh\,[(z-z_R)/\Delta z])$), where β is the power law index, z_R is the location and Δz is the width of the peak) can be fitted to the measured RMS vs. z data to reliably extract information about the redshift of reionization $\sim z_R$ and the duration of reionization $\sim \Delta z$ (Patil et al. 2014b). The conclusion was based on a reionization model similar to A where the RMS vs. z curve has just one peak around $x_{\rm HII} \sim 0.5$. However in Figure 3.10, we find that there could be two additional peaks at large scales, due to inhomogeneous Lyα coupling and heating respectively. The presence of these two additional peaks makes the interpretation of the measured RMS vs. z slightly more complicated. In particular, the peak corresponding to the inhomogeneous heating can have a very large amplitude and can affect the detection of the low-redshift peak in a noisy data. Fitting a single peak function over the entire range of redshifts could thus possibly result in misinterpretation of the observations. One should thus either restrict the analysis within lower redshifts (e.g., $8 < z < 11$ for model C) or choose a function having three peaks. One should also keep in mind that the influence of the spin temperature fluctuations in the RMS (and also in the power spectrum) remains for a while even after the entire IGM is heated above the CMBR temperature.

As expected, we find that the effects of redshift-space on the RMS are negligible when $T_{\rm S}$ fluctuations are accounted for in the model (model C). This implies that the modelling of the 21-cm signal at large scales is possible without account-

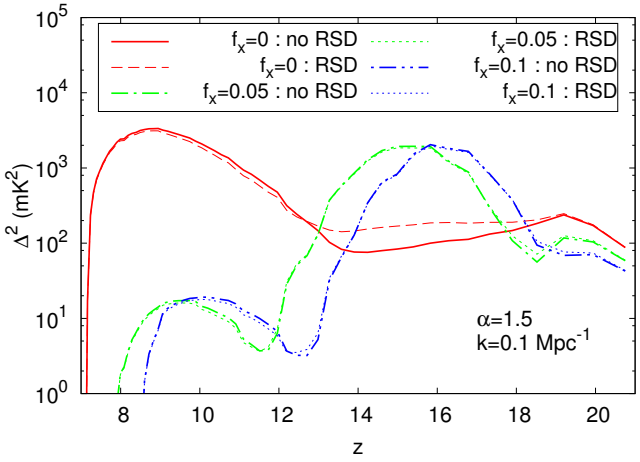

Figure 3.11: Evolution of $\delta T_{\rm b}$ power spectra at $k = 0.1$ Mpc^{-1} for three different values of f_X with and without the effects of redshift-space distortion. These models have only haloes which could be identified using the spherical overdensity halo-finder.

ing for peculiar velocities of the gas, however, it is critical that one accounts for the fluctuations in $T_{\rm S}$.

3.3.1.4 Effect of different X-ray source properties on 21-cm power spectrum

It is clear from the previous section that the redshift-space effects are negligible when the X-ray heating and Lyα coupling are accounted for self-consistently. It is necessary to check whether this result is independent of the parameters related to the X-ray emissivities, which we do in this section. We will essentially consider model C where all the physical effects are accounted for self-consistently, and vary the parameters f_X and α to see the effects on the real and redshift-space power spectrum. In particular, we would concentrate on the evolution of the power spectrum amplitude at a scale $k = 0.1$ Mpc^{-1}.

Let us first consider the effect of varying f_X and take three representative values $f_X = 0, 0.05, 0.1$. The corresponding power spectra are shown in Figure 3.11. When $f_X = 0$, the neutral hydrogen will contain almost no photons of higher energies and hence there would be almost no heating. As a result, the

neutral regions will be visible in absorption while the ionized regions will show no signal. This also means there will be no fluctuations in $T_{\rm K}$ once the Lyα coupling is complete. This is clear from the figure which shows that the case with $f_X = 0$ contains the initial peak at $z \sim 20$ arising from inhomogeneities in the Lyα coupling. However, as expected the model does not have the subsequent peak corresponding to the $T_{\rm K}$ fluctuations. The amplitude again peaks because of the increase in bubble sizes and then decreases as reionization is completed. The amplitude at these last stages, interestingly, is much larger compared to the X-ray heated models which is because of the fact that the IGM is cold and shows strong absorption signal. This model is essentially same as the model A discussed above but the mean brightness temperature $\overline{\delta T_{\rm b}}$ being replaced by the mean kinetic temperature of the IGM. When $f_X > 0$, the signal shows the prominent peak corresponding to the $T_{\rm K}$ fluctuations. It is expected that the amount of heating and the size of the heated regions would increase as the X-ray intensity increases. This suggests that the IGM will be heated at an earlier redshift when f_X in increased which is clearly seen from Figure 3.11. In fact, the peak arising from $T_{\rm K}$ fluctuations appear earlier when the value of f_X is increased. Hence the position of the peak as a function of redshift (or frequency of radio observations) can be used for probing the level of total X-ray background. This is consistent with earlier results (Christian and Loeb 2013).

As far as the effect of redshift-space distortion is concerned, we find that there is some difference between the redshift and real-space amplitudes at $13 < z < 18$ when $f_X = 0$. This is arising because there are no fluctuations in the spin temperature at these epochs and hence the model is similar to model A. However, the moment when $f_X > 0$, the effect of redshift-space distortion vanishes and becomes independent of the actual value of f_X.

The conclusions remain similar when we vary the value of the spectral index α. The effect of considering different values of α is shown in Fig. 3.12. We find that the peak related to $T_{\rm K}$ fluctuations appear earlier when α is increased. This is because for the same value of f_X, increasing α means redistributing photons to relatively lower energies. Since lower energy photons are easier to be absorbed by H I, the amount of ionization and heating is more. The most interesting aspect to check is the effect of redshift-space distortions, and we find that the effect is negligible independent of the value of α.

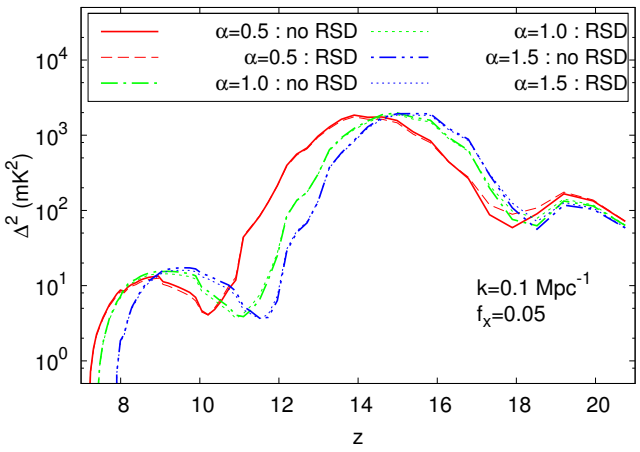

Figure 3.12: Evolution of $\delta T_{\rm b}$ power spectra with redshift at scale $k = 0.1$ Mpc^{-1} for three different values of the spectral index α of the mini-quasar SED. The results are shown for cases with and without the effects of redshift-space distortion. The value of f_X is kept fixed to 0.05. The plot is for the reionization scenario driven by haloes identified by spherical overdensity halo-finder.

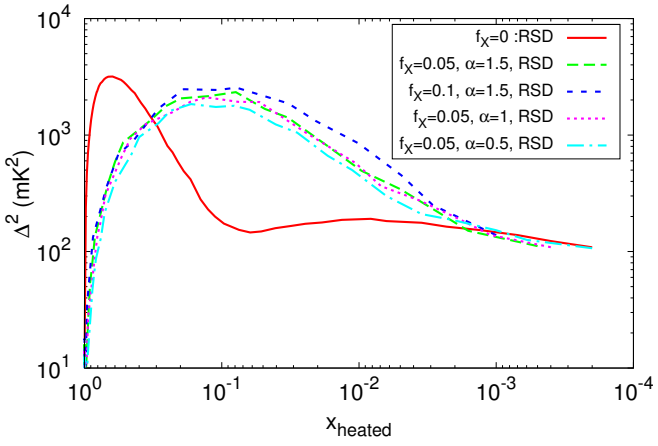

Figure 3.13: Evolution of the $\delta T_{\rm b}$ power spectra at $k = 0.1$ Mpc^{-1} as a function of heated volume fraction in the IGM. Regions with $T_{\rm K} > T_\gamma$ are referred to as heated regions. The plot is for the reionization scenario driven by haloes identified by spherical overdensity halo-finder.

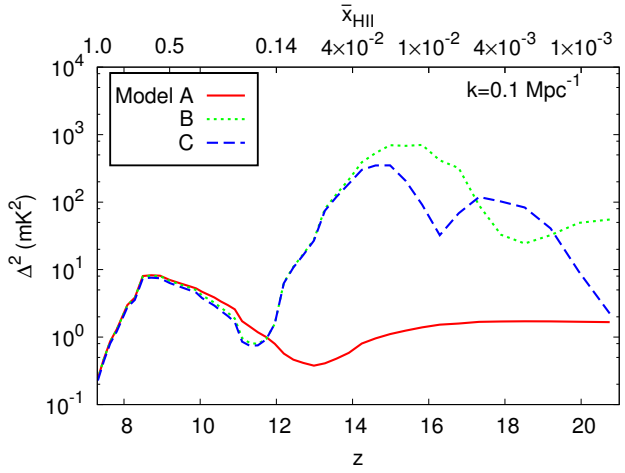

Figure 3.14: The brightness temperature power spectra as a function of redshift for models A, B and C at a scale $k = 0.1$ Mpc^{-1} for the scenario where small-mass haloes are taken into account using a subgrid prescription.

It is clear that our results on redshift-space distortion are independent of the exact X-ray background chosen, as long as it is non-zero. The only effect of varying f_X and α is to change the location of the peak in the power spectrum amplitude arising from $T_{\rm K}$ fluctuations. In Fig. 3.13, we show the evolution of the power spectrum amplitude as a function of the heated fraction $x_{\rm heated}$ for different values of f_X and α. We should mention that the quantity $x_{\rm heated}$ is defined as the fraction of points which have $T_{\rm K} > T_\gamma$. It is interesting that for $f_X > 0$, the location of the peak is independent of the level of X-ray background or the spectral index of the X-ray sources and appears when $x_{\rm heated} = 0.1$. It would be interesting to discuss the possibility of detecting this peak using the next generation of radio telescopes as that would clearly establish the signature of fluctuations in the IGM heating. Additionally, the position of the peak will tell us about the redshift when 10% of the IGM volume was heated above the CMBR temperature.

3.3.2 Effect of small-mass haloes

In this section, we describe the effects of small-mass haloes on the 21-cm signal, particularly at large scales. The initial stages of reionization are expected to

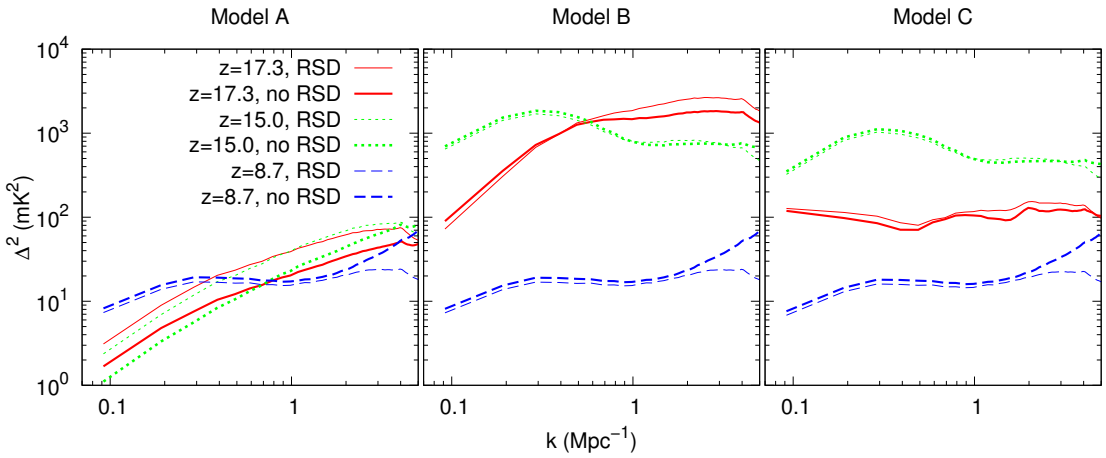

Figure 3.15: The brightness temperature power spectrum as a function of scale at three different redshift for model A, B and C in a scenario which accounts for small-mass haloes through a subgrid prescription.

be driven by sources in haloes as small as $\sim 10^8\,\mathrm{M}_\odot$. One difficulty with the models we have considered so far is that they do not contain haloes smaller than $3.89 \times 10^9\,h^{-1}\,\mathrm{M}_\odot$ (set by the particle mass of the simulation and the halo-finding algorithm), and hence the ionization field is not sufficiently correlated with the underlying density field. In order to address this issue, we use a sub-grid prescription to identify haloes with $M_{\rm halo} < 3.89 \times 10^9\,h^{-1}\mathrm{M}_\odot$ inside the $100\,h^{-1}$ Mpc box. The details of the prescription is discussed in Section 2.3.2. The results in this section are obtained using the parameters $f_X = 0.05$ and $\alpha = 1.5$. We have varied the parameter $f_\star$ to obtain a reionization history identical to that in Section 3.3.1.1. Note that we have not included any effects of radiative feedback on the small-mass haloes.

The evolution of the brightness temperature power spectra for the three models A, B and C at a scale $k = 0.1$ Mpc^{-1} is shown in Figure 3.14. One can see that the broad features are similar to that obtained for the scenario with only high-mass haloes. During the initial stages of reionization, the ionization field is highly correlated with the density field and hence the trough in the evolution curve for model A is deeper than previously obtained in Figure 3.5. In the presence of a large number of small-mass sources, the patchiness in the ionization

field is decreased as expected. The overall amplitude of the fluctuations in the brightness temperature is also lower at large scales compared to our fiducial case. As a result, the amplitude of the heating peak is lower than previously obtained in model B and C. For example, the heating peak in the evolution of the power spectrum is ~ 5 times smaller than that in the previous scenario (reionization driven by only high-mass sources). We also see a significant difference in the power spectrum when plotted as a function of the scale shown in Figure 3.15. First of all, peakiness of the "bump" like feature at large scale noted earlier is somewhat diminished. This is because the fluctuations are less when small sources are taken into account. As the number of small-mass sources is very large in this scenario, the characteristic heated region is also smaller than what was obtained previously at high redshift. As a result, the scale corresponding to the "bump" shifts, in general, towards the smaller scales when smaller sources are taken into account at high redshift. Like in the previous scenario, the heating peak (in the evolution curve of the power spectrum) occurs when ~ 10 % gas (by volume) is heated above T_γ.

For model A, the effect of redshift-space distortion is similar to the results of the previous scenario (as shown in Figure 3.15). In order to understand the effect of RSD, we have plotted the ratio of the redshift-space and real-space power spectra at $k = 0.1$ Mpc^{-1} as a function of z in Figure 3.16 for the three models A, B and C. In this case, the ratio increases initially, which was not found in the previous scenario (see Figure 3.9). This ratio increases to ~ 3 when the universe is $\sim 20\%$ ionized by mass for model A, which is similar to the results of previous studies like Jensen et al. (2013); Majumdar et al. (2013); Mao et al. (2012). This increment of the ratio depends on the level of coupling of the ionization field to the density field. We also checked with a source model similar to Jensen et al. (2013) and we found the ratio increase even larger than 3 for model A.

For models B and C, the effect of redshift-space distortion is similar at large scales, as shown in Figure 3.15. The effect of redshift-space distortion is smaller even in small scales $k \gtrsim 0.4$ Mpc^{-1}, which was not seen previously. The reason behind this is the fact that, with a large number of small sources taken into account, the fluctuations in brightness temperature at small scales too is dominated by $T_{\rm S}$ fluctuations. In another words, the power spectrum at redshift ~ 15 is dominated by the term $P_{\delta_\eta \delta_\eta}$ (see equation 3.10) even at small scales $k \sim 3$

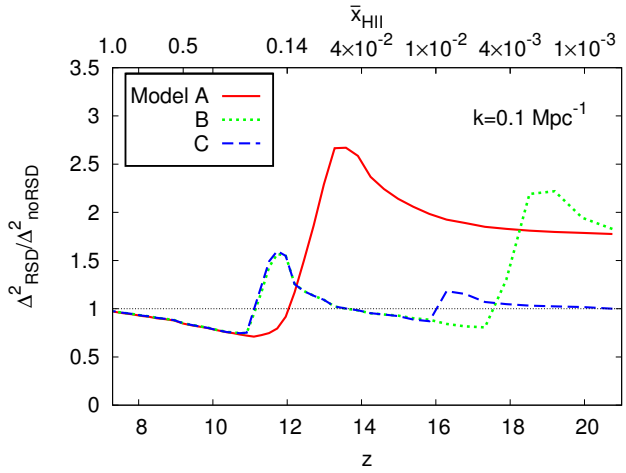

Figure 3.16: Ratio of redshift and real-space power spectrum as a function of redshift at large scale for model A, B and C (small-mass sources included using a subgrid prescription).

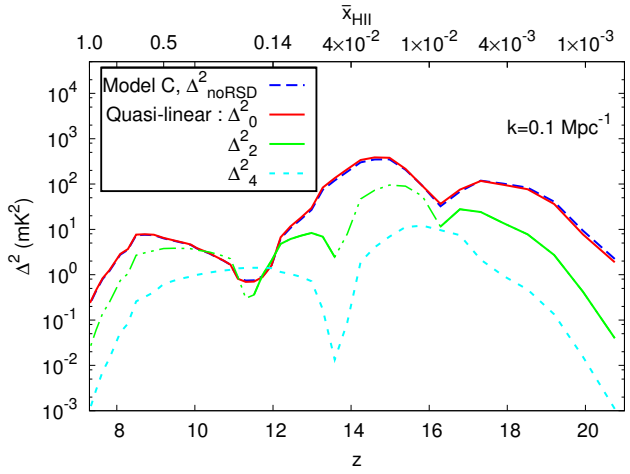

Figure 3.17: Evolution of different components of redshift-space power spectrum (in linear theory) with redshift in model C for a scenario where small-mass sources are included using a subgrid prescription. Solid part in the green curve represent positive value, whereas the dotted dashed part represent negative value.

Mpc^{-1}.

The ratio of the redshift-space and real-space power spectrum for model C, when plotted as a function of redshift, shows negligible effects for most of the time as can be seen from Figure 3.16. The effect of RSD is prominent only when the power spectrum has minima in its evolution, but this effect is for a short period. As shown in Figure 3.17, the anisotropies in the power spectrum are quite smaller (except for near the minima or dip in the evolution) than the real-space power spectrum at large scales and thus the effect of redshift-space distortion is not able to boost the power spectrum significantly at large scale for model C.

3.3.3 Effect of box size on the 21-cm power spectrum

As mentioned earlier, our fiducial simulation volume does not contain haloes smaller than $3.89 \times 10^9\, h^{-1}\, \mathrm{M}_\odot$ which are believed to be the main drivers of reionization at early stages. We have tried to overcome this difficulty by including small haloes using a sub-grid prescription in Section 3.3.2, however, such prescriptions may not be completely accurate. Resolving such small haloes using any halo-finder requires simulations of very high dynamic range. In order to address this issue, we run an additional dark matter simulation of size 30 h^{-1} cMpc with 768^3 particles. The mass resolution achieved in this case is $5.254 \times 10^6\, h^{-1}\, \mathrm{M}_\odot$, thus giving a minimum halo mass of $1.05 \times 10^8\, h^{-1}\, \mathrm{M}_\odot$. This box is helpful in probing the effects of small-mass haloes at early stages and also study the effects of box size and resolution. One should, however, note that this box is too small for studying the large scales which are expected to be accessible to the first generation radio telescopes. In this section, we compare the results from the $100\, h^{-1}$ and $30\, h^{-1}$ cMpc boxes, where in both cases the haloes are identified using the spherical overdensity algorithm.

Figure 3.18 show the effects of including small haloes in the analysis. The dashed blue curve represents the evolution of Δ^2 at a scale $k = 0.3$ Mpc^{-1} for the fiducial model in $100\, h^{-1}$ cMpc box, while the solid red curve represents the same for the $30\, h^{-1}$ cMpc box with $f_\star$ kept same as that for $100\, h^{-1}$ cMpc box[1]. For

[1]We should mention that we have plotted the power spectra at scale $k = 0.3$ Mpc^{-1} in Figure 3.18 rather than at $k = 0.1$ Mpc^{-1} as we had done in earlier sections. This is because larger scales are not accessible in the smaller $30\, h^{-1}$ cMpc box.

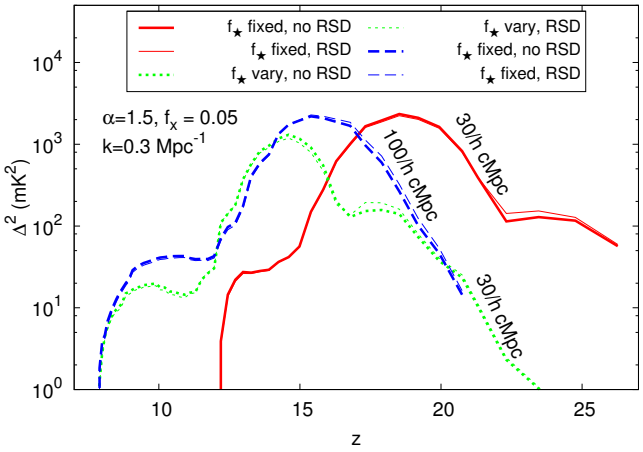

Figure 3.18: Comparison of the evolution of $\delta T_{\rm b}$ power spectra at $k = 0.3$ Mpc^{-1} for two simulations with $30\,h^{-1}$ cMpc and $100\,h^{-1}$ cMpc boxes. The results are shown for cases with and without the effects of redshift-space distortion.

the same value of the efficiency parameter $f_\star$, the presence of small haloes drive the reionization faster than what is found with the $100\,h^{-1}$ cMpc box. However, the basic features, i.e., the three peaks in the power spectrum remain the almost similar in the smaller box. What is interesting to note is that the effect of redshift-space distortion at these scales is negligible even when the small-mass haloes are taken into account.

We also study the case where $f_\star$ is varied for the small box so as to recover the ionization history identical to what we studied using the $100\,h^{-1}$ cMpc box. The dotted green curve in Figure 3.18 represents the results for such scenario. We find that the plots with and without the redshift-space distortion fall on top of each other. Thus the conclusion that the peculiar velocities do not affect the large scale power remains unchanged.

3.4 Summary and discussion

The main aim of this chapter is to investigate the effects of peculiar velocities of the neutral gas and spin temperature fluctuations in the IGM on the spherically averaged power spectrum of 21-cm brightness temperature during the early

stages of reionization, i.e, cosmic dawn. We have developed a code, based on the methods of Thomas and Zaroubi (2008); Thomas et al. (2009), to generate self-consistent brightness temperature maps. Our method consists of the following main steps: (i) We generate the dark matter density and velocity field using a N-body code CUBEP^{3}M (Harnois-Déraps et al. 2013). The same simulation data is used for identifying locations and masses of collapsed haloes. Since the main purpose of this work is to study the effects of peculiar velocities, it is important to model the velocity fields and the correlation between density and velocity fields as accurately as possible, which is only achieved in N-body simulations. (ii) The sources of reionization are modelled assuming each source has a stellar component and a mini-quasar like component for producing photons. The stellar component is modelled using a population synthesis code PEGASE2 (Fioc and Rocca-Volmerange 1997), while the other component was assumed to have a power-law spectrum. (iii) The radiative transfer was implemented using a one-dimensional code for isolated sources, and we have accounted for overlaps in ionized and heated regions of different sources appropriately.

We have validated our code by comparing with various existing results and found that all the features expected in the fluctuation power spectrum at early stages of reionization are nicely reproduced in our calculations (see e.g. Baek et al. 2010; Christian and Loeb 2013; Mesinger et al. 2011; Pritchard and Furlanetto 2007; Santos et al. 2008). In particular, we have studied in some detail the effects of inhomogeneities in the gas temperature and the Lyα coupling. Each of these effects produces distinct peak-like features in the large-scale power spectrum when plotted as a function of redshift. The peak which appears the latest in the history corresponds to the fluctuations in the H I field, which is targeted by the present generation of radio telescopes. The second peak corresponds to fluctuations in heating and occurs when $\sim 10\%$ of the volume is heated above the CMBR temperature. The third peak, which occurs the earliest in reionization history, arises because of inhomogeneities in the Lyα coupling.

Since the spin temperature fluctuations during the early stages of reionization introduce two additional peaks in the RMS vs. redshift plot, fitting a single peak function over the entire redshift range like the one proposed earlier (Patil et al. 2014b) could possibly result in misinterpretation of the data. One can, however, restrict the analysis within lower redshift (e.g, $8 < z < 11$ for model C) or choose

a function with three peaks. One should also be careful that the influence of the spin temperature fluctuations in the RMS (and also in the power spectrum at large scales) remains for a while even when the entire IGM is heated above the CMBR temperature.

We have considered two different scenarios: (i) when reionization is driven by only high-mass sources and (ii) when small-mass sources are included as well. In scenario (i), the heated bubble sizes are large and as there are only rare high-mass sources, fluctuations in the brightness temperature are larger at large scale compared to small scale. This causes a "bump" like feature in the power spectrum when plotted as a function of k, in a situation when the spin temperature is coupled to the kinetic temperature but the gas is heated inhomogeneously. The "bump" corresponds to a typical size of the heated bubbles. Thus, this peak can be used to constrain the sizes of heated bubbles which has further implications in constraining properties of X-ray sources. In the presence of a large number of small sources, the fluctuations in $\delta T_{\rm b}$ is much larger than scenario (i) at small scale and thus the "bump" is smoothed out to some extent and shifts towards small scales.

Once we incorporate the effects of peculiar velocities in our model and compare with the case when such effects are absent, we find that at large scales, i.e., $k \lesssim 0.4\,{\rm Mpc}^{-1}$, the effects on the spherically averaged power spectra are negligible throughout reionization history for scenario (i). It is not difficult to understand the reasons for this: the effect of peculiar velocities is substantial only when the 21-cm fluctuations are correlated with the underlying baryonic density field. At late stages of reionization ($x_{\rm HII} \gtrsim 0.2$), the 21-cm fluctuations are dominated by the fluctuations in H I field. The ionization fronts at these epochs have percolated in the low-density cosmological density field and the H I field is not correlated with the density field any more. Hence one finds no effect of the peculiar velocities on the 21-cm signal. On the other hand, during early stages of reionization ($x_{\rm HII} \lesssim 0.2$), the fluctuations at large scales are dominated by the $T_{\rm S}$ fluctuations, which too are only very mildly correlated with the density field. Interestingly, if the $T_{\rm S}$ fluctuations are not accounted for in the model, the 21-cm fluctuations are dominated by H I fluctuations even during early stages. In the inside-out models of reionization, the H I fluctuations are highly correlated with the density field and thus one seems to find relatively stronger effects of peculiar velocities on

the 21-cm fluctuations (see e.g. Jensen et al. 2013; Majumdar et al. 2013, 2014). In fact for reionization scenario with only high-mass sources, at smaller scales $k \gtrsim 0.4$ Mpc^{-1}, the 21-cm fluctuations even at the early stages of reionization are dominated by patchiness in the H I field, and it is not surprising that the power spectrum in the redshift-space is enhanced in the amplitude compared to the real-space counterpart. In the presence of small-mass sources, the 21-cm fluctuation is dominated by $T_{\rm S}$ fluctuation and thus the effect of RSD is not significant even at small scales. It was suggested that for a reionization scenario where the spin temperature is much higher than the CMBR temperature, the redshift-space distortion effect which makes the power spectrum anisotropic is detectable with 2000 hrs of observations using LOFAR. It was also suggested that such observations could tell us whether reionization occurred inside-out or outside-in (Jensen et al. 2013; Majumdar et al. 2013). However, since the isotropic component of the power spectrum dominates over the anisotropic terms in scenarios where spin temperature fluctuations are important, the detectability of the redshift-space distortion effect in the power spectrum needs to be reassessed.

We have checked our conclusions for different X-ray properties of the sources (i.e., the amount of X-rays produced compared to the UV and the steepness of the X-ray spectra), and also on the resolution of the simulation box. The conclusions seem to be quite robust in this respect. It thus implies that the 21-cm fluctuations would be quite isotropic at large scales throughout the reionization epoch, while one expects some departures from isotropy at relatively smaller scale $k \gtrsim 0.4$ Mpc^{-1} if reionization is solely driven by high-mass sources.

In future, it would be interesting to study the anisotropies in the 21-cm power spectrum arising from peculiar velocities at early stages of reionization. While we expect that the detectability of anisotropies at large scales could be somewhat challenging because of cosmic variance, it may be easier to detect the anisotropic signal at smaller scales. The exact nature of this signal depends on the lowest mass source at that epoch. It would be interesting to explore the possibilities of constraining early source properties using this feature. Also, one should keep in mind that we have concentrated only on peculiar velocity effects, while there could be other sources of anisotropy in the signal. A prominent effect is that of the evolution of ionization history i.e., the light cone effect (Datta et al. 2014, 2012b; La Plante et al. 2014; Zawada et al. 2014). The only X-ray sources considered in

this chapter are mini-quasar like. It would be interesting to extend our analyses to other types of X-ray sources (e.g., high-mass X-ray binaries) and verify if the conclusions remain unchanged.

3. 21-CM SIGNAL FROM COSMIC DAWN: IMPRINTS OF SPIN TEMPERATURE FLUCTUATIONS AND PECULIAR VELOCITIES

4 | 21-cm signal from cosmic dawn: Imprints of the light-cone effects

The contents of this chapter are taken from Ghara et al. (2015b).

4.1 Introduction

In this chapter, we investigate one of the important line of sight effects i.e, the 'light-cone effect' on the 21-cm signal from the cosmic dawn and EoR. While simulating the signal, it is generally assumed that every part of a simulation box has the same redshift. We call each such simulation snapshot as 'coeval box'. In reality, regions which are nearer to the observer along a line of sight will have lower redshifts than the regions which are far away. As a result, the observed signal will have effects of redshift evolution imprinted on it. Studies through analytical modelling and simulations have been done to understand this so-called 'light-cone' effect on the two-point correlation function (Barkana and Loeb 2006; Zawada et al. 2014) and power spectrum (Datta et al. 2014, 2012b; La Plante et al. 2014). Datta et al. (2014) find that, depending on the observational bandwidth, the effect could enhance the power spectrum by a factor of up to ~ 5 at the initial stages of the EoR and suppress by a significant amount at the last stages of the EoR. Interestingly, no significant light-cone anisotropy has been found in Datta et al. (2014). It has also been noticed that the light-cone effect on the power spectrum will be significant when it evolves non-linearly with redshift as the linear evolution is smoothed out (Datta et al. 2012b). However, these

studies assume that the entire IGM is always heated significantly higher than the CMBR brightness temperature and that the Lyα coupling is very strong. These assumptions may hold during the later stages of reionization but may not be true at the cosmic dawn and the initial phase of reionization. It is believed that the inhomogeneities in heating and Lyα coupling will significantly influence the signal during cosmic dawn and early phase of the EoR (when the mass averaged ionization fraction $x_{\rm HII} \lesssim 0.2$). These make the evolution of the H I power spectrum with redshift more dramatic and thus we expect a very strong light-cone effect on the signal. Zawada et al. (2014) too have studied this using numerical simulations with the main focus on the two-point correlation functions. In this chapter, we self-consistently calculate the Lyα coupling, heating of the IGM for various source models and reionization histories and study the light-cone effect on the H I power spectrum.

We have organized the chapter in the following way. In Section 4.2, we have briefly described the N-body simulation used for this study and the method to incorporate the light-cone effect in the coeval box. We have presented our results in Section 4.3 before summarizing and discussing our results in Section 4.4. The cosmological parameters used for the simulation are $\Omega_m = 0.32$, $\Omega_\Lambda = 0.68$, $\Omega_B = 0.049$, $h = 0.67$, $n_{\rm s} = 0.96$, and $\sigma_8 = 0.83$, consistent with the recent results of *Planck* mission (Planck Collaboration et al. 2014a).

4.2 Simulations

4.2.1 Anisotropy in the 21-cm signal

As described in Chapter 2, the H I 21-cm signal depends on the neutral fraction, the spin temperature of H I and the background cosmology. In general, the universe is expected to be isotropic at large scales, though several effects can generate anisotropy in the observed signal. The line of sight peculiar velocity of gas (or the so-called redshift-space distortion (RSD)) in the IGM can affect the $\delta T_{\rm b}$ fluctuations and hence the signal along the line of sight and thus can introduce a difference in the power spectrum along and perpendicular to the observed direction (Jensen et al. 2013; Majumdar et al. 2013; Mao et al. 2012). On the other hand, the Alcock-Paczynski effect can also significantly contribute to

the anisotropy in the observed signal (Alcock and Paczynski 1979; Ali et al. 2005; Barkana 2006). In general, the anisotropic 21-cm power spectrum is denoted as $\Delta^2(k, \mu)$, where $\mu = \cos\theta$ with θ being the angle between the line of sight and the Fourier mode $\mathbf{k}$. Since the light-cone effect too influences the signal only along the line of sight, it can in principle make the signal anisotropic. In this chapter, we mainly focus on the light-cone effect on the spherically averaged power spectrum and we will discuss the anisotropy introduced by this to the 21-cm power spectrum in Section 4.3.5.

The simulation of the $\delta T_{\rm b}$ signal involves three main steps: (i) generation of underlying baryonic density and velocity fields, (ii) modelling the radiation sources and (iii) computing the propagation of ionization and heating fronts using a 1D radiation transfer code. Here, we will briefly describe the N-body simulation used in this study as this is different than the dark matter simulations used for the study of the effect of redshift-space distortion on the 21-cm signal. The method to generate the $\delta T_{\rm b}$ maps and the source selection procedure are same as described in Chapter 2. In this case, we have used the cell movement method (or Mesh-to-Mesh (MM)-RRM scheme) described in Chapter 3 for implementing the RSD effect to the simulation cubes.

Note that we have included the effect of radiative feedback in this chapter, while it was excluded in Chapter 3. We assume that no star formation occurs within low-mass haloes ($< 10^8\,{\rm M}_\odot$). In order to incorporate radiative feedback, we suppress the galaxy formation within newly formed haloes having mass $M < 10^9\,{\rm M}_\odot$ if they form in already ionized regions, i.e., regions of the IGM with $x_{\rm HII}$ larger than 0.5. [1] Since $x_{\rm HII}$ profile drops sharply from 1 to 0.1 for different values of f_X and α considered in this thesis, the results should not differ much while varying the threshold in the range $0.1 < x_{\rm HII}^{\rm th} < 1$.

[1] The radiative feedback is effective when the IGM is photo-heated to a temperature $> 10^4\,{\rm K}$, which raises the cosmological Jeans mass and thus suppresses galaxy formation in low-mass haloes with mass $M < 10^9\,{\rm M}_\odot$. In general, regions with temperature $> 10^4\,{\rm K}$ are highly ionized (with $x_{\rm HII} > 0.5$), hence our implementation of feedback should be reasonable. In more realistic scenarios, the feedback is not expected to be so drastic, e.g., $M < 10^9{\rm M}_\odot$ haloes within ionized regions can retain a fraction of their gas and possibly form stars at a lower rate. Our method does not account for such effects.

4.2.2 N-body simulations

The density and velocity fields, used in our simulation, are generated using the publicly available code CUBEP^{3}M[1] (Harnois-Déraps et al. 2013) which is a massively parallel hybrid particle-particle-particle-mesh (P^{3}M) code. The simulation started at redshift $z = 200$ with the initialization of the particle positions and velocities using CAMB transfer function[2] (Lewis et al. 2000) and employing Zel'dovich approximation.

The properties of the simulations we have used in this chapter are: (i) the number of particles used is 1728^3, (ii) the box size is 200 h^{-1} comoving Mpc (cMpc), (iii) the number of grid points used are 3456^3 and (iv) the mass of each dark matter particle is $2 \times 10^8\,\mathrm{M}_\odot$. Since the position and velocity arrays of the simulation are too large in size, we prefer to generate the density and velocity fields on a grid 8 times coarser than the simulation grid using a top-hat filter. These snapshot files are generated between $25 \geq z \geq 6$ in an equal time gap of 10^7 years. The baryons are assumed to be simply tracing the dark matter, i.e., if dark matter density at position $\mathbf{x}$ is $\rho_{\rm DM}(\mathbf{x})$, then the baryonic density will be $\rho_{\rm B}(\mathbf{x}) = (\Omega_B/\Omega_m) \times \rho_{\rm DM}(\mathbf{x})$. The velocity files on the coarse grid are used to incorporate the peculiar velocity effects in the 21-cm brightness temperature.

For each snapshot, haloes were identified using a runtime halo finder algorithm which uses spherical overdensity method. The minimum halo mass resolved using this method is $\sim 2 \times 10^9\,\mathrm{M}_\odot$. Apart from these haloes, it is expected there will also be a considerable number of small mass haloes $\sim 10^8\,\mathrm{M}_\odot$ where the gas can cool via atomic transitions and form stars. As the number of such small mass haloes is quite high, these haloes may have a significant impact on the reionization scenarios, particularly at the early stages. Identifying such small mass haloes with the spherical overdensity method requires simulation box of a higher resolution, which is somewhat beyond our ability right now. Hence we employ a sub-grid method to find the haloes down to masses as small as $\sim 10^8\,\mathrm{M}_\odot$. We have followed the extended Press-Schechter model of Bond et al. (1991) and hybrid prescription of Barkana and Loeb (2004) for implementing the sub-grid model (for details see Chapter 2).

[1] `http://wiki.cita.utoronto.ca/mediawiki/index.php/CubePM`
[2] `http://camb.info/`

4.2.3 Implementing the light-cone effect

The light-cone effect essentially accounts for the evolution of the signal with redshift within the simulation box or the so-called "coeval cube" (CC). Datta et al. (2012b) have described the procedure to incorporate the effect and produce the light-cone cube. In our study, we have incorporated the effect in individual coeval cubes instead of generating the full redshift range light-cone cube as done in Datta et al. (2012b). We assume that the central "slice" of the coeval cube represents the cosmological redshift, where a "slice" is a 2D map having width ~ 0.7 cMpc (corresponding to one pixel of the simulation box). Along a given line of sight, different distances represent different redshifts, and thus $\delta T_{\rm b}$ will be different from that in the coeval cube. The steps to include the light-cone effect are as follows:

(i) We generate the so-called "coeval cubes" of 21-cm $\delta T_{\rm b}$ maps at different redshifts following the method stated in Section 2.7 of Chapter 2 and including the RSD effect. Let us assume that we have N numbers of such cubes which correspond to the cosmological redshifts z_i, where $i = 1, N$, with $z_1(z_N)$ being the lowest (highest) redshift in our simulation (in our case, we have 77 such coeval cubes between redshift 6 and 20 while we have used fixed time sampling of 10 Myr).

(ii) Each of these coeval cubes has a length L and contain n^3 grid points, which in our case have the values 200 h^{-1} cMpc and 432^3 respectively. We assume the central 2D slice of the cube, in the perpendicular plane of the line of sight (x-axis in this case), correspond to the cosmological redshift of the coeval cube. The comoving distance $D(z_l, z_u)$ between two redshifts z_l and z_u is given by,

$$D(z_l, z_u) = \int_{z_l}^{z_u} \frac{c}{H(z)} dz, \tag{4.1}$$

where c is the speed of light and $H(z)$ is the Hubble constant at redshift z. Depending on the distance from the central slice along the line of sight, we calculate the corresponding redshift for each slice. For example, the redshift z_p corresponding to the pth slice is calculated by demanding that $D(z_c, z_p)$ in equation (4.1) is equal to the distance $(p - n/2) \times L/n$ of the pth slice from the central slice. Note that z_c is the redshift corresponding to the central slice. In the light-cone cube,

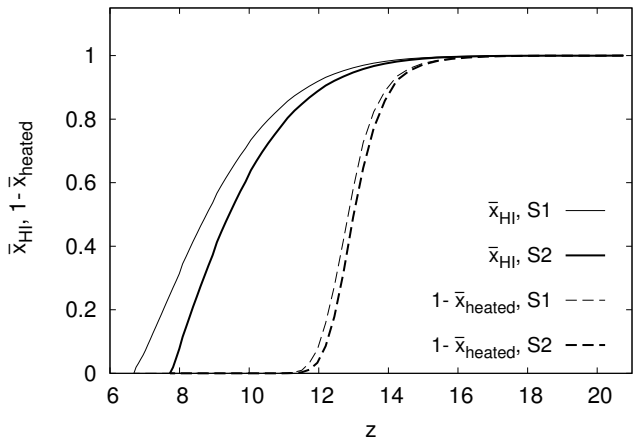

Figure 4.1: The solid curves represent the evolution of the mass averaged neutral fraction of hydrogen ($\bar{x}_{\rm HI}$) in the IGM. The dashed curves represent the evolution of $(1-\bar{x}_{\rm heated})$, where $\bar{x}_{\rm heated}$ is the volume averaged heated fraction of the IGM. The thin and thick curves represent models $S1$ and $S2$ respectively. We have defined 'heated region' as a region with $T_{\rm K}$ larger than T_γ. The X-ray spectrum from the central mini-quasar follows a power law with index α =1.5 and the X-ray to UV luminosity of the source is 0.05 for this model.

the signal at each slice would be at the redshift corresponding to that slice and not the cosmological redshift of the coeval cube.

(iii) If the pth slice corresponds to a redshift z_p, which satisfies the condition $z_i < z_p < z_{i+1}$, then the $\delta T_{\rm b}$ maps for that slice is computed by linearly interpolating the maps of the slices at redshifts z_i and z_{i+1}. Applying the same procedure to all the slices, the "light-cone cube" is generated which corresponds to the redshift of the central slice.

Note that the redshift-space distortion needs to be applied to the brightness temperature maps before implementing the light-cone effect, otherwise, the redshift evolution of the gas velocities will not be incorporated properly.

4.3 Results

In order to compute the $\delta T_{\rm b}$ maps, one first has to choose appropriate reionization and heating histories, which in turn depend on the nature of sources. In this

chapter, we consider three models of radiation sources $S1, S2$ and $S3$ as listed in Table 4.1 to investigate the effect of different reionization histories on the $\delta T_{\rm b}$ maps. For all the three source models, we assume each galaxy to contain a mini-quasar like source at the centre which radiates X-rays with a power law distribution having index α =1.5, and the X-ray to UV luminosity fraction of the source f_X is 0.05. We have fixed the parameter $f_\star$ to 0.1 throughout the reionization history, while the escape fraction $f_{\rm esc}$ is taken to be different in different models. In model $S1$, we take $f_{\rm esc} = 0.1$ which causes the reionization to start at $z \sim 20$ and complete at $z \sim 6.5$. The electron scattering optical depth τ turns out to be 0.07, which is consistent with the recent constraints from Planck (Planck Collaboration et al. 2015b). The mass averaged neutral hydrogen fraction, shown in Figure 4.1, attains a value 0.99 and 0.5 around redshift 14 and 8.5 respectively for $S1$.

The value of $f_{\rm esc} = 0.2$ is higher in model $S2$ leading to early reionization completing at $z \sim 8$. The resulting value of $\tau = 0.076$ is higher than that in model $S1$ but is still consistent with the recent Planck constraints (Planck Collaboration et al. 2015b). In the presence of a mini-quasar like X-ray source at the centre of each galaxy, the evolution of the heated fraction (defined as the volume fraction of regions with $T_{\rm K} > T_\gamma$) is much faster than the evolution of ionization fraction. As shown in Figure 4.1, the universe becomes completely heated below redshift ~ 12 for both the source models $S1$ and $S2$.

Note that the minimum halo mass for $S1$ and $S2$ source models is $\sim 2 \times 10^9\,{\rm M}_\odot$, i.e., we have not included any sub-grid sources in these two models. The effect of small mass haloes is studied in model $S3$ where haloes as small as $10^8\,{\rm M}_\odot$ are included using the sub-grid prescription discussed in Section 4.2.2. The value of $f_{\rm esc}$ is varied at every redshift so as to generate a reionization history (i.e., mass averaged neutral fraction) identical to the model $S2$. In addition, we have included the effects of radiative feedback in model $S3$.

As in Chapter 3, we will consider three different models of heating and Lyα coupling and study the light-cone effect. The models are listed in Table 3.1 of Chapter 3. Model A assumes $T_{\rm S}$ to be much larger than T_γ, this model is identical to models used in Datta et al. (2014, 2012b); La Plante et al. (2014). Model B assumes the IGM kinetic temperature to be coupled with the spin temperature through Lyα radiation (i.e, the Lyα coupling coefficient $x_\alpha(\mathbf{x}) \gg 1$), but the

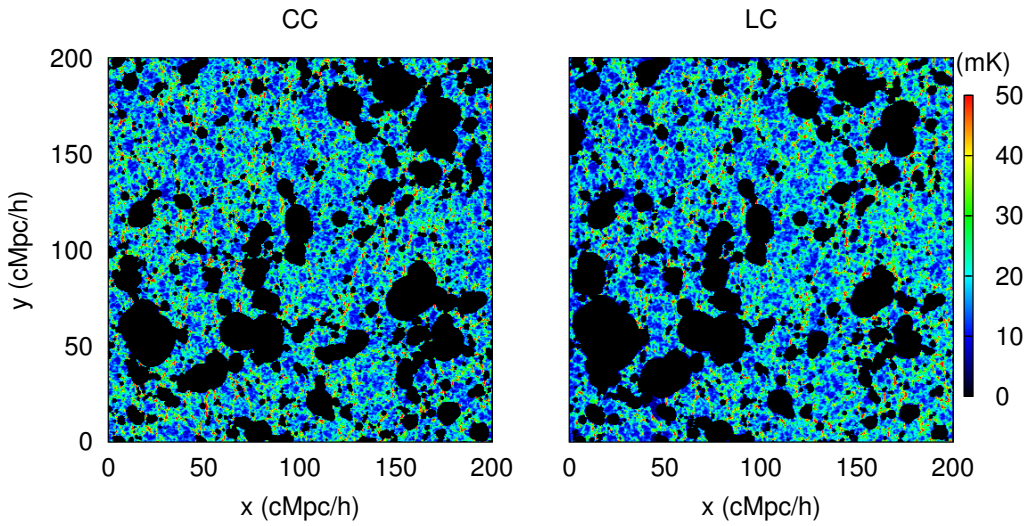

Figure 4.2: Randomly chosen two-dimensional slice of the $\delta T_{\rm b}$ distribution with RSD included from the coeval cube (left) and light-cone cube (right) at redshift 9.5 (with mass averaged ionization fraction 0.5) for the model A with the source model $S2$. The comoving size of the box is 200 cMpc h^{-1}. The central redshift of the light-cone (LC) cube is 9.5, whereas the redshift span from left to right along the x-axis (LOS direction) is 8.86 to 10.13. Note that this model makes the assumption $T_{\rm S} \gg T_{\gamma}$ and is driven by haloes identified using spherical overdensity halo-finder in the simulation box.

heating is calculated self-consistently. Finally in model C, we have calculated the heating and Lyα coupling self-consistently and thus it is the most realistic model to be considered while generating $\delta T_{\rm b}$ maps. The ionization history in Figure 4.1 is same for all the three models A, B and C, while the heating history is same for the models B and C. The effect of peculiar velocities of the gas is also taken into account in all the three models.

4.3.1 Visualizing the light-cone effect

The light-cone effect can be easily visualized in the maps of $\delta T_{\rm b}$ distribution for different models. Figure 4.2 shows the $\delta T_{\rm b}$ map computed on a randomly chosen slice from the simulation box for the model A with the source model $S2$. The

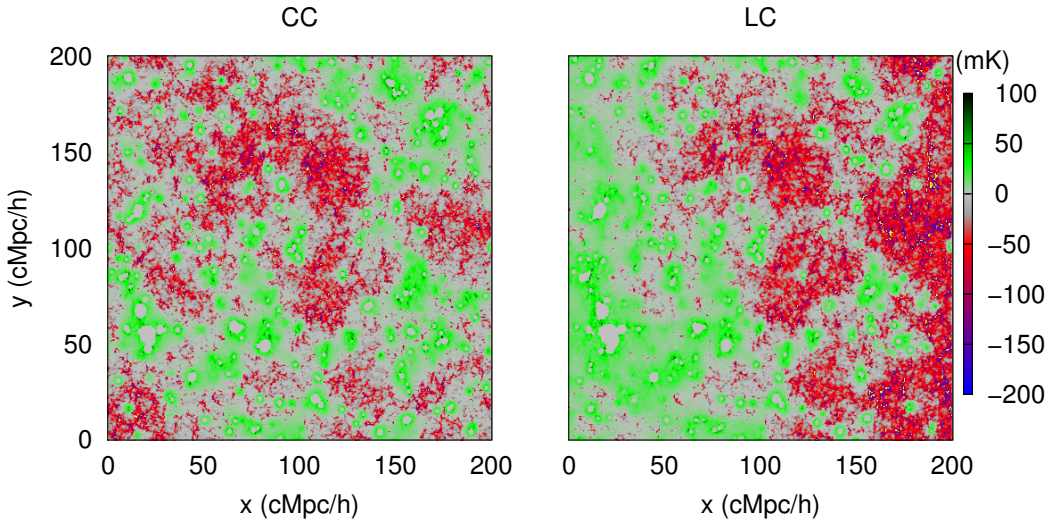

Figure 4.3: Similar to Figure 4.2, but for the model C and the coeval cube corresponding to redshift 13 when the universe was 50 % heated by volume for the source model $S2$. The left and right hand edge of the 'LC' box correspond to redshifts 12 and 14 respectively.

Source model	$f_{\rm esc}$	τ	$z_{\rm end}$	$M_{\rm halo}^{\rm min}$ ($\rm M_\odot$)	sub-grid halo	radiative feedback
$S1$	0.1	0.07	6.5	2×10^9	no	no
$S2$	0.2	0.076	7.8	2×10^9	no	no
$S3$	varying	0.076	7.8	10^8	yes	yes

Table 4.1: Properties of the source models considered in this chapter. The UV escape fraction $f_{\rm esc}$ for the model $S3$ is varied to get similar ionization history like $S2$.

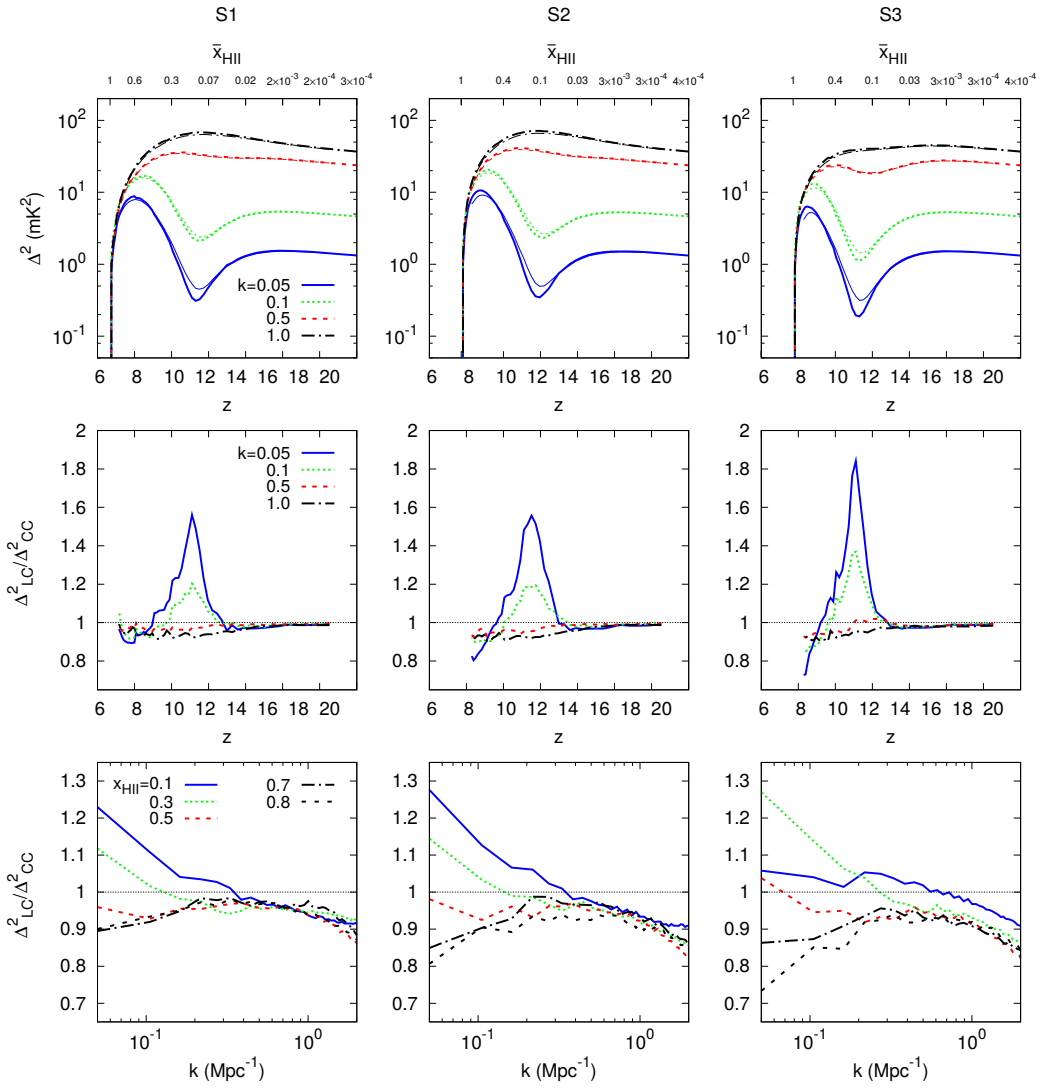

Figure 4.4: Model A: The light-cone effect on the power spectrum of 21-cm brightness temperature fluctuation. The upper most panels show the spherically averaged power spectrum of $\delta T_{\rm b}$ with (thin curves) and without (thick curves) light-cone effect as a function of redshift for four different scales $k/{\rm Mpc}^{-1} = 0.05$ (solid), 0.1 (dotted), 0.5 (dashed) and 1.0 (dot-dashed). The middle row panels show the ratio of the power spectra with and without light-cone effect as a function of redshift. The bottom most panels show the ratio of the power spectra with and without light-cone effect as a function of scales for different ionization fractions (0.1,0.3, 0.5, 0.7 and 0.8). This model makes the assumption that $T_{\rm S} \gg T_{\gamma}$. Three columns represent three different source models $S1, S2$ and $S3$ respectively. Redshift-space distortion is included in all the panels.

left-hand panel shows the distribution of $\delta T_{\rm b}$ from the coeval cube (with redshift-space distortion included, but without the light-cone effect) at redshift 9.5 with mass averaged ionization fraction 0.5. The right-hand panel shows the same slice with the light-cone effect incorporated. Along the line of sight (horizontal axis), the central redshift of the light-cone (LC) cube is 9.5, whereas the light-cone cube spans from redshift 8.86 (left edge of the box) to 10.13 (right edge of the box). The ionization bubbles (black regions) are larger at the left-hand side of the middle of the light-cone cube as compared to the coeval cube. This is because of the fact that the left-hand side regions correspond to lower redshifts than the middle region of the box and thus correspond to later stages of reionization where the bubbles are of systematically larger. It is opposite in the case of right-hand side regions.

Figure 4.3 shows similar slices at redshift 13 for the model C. In this case not only the ionized regions appear larger in the front side of the light-cone cube compared to the coeval cube, but the heated regions (regions with $T_{\rm K} > T_{\gamma}$) too show similar trend. One should notice that the left half shows the signal predominantly in emission whereas the right half shows the same mostly in absorption, although the corresponding coeval slice shows that emission and absorption regions are homogeneously distributed over the entire slice. This significant imbalance of the emission regions between the left and right-hand regions of the light-cone cube is expected to introduce effects on the observable signal at initial stages of reionization.

4.3.2 Comparison with previous studies

It is possible to validate our formalism by comparing the model A where we have assumed $T_{\rm S} \gg T_{\gamma}$ with the existing works in the context of the light-cone effect on the 21-cm signal. Figure 4.4 shows the light-cone effect on the spherically averaged power spectrum of the 21-cm $\delta T_{\rm b}$ fluctuations (with redshift-space distortion included) for the model A.[1] The upper panels show the evolution of the dimensionless power spectrum for the three source models as a function of redshift for four different scales $k = 0.05$, 0.1, 0.5 and 1 Mpc^{-1} which are represented

[1]Note that we exclude modes with $\mathbf{k}_{\perp} = 0$ while calculating the power spectrum, as these modes are not accessible to the interferometers.

by the solid, dotted, dashed and dot-dashed curves, respectively. The signal is always in emission for this model and thus the power spectra have relatively smaller amplitudes ($\sim 10\,\mathrm{mK}^2$) at large scales. The large-scale power spectrum for each of the three source models shows one trough and one peak when plotted as a function of redshift around the period when the universe was $\sim 10\%$ and $\sim 65\%$ ionized by mass. Initially the highly dense regions get ionized and thus H I fluctuations at large scales are suppressed. This results in the trough-like feature in the evolution of the power spectrum (e.g, Datta et al. 2014; Majumdar et al. 2013). The power spectrum then increases with the growth of bubble size and finally decreases with the decrease in ionization fraction, which generates the prominent peak around ionization fraction 0.65 for this model.

The thick (thin) curves in the upper panels of the figure represent the power spectra without (with) the light-cone effect included. It is clear that the light-cone effect is most substantial around the trough and the peak regions in the evolution of the power spectra. Because of this effect, the power spectra can be enhanced by a factor as large as $\sim 50\%$ (when $x_{\rm HII} \sim 0.15$) and suppressed by $\sim 20\%$ (when $x_{\rm HII} \sim 0.8$) for the model $S2$ at large scales $k = 0.05\,\mathrm{Mpc}^{-1}$, as shown in the middle panels of Figure 4.4. The effect is minimum around the period when the universe is $\sim 50\%$ ionized. This is because of the fact that around 50% ionization, any linear evolution of the power spectrum as a function of z is smoothed out [1], as was pointed out by Datta et al. (2012b) . On the other hand, when $x_{\rm HII} \sim 0.1$ and 0.8 the evolution of the power spectrum is highly non-linear which makes the

[1] The coeval cube spherically averaged 3D power spectrum can be expanded in a Taylor series around the central redshift (z_c) as (Datta et al. 2012a),

$$\Delta^2_{\rm CC}(k,z) = \Delta^2_{\rm CC}(k,z_c) + a(\Delta L) + b(\Delta L)^2 + .. \tag{4.2}$$

where a, b are the coefficient of the Taylor series and ΔL is the comoving distance between the redshifts z and z_c. The light-cone power spectrum can be written as average of the coeval power spectrum in the range $\pm L/2$ around the central redshift.

$$\begin{aligned}\Delta^2_{\rm LC}(k,z) &= \frac{1}{L}\int_{L/2}^{L/2} \Delta^2_{\rm CC}(k,z)dL \\ &= \Delta^2_{\rm CC}(k,z_c) + b\frac{L^2}{12} + ..\end{aligned} \tag{4.3}$$

One can see that all the odd powered terms including the linear term vanish and only the quadratic terms remain.

effects strong (Datta et al. 2014, 2012b). We also see that the effects are less for a smoother ionization model like $S1$ compared to $S2$. The reason is that in the case of $S1$, the evolution of the ionized bubbles is less rapid compared to model $S2$. The evolution of power spectrum is more non-linear at the trough and the peak regions in the presence of small mass haloes as shown in the upper panel for the model $S3$. Thus the light-cone effect in model $S3$ is larger compared to the other two models. The bottom most panels of the figure show the scale dependence of the ratio of the power spectrum with and without light-cone effect at different stages of the reionization history. The evolution of the power spectrum at small scales is much more linear as shown in the upper panels of the figure and thus the light-cone effect is smaller at small scales compared to larger scales. Our results for the model A are consistent with a similar model presented in Datta et al. (2014).

4.3.3 Effect of inhomogeneous heating and Lyα coupling on the light-cone effect

We now discuss the light-cone effect in the presence of non-uniform heating and Lyα coupling. Figure 4.5 shows the same quantities plotted in Figure 4.4 but for the model B (where the fluctuations in heating are calculated self-consistently, but the Lyα coupling process is assumed to be very efficient all throughout). The top panels show the evolution of power spectra for different length scales. One can compare the plots with those in Figure 4.4 and immediately conclude that the evolution is much more rapid in the model B. For example, the amplitude of the power spectrum is ~ 50 mK^2 at $z \sim 20$ which increases up to ~ 500 mK^2 at $z \sim 15$ and then decreases rapidly to ~ 0.5 mK^2 at $z \sim 11$ for $k = 0.05$ Mpc^{-1} (in the $S2$ model). The corresponding evolution is much less rapid for the model A where the amplitude is almost constant at ~ 1 mK^2 from $z = 20$ till $z \sim 14$. The light-cone effect is thus expected to be more significant for the model B.

The evolution of the power spectrum is faster in model B, due to the fact that the heated bubbles are larger and grow much faster than the ionized bubbles. This causes the evolution of the heated fraction to be very rapid compared to the evolution of the ionization fraction (see Figure 4.1). As a large fraction of the gas in the IGM has temperature $T_{\rm K}$ less than T_γ during cosmic dawn and initial phase

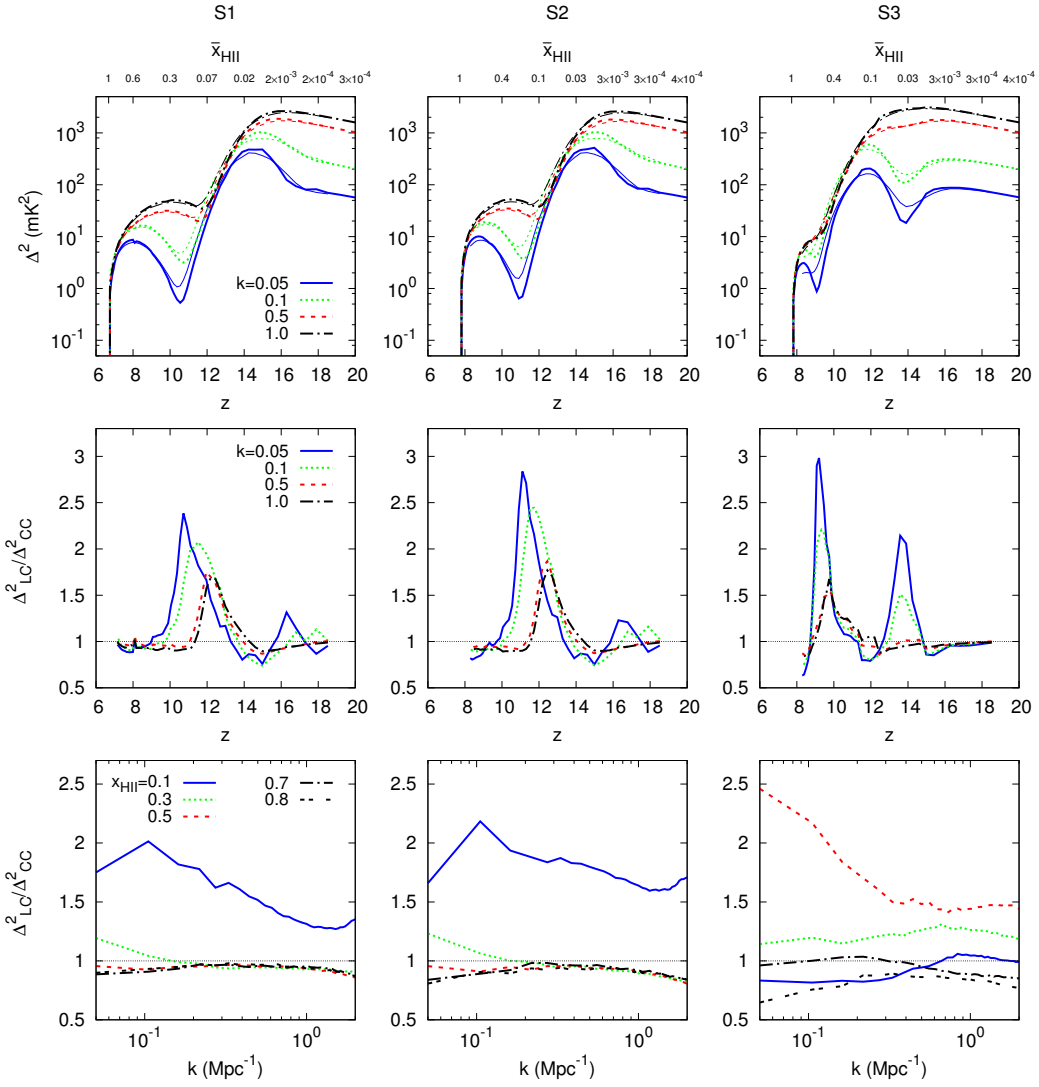

Figure 4.5: Same as Figure 4.4, but for the model B where the IGM is assumed to be Lyα coupled while the heating is calculated self-consistently.

of reionization (as gas temperature falls as $(1+z)^2$ due to adiabatic expansion of the universe after the decoupling around redshift $z_{\rm dec} \sim 150$ and T_γ falls as $(1+z)$) and the model assumes $T_{\rm S} = T_{\rm K}$, the model shows very large absorption signal from the cosmic dawn until the IGM is sufficiently heated to follow the model A from $z \sim 10$ for $S2$. The inhomogeneous X-ray heating from the mini-quasars results in increasing the $\delta T_{\rm b}$ fluctuations, which produces a distinct peak in the power spectrum at large scales around $z \sim 15$ when plotted against z. The second prominent peak occurs at $z \sim 9$ because of ionization fluctuations analogous to the model A. The amplitude of the power spectrum at the heating peak ($\sim 10^3\,{\rm mK}^2$) is significantly higher compared to the ionization peak ($\sim 10\,{\rm mK}^2$) and hence this redshift range might be of interest to interferometers like the SKA. The reason for this is that at the ionization peak around $z \sim 9$, the power spectrum is dominated by ionization fluctuations and the signal is in emission because the heating is already substantial. On the other hand, at the heating peak around $z \sim 15$, the $\delta T_{\rm b}$ field consists of both emission and absorption regions, and the power spectrum is dominated by $T_{\rm S}$ fluctuations (see Chapter 3).

As can be seen from Figure 4.5, the light-cone effect is much more prominent in the model B compared to the model A. When the light-cone effect is included in the analysis, we find maximum suppression of power spectrum around the two peak regions and increase around the trough region between the two peaks. Inhomogeneous heating makes the evolution of the power spectrum much more non-linear and results in a stronger light-cone effect on the power spectrum than that in the model A. The figure also shows that the light-cone effect can increase the power spectrum by a factor as large as 1.23 and 2.84 times around redshifts 16 and 11 respectively at large scales ($k \sim 0.05\,{\rm Mpc}^{-1}$) for the model $S2$. The suppression of the power spectrum around the peaks around redshifts 8 and 15 can be $\sim 20-25\%$ at large scales. The redshift evolution of the power spectrum at small scales is almost linear during the cosmic dawn and initial phase of reionization as shown in the uppermost panels of the figure and thus the light-cone effect is minimum at small scales during these epochs. Around redshift 12 when the IGM becomes highly heated, the evolution in the small scale $\delta T_{\rm b}$ fluctuations becomes extremely fast which results in the increment of the power spectrum by a factor of 1.5 due to the light-cone effect at small scales ($k \sim 1\,{\rm Mpc}^{-1}$). The light-cone effect is less in the model $S1$, as the evolution of the ionized, as well

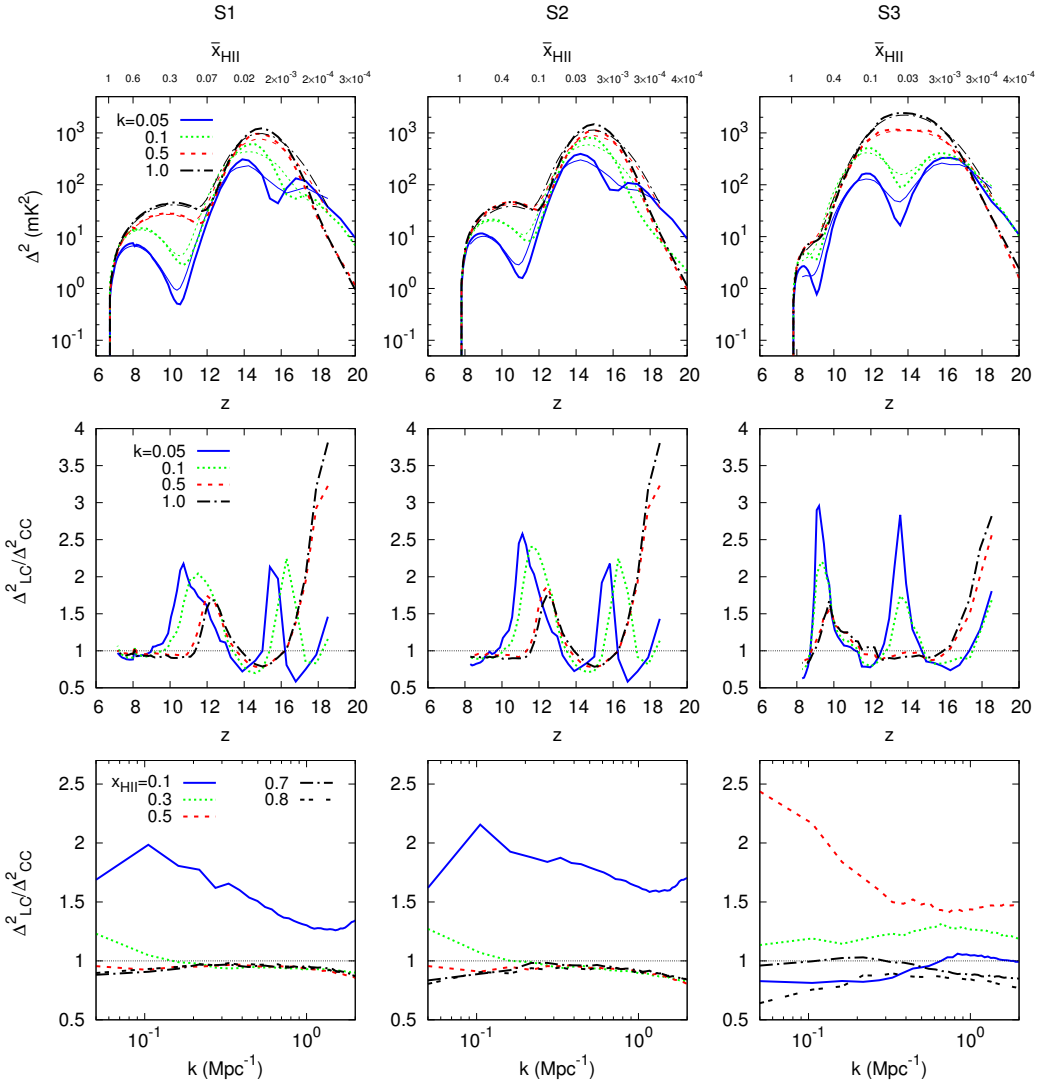

Figure 4.6: Same as Figure 4.5, but for the model C where both Lyα coupling and heating are calculated self-consistently.

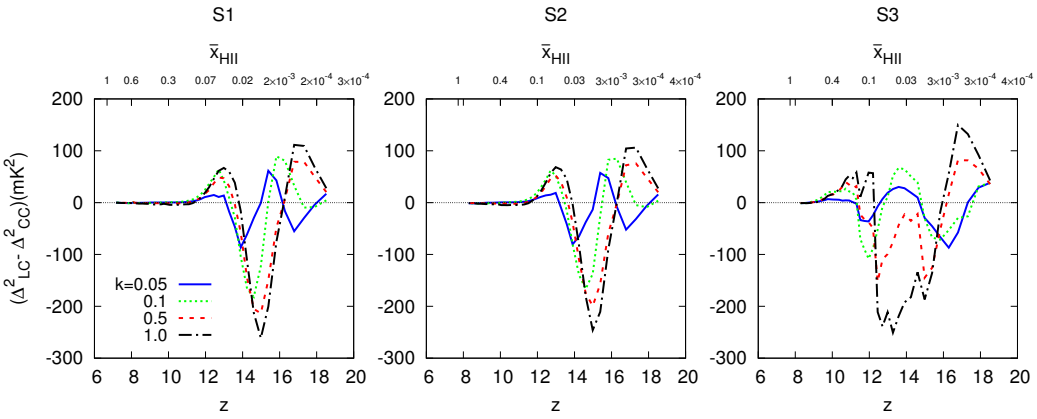

Figure 4.7: The redshift evolution of the difference between the power spectrum with and without light-cone effect at scales $k/\mathrm{Mpc}^{-1} = 0.05$ (solid), 0.1 (dotted), 0.5 (dashed) and 1.0 (dot-dashed) for the model C. Left-hand to right-hand panels represent source models $S1, S2$ and $S3$ respectively.

as the heated regions, is less rapid compared to that in the model $S2$. In the presence of small mass haloes in the model $S3$, the heating is delayed compared to the model $S2$ as we have varied $f_{\rm esc}$ and kept f_X fixed. In this case, the fluctuations in $\delta T_{\rm b}$ at large scales is smaller compared to that in the model $S2$ and thus the amplitude of the heating peak is smaller. As the heated regions around the sources are very small in $S3$ and eventually increase, the power spectrum shows a dip in its evolution with the redshift as shown in the top right-hand panel of the figure. The light-cone effect is able to increase the coeval power spectrum ~ 2 times around the dip (at $z \sim 14$).

The amplitude and overall nature of the heating peak around redshift 15 depend on the nature of X-ray sources. As for example, the peak may not present if heating is driven by X-ray sources like high-mass X-ray binaries (HMXBs) as they do not have a large number of soft X-ray photons and thus the heating will be almost homogeneous (e.g, Fialkov et al. 2014). In such cases, $\delta T_{\rm b}$ fluctuations will be dominated by the neutral hydrogen fluctuations if we consider the Lyα coupling to be very high from the beginning. Thus the light-cone effect in such scenarios will be similar to the model A. Whereas, for X-rays, from sources like supernova, hot interstellar gas, follow similar profile like mini-quasar and thus

expected to have a similar light-cone effect.

The difference between models B and C is that the Lyα coupling is calculated self-consistently in model C whereas in model B it is assumed that the IGM is Lyα coupled. As the condition $x_\alpha(\mathbf{x}) \gg 1$ is not valid for major part of the IGM during the cosmic dawn, the amplitude of $\delta T_\mathrm{b}(\mathbf{x})$ in the model C will be much less than the predicted δT_b in the model B. As a result, the amplitude of the power spectrum is much lower than in the model B initially. The inhomogeneous Lyα coupling during the cosmic dawn in the model C increases the fluctuations in δT_b and results in a distinct peak in the evolution plot of the large-scale power spectrum as a function of redshift as shown in the upper panels of Figure 4.6. We note that a very small amount of Lyα photons is sufficient to couple T_S with T_K of the IGM, thus the model C follows the model B very soon the first sources formed (around redshift 13).

In the presence of inhomogeneous Lyα coupling the evolution of the power spectrum is more dramatic at both large and small scales at cosmic dawn. The non-linear rise of the power spectrum, from $\sim 1\,\mathrm{mK}^2$ to $\sim 100\,\mathrm{mK}^2$ within redshift interval 20 to 16, results in a stronger light-cone effect at the very beginning of the reionization epoch. This increases the power spectrum by a factor of ~ 1.5 around redshift 18.5 and suppresses by a factor of 0.6 around redshift 16.5 (which corresponds the Lyα peak for the source model $S2$). The light-cone effect further enhances the power spectrum by a factor of ~ 2 around redshift 15.5 (trough region between the Lyα and heating peaks), followed by a suppression by a factor of 0.7 around redshift 14. For redshift $z < 14$, the light-cone effect is similar to the model B, only difference being that in presence of inhomogeneous Lyα coupling the effect is little weaker than that predicted by the model B. The power spectrum evolves rapidly at small scales at the cosmic dawn, which results in a large light-cone effect at small scales ($\sim 3-4$ times enhanced). As expected, the light-cone effect is found to be smaller in model $S1$ compared to model $S2$. The enhancement in the power spectrum due to the light-cone effect is ~ 3 around redshift 14 which corresponds to the trough region between the Lyα coupling and heating regions for the model $S3$.

Importantly, we also notice that the peaks and dips found in the evolution of the power spectra for the models B and C are smoothed out to some extent due to the light-cone effect (upper panels of Figures 4.5 and 4.6). The effect is more

prominent at large scales $k \lesssim 0.1$ Mpc^{-1}. The light-cone effect lowers the peak height and raises the dip by some amount. This is particularly important for $S3$ in model C, which is probably the most realistic reionization model we consider here. It has been suggested (e.g., Mesinger et al. 2014) that the peaks can be used to extract source properties, put constrain on the X-ray and Lyα background during the cosmic dawn. We argue that the light-cone effect should be considered while extracting those parameters from the peak and dip measurements.

Finally, in Figure 4.7 we show the redshift evolution of the difference in the power spectra with and without the light-cone effect for the model C for the three source models at different scales. As expected, the difference is maximum at the peak and the trough regions found in the evolution of the power spectra. At large scales ($k \sim 0.05\,\mathrm{Mpc}^{-1}$), the difference can be as large as ~ -100 to 100 mK^2 . The difference is ~ -250 to 100 mK^2 at intermediate scales like $k \sim 1\,\mathrm{Mpc}^{-1}$. In principle, such a strong effect should easily be detected by future experiments like the SKA.

4.3.4 Effect of simulation box size

It has been found earlier by Datta et al. (2014) that the light-cone effect is larger when larger simulation box is used. In order to quantify the effect of box size on our results, we estimated the signal using a smaller box of length $100\,h^{-1}$ cMpc (in addition to our default box of $200\,h^{-1}$ cMpc). The results are shown in Fig. 4.8. In the left-hand panel, we plot the evolution of Δ^2 at a scale $k = 0.1$ Mpc^{-1} for the two boxes with and without the light-cone effect. As expected, the power spectra without the light-cone effect (thick lines) for the two boxes agree with each other. However, we can see that the light-cone effect is considerably less prominent for the smaller box in agreement with Datta et al. (2014). In particular, the smoothing of the three peak nature in the evolution plot of the power spectrum is more prominent for the larger box [1]. The effect

[1] The light-cone effect arises due to the evolution of the H I signal over the observing band. Larger observing bandwidth corresponds to a large evolution of the signal which results in a large impact on the spherically averaged 3D power spectrum. One can choose other statistical quantities like the angular power spectrum to reduce the impact of the light-cone effect. However, this may increase the covariance error. On the other hand, one can implement wavelet transform to reduce the impact of light-cone effect and still can work with large frequency band

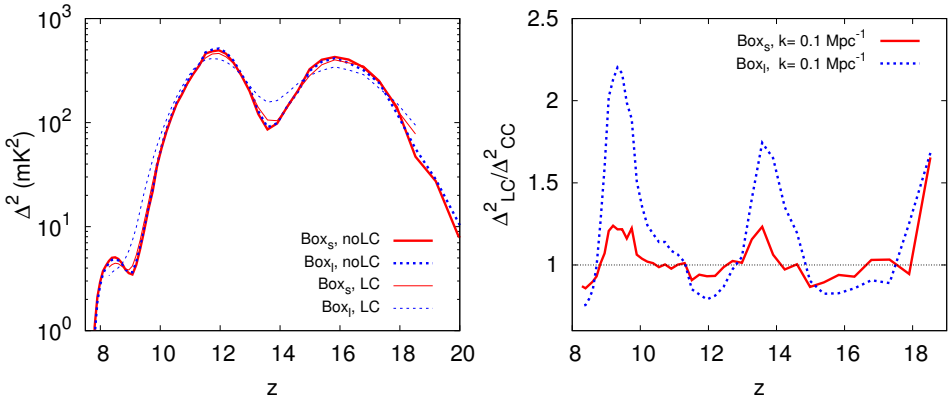

Figure 4.8: The dependence of the light-cone effect on the simulation box size. The left-hand panel shows the evolution of the power spectrum at a scale $k = 0.1$ Mpc^{-1} for the two different boxes Box$_\mathrm{l}$ ($200\,h^{-1}$ cMpc, blue-dotted curves) and Box$_\mathrm{s}$ ($100\,h^{-1}$ cMpc, red-solid curves) respectively with (thin) and without (thick) the light-cone effect. The right-hand panel shows the redshift evolution of the ratio of the power spectra with and without the light-cone effect. The plots are for $S3$ model and redshift-space distortion effect is included while calculating the power spectrum.

can be much stronger in simulation box with size ~ 600 cMpc (e.g., Datta et al. 2014; Mesinger et al. 2014), which may completely smooth out the three peak nature of the evolution plot of the power spectrum. This will constrain us to choose smaller frequency bands during 21-cm experiments to avoid strong light-cone effects and restore the peakiness feature of the power spectrum which is very useful for parameter estimation etc. The same conclusions can be drawn from the right-hand panel too where we have shown the ratio of the power spectra with and without the light-cone effect for $k = 0.1$ Mpc^{-1}. Clearly, the ratio deviates from unity quite prominently for the larger box compared to the smaller one.

4.3.5 Anisotropy from the light-cone effect

Since the light-cone effect modifies the 21-cm signal along the line of sight direction similar to the RSD, it is expected that it may cause anisotropies in the signal. This was investigated in detail by Datta et al. (2014) for a model similar to our model A, and they concluded that the light-cone effect does not induce any significant anisotropies in the signal. We confirm their findings for the model A. In addition, we find that the light-cone effect does not cause any prominent anisotropies for the models B and C too for relevant scales of interest. In fact, for large scales $k \lesssim 0.1$ Mpc^{-1}, our simulation box does not contain a sufficient number of modes leading to large sample variance. Hence it is difficult to draw any significant conclusion on anisotropies at large scales.

In order to explain the effect in a somewhat simpler manner, we have calculated the 'anisotropy ratio' defined as (e.g., Fialkov et al. 2015):

$$r_\mu(k,z) = \frac{\left\langle \Delta^2(\mathbf{k},z)_{|\mu_k|>0.5} \right\rangle}{\left\langle \Delta^2(\mathbf{k},z)_{|\mu_k|<0.5} \right\rangle} - 1, \tag{4.4}$$

where the averages are over angles. If the signal is isotropic then $r_\mu(k,z)$ will be identically zero, otherwise it can be positive or negative. The redshift evolution of the anisotropy ratio for scales $k = 0.5, 1$ Mpc^{-1} is plotted in Figure 4.9. The source model chosen is $S3$. We find from the top panels that the RSD can cause significant anisotropies ($r_\mu \sim 1.5$ for $k \sim 0.5$ Mpc^{-1}) for all the three

(Trott 2016).

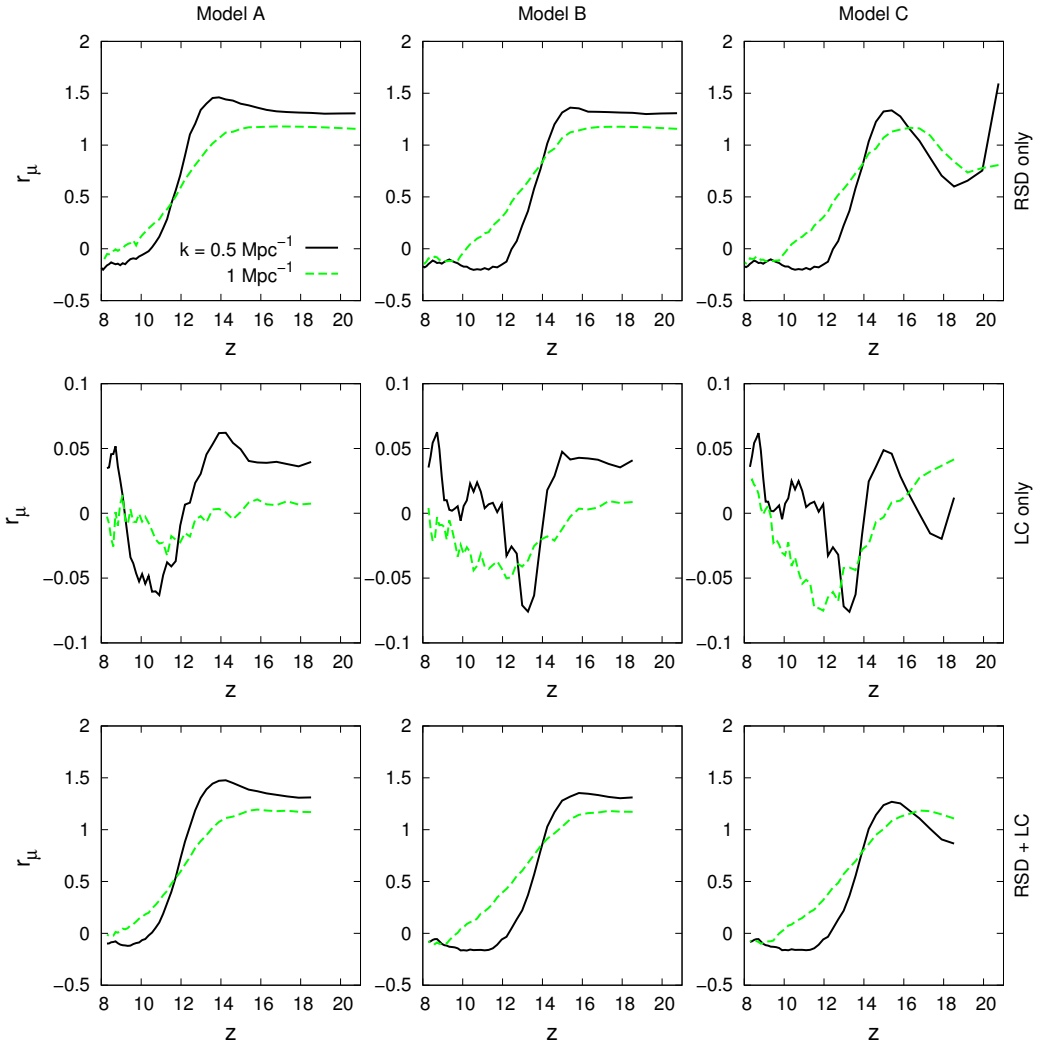

Figure 4.9: Evolution of the 'anisotropy ratio' r_μ as a function of redshift for the source model $S3$ at two different scales $k = 0.5, 1\,\mathrm{Mpc}^{-1}$. The three columns from left to right represent models A, B and C respectively. The top (middle) row represents the case where only the RSD (light-cone) effect is included, while the bottom most row represents the case where both the effects are included.

models[1]. The redshift where the r_μ is maximum corresponds to prominent dip in the evolution of the power spectrum.

In contrast, the light-cone effect does not cause any significant anisotropy on the signal as can be seen from the middle panels for the scales considered. The anisotropy, when both the effects are included, is thus dominated by the contribution from the RSD. We should mention here that it is possible that the anisotropy arising from light-cone effect behave differently for larger scales $k \lesssim 0.1$ Mpc^{-1}. In order to have a sufficient number of modes at such large scales, one requires boxes of much larger size which, unfortunately, are beyond the scope of this chapter.

4.4 Summary and discussion

The main focus of the chapter is to investigate the impact of the light-cone effect on the H I 21-cm signal from the cosmic dawn. The 21-cm brightness temperature maps are generated by post-processing a dark matter N-body simulation with a 1D radiative transfer code. In addition to the usual stellar-like sources, we have accounted for X-ray emitting mini-quasar like sources. The fluctuations in the spin temperature due to inhomogeneous Lyα coupling and heating of the IGM not only boost the 21-cm power spectrum but introduce several peaks and dips in it when plotted as a function of redshift. The boosted power spectrum, together with additional peaks and dips along the redshift axis, makes it an ideal case for studying the light-cone effect. Here, we calculate the spin temperature fluctuations self-consistently for various possible source models and reionization histories. We then study, for the first time, the light-cone effect on the 21-cm power spectrum arising from the cosmic dawn when the signal is dominated by spin temperature fluctuations (unlike other previous studies which concentrated mainly on the ionization fluctuations).

The main findings of our work are summarized below:

[1]For the models B and C, the level of anisotropies arising from the RSD depends on the source model too. The anisotropies are caused by the correlation of the $\delta T_{\rm b}$ fluctuations with the dark matter density field, which is enhanced when small sources are included. For $S1$ and $S2$ which do not contain haloes smaller than $\sim 10^9 {\rm M}_\odot$, we find that $|r_\mu| \lesssim 1$ from RSD effects (in agreement with results of Chapter 3).

1. We find that our results are consistent with previous studies (Datta et al. 2014) for the model which assumes that the H I spin temperature to be fully coupled with the IGM temperature and very high compared to the CMBR temperature throughout the reionization history (model A). The light-cone effect is most significant when the universe is $\sim 15\%$ and 80% ionized as the spherical averaged power spectrum is increased/suppressed by a factor of ~ 1.5 and ~ 0.8 respectively. The effect is found to be minimum while the universe is $\sim 50\%$ ionized.

2. The light-cone effect is much more dramatic in the model B where the inhomogeneous heating is taken into account. We find that the maximum suppression of the large-scale power spectrum due to the light-cone effect occurs around the two peaks and enhancement occurs around the dip between the two peaks when plotted against z. We notice that the light-cone effect can increase the power spectrum by a factor of ~ 1.25 and ~ 3 times around redshift 16 and 11 respectively at large scales ($k \sim 0.05\,\mathrm{Mpc}^{-1}$). The suppression of the power spectrum around the peaks around redshifts 8 and 15 can be ~ 20 to 25% at large scales. We find the enhancement/suppression to be higher for models where contributions of small sources have been included ($S3$ source model). Unlike the previous studies, we find a significant light-cone effect at small scales ($k \sim 1\,\mathrm{Mpc}^{-1}$) as well at high redshifts.

   In addition, when we calculate the Lyα coupling self-consistently (model C), we find that the power spectrum increases very rapidly at the very beginning of cosmic dawn and thus the light-cone effect can enhance the 21-cm power spectrum by a factor ~ 1.5 at large scales ($k \sim 0.05\,\mathrm{Mpc}^{-1}$). At these scales, the three peaks of the power spectrum are suppressed by factors of 0.6, 0.75 and 0.8 around redshifts $16.5, 14$ and 8.5 respectively. The light-cone effect can enhance the power spectrum in the dips by factors of 2 and 2.5 around redshift 15.5 and 11 respectively. In general, the light-cone effect at small scales is found to be smaller than the effect at larger scales, except during the cosmic dawn (may increase the power spectrum by a factor of few at scales like $k \sim 1\,\mathrm{Mpc}^{-1}$).

3. Our results can be understood from the fact that the light-cone effect is strong in a situation where the power spectrum evolve non-linearly with

redshift (or comoving distance) as any linear evolution gets cancelled out to a large extent (Datta et al. 2012a). Non-linear evolution of the 21-cm power spectrum is maximum when it takes a turn. For example, for the A model it happens twice, first time when $x_{\rm HI} \sim 0.8$ and second time when $x_{\rm HI} \sim 0.3 - 0.4$. These are the places where the light-cone effect is very strong. For the B type model, one more peak in the power spectrum gets added. Because of this non-linear evolution around the heating peak, we see that the light-cone effect becomes very strong (power spectrum is suppressed substantially) around this peak. Similarly, Lyα coupling inhomogeneities give rise to two more episodes of non-linear evolution of the power spectrum (one dip and one peak) in the very beginning of cosmic dawn where the light-cone effect is very strong.

4. The large scale ($k \sim 0.05\,{\rm Mpc}^{-1}$) power spectrum with light-cone effect included can differ by ~ -100 to 100 mK^2 from the case where light-cone effect is not included. The difference increases at small scales ($k \gtrsim 0.5\,{\rm Mpc}^{-1}$) to the range ~ -250 to 100 mK^2. In principle, such a strong effect should easily be detected by future experiments like the SKA. We also notice that the peaks and dips in the power spectrum are somewhat smoothed out due to the light-cone effect. It has been suggested (e.g., Mesinger et al. 2014) that the peaks can be used to extract source properties, X-ray and Lyα background etc. We argue that the light-cone effect should be considered while extracting those parameters from the peak and dip measurements.

5. The light-cone effect can, in principle, introduce anisotropies in the power spectrum, similar to the RSD effects. It is somewhat difficult to predict the large scale $k \lesssim 0.1$ Mpc^{-1} anisotropies because of the lack of number of modes in the simulation box. However, for intermediate scales $k \sim 0.5$ Mpc^{-1}, we do not find any significant anisotropy arising from the light-cone effect.

The light-cone effect, during the cosmic dawn ($x_{\rm HII} \lesssim 0.2$) is highly dependent on nature of the X-ray sources present during that time in the universe. For example, the heating of the IGM will be much more homogeneous if it is mainly driven by the HMXBs (Fialkov et al. 2014). In such a scenario the evolution

of the signal will be solely dominated by the H I neutral fraction and thus the light-cone effect during the cosmic dawn will not be as strong as we see here. Although, we expect similar light-cone effect if supernova or hot interstellar gas dominate the X-ray budget since they are expected to have similar kind of SED like mini-quasars which emit large number of soft X-ray photons.

Finally, further investigation is required in order to understand the light-cone effect for different source models and reionization scenarios. The main result from this study is that the light-cone effect can change the amplitude of the 21-cm power spectrum as well as the shape of the evolution of the power spectrum at large scale quite substantially. Therefore, it is important that the effect is incorporated while modelling the 21-cm power spectrum, particularly during the cosmic dawn and early stages of reionization.

5 | 21-cm signature of the first sources in the Universe: Prospects of detection with SKA

This chapter contains material that has been published in Ghara et al. (2016a).

5.1 Introduction

In recent times, a large number of galaxies at $z > 6$ have been detected using narrow-band Lyα emission (e.g., Hu et al. 2010; Kashikawa et al. 2011; Ouchi et al. 2010b) and broad-band colour (Bouwens et al. 2015; Ellis et al. 2013). In addition, various surveys have been used to detect tens of quasars at $6 \lesssim z \lesssim 7$ (Fan et al. 2006a; Mortlock et al. 2011a; Venemans et al. 2015). These sources are believed to play an important role during the last phase of the epoch of reionization (EoR). As a next step, it is natural to ask the question whether one can detect the very first galaxies in the Universe using similar techniques. In spite of significant progress in theoretical modelling of the first sources (Thomas and Zaroubi 2008; Yajima and Li 2014), there are still no observational signatures. It is expected that future space missions like the James Webb Space Telescope (JWST)[1] will be able to detect at least the brightest of these sources (de Souza et al. 2013, 2014; Zackrisson et al. 2011). It is believed that the UV photons from these sources created ionized bubbles around them, which eventually overlapped and completed the reionization process by redshift ~ 6 (Choudhury and Ferrara 2006; Fan et al. 2006b; Goto et al. 2011; Mitra et al. 2011, 2012, 2015). The presence of these

[1] http://jwst.nasa.gov

bubbles motivated various groups to explore an alternate, perhaps somewhat indirect, method of detecting the high-redshift sources. It has been suggested that one can detect the 21-cm signatures around these sources using low-frequency telescopes (Datta et al. 2007a, 2012b; Geil and Wyithe 2008) which can be helpful in constraining the source properties (Majumdar et al. 2012).

According to our current understanding, the first stars, usually known as the Population III (PopIII) stars, formed in a metal free (or low-metallicity) environment and thus are expected to be much more massive than the present day stars (Abel et al. 2002; Bromm et al. 2009; O'Shea and Norman 2007; Wise et al. 2012). A population of these stars would have caused supernova explosions, which would contaminate the surrounding medium with metals. The resulting chemical feedback would result in formation of the Population II (PopII) stars. In addition to the stellar population, one expects the galaxies to host X-ray sources like the mini-QSOs, the hot interstellar gas or the high-mass X-ray binaries (HMXBs). These X-ray sources are important in increasing the kinetic temperature of the gas in the intergalactic medium (IGM) above the brightness temperature of the cosmic microwave background radiation (CMBR). All such source properties are imprinted in the redshifted 21-cm signal from the neutral hydrogen from these epochs. Analytical calculations (e.g., Furlanetto et al. 2004a; Paranjape and Choudhury 2014), semi-numerical simulations (Choudhury et al. 2009; Ghara et al. 2015a,b; Mesinger and Furlanetto 2007; Santos et al. 2008; Thomas et al. 2009; Zahn et al. 2007), and full numerical simulations involving radiative transfer (Baek et al. 2009; Iliev et al. 2006; McQuinn et al. 2007b; Mellema et al. 2006; Shin et al. 2008) have been carried out to understand the effect of different sources on the global and statistical quantities (e.g., the power spectrum) of the signal. Relatively less attention has been paid to understand the nature of the 21-cm signal around individual sources, though there have been studies which show that the 21-cm structure around the different sources depend on the nature of spectral energy distribution (SED) of the sources and IGM properties (Alvarez et al. 2010; Majumdar et al. 2012; Thomas and Zaroubi 2008; Yajima and Li 2014; Zaroubi et al. 2012).

Though the high-redshift 21-cm signal is expected to carry information about the first sources, it is quite challenging to detect the signal and extract this information. The main difficulty is that the strength of the cosmological signal is

very weak compared to the typical system noise and the foregrounds. The system noise increases at low frequencies and hence one requires optimal baseline design and large observation times to keep the noise below the expected signal. While the first generation of low-frequency radio telescopes like the LOFAR, PAPER, MWA, and GMRT are engaged in detecting the signal statistically at $z < 12$, a highly sensitive telescope like the SKA will have much better sensitivity at lower frequencies allowing us to probe even higher redshifts.

Given that the signal from the first sources is very weak, the first task would be to simply make a detection of the signatures of these early sources in low-frequency observations. Once the detection is confirmed, one can follow it up and make further progress by constraining various properties of these sources. It would thus be interesting to explore the detectability of these first sources with telescopes like the SKA1-low within reasonable observation time. Keeping this in mind, we have modelled the 21-cm signal around the first sources with the source properties and the properties of the surrounding medium being characterized by a number of parameters. The main goal of this study is to characterize the detectability of the 21-cm signal as a function of these parameters. This would help in planning observations using the SKA1-low so as to make the detection of the signal around the first sources. Similar studies have been done, e.g., by Datta et al. (2007a, 2012b); Geil and Wyithe (2008), who showed that the large ionized bubbles around individual sources can be detected using telescopes like the GMRT, LOFAR and the MWA within reasonable integration time around redshift ~ 8. In our case, however, the situation is much more complex as we are interested in the very early stages of reionization (i.e., the cosmic dawn) where the IGM contains both emission and absorption regions.

We have organized the chapter in the following way. In Section 5.2, we calculate the expected 21-cm pattern for different source models and also obtain the expected visibilities and noise for typical observations. The main results are presented in Section 5.3, before we summarize our findings in Section 5.4. Throughout the chapter, we have used the cosmological parameters $\Omega_m = 0.32$, $\Omega_\Lambda = 0.68$, $\Omega_B = 0.049$, $h = 0.67$, $n_\mathrm{s} = 0.96$, and $\sigma_8 = 0.83$, which are consistent with the recent results of *Planck* mission (Planck Collaboration et al. 2014a).

5.2 Calculation of the signal

5.2.1 Isolated radiation source

In general, we expect the heating and ionization signatures around an individual source to be complicated by the presence of other sources nearby. The signal pattern of other sources would tend to overlap with the target source under consideration, thus making the analysis complicated. However, a large amount of information regarding the detectability of the signal can be extracted by studying the pattern around an isolated source, i.e., ignoring the effect of overlap from other sources. A large fraction of this chapter is devoted to understanding the signal properties around an individual isolated source. We will study a more realistic scenario later in Section 5.3.4.

Since the exact nature of the first sources of radiation is still unknown, we consider a variety of source models as listed below. The spectral energy distribution (SED) of these sources are shown in Figure 5.1.

- **PopIII:** In many models of reionization (Chen and Miralda-Escudé 2008; Choudhury and Ferrara 2007; Furlanetto and Oh 2006; Wyithe and Loeb 2003), the first stars are expected to be massive since they form in a metal free environment. These are commonly known as the PopIII stars. Here, we have modelled radiation from these sources as black-body spectrum with an effective temperature given by (Bromm et al. 2001b),

$$T_{\rm eff}(M_\star) = 1.1 \times 10^5 \left(\frac{M_\star}{100\ {\rm M}_\odot}\right)^{0.025} {\rm K}, \tag{5.1}$$

  where $M_\star$ is the mass of the star. The spectral energy distribution (SED) of a PopIII star is normalized by the bolometric luminosity corresponding to the star, which can be written as,

$$L_{\rm bol}(M_\star) = 10^{4.5} \frac{M_\star}{{\rm M}_\odot} {\rm L}_\odot, \tag{5.2}$$

  where $\rm L_\odot = 3.846 \times 10^{33}$ erg $\rm s^{-1}$ is the solar luminosity. We assume that a galaxy hosts only one PopIII star, however, our analysis would be valid also for a cluster of several PopIII stars which have a black-body like SED.

We also assume that all photons produced within a PopIII hosting galaxy escape into the IGM.

- **Galaxy:** The effectiveness of PopIII stars in ionizing and heating the IGM is somewhat uncertain as the gas within galaxies can get polluted by metals after the first burst of star formation. Hence, we have taken an alternate source model which consists of normal (PopII) stars. We have generated the SED of these model galaxies using the stellar population synthesis code PEGASE2[1] (Fioc and Rocca-Volmerange 1997) for standard star formation scenarios. We assume that the galaxies form in a metal-poor environment with metallicity $10^{-3}\,Z_{\odot}$, where $Z_{\odot}$ is solar metallicity and follow a Salpeter IMF for stars with mass between 1 to 100 $M_{\odot}$.[2] The main difference of this model compared to PopIII stars is that these galaxies do not produce very high-energy photons (i.e., larger than 50 eV, see Figure 5.1). Also, one should keep in mind that a substantial fraction of ionizing photons produced is absorbed within the host galaxy, only a fraction $f_{\rm esc}$ is assumed to escape into the IGM and contribute to reionization.

- **Mini-QSO:** An important component of the SED at high redshifts is the X-ray radiation which plays an important role in heating the IGM. It is possible that the galaxies, in addition to the stellar component, host mini-QSOs that are powered by intermediate mass accreting black holes of mass $10^3 - 10^6\,M_{\odot}$. For such sources, we assume that the SED has a stellar component as discussed in the previous paragraph and also a high-energy component that follows a power-law with a spectral index α (Vanden Berk et al. 2001; Vignali et al. 2003),

$$I_q(E) = A\ E^{-\alpha}. \tag{5.3}$$

The normalization factor A can be calculated in terms of the UV lumi-

[1] `http://www2.iap.fr/pegase/`

[2] The stars in the primordial galaxies are expected to form in metal-poor environments (Finkelstein et al. 2009; Lai et al. 2007). The transition from PopIII to PopII stars occurs when the metallicity approaches some critical value $Z_{\rm crit}$, which is typically in the range $10^{-6} - 10^{-3}\,Z_{\odot}$ (Bromm et al. 2001a; Maio et al. 2010). Hence we make a conservative assumption that the PopII stars form in an environment with metallicity $10^{-3}\,Z_{\odot}$.

nosity[1], the X-ray to UV luminosity fraction f_X and the spectral index α. Unlike the previous two source models, these mini-QSOs emit a large number of soft X-ray photons, which are very effective in partially ionizing and heating the surrounding neutral medium (Shull and van Steenberg 1985). We should mention that the power-law SED represents not only the mini-QSO type sources, but also other sources of X-rays like supernovae, hot interstellar medium etc (Pacucci et al. 2014).

- **HMXBs:** A different source of X-ray photons could be the HMXBs within galaxies. These sources are different from the mini-QSOs because the soft X-rays, in this case, will be substantially absorbed due to interstellar absorption (as shown in Figure 5.1) and thus the spectrum can not be fitted with any power-law in X-ray band. The level of interstellar absorption of the soft X-ray photons is quite uncertain for the high-redshift HMXBs. We have used the SED given by Fragos et al. (2013a,b) and we have assumed that the SED shape is independent of other galaxy properties, i.e., the stellar mass, the age of the galaxies, etc. It is possible that the SED of the HMXBs may change with the mean stellar population age because of the evolution in the metallicity (Fragos et al. 2013b; Kaaret 2014). In order to keep our model simple, we assume that the metallicity does not evolve significantly over the time scale which corresponds to the age of the source.

The fiducial values of the parameters used in this study are chosen as follows: The fiducial stellar mass is taken to be $M_\star = 10^3\,\mathrm{M}_\odot$ for the PopIII model, which can either be a single star or a cluster of several PopIII stars with mass $M_\star \sim 10^2\,\mathrm{M}_\odot$. For the other three source models the fiducial stellar mass is chosen to be $M_\star = 10^7\,\mathrm{M}_\odot$ which corresponds to stars in dark matter haloes of mass $M_{\rm halo} \sim 6 \times 10^8\,\mathrm{M}_\odot$ (assuming a fraction $f_\star = 0.1$ of the baryons to convert into stars). The value of the escape fraction is taken to be $f_{\rm esc} = 0.1$ for all these sources. We have assumed a power-law spectrum for the Mini-QSO source model with a fiducial spectral index $\alpha = 1.5$, consistent with the observational constraints from Laor et al. (1997); Vanden Berk et al. (2001); Vignali et al. (2003). The X-ray to UV luminosity f_X of the Mini-QSO and HMXBs models

[1]We have assumed that the UV band span from 10.2 to 100 eV and the X-ray band span from 100 eV to 10 keV.

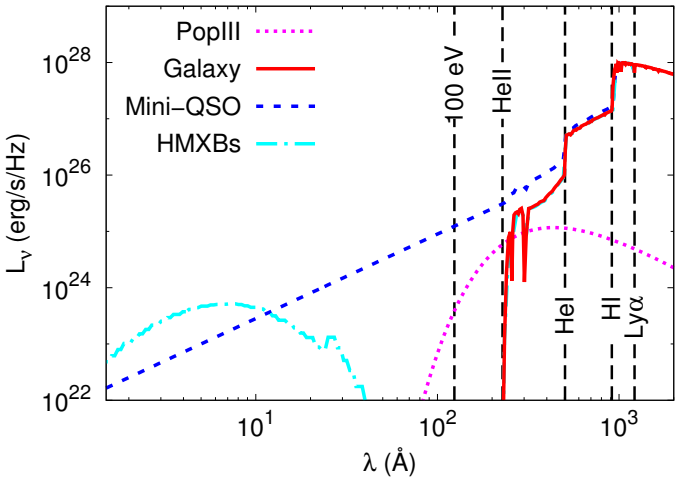

Figure 5.1: The SED of the source models considered in this chapter, i.e., PopIII, Galaxy, Mini-QSO and HMXBs. The mass of the PopIII star is taken to be $10^3\,M_\odot$. The stellar mass in the three models Galaxy, Mini-QSO and HMXBs is taken as $M_\star = 10^7\,M_\odot$. The sources are assumed to form in a metal-poor environment in the IGM with metallicity $10^{-3}\,Z_\odot$. The ratio of X-ray to UV luminosity (f_X) for the Mini-QSO and HMXBs models are fixed to 0.05. We have fixed the power-law index $\alpha = 1.5$ for the Mini-QSO model. The vertical lines from right to left represent the wavelengths corresponding to Lyα (10.2 eV), hydrogen ionization energy (13.6 eV), the ionization energy of He I(24.6 eV), the ionization energy of He II(54.4 eV) and 100 eV respectively.

can be related to the ratio of the mass of the intermediate mass black hole to the galaxy mass. Recent observations of high-z quasars predict the accretion rate of the black holes (BH) to be similar to the Eddington limit (e.g., Willott et al. 2010). We choose the fiducial value of the parameter f_X to be 0.05, which corresponds to a BH to galaxy mass ratio $\sim 10^{-3}$, consistent with observations (e.g., Rix et al. 2004). Very little is known about the lifetime of the first sources. It is believed that they are short-lived (Meynet and Maeder 2005), hence we choose the fiducial age $t_{\rm age}$ of the sources as 20 Myr. The densities of hydrogen and helium in the IGM are assumed to be uniform and the density contrast δ is set to 0.

5.2.2 Heating and ionization maps around the source

For each source model, we generate the ionization and heating maps around an isolated source using a one-dimensional radiative transfer code. The details of the method are given in Chapter 2. Here, we briefly describe the main features of the method.

- The procedure is simplified by assuming a constant density of hydrogen and helium in the IGM surrounding the source. The initial state (i.e., at the instant when the source produces the first radiation) of the IGM is taken to be completely neutral and the initial temperature is computed assuming that the gas temperature evolves as $(1 + z)^2$ after decoupling from the radiation temperature around redshifts ~ 150.

- We divide the IGM into several spherical shells along the radial direction from the centre of the source. We assume that the radiation from the source can influence the IGM up to a distance '$c \times t$' from the centre of the source when the age of the source is 't', with 'c' being the speed of light.

- The intensities at UV and X-ray bands will decrease due to absorption in the medium around the source. We pre-calculate the ionization and heating rates for different values of optical depths. These are later used for calculating the time evolution of ionized species of hydrogen and helium along with the kinetic temperature ($T_{\rm K}$) of the medium.

- The physical processes that affect the population of the ionization states of hydrogen and helium are photo-ionization by the continuum photons, secondary ionization by high-energy primary electrons emitted due to photoionization, collisional ionization and recombination. The temperature of the IGM is set by different heating and cooling mechanisms like photo-heating, Compton heating, energy loss due to recombination, collisional excitation etc.

- The Lyα photons are assumed to be contributed by the continuum spectrum of the source, recombination of hydrogen in the ionized ISM and collisional excitation due to secondary electrons. Here, we do not solve a detailed radiative transfer for the Lyα photons. We have instead assumed that the

Lyα flux decreases as $1/R^2$, where R is the radial distance from the centre of the source.

- In the initial parts of this study, we have not incorporated the effect of gas velocities on the brightness temperature calculation. In reality, the situation may be complex and one needs to incorporate the density fluctuations and velocity effects while generating the 21-cm signal. We have addressed such complex scenario in Section 5.3.4.

- In order to understand the characteristics of the signal at various epochs, we consider three different models of heating and Lyα coupling, namely:

  (i) **Model** A**:** We assume that the IGM is highly heated and Lyα coupled, i.e., the spin temperature $T_{\rm S} \gg T_\gamma$, where T_γ is the CMBR brightness temperature at redshift z.

  (ii) **Model** B**:** We assume high Lyα coupling in the IGM ($T_{\rm S} = T_{\rm K}$), however we calculate the $T_{\rm K}$ distribution around the sources self-consistently.

  (iii) **Model** C**:** The $T_{\rm S}$ profile around the source depends on the source properties and is generated self-consistently.

  Note that these models are also used in Chapter 3 and 4. Model C is probably the most realistic model for the very first sources in the universe as the number density of these sources is small and thus no significant overlap between the signal pattern from different sources is expected. Once the Lyα coupling becomes efficient during the very early stages of reionization, one expects model B to represent the IGM conditions. In the presence of X-ray sources, e.g., mini-QSOs, a major fraction of the universe is heated above T_γ once the universe becomes $\gtrsim 10\%$ ionized and thus model A is expected to hold thereafter (Ghara et al. 2015a).

5.2.3 The 21-cm signal

The form of the differential brightness temperature as described in equation 2.5 can be modified as,

$$\delta T_b(\vec{\theta},\nu) = 27\ x_{\rm HI}(\mathbf{x},z)[1+\delta_{\rm B}(\mathbf{x},z)]\left(\frac{\Omega_B h^2}{0.023}\right) \times\left(\frac{0.15}{\Omega_m h^2}\frac{1+z}{10}\right)^{1/2}\left[1-\frac{T_\gamma(z)}{T_{\rm S}(\mathbf{x},z)}\right]\ {\rm mK}, \tag{5.4}$$

where $\vec{\theta}$ is a two-dimensional vector on the sky plane characterising the sky position and ν is the frequency of observation. The quantities $x_{\rm HI}(\mathbf{x},z)$ and $\delta_{\rm B}(\mathbf{x},z)$ denote the neutral hydrogen fraction and the baryonic density contrast respectively at the comoving coordinate $\mathbf{x}$ at a redshift $z = 1420\ {\rm MHz}/\nu - 1$. The three-dimensional position $\mathbf{x}$, if measured from the location of the observer at $z = 0$, is related to the sky position $\vec{\theta}$ by the relation $\mathbf{x} = \left\{r(z)\vec{\theta},\ r(z)\right\}$, where $r(z)$ is the comoving distance to z, respectively. The quantity $T_\gamma(z) = 2.73 \times(1+z)$ K is the CMBR brightness temperature at redshift z. We have not considered the effect of the peculiar velocities of the gas in the IGM in the above equation.

We have generated the expected signal in a rectangular box with length along the frequency axis corresponding to the observational bandwidth considered in this work. For example, a bandwidth of 16 MHz at redshift 15 corresponds to a simulation box of length 357 comoving Mpc (cMpc) along the corresponding axis.

5.2.4 Signal visibilities

The measurable quantity in a radio interferometric observation is the visibility. In general, observations are carried out over many frequency channels with frequency resolution $\Delta\nu_c$ over a bandwidth B_ν. The visibility is measured for each frequency channel and for each antenna pair. Thus the visibility $V(\vec{U},\nu)$ is a function of the channel frequency ν and baseline $\vec{U} = \vec{d}_{\rm ant}/\lambda$, where $\vec{d}_{\rm ant}$ is the two-dimensional separation vector between the antenna pair and λ is the wavelength of the observation. Under the approximation that either the antennae are

confined to a two-dimensional plane or the field of view (FOV) is small, the visibility can be related to the two-dimensional Fourier transform of the sky intensity distribution, i.e.,

$$V(\vec{U},\nu) = \int d^2\theta \; I_\nu(\vec{\theta}) \; A(\vec{\theta}) \; e^{i2\pi\vec{\theta}\cdot\vec{U}}, \tag{5.5}$$

where $I_\nu(\vec{\theta})$ is the sky specific intensity at frequency ν and $A(\vec{\theta})$ is the primary beam pattern for individual antenna, which can be assumed to be Gaussian $A(\vec{\theta}) = e^{-\theta^2/\theta_0^2}$ with $\theta_0 \approx 0.6 \; \theta_{\rm FWHM}$. For relatively wide field beam pattern of the antenna, the beam pattern can be taken out from the integral as $A(\vec{\theta_c})$, where $\vec{\theta_c}$ is the position of the centre of the source. For the rest of the chapter, we shall assume that $A(\vec{\theta_c}) \approx 1$. This assumption works quite well when the 21-cm emitting region is confined to a small angular extent around the centre of the FOV, e.g., for an isolated source with a short life time. The sky intensity can be related to the differential brightness temperature as

$$I_\nu(\vec{\theta}) = \frac{2k_B\nu^2}{c^2}\delta T_{\rm b}(\vec{\theta},\nu), \tag{5.6}$$

where k_B is Boltzmann constant.

In any observation, the total signal measured by the telescope will include, in addition to the cosmological signal of interest, the inherent system noise and the foreground from the astrophysical sources. In the case of 21-cm observations, these can create enormous difficulties as the cosmological signal is very weak compared to all other sources that contribute to the visibility. In addition, there could be man-made radio frequency interference (RFI). For simplicity, we assume that the RFI can be identified and the corrupted data can be discarded. We will also assume that the astrophysical foregrounds can be modelled accurately and subtracted from the data[1]. Under such assumptions, we need to account for only the system noise, which too can be quite large at low frequencies. We then write the measured visibility as

$$V(\vec{U},\nu) = S(\vec{U},\nu) + N(\vec{U},\nu), \tag{5.7}$$

[1]Complete subtraction of the foregrounds without affecting the cosmic signal and system noise is an overly idealistic assumption. In principle, some amount of signal and system noise will be lost while subtracting the foregrounds. In addition, some residual foregrounds would remain as a contaminant within the signal, which in turn may affect to the detectability. We have discussed the detectability of the signal in the presence of foregrounds in Section 5.3.5

Parameters	Values
Redshift (z)	15
Central frequency (ν_c)	88.75 MHz
Band width (B_ν)	16 MHz
Frequency resolution ($\Delta\nu_c$)	50 kHz
Observational time ($t_{\rm obs}$)	1000 h
System temperature ($T_{\rm sys}$)	$60 \times (300\ {\rm MHz}/\nu_{\rm c})^{2.55}$ K
Number of antennae ($N_{\rm ant}$)	512 (SKA), 30 (GMRT),
	128 (MWA), 48 (LOFAR)
Effective collecting area ($A_{\rm eff}$)	962 m^2 (SKA), 1590 m^2 (GMRT),
	16 m^2 (MWA), 526 m^2 (LOFAR)

Table 5.1: The SKA1-low, GMRT, MWA and LOFAR parameters used in this study for observations at redshift z.

where $S(\vec{U},\nu)$ is the 21-cm signal visibility given by equations (5.5) and (5.6) and $N(\vec{U},\nu)$ is the system noise contribution to the measured visibility.

The system noise $N(\vec{U},\nu)$ in different baselines and frequency channels are uncorrelated and are expected to be Gaussian random variables with zero mean. The rms noise σ_N for each baseline, polarization and frequency channel of width $\Delta\nu_c$ and correlator integration time Δt_c is given by (Thompson et al. 2001),

$$\sqrt{\langle N^2\rangle} = \frac{\sqrt{2}k_B T_{\rm sys}}{A_{\rm eff}\sqrt{\Delta\nu_c\ \Delta t_c}}, \tag{5.8}$$

where $A_{\rm eff}$ is the effective collecting area of each antenna and $T_{\rm sys}$ is the system temperature. Note that $\langle N^2\rangle$ is independent of U, however it depends on the frequency implicitly through the quantity $T_{\rm sys}$.

Table 5.1 shows the antenna parameters for various telescopes of interest, i.e., SKA1-low, GMRT, MWA and LOFAR, along with the default observational criteria used in this study. At low frequencies, the system temperature is dominated by the sky temperature which is taken to be $T_{\rm sys} = 60 \times (300\ {\rm MHz}/\nu_{\rm c})^{2.55}$ K (Dewdney 2013; Jensen et al. 2013). The frequency channel width is taken to be

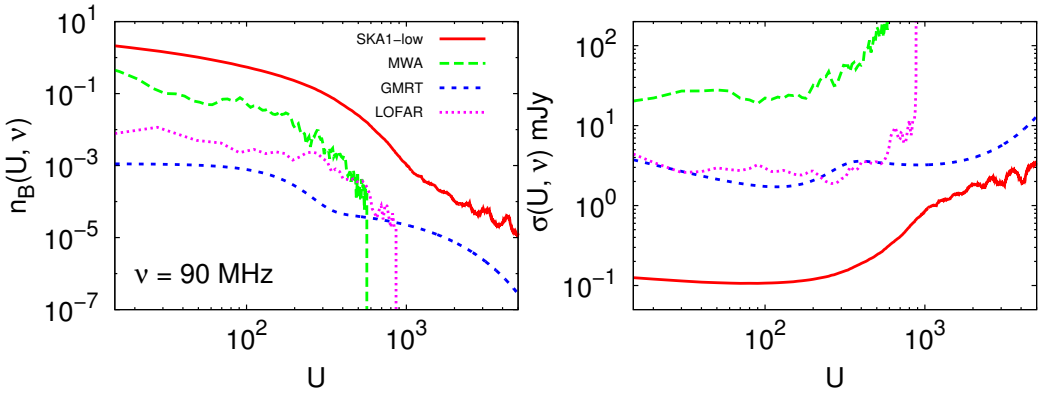

Figure 5.2: The baseline distributions (left-hand panel) and the corresponding rms noise in visibilities (right-hand panel) for the SKA1-low, MWA, GMRT and LOFAR at frequency 90 MHz. $n_{\rm B}(U,\nu)$ denote the number of antenna pairs having same baseline U at frequency ν. The rms is computed for an observation time of 1000 hours and frequency resolution of 50 kHz. We have fixed ΔU=10 while calculating the rms noise using equation (5.9).

50 kHz, which corresponds to a spatial resolution of $\sim$ 1.1 cMpc at redshift 15.

There are various ways of reducing the rms noise in observations. An obvious option is to average over long observation time $t_{\rm obs}$ which reduces the noise by a factor of $\sqrt{\Delta t_c/t_{\rm obs}}$. Also, it is possible that different combinations of antenna pairs can give the same baseline $\vec{U}$ for the same frequency channel. Assuming the antenna distribution to have circular symmetry, the rms noise can be further reduced by a factor of $1/\sqrt{2\pi n_{\rm B}(U,\nu)U\Delta U}$, where $2\pi n_{\rm B}(U,\nu)U\Delta U$ is the number of pair of antennas that have baseline lengths between U and $U+\Delta U$ at a frequency ν. We denote this reduced rms as $\sigma(U,\nu)$ which can be written as

$$\sigma(U,\nu) = \frac{\sqrt{2}\ k_B T_{\rm sys}}{A_{\rm eff}\sqrt{\Delta\nu_c\ t_{\rm obs}}} \times \frac{1}{\sqrt{2\pi n_{\rm B}(U,\nu)U\Delta U}}. \tag{5.9}$$

The quantity $n_{\rm B}(U,\nu)$ is normalized such that

$$\int n_{\rm B}(U,\nu)\ d^2U = \frac{N_{\rm ant}(N_{\rm ant}-1)}{2}, \tag{5.10}$$

where $N_{\rm ant}$ denotes the number of antennae in the system such that the total number of baselines is given by the right-hand side of the above equation. The

baseline distributions $n_{\rm B}(U,\nu)$ for various telescopes (GMRT, LOFAR, MWA and SKA1-low) are plotted in the left-hand panel of Figure 5.2.[1] The right-hand panel shows the corresponding rms defined in equation (5.9) as a function of baseline U. We can see that, for the same amount of observing time, the rms for SKA1-low at smaller baselines $U \lesssim 100$ is at least 10 times better than any other existing facilities. This is because of the significantly greater number of antennae in the core of SKA1-low. As we will see later, the signal we are studying in this chapter is mostly concentrated at $U \lesssim 100$, and its amplitude is such that only SKA1-low will be sensitive enough to make a detection. Hence, we will concentrate our discussions mainly on SKA1-low in the rest of the chapter.

One way of increasing the possibility of detecting the faint 21-cm signal is to integrate it over a wide range of baselines and frequency channels. We define an estimator $\hat{E}$ as

$$\hat{E} = A_{\rm NS} \int {\rm d}^2U \int {\rm d}\nu \; n_B(U,\nu) \; V(\vec{U},\nu), \tag{5.11}$$

where $A_{\rm NS}$ is a normalization constant given by

$$A_{\rm NS}^{-1} = \int {\rm d}^2U \int {\rm d}\nu \; n_B(U,\nu) = \frac{N_{\rm ant}(N_{\rm ant}-1)}{2} B_\nu. \tag{5.12}$$

Since the noise can be treated as random numbers with zero mean, the expectation value of the estimator is given by

$$\langle \hat{E} \rangle = A_{\rm NS} \int {\rm d}^2U \int {\rm d}\nu \; n_B(U,\nu) \; S(\vec{U},\nu). \tag{5.13}$$

The contribution of the noise term will be included in the standard deviation

$$\sqrt{\left\langle \left(\Delta\hat{E}\right)^2 \right\rangle} \equiv \sigma_N = \frac{\sqrt{2}\; k_B T_{\rm sys}}{A_{\rm eff}\; \sqrt{t_{\rm obs}\; B_\nu\; N_{\rm ant}(N_{\rm ant}-1)/2}}, \tag{5.14}$$

where we have used the fact that the noise in different baselines and frequency channels are uncorrelated. The resulting signal to noise ratio (SNR) will then be given by

$$\mathrm{SNR} = \frac{1}{\sigma_N} \frac{\int d^2U \int d\nu \; n_{\rm B}(U,\nu) \; S(\vec{U},\nu)}{\int d^2U \int d\nu \; n_{\rm B}(U,\nu)}. \tag{5.15}$$

[1] We have used the previously proposed form of the SKA baseline distribution for 1024 antennae, but normalized the distribution for 512 antennae using equation (5.10). This baseline distribution is not significantly different from the recently finalized baseline distribution of the SKA1-low as given in http://astronomers.skatelescope.org/wp-content/uploads/2015/11/SKA1-Low-Configuration_V4a.pdf. For GMRT baseline distribution, we have used the fitting function of Datta et al. (2007a).

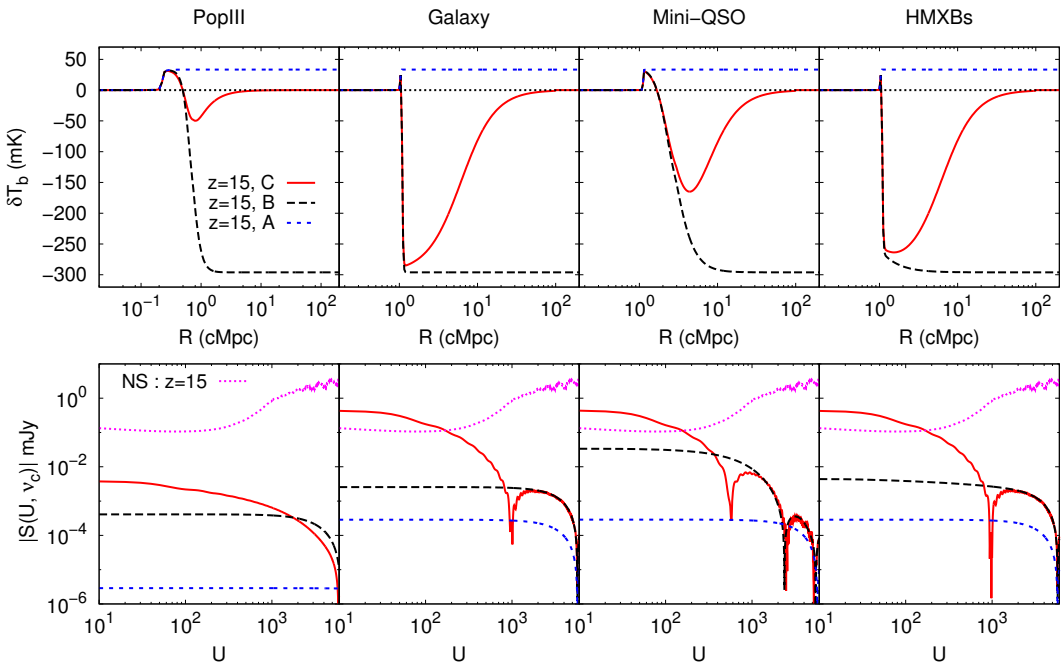

Figure 5.3: Upper panel: The brightness temperature distribution around an isolated source for different source models, i.e., PopIII, Galaxy, Mini-QSO and HMXBs. The source properties are taken to be those corresponding to the fiducial values. The results are shown for all three coupling models. Bottom panel: The absolute value of the corresponding visibility amplitude as a function of baseline U. Also shown are rms noise in the visibilities calculated for 1000 h of observation with the SKA1-low with a frequency resolution of 50 kHz. We have fixed ΔU=10 while calculating the rms noise using equation (5.9).

The bandwidth B_ν of the observations is simply the frequency resolution $\Delta\nu_c$ times the number of frequency channels. Note that the above definition (Equation 5.15) of the SNR implies that we weight the visibility signal $S(\vec{U},\nu)$ at individual baselines by the number $n_{\rm B}(U,\nu)$ of baselines. Since $n_{\rm B}(U,\nu) \propto \sigma^{-2}(U,\nu)$, we have simply weighed the visibilities according to inverse of the noise error.

5.3 Results

5.3.1 21-cm signal pattern around the sources

In this section, we describe the 21-cm brightness temperature distribution around different types of isolated source models, i.e., PopIII, Galaxy, Mini-QSO and HMXBs. We have already discussed the fiducial values of different parameters in these models in Section 5.2.1.

We choose the fiducial redshift to be 15 for presenting our results. The favoured reionization models, after the recent release of constraints by the Planck team (Planck Collaboration et al. 2015b), prefer a reionization history which begins at $z \sim 15$ (Mitra et al. 2015). Hence one expects that the overlap of the brightness temperature patterns will not be significant at these redshifts. The corresponding frequency of observations will be ~ 90 MHz, well within the band of SKA1-low.

The upper panels of Figure 5.3 show the brightness temperature pattern as a function of radial distance from an isolated source for four different source models. We have shown results for three different coupling models A, B and C in each panel. For model C, the signal pattern in general can be divided into four prominent regions: (i) The signal is absent inside the central ionized H II bubble of the source. (ii) The H II region is followed by a region which is neutral and heated by X-rays. In this region, $T_{\rm K} > T_\gamma$ and thus the signal is seen in emission. (iii) The third is a strong absorption region which is colder than T_γ as the X-rays have not been able to penetrate into this region. (iv) Beyond the absorption region, the signal gradually approaches to zero as the Lyα coupling becomes less efficient far away from the source. In model B the Lyα coupling is assumed to be efficient throughout and hence the fourth region is absent. In addition, we assume the heating to be efficient in model A, and hence both the third and

fourth regions are absent in this case.

If we now look at the difference between different source models, we find that all the models produce a prominent H II bubble around the source, irrespective of the coupling model. The size of the ionized bubble[1] is significantly smaller for the PopIII model compared to the other three because the stellar mass in this model is considerably smaller than the others. In fact, if we compare these models for the coupling model A, we find that all the models are qualitatively similar showing a H II region followed by a prominent emission region, the only difference being the size of the H II region for the PopIII case.

If we now concentrate on the coupling models B and C, we find that the Galaxy and HMXBs models do not show any substantial emission beyond the H II region. The Galaxy model does not have any X-ray photons, hence the heating in the neutral / partially ionized IGM is negligible. The X-rays produced by the HMXBs, on the other hand, are mostly in the very high-energy regime (hard X-rays) which have relatively smaller interaction cross section. Hence these photons are not efficient in heating the medium. The presence of these hard X-rays, however, makes the transition from H II region to the absorption region somewhat smoother for the HMXBs compared to the Galaxy model. The other two models, PopIII and Mini-QSO contain sufficient soft X-rays so as to produce a prominent emission region. The transition between the emission and the absorption regions is very smooth in these two models because of the same soft X-rays.

5.3.2 A simple model for calculating the visibility signal around isolated sources

We present a simple model for calculating the 21-cm signal around a source which makes it easier to understand some of the properties. The main simplification is that we will approximate the signal in each zone, i.e., emission and absorption, by simple step-like functions of various sizes. For model A, where the Lyα coupling is efficient all over the IGM and the gas temperature is much larger than the CMBR temperature, the signal is zero within the H II bubble and in emission uniform outside (assuming a uniform IGM). The signal can be represented by the shape shown in the top panel of Figure 5.4. Datta et al. (2007a) showed that the

[1]We define ionized regions as those with ionization fraction larger than 0.5.

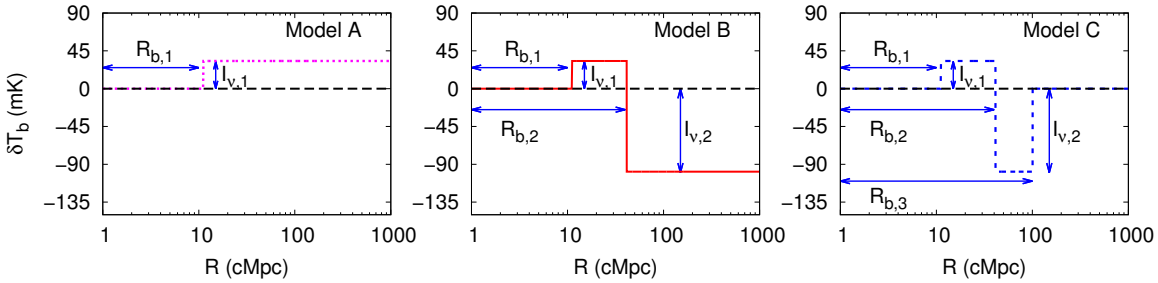

Figure 5.4: Differential brightness temperature as a function of the distance from the source for three simple scenarios.

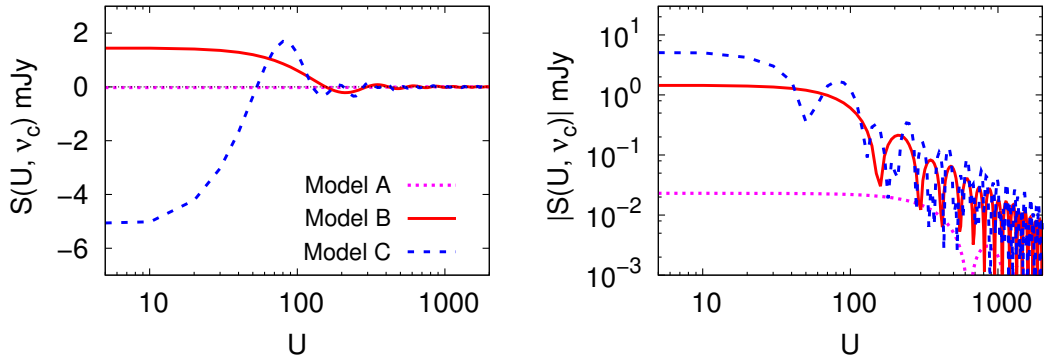

Figure 5.5: The visibility amplitude (left-hand panel) and the absolute visibility (right-hand panel) as a function of the baseline U for three models A, B and C as shown in Figure 5.4.

visibility for $U > 0$ of a spherical bubble in the uniform IGM can be written as

$$S_{\rm c}^{(A)}(U,\nu) = -2\pi I_{\nu,1}\theta_{\nu,b,1}^2 \left[\frac{J_1(2\pi U\theta_{\nu,b,1})}{2\pi U\theta_{\nu,b,1}}\right] \Theta\left(1 - \frac{|\nu-\nu_c|}{\Delta\nu_{b,1}}\right), \tag{5.16}$$

where $I_{\nu,1}$ is the 21-cm intensity in the neutral region, $\theta_{\nu,b,1}$ is the angular size of the bubble in the frequency channel ν and $\Delta\nu_{b,1}$ is the frequency extent of the bubble. The first zero crossing occurs at the baseline $U_0^{(A)} = 0.61/\theta_{\nu,b,1}$. Note that the angular extent in any frequency channel ν is related to that in the central frequency ν_c by $\theta_{\nu,b,1} = \theta_{b,1}\sqrt{1-[(\nu-\nu_c)/\Delta\nu_{b,1}]^2}$.

We can similarly approximate the signal for model B as that shown in the middle panel of Figure 5.4. We have assumed that both the emission and absorption regions have uniform intensity $I_{\nu,1}$ and $I_{\nu,2}$, with $I_{\nu,2} < 0$. The positions of the transition between the regions are denoted as $\theta_{\nu,b,1}$ and $\theta_{\nu,b,2}$ respectively. In this case, the visibility for $U > 0$ is given by

$$\begin{aligned} S_{\rm c}^{(B)}(U,\nu) &= -2\pi I_{\nu,1}\theta_{\nu,b,1}^2 \left[\frac{J_1(2\pi U\theta_{\nu,b,1})}{2\pi U\theta_{\nu,b,1}}\right] \Theta\left(1 - \frac{|\nu-\nu_c|}{\Delta\nu_{b,1}}\right) \\ &+2\pi(I_{\nu,1}-I_{\nu,2})\ \theta_{\nu,b,2}^2 \left[\frac{J_1(2\pi U\theta_{\nu,b,2})}{2\pi U\theta_{\nu,b,2}}\right] \Theta\left(1 - \frac{|\nu-\nu_c|}{\Delta\nu_{b,2}}\right). \end{aligned} \tag{5.17}$$

Note that since $I_{\nu,2} < 0$, the visibility amplitude for model B is larger than that in model A as can be seen in Figure 5.5. In fact, for model B we find $|I_{\nu,2}| \gg I_{\nu,1}$ for most source models, hence we can approximate the signal by

$$S_{\rm c}^{(B)}(U,\nu) \approx 2\pi|I_{\nu,2}|\ \theta_{\nu,b,2}^2 \left[\frac{J_1(2\pi U\theta_{\nu,b,2})}{2\pi U\theta_{\nu,b,2}}\right] \Theta\left(1 - \frac{|\nu-\nu_c|}{\Delta\nu_{b,2}}\right). \tag{5.18}$$

Under this approximation, we find that the location of the first zero will be at $U_0^{(B)} \approx 0.61/\theta_{\nu,b,2}$. Thus the extent of the signal in model B is mostly determined by the position of the transition between emission and absorption regions. Also, we find that the position of the first zero is smaller for model B than in model A, i.e., $U_0^{(B)} < U_0^{(A)}$. Since the amplitude $|I_{\nu,2}|\theta_{\nu,b,2}^2 \gg I_{\nu,1}\theta_{\nu,b,1}^2$, we see from the equations (5.16) and (5.18) that the amplitude of the signal at smaller baselines would be larger for model B than for A.

Extending the above calculations to model C, as shown in the bottom panel

of Figure 5.4, we find the visibility to be

$$S_{\rm c}(U,\nu) = -2\pi I_{\nu,1}\theta^2_{\nu,b,1}\left[\frac{J_1(2\pi U\theta_{\nu,b,1})}{2\pi U\theta_{\nu,b,1}}\right]\Theta\left(1-\frac{|\nu-\nu_c|}{\Delta\nu_{b,1}}\right)$$
$$+2\pi(I_{\nu,1}-I_{\nu,2})\ \theta^2_{\nu,b,2}\left[\frac{J_1(2\pi U\theta_{\nu,b,2})}{2\pi U\theta_{\nu,b,2}}\right]\Theta\left(1-\frac{|\nu-\nu_c|}{\Delta\nu_{b,2}}\right)$$
$$+2\pi I_{\nu,2}\ \theta^2_{\nu,b,3}\left[\frac{J_1(2\pi U\theta_{\nu,b,3})}{2\pi U\theta_{\nu,b,3}}\right]\Theta\left(1-\frac{|\nu-\nu_c|}{\Delta\nu_{b,3}}\right). \quad (5.19)$$

In this case too, let us make the assumption that $|I_{\nu,2}| \gg I_{\nu,1}$, which is reasonable for all the source models except PopIII. In addition, one can also make the assumption that $\theta_{\nu,b,3} \gg \theta_{\nu,b,2}$, i.e., the extent of the absorption zone is much larger than that of the emission. This too is a reasonable assumption (except for PopIII) as can be seen from the top panels of Figure 5.3. In that case, the signal takes a simpler form

$$S^{(C)}_{\rm c}(U,\nu) \approx -2\pi|I_{\nu,2}|\ \theta^2_{\nu,b,3}\left[\frac{J_1(2\pi U\theta_{\nu,b,3})}{2\pi U\theta_{\nu,b,3}}\right]\Theta\left(1-\frac{|\nu-\nu_c|}{\Delta\nu_{b,3}}\right). \quad (5.20)$$

In this case, the signal at small baselines would larger than those in model B by a factor $\sim \theta^2_{\nu,b,3}/\theta^2_{\nu,b,2}$. Also, the location of the first zero would be $U_0^{(C)} \approx 0.61/\theta_{\nu,b,3}$, which is smaller than that found in models B and A.

We thus find, with the help of the simplified models and by making reasonable approximations, that the first zero of the visibility signal for models A, B and C are determined by the extent of the ionized bubble, emission region and absorption region respectively. The strength of the signal at small baselines (i.e., those smaller than the location of the first zero) would be determined by a combination of the intensities and region sizes.

5.3.3 Visibilities of the sources

If we ignore the contributions from the system noise and other astrophysical foregrounds, the strength of the 21-cm visibility signal around a single source depends on the source properties and the state of the IGM itself. The lower panels of Figure 5.3 show the expected visibilities for different source models and different coupling models for our fiducial redshift of 15. The properties of the sources are taken to be identical to that used in the upper panels. Note that

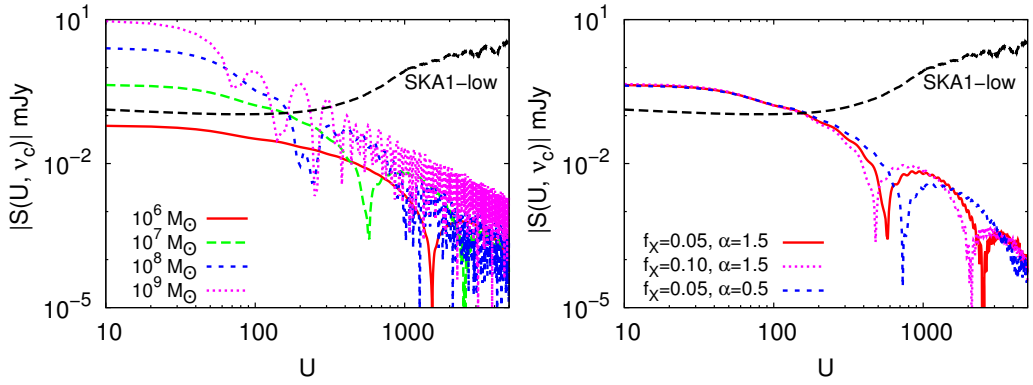

Figure 5.6: The dependence of the visibility on model parameters for the Mini-QSO source model. The coupling model is taken to be C. Left-hand panel : The absolute visibility amplitudes for different values of stellar mass $M_\star = 10^6, 10^7, 10^8, 10^9\,\mathrm{M}_\odot$ at redshift 15 as a function of baseline. All the other parameters are fixed to their fiducial values. Right-hand panel : The absolute visibility amplitudes as a function of baseline for different values of f_X and α. In both the panels, the black dashed lines correspond to rms noise for 1000 h of observation with the SKA1-low with a frequency resolution of 50 kHz and ΔU=10 (see equation 5.9).

we plot only the absolute value of the visibilities. We also show the expected system noise for SKA1-low assuming 1000 hours of observation time and a single frequency channel of width 50 kHz.

The coupling model A represents visibility of an ionized bubble around a source, similar to what was studied in Datta et al. (2007a). The signal is expected to show an oscillatory pattern arising from the spherical nature of the bubble (see Section 5.3.2). Datta et al. (2007a) showed that the first zero crossing of the visibility will occur at a baseline $U_0 = 0.61 r_\nu [R_b \sqrt{1 - (\Delta\nu/\Delta\nu_b)^2}]^{-1}$, where r_ν is the comoving distance to the centre of the bubble (same as the $r(z)$ defined earlier), R_b is the comoving radius of the H II bubble, $\Delta\nu_b$ is the bubble size in frequency space and $\Delta\nu$ is the difference in frequency space between the centre of the bubble and the observed sky plane. For the source model PopIII, the size of the H II region is $R_b \sim 0.23$ cMpc for which the first zero crossing occurs around $U_0 \sim 28000$, while the size is larger $R_b \sim 1.13$ cMpc for the other three source models which gives the first zero crossing at $U_0 \sim 5700$. These values

are consistent with the prediction of Datta et al. (2007a). We also find that the visibility amplitude, which is proportional to R_b^2 at small U (see Section 5.3.2 for details), is smaller for PopIII compared to the other three models. This too is because of the fact that the PopIII model produces a much smaller H II region.

For models B and C, the 21-cm signal visibilities are more complex and cannot be explained by a simple scenario as in model A. In general, we find that the emission and absorption bubbles are larger than the H II bubble for B and C respectively, and hence the first zero crossings occur at lower values of U compared to model A. For example, the first zero crossing in the source model Mini-QSO appears around $U_0 = 2390$ and 590 for models B and C respectively, while it appears around $U_0 = 5650$ for model A. In addition, we find that the amplitude of the visibility signal at small U is the largest (smallest) for C (A). The amplitude of the visibility at small baselines scales roughly as $\sim I_\nu \; R_{b,\nu}^2$, where I_ν is the signal amplitude in the emission region for model A and in the absorption region in models B and C, and $R_{b,\nu}$ is the total radial extent (in the frequency channel ν) of the ionized region for model A, ionized and emission regions for model B and ionized, emission and absorption regions for models C. We have explained this aspect of the signal using simple models in Section 5.3.2. Given this scaling, it is easy to see that since the size of the absorption region is much larger than the ionized and emission regions, the visibility amplitude in model C would be the largest. This is further assisted by the fact that the I_ν itself is very high in the absorption region.

At this point, we can make some preliminary comment on the detectability of the signal with SKA1-low. In the bottom panels of Figure 5.3, we have plotted the expected noise for an observing time of 1000 hours and for a frequency channel of width 50 kHz and $\Delta U = 10$. One can clearly see that the signal is detectable for smaller baselines $U \lesssim 100$ for model C and for the source models Galaxy, Mini-QSO and HMXBs. The signal for the PopIII model, on the other hand, is substantially below the noise, and hence it is almost impossible to detect 21-cm signatures around a PopIII star. This result is consistent with other previous works, e.g., Yajima and Li (2014). The signal for the coupling models A and B too are well below the noise leading to SNR < 1, and hence detecting the first sources would be quite difficult once the Lyα coupling becomes efficient all throughout the IGM and/or the IGM is heated. We can also infer that detecting

the first sources using the present telescopes (GMRT, LOFAR, MWA) will require an unrealistically large amount of observing time as the noise amplitudes are at least an order of magnitude larger than the SKA1-low (see the right-hand panel of Figure 5.2). Keeping these in mind for the rest of the chapter, we will consider the signal only from model C and compare with SKA1-low noise levels. Also, for definiteness, we concentrate on the source model Mini-QSO, though many of the conclusions would hold for the models Galaxy and HMXBs.

Until now, we have presented our results for the fiducial values of the source and IGM parameters. To understand the dependence of the visibility signal on different parameters, we show in the left-hand panel of Figure 5.6 the absolute visibility for the source model Mini-QSO having different values of stellar mass. The coupling model used is C and all other parameters have been set to their fiducial values. As expected, the absolute visibility increases with mass at small baselines. In addition, the position of the first zero crossing shifts towards lower baselines as the mass increases which is because of the increase in the size of the 21-cm pattern around the source. We expect similar changes in the visibility signal when we increase the age of the source. The right-hand panel of the figure shows the effect of different X-ray parameters on the signal visibility. We find that the visibility at small baselines is relatively insensitive to the parameters f_X and α. There is a slight change in the position of the first zero crossing for different f_X and α because of the change in size of the heated regions. Also the signal at large baselines can be quite different when we change the parameters. However, the detectability of the signal, which is mostly driven by the smaller baselines, is expected to be relatively independent of the X-ray parameters.

Figure 5.7 shows frequency dependence of the absolute visibility. The left-hand panel shows the signal for different baselines when all the parameters are fixed to their fiducial values. The visibility peaks at the central channel at the position of the centre of the source and extends up to the size of the signal in the frequency space. As expected, the signal is larger for smaller baselines. The signal seems to increase more rapidly for smaller baselines than for larger ones. We found that the frequency dependence of the visibility for the Galaxy and HMXBs models is similar to that for the Mini-QSO model at small baselines. The amplitude of the absolute visibility increases with the age of the Mini-QSO, as shown in the right-hand panel of Figure 5.7. We also see the extent of the

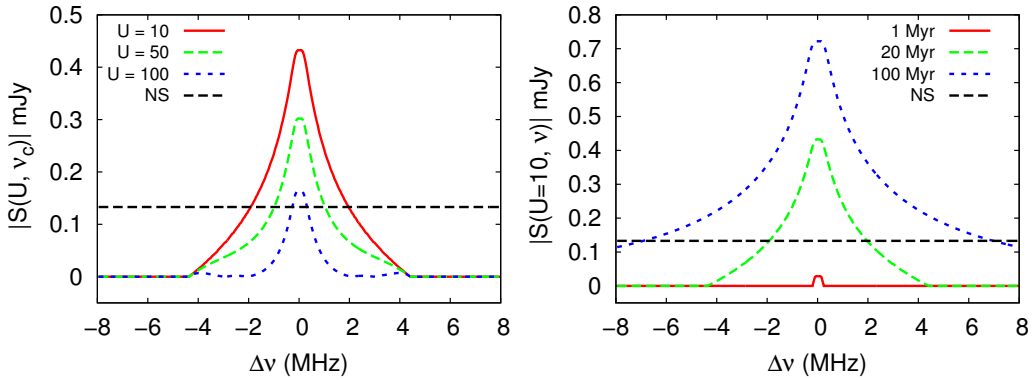

Figure 5.7: Left-hand panel: The absolute visibility amplitude as a function of frequency channels at baselines $U = 10, 50$ and 100 for the Mini-QSO source model and coupling model C. The parameters are fixed to their fiducial values. The quantity $\Delta\nu$ represents the difference between the frequency channel under consideration and the central frequency (ν_c) of observation. Right-hand panel : The absolute visibility amplitude as a function of frequency channels for different values of the source age $t_{\rm age} = 1, 20$ and 100 Myr at a baseline $U = 10$. The horizontal dashed lines in both panels represent the rms noise at baseline $U = 10$ for 1000 h of observation time and 50 kHz frequency resolution with the SKA1-low.

signal in the frequency space increase with age as expected.

As we have seen, the detectability of the signal around a source is mostly determined by the smaller $U \lesssim 100$ baselines. At larger baselines, the signal amplitude decreases while the noise increases, thus making them unsuitable for detection. A possible way of characterizing the possibility of detection would be through integrating the signal over all baselines and frequency channels and define an SNR by using a inverse noise weighting as done in equation (5.15). The SNR we have defined contains contributions from all possible baselines and frequency channels. This may not be the optimum SNR possible for this scenario because, e.g., the SNR can be increased by neglecting large baselines and frequency channels away from the frequency channel that contains the source centre. However, constructing a optimum weighting scheme would require prior knowledge of the signal we are willing to detect. We rather concentrate on a robust estimate of the SNR which does not require any assumption about the nature of the signal around the source, which is more appropriate for the first detection of its kind.

Different panels of Figure 5.8 show the SNR as a function of various parame-

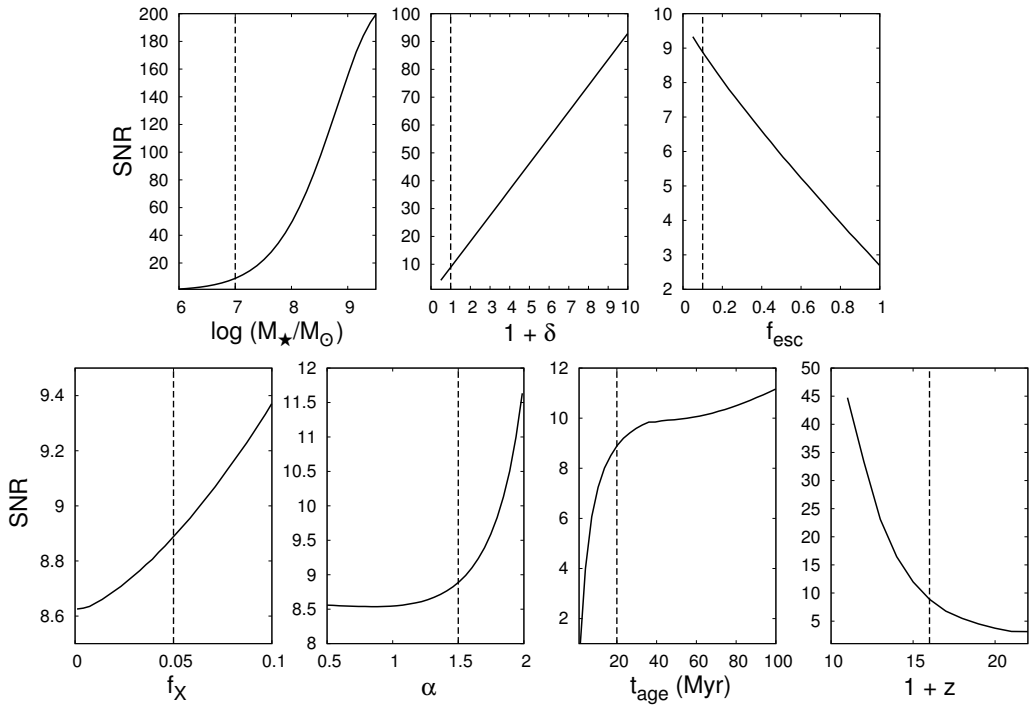

Figure 5.8: The SNR as a function of different model parameters for the source model Mini-QSO and coupling model C. The panels from top to bottom and left to right correspond to parameters stellar mass $M_\star$, overdensity $1+\delta$ of the medium around the source, escape fraction $f_{\rm esc}$ of ionizing photons, X-ray to UV luminosity ratio f_X, X-ray spectral index α, age $t_{\rm age}$ of the source and redshift z. While calculating the dependence of the SNR on a particular parameter, we have fixed the other parameters to their fiducial values. The fiducial value for each parameter is denoted by the vertical dashed line in the corresponding panel. The SNR is calculated for 1000 hours of observation with SKA1-low with a bandwidth of 16 MHz.

ters related to the source properties (e.g., stellar mass, escape fraction of ionizing photons, X-ray to UV luminosity ratio, spectral index and age of the source) and the overdensity of the surrounding IGM. Recall that the fiducial value of the parameters are $M_\star = 10^7\,\mathrm{M}_\odot,\ \delta = 0,\ f_{\rm esc} = 0.1,\ f_X = 0.05,\ \alpha = 1.5,\ t_{\rm age} = 20$ Myr. While showing the dependence of the SNR on a particular parameter, we have fixed all the other parameters to their fiducial values. The characteristics of the observations are chosen such that the total observational time is 1000 hours, while the bandwidth is 16 MHz[1]. As shown in the figure, the SNR is quite sensitive to the stellar mass $M_\star$, $f_{\rm esc}$, age $t_{\rm age}$ of the source and the IGM overdensity $1+\delta$. The SNR increases with the stellar mass (top left-hand panel) as the strength of the 21-cm signal increases and thus the visibility amplitude increases (see the left-hand panel of Figure 5.6). On the other hand, the radius of both the ionized and heated bubbles increase with the mass of the source, which result in faster decrease of the visibility with the baseline. Although the visibility signal is much stronger at smaller baselines for large stellar mass sources, the very small baselines $U_{\rm min} \lesssim 8$ are not available for SKA1-low baseline distribution at redshift 15. This slows the growth of the SNR for the extremely high mass $M_\star \gtrsim 10^9\mathrm{M}_\odot$ sources. From the top right-hand panel, we find that the SNR decreases with increase of escape fraction. This is because the amount of Lyα photons, produced due to the recombination of ionized hydrogen in the ISM, is proportional to $1 - f_{\rm esc}$ and thus the Lyα coupling becomes less effective as $f_{\rm esc}$ increases[2]. This leads to a smaller absorption region and thus a smaller amplitude of the 21-cm signal. The size of the 21-cm signal region increases with the age of the source as the photons are able to propagate longer distance and thus the visibility amplitude at lower baselines as well as the SNR increase with the age of the source, as shown in the bottom second right-hand panel of Figure 5.8. Since $\delta T_{\rm b} \propto 1+\delta$ (see equation 5.4), the strength of the signal increases with the increase in the overdensity $1+\delta$.

[1]We choose the bandwidth to be smaller than the total bandwidth of SKA1-low which is ~ 300 MHz. This is done to avoid contribution from other possible sources along the frequency direction.

[2]A fraction ~ 0.68 of the ionizing photons absorbed in the ISM can be converted into Lyα photons because of the recombination of ionized hydrogen. Thus, in our calculation, we take the rate of Lyα photons, produced because of recombinations in the ISM, to be $0.68(1-f_{\rm esc})\dot{N}_{\rm ion}$ (Dijkstra 2014), where $\dot{N}_{\rm ion}$ is the number of ionizing photons produced by the source per unit time.

Parameter P	$M_\star$	$1+\delta$	$f_{\rm esc}$	f_X	α	$t_{\rm age}$	$1+z$
$P_{\rm fid}$	$10^7 {\rm M}_\odot$	1	0.1	0.05	1.5	20 Myr	16
γ_P	0.80	1.023	-0.42	0.02	0.14	0.52	-3.69
applicable range	1.3×10^6 – $1.4 \times 10^8 {\rm M}_\odot$	0.5 – 10	0.05 – 0.9	0.05 – 0.1	0.5 – 2	4 – 100 Myr	11 – 24

Table 5.2: Dependence of the SNR on the parameters used in the study where the dependence is modelled as ${\rm SNR}(P) = 8.89\,(P/P_{\rm fid})^{\gamma_P}$. The final row of the table denotes the parameter range within which the fit produces the SNR to within 20% of the actual value. The coupling model is taken to be C. The SNR is calculated for 1000 hours of observation with SKA1-low with a bandwidth of 16 MHz.

Hence the SNR increases almost linearly with $1+\delta$, as shown in the top middle panel of Figure 5.8. The SNR in Figure 5.8 shows relatively weaker dependencies on the two X-ray parameters f_X and α.

Finally, we provide some scaling relations which would allow one to compute the SNR for a wide range of model parameter and redshift values. We model the relation as a simple power law

$$ {\rm SNR}(P) = {\rm SNR}_{\rm fid} \left(\frac{P}{P_{\rm fid}} \right)^{\gamma_P}, \quad {\rm SNR}_{\rm fid} = 8.89 \tag{5.21} $$

where P is one of the seven parameters of interest, i.e., $M_\star$, $1+\delta$, $f_{\rm esc}$, f_X, α, $t_{\rm age}$ and $1+z$. The fiducial value of the parameter P is denoted as $P_{\rm fid}$, and the corresponding SNR is given by ${\rm SNR}_{\rm fid}$. The power law index γ_P determines the scaling relation for the parameter P and the values are given in Table 5.2. We have also indicated the values of the parameters where the scaling law reproduces the SNR to within 20% of the actual value. It is possible to provide more accurate fits, however, those fits are more complex. Given the assumptions made in the physical modelling of the heating and ionized regions, the fit provided here should be sufficient to estimate the parameters which are favourable for detection. Note that the SNR also has dependence on the observational time as $t_{\rm obs}^{1/2}$. This is because of the fact that the ${\rm SNR} \propto \sigma_N^{-1}$ (see equation 5.15), which in turn depends on the observation time as $\sigma_N \propto t_{\rm obs}^{-1/2}$ (see equation 5.14).

We can see from Table 5.2 that the dependence of the SNR on parameters $M_\star$, $f_{\rm esc}$, $t_{\rm age}$, $1+\delta$ and z are the most significant. In particular, we find that the SNR decreases sharply with increasing redshift which follows from the fact that $T_{\rm sys}$ increases rapidly at lower frequencies. For fiducial values of other

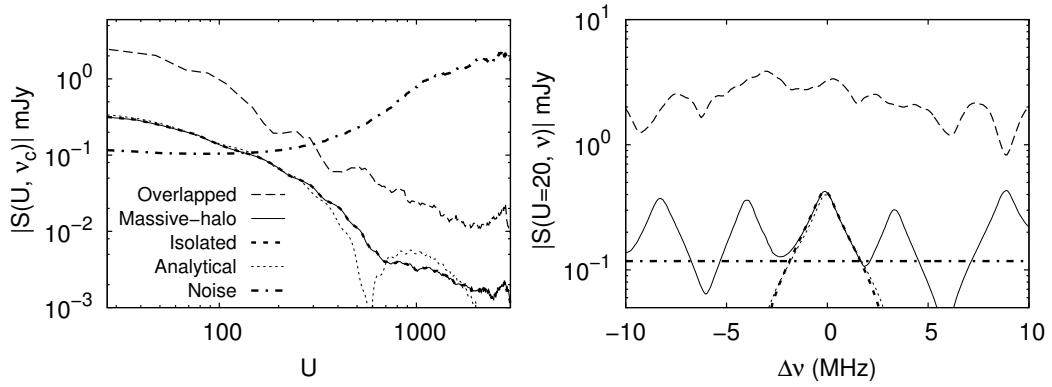

Figure 5.9: The absolute visibility amplitude calculated from the simulation box for different models. The model *Isolated* (short-dashed) refers to the case where there is only one source in the box, while *Massive-Halo* (solid) is the model where all haloes with masses $\gtrsim 2 \times 10^{10} \mathrm{M}_{\odot}$ contain radiation sources. The model *Overlapped* (long-dashed) corresponds to the case where all haloes in the box contain radiation sources and thus the individual 21-cm regions of individual sources overlap significantly. The model *Analytical* (dotted) is simply the result from analytical calculation of the earlier sections. The coupling model is taken to be C. Left-hand panel: The absolute visibility amplitude as a function of baseline. The dash-dotted curve represents the rms noise for SKA1-low for 1000 h of observation with a frequency resolution of 60 kHz. Right-hand panel: The absolute visibility amplitude as a function of frequency channels at a baseline $U = 20$. The dash-dotted line represents the rms noise at a baseline $U = 20$.

parameters, the SNR would reduce from ~ 9 at $z = 15$ to ~ 3 at $z = 20$. We should mention here that, throughout the chapter, we have calculated the rms noise for single polarization. The rms noise will decrease by a factor $\sqrt{2}$ for when both the polarizations are taken into account, and therefore the SNR will improve by a factor ~ 1.4.

5.3.4 Overlap between the sources

Till now we have been working under the assumption that there is only one source in the FOV for which the signal can be computed analytically. However, in reality there will be multiple sources in the FOV of interest and there could be overlap

between the 21-cm regions of the individual sources. In addition, there could be effects arising from peculiar velocities along the line of sight. In such a scenario, it is almost impossible to find any analytical form of the visibility and the only way we can compute the expected signal is by using a simulation box. To study such realistic scenarios, we have run a dark matter N-body simulation in a box of size 300 h^{-1} cMpc with 2592^3 particles. The mass resolution of the dark matter particles is $2 \times 10^8\,\mathrm{M}_\odot$ and we are able to identify dark matter haloes down to $\sim 4 \times 10^9\,\mathrm{M}_\odot$ using the spherical overdensity method. We present our results for $z = 15$ assuming coupling model C, the main reason being that the other models are not quite favourable for detection. The box length corresponds to a frequency bandwidth of 20 MHz at $z = 15$ and the grid size gives a frequency resolution of ~ 60 kHz. Once we assign photon sources to the dark matter haloes, we use the method of Ghara et al. (2015a,b) to generate the brightness temperature maps. Note that the method naturally accounts for the effects of density fluctuations and the peculiar velocities of the gas in the IGM, as well as fluctuations in the spin temperature, while calculating the brightness temperatures maps. The method for generating the δT_b maps has been discussed in our earlier works (Ghara et al. 2015a,b) and in Chapter 2 of the thesis.

In order to test the results of the analytical results of the previous sections against the simulations, we first study a simple scenario where we assume that there is only one source in the box. We ensure that this source is at the centre of the FOV and calculate the visibility signal for the whole box. We fix the fraction of the baryon residing in the form of stars in the galaxy $f_\star = 0.005$. This is chosen such that the stellar mass of the source is $M_\star \sim 10^7\,\mathrm{M}_\odot$. We choose Mini-QSO source model and assume the age of the source to be 20 Myr. We choose the default values $f_X = 0.05$ and $\alpha = 1.5$ for the source. The comparison between this model, which we call *Isolated*, and the analytical calculations is shown in Figure 5.9. In the left-hand panel, we plot the absolute visibility for a single frequency channel of width 60 kHz as a function of baseline U, while in the right-hand panel we show the same as a function of frequency channels for a baseline $U = 20$. One can see from the both the panels that the match between *Isolated* and *Analytical* is almost perfect. There is some deviation at larger baseline $U \gtrsim 300$ where the analytical results show sharp features while the simulation results are slightly smoothed out. This difference arises from the fluctuations in the density and

velocity fields which are present in the simulations box (but do not exist in our analytical calculations). The resulting SNR, which is anyway dominated by the smaller $U \lesssim 100$ baselines, turns out to be very similar for the two cases.

We next study a more realistic model where the box contains more than one source. In order to ensure that there is no significant overlap between the 21-cm patterns around the sources, we populate only haloes which have masses larger than $\sim 4 \times 10^9\,\mathrm{M}_\odot$ with ionizing sources. As before, we choose $f_\star = 0.005$ so that the most massive source in the box has $M_\star \sim 10^7\,\mathrm{M}_\odot$. The resulting heating fraction is 3×10^{-5} and the ionization fraction is 1.4×10^{-5}. The signal, labelled as *Massive-halo*, is shown in Figure 5.9. One can see from the left-hand panel that there is no difference between the *Massive-halo* and *Isolated* models as far as the U-dependence of the visibility in the central frequency channel is concerned. The main difference can be seen when we plot the signal as a function of the frequency channel as is done in the right-hand panel. Clearly, the *Massive-halo* shows multiple peaks arising from multiple sources in the FOV. However, the signal around each of the peak follows the prediction from the *Analytical* model. In fact, the presence of such peak-like features in the visibility along the frequency axis could be a potential way of identifying the location of the sources in the frequency space[1]. The SNR obtained, by integrating over the full bandwidth of 20 MHz, turns out to be 34.7 for the *Massive-halo* which is considerably higher than that in the *Analytical* model (where the SNR is 7.5). This is simply because the signal is contributed by multiple sources. In case one is interested in focussing on signal from a single isolated source, one should integrate over a smaller bandwidth around the source. For example, if we reduce the bandwidth to 4 MHz, the SNRs for the *Massive-halo* and *Analytical* models come out to be very similar ~ 16.

For completeness, we study another model *Overlapped* where all haloes in the box are assigned ionizing sources. In this case, the overlap between 21-cm pattern of individual sources is quite significant, and hence we do not expect any match with the analytical results. We can see from the left-hand panel of Figure 5.9 that

[1]In principle, it should also be possible to locate the positions of the sources in the image plane using the observed visibilities. In general, if the source centre is offset by $\vec{\theta}_c$ from the centre of the field of view, there will be an additional phase shift of $\mathrm{e}^{2\pi \vec{U}.\vec{\theta}_c}$ in the observed visibilities. Thus the information on $\vec{\theta}_c$ can be obtained by measuring the phases of the visibility.

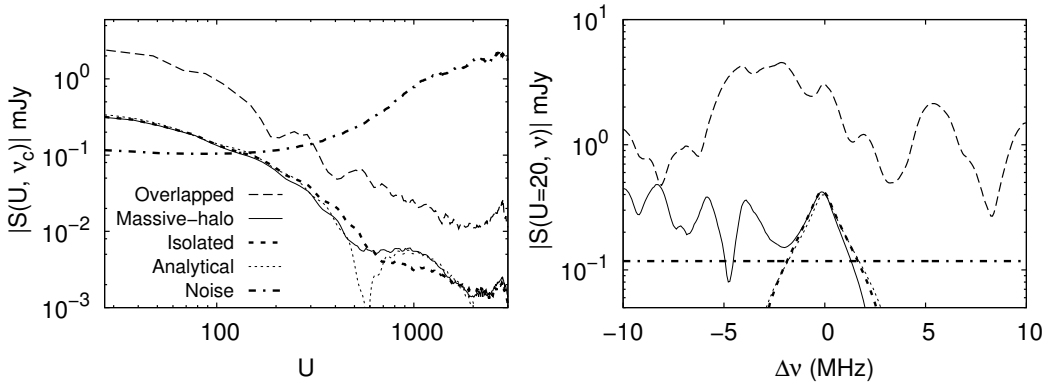

Figure 5.10: Same as Figure 5.9, but with the light-cone effect included.

the signal for the *Overlapped* model is much higher than the other three models, even for a single frequency channel. This implies that even a channel of width 60 kHz contains multiple sources in this case unlike the other models. While studying the frequency dependence of the signal (right-hand panel), we find that the visibility does not show any prominent peak-like structure as was seen in the other models. This clearly implies that the 21-cm pattern of the individual sources have overlapped significantly, and hence it may not be straightforward to extract the signature of a single source from the complex signal. In such a scenario, it is probably worth exploring lower frequencies (i.e., higher redshifts) where the overlap is expected to be less than what is found at $z = 15$.

In addition, it is also important to account another line of sight effect while generating the redshifted 21-cm signal, namely the light-cone effect (Ghara et al. 2015b). This effect is caused by the redshift evolution of the signal along the frequency direction. The detailed method of incorporating the light-cone effect in the 21-cm signal can be found in Ghara et al. (2015b) and in Chapter 4. While we expect the signal to be unaffected when there is only one source in the FOV, it can get modified significantly in more realistic scenarios where there are multiple sources in the FOV. On the average there will be less number of sources at the far end of the simulation box (i.e., at lower frequencies) along the line of sight direction. In order to study this effect we set the parameter $f_\star$ such that the stellar mass of the highest mass source at redshift 15 is $\sim 10^7$ $M_\odot$. The effect of the light-cone is shown in Figure 5.10, which should be compared with Figure

5.9. By construction, the signal at the central frequency channels look similar with and without the light-cone effect (as shown in the left-hand panels of the two figures) as both correspond to the same redshift 15. The main effect can be seen by comparing the right-hand panels. For example, in the *Massive-halo* scenario, there are less number of sources at channels with frequency smaller than the central frequency when the light-cone effect is included. On the other hand, there are more sources (and also the signal amplitude is higher) at channels with $\nu > \nu_c$ compared to the case where the light-cone effect was not considered. In the *Overlapped* scenario, the amplitude of the signal is lower compared to the previous case (i.e., without light-cone effect) at smaller frequencies (far end of the simulation box) as the number density of sources is smaller. We see that the signal is also lower at the larger frequencies (near end of the box). This is because of the presence of larger number of sources in this region thus making the Lyα coupling relatively stronger. As a result the model C approaches the model B and gives rise to a signal visibility that is weaker compared to the case where light-cone effect was not considered. When the signal is integrated over the full bandwidth of 20 MHz, the SNR of the box including the light-cone effect is ~ 48. This is $\sim 40\%$ higher than the SNR without the light-cone effect. The main reason is that there are larger number of sources at the low-redshift end of the simulation box. If we reduce the observational bandwidth to 4 MHz, the SNR is ~ 15, which is similar to the case without the light-cone effect.

We end this section by commenting upon identifying the possible location of the first sources. As long as the overlap between individual 21-cm patterns is not significant, it is possible to identify the position of the source in the frequency space by plotting the visibility against ν. The channels which show prominent peaks could be possible location of sources. A more direct method of identifying sources could be to use future NIR observations from an instrument like the JWST. It will probe the wavelength range of $0.6 - 29\mu$m, which in principle can be used to detect the very first source in the universe. For example, the flux from a galaxy of stellar mass $M_\star = 10^7\,\mathrm{M}_\odot$ at redshift 15, observed using the Near Infrared Camera (NIRCam), is expected to be $\sim 5 \times 10^{-7}$ Jansky. This corresponds to AB magnitude of 24.6, while the limiting magnitude of JWST is 29 (Zackrisson et al. 2011). These sources should be detected by the telescope with SNR larger than 10 for an observation time of 10^4 second.

5.3.5 Effect of the astrophysical foregrounds

We have assumed till now that the astrophysical foregrounds can be modelled perfectly and subtracted from the observed visibilities. In this section, we relax this assumption to some extent and investigate whether the signal can still be recovered. In general, an additional term $F(\vec{U},\nu)$ arising from the foregrounds needs to be added to the expression for the measured visibility, i.e., to the right-hand side of equation 5.7.

Astrophysical foregrounds, mostly contributed by the synchrotron radiation from our galaxy and extragalactic point sources, are generally several order stronger than the expected 21-cm signal. For the purpose of this analysis, the foreground contribution at each baseline and frequency channel is assumed to be a random variable with $\left\langle F(\vec{U},\nu)\right\rangle = 0$ (for all baselines except $\vec{U} = 0$, which is anyway not considered in this study). The foreground contributions can be quantified in terms of the two-visibility correlation $\left\langle F(\vec{U_1},\nu_1)F(\vec{U_2},\nu_2)\right\rangle$ given by (Datta et al. 2007a),

$$\left\langle F(\vec{U_1},\nu_1)F(\vec{U_2},\nu_2)\right\rangle = \delta_D^{(2)}(\vec{U_1}+\vec{U_2})\left(\frac{2k_B}{c^2}\right)^2(\nu_1\nu_2)^2 \times C_{2\pi U_1}(\nu_1,\nu_2), \tag{5.22}$$

where $C_l(\nu_1,\nu_2)$ is the multi-frequency angular power spectrum and the term $(2k_B\nu^2/c^2)$ is the conversion factor from brightness temperature to specific intensity.

We consider three components of the foreground, namely, (i) the galactic synchrotron radiation, (ii) the Poisson noise arising from discrete point sources and (iii) the clustering contribution of the point sources. We assume that all these components have a power law dependence on the frequency (Datta et al. 2007a; Santos et al. 2005). The angular power spectra of these components can be expressed as,

$$C_l(\nu_1,\nu_2) = A_{\nu_f}\left(\frac{\nu_f}{\nu_1}\right)^{\bar{\alpha}}\left(\frac{\nu_f}{\nu_2}\right)^{\bar{\alpha}}\left(\frac{1000}{l}\right)^{\bar{\beta}} \times \exp\left(-\log_{10}^2\frac{\nu_2}{\nu_1}\frac{1}{2\xi^2}\right) \tag{5.23}$$

We have taken the values of the parameters A_{ν_f}, ν_f, $\bar{\alpha}$, $\bar{\beta}$, ξ from Datta et al. (2007a), see their Table 1. While estimating the contribution from point sources we have assumed that all objects having flux larger than 5σ, where σ is the rms noise in the high-resolution continuum image, are identified and removed.

Figure 5.11 shows the contribution of the expected foreground for the SKA1-low for the instrument parameters listed in Table 5.1. Among the different components of the foreground considered in this study, the diffuse galactic synchrotron radiation is the most dominant one. The amplitude of the foreground is several orders larger than the expected signal and system noise for all relevant values of the baselines (left-hand panel) and frequencies (right-hand panel). Thus it is not possible to recover the signal by simply integrating over all baselines and frequency channels. One is hence compelled to use a different estimator, e.g., using a suitable filter (Datta et al. 2007a), to recover the signal in presence of such a huge foreground contamination.

Unlike the redshifted 21-cm signal, the foregrounds have smooth frequency dependencies which is shown in the right-hand panel of Figure 5.11. This feature can be used to construct suitable filters to substantially reduce the foreground contributions. We essentially follow the method of Datta et al. (2007a) for constructing such a filter $S_f(\vec{U},\nu)$. The estimator $\hat{E}$ defined in equation (5.11) can be modified to

$$\hat{E} = A_{\rm NS} \int {\rm d}^2U \int {\rm d}\nu \; V(\vec{U},\nu) \; S_f^\star(\vec{U},\nu) \; n_{\rm B}(\vec{U},\nu). \tag{5.24}$$

Since the noise and the foregrounds are random numbers with zero mean, the expectation value of the estimator can be written as,

$$\left\langle \hat{E} \right\rangle = A_{\rm NS} \int {\rm d}^2U \int {\rm d}\nu \; S(\vec{U},\nu) \; S_f^\star(\vec{U},\nu) \; n_{\rm B}(\vec{U},\nu) \tag{5.25}$$

It can be shown that the noise contribution is given by

$$\begin{aligned} \left\langle (\Delta\hat{E})^2 \right\rangle_{\rm NS} &= \sigma_N^2 A_{\rm NS} \\ &\times \int {\rm d}^2U \int {\rm d}\nu \; |S_f(\vec{U},\nu)|^2 \; n_{\rm B}(\vec{U},\nu), \end{aligned} \tag{5.26}$$

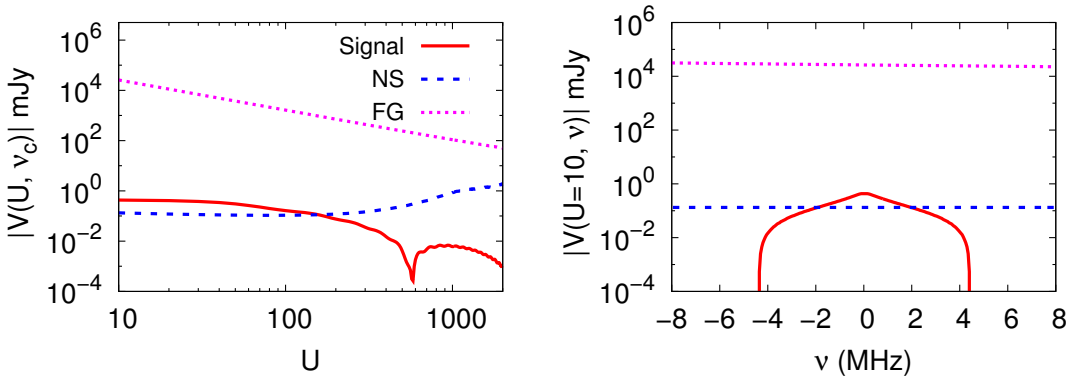

Figure 5.11: Left-hand panel: The amplitude of the signal, the system noise and the foregrounds as a function of the baseline at the central frequency channel. Right-hand panel: The same quantities as a function of frequency difference from the central frequency of the observation at a baseline $U = 10$.

while the contribution from the foregrounds are written as

$$\begin{aligned}\left\langle(\Delta\hat{E})^2\right\rangle_{\rm FG} = A_{\rm NS}^2 \int {\rm d}^2U \int {\rm d}\nu_1 \int {\rm d}\nu_2 \left(\frac{2k_B}{c^2}\right)^2 (\nu_1\nu_2)^2 \\ \times\, n_{\rm B}(\vec{U},\nu_1)\; n_{\rm B}(\vec{U},\nu_2)\; C_{2\pi U}(\nu_1,\nu_2) \\ \times\, S_f^{\star}(\vec{U},\nu_1) S_f(\vec{U},\nu_2).\end{aligned} \tag{5.27}$$

The signal to noise ratio in presence of the foregrounds becomes

$$\mathrm{SNR} = \frac{\left\langle\hat{E}\right\rangle}{\sqrt{\left\langle(\Delta\hat{E})^2\right\rangle_{\rm NS} + \left\langle(\Delta\hat{E})^2\right\rangle_{\rm FG}}} \tag{5.28}$$

The form of the filter S_f is taken to be

$$\begin{aligned}S_f(\vec{U},\nu) = \left(\frac{\nu}{\nu_c}\right)^2 \left[S_T(\vec{U},\nu,B_f) - \frac{\Theta(1-|\nu-\nu_c|/B')}{B'}\right. \\ \left.\times \int_{\nu_c-B'/2}^{\nu_c+B'/2} S_T(\vec{U},\nu',B_f)\; {\rm d}\nu'\right],\end{aligned} \tag{5.29}$$

where $S_T(\vec{U},\nu,B_f)$ is an ideal bandpass filter of width B_f and is given by the

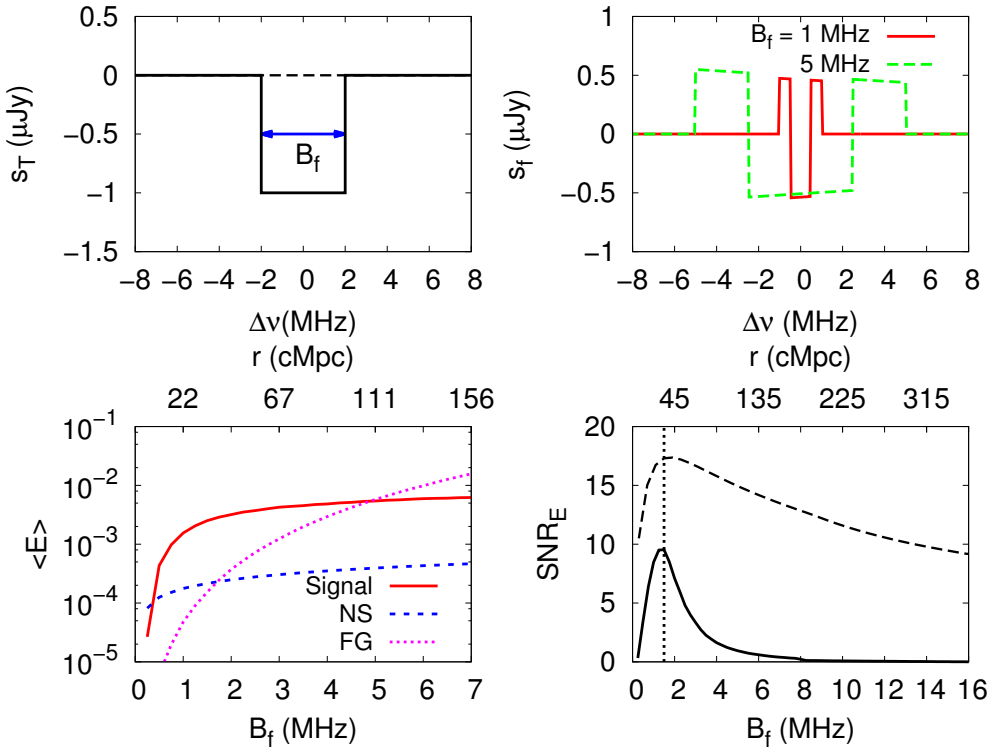

Figure 5.12: Top left: The bandpass filter function $S_T(\vec{U}, \nu, B_f)$ used for defining the filter used in this study (see equation 5.30). Top right: The filter $S_f(\vec{U}, \nu, B_f)$ used in this study (see equation 5.29). Bottom left: The expectation value $\left\langle \hat{E} \right\rangle$ of the estimator of the signal as a function of the parameter B_f. Also shown are the contributions of the system noise and the foregrounds quantified as the rms $\sqrt{\left\langle (\Delta\hat{E})^2 \right\rangle}$. The upper horizontal axis denotes the length scale corresponding to the band width B_f. Bottom right: Signal to noise ratio as a function of the parameter B_f (solid line) in presence of the system noise and the foregrounds. The dashed line represents the foreground free case where the signal is integrated over a frequency bandwidth B_f. The vertical dotted line corresponds to the value of B_f for which the SNR is maximum. The upper horizontal axis denotes the length scale corresponding to the band width B_f.

rectangular function

$$S_T(\vec{U},\nu,B_f) = 0 \text{ if } |\nu-\nu_c| > \frac{B_f}{2}$$
$$= -1 \text{ if } |\nu-\nu_c| \leq \frac{B_f}{2} \quad (5.30)$$

The $(\nu/\nu_c)^2$ term on the right-hand side of equation (5.29) accounts for the frequency dependence of the baseline distribution for a given array. The first term in the brackets on the right-hand side ensures that the signal is integrated only over a frequency bandwidth of B_f (rather than the full bandwidth B_ν of the observations), while the second term subtracts out the frequency-independent component in the range $\nu_c - B'/2$ to $\nu_c + B'/2$. The choice of B' affects the results significantly. After some trial and error we choose $B^{'} = 2B_f$ if $B^{'}$ is less than B_ν, else $B^{'} = B_\nu$. The advantage of the above filter is that it does not require any knowledge about the signal and the foregrounds, except for the fact that the foregrounds are smoother in the frequency. One can, in principle, improve the analysis by incorporating some knowledge of the signal into the filter (using, e.g., the so-called match filter technique), however, the purpose of this analysis is to show that the foregrounds can be dealt with even with simple filtering techniques.

The top left-hand panel of the Figure 5.12 shows the frequency dependence of the bandpass function $S_T(\vec{U},\nu,B_f)$. The top right-hand panel shows the form of the filter $S_f(\vec{U},\nu,B_f)$ for two different values of B_f. The bottom left-hand panel shows the expectation value of the estimator $\left\langle \hat{E} \right\rangle$ as a function of B_f. We also plot the contributions from the noise $\sqrt{\left\langle (\Delta\hat{E})^2 \right\rangle_{\rm NS}}$ and the foregrounds $\sqrt{\left\langle (\Delta\hat{E})^2 \right\rangle_{\rm FG}}$. The signal is calculated using the Mini-QSO model with fiducial parameters as in Figure 5.3. We can see that the filter works quite efficiently in suppressing the foreground contributions for values of B_f which roughly correspond to the size of the 21-cm pattern around the source. The contribution from the 21-cm signal saturates for larger values of B_f while that for the foregrounds keeps on increasing. This suggests that the SNR should have a maximum for a B_f corresponding to the size of the 21-cm pattern. The bottom right-hand panel shows the dependence of SNR on B_f. The maximum SNR is found to be ~ 9, which corresponds to $B_f = 1.5$ MHz and an equivalent length scale of ~ 33 cMpc. This length scale corresponds to the radius of the strongest absorption region as shown in Figure 5.3. For comparison, we also show the SNR calculated when the foregrounds

are not included in the analysis, and the signal is integrated over a bandwidth equal to B_f. Clearly, the SNR is larger than that in presence of foregrounds, and approaches a value ~ 9 when $B_f \to 16$ MHz, consistent with results we obtained earlier.

We thus find that it should be possible to use the smooth frequency dependence of the foregrounds to suppress their contribution below the noise using appropriate filters. We obtain an SNR ~ 9 for our fiducial set of parameters using a simple filter that subtracts out the frequency-independent component. The analysis can be significantly improved by using detailed simulations of the foregrounds (Choudhuri et al. 2014; Gleser et al. 2008; Jelić et al. 2010; Wang et al. 2006) and using more sophisticated subtraction techniques, e.g., (Alonso et al. 2015; Bowman et al. 2009; Gu et al. 2013; Harker et al. 2010). In Chapter 6 we look into the effect of such advanced algorithms on the detectability of the 21-cm signal from the first stars.

5.4 Summary and discussion

The main aim of this chapter is to predict the 21-cm visibility signal for different types of isolated sources at very high redshift and investigate the detectability of these sources using the SKA1-low. The source models we have considered are the PopIII stars, galaxies consisting of PopII stars, mini-quasars and HMXBs. We have used a one-dimensional radiative transfer code to track the time evolution of the ionization fractions of different ionization stage of hydrogen and helium as well as the kinetic temperature of the gas in the IGM.

In general, the 21-cm signal around a source can be divided into four zones: (i) a central H II region where the signal vanishes, (ii) followed by region where the signal is in emission, (iii) a strong absorption region just beyond the emission region, and finally (iv) the signal vanishes at very large distances from the source where the Lyα coupling is not efficient. Depending on the source model under consideration, one or more of these four regions may be non-existent or very small in size.

Our main findings can be summarized as follows:

- The signal from a PopIII star of mass $M_\star \sim 10^3 \mathrm{M}_\odot$ will *not* be detectable

within any reasonable observing time with the SKA1-low. This is because the size of the region where the signal exists is too small, and so is the amplitude of the signal.

- For other source models, i.e., normal galaxies, mini-quasars and HMXBs, the visibility signal is appreciable for small baselines $U \lesssim 100$. This indicates that the detection possibility can be increased by building large number of antenna elements in the core of the baseline design.

- The detectability of the visibility signal is better for a model where the ionization, heating and Lyα coupling is determined by the radiation from the source itself (called model C in this thesis), i.e., there is no significant overlap between the signal patterns of individual sources. The overlap washes out the characteristics of the signal around a source, and in that case standard methods like estimating the power spectrum would be a better way to detect the signal.

- In order to maximize the detection prospects, we integrate the signal around the source over all baselines and a frequency bandwidth of 16 MHz. We find that it is possible to detect the signal around a source at $z = 15$ with an SNR ~ 9 in 1000 hours using the SKA1-low. This number is calculated for a source model where the galaxy contains standard stellar sources with stellar mass $M_\star = 10^7 \mathrm{M}_\odot$ and age $t_{\rm age} = 20$ Myr. The escape fraction of the ionizing photons is $f_{\rm esc} = 0.1$. In addition to stellar sources, the galaxy is assumed to harbour a mini-quasar which produces X-rays with a power-law spectral index $\alpha = 1.5$ and a X-ray fraction $f_X = 0.05$. The surrounding IGM is assumed to have the mean cosmic density $\delta = 0$. The numbers are similar even when the mini-quasar is absent (i.e., no X-ray heating), or the X-ray is contributed mainly by HMXBs (i.e., almost no soft X-rays).

- We also provide scaling relations which can be used for estimating the SNR for any other value of the parameters. We find that the SNR is quite sensitive to the stellar mass and age of the galaxy, as well as the escape fraction of ionizing photons. It is relatively less sensitive to the X-ray properties of the source. There is also a strong redshift dependence arising mainly from the fact that the system noise increases at lower frequencies.

- We have verified our analytical calculations by comparing with the signal calculated using a more realistic simulation box which includes many sources. The visibility calculated from the simulation box is similar to the analytical calculations as long as the overlap between individual patterns is not significant. It is interesting to note that the visibility signal for smaller baselines as a function of frequency shows prominent peaks at channels where the source is present. This can potentially indicate channels around which the signal should be integrated.

- While the galactic and the extragalactic foregrounds are several order higher than the signal we are trying to detect (and the system noise), it is possible to reduce the contribution of these by using suitable filters. We have shown that it is possible to achieve a signal to noise ratio ~ 9 even in the presence of the foregrounds by using filters which subtract out the frequency-independent component of the signal.

It is worth discussing some of the implications and caveats of our findings. For example, we have shown that the detection of the signal requires that the signal patterns of the individual sources do not overlap significantly, in particular, we require the Lyα coupling to become less efficient as we move away from the source. Now, this assumption can be violated in models where the Lyα background is set by a population of small mass $M_{\rm DM} \lesssim 10^8 {\rm M}_\odot$ haloes. In that case one needs to look for signals either in objects with rather small stellar mass or in a scenario where model B is the more appropriate one, both of which lead to smaller SNR. If we assume $f_\star$ to be 10%, then a halo of $M_{\rm DM} \approx 3 \times 10^8 {\rm M}_\odot$ produces an SNR of ~ 5 for model C, which probably is just above the detection threshold. For smaller mass haloes, one may need to implement more sophisticated detection techniques, e.g., stacking of the signal in source position, or a better weighing of the baselines while calculating the estimator.

The analysis in this chapter ignores various challenges which would arise while extracting the cosmological information. The presence of galactic and extragalactic foregrounds would contaminate the weak 21-cm signal from redshifted H I, thus making the extraction a very difficult task. We have assumed in our work that the foregrounds have been subtracted perfectly from the data. Our conclusions need to be verified for the case where there is some residual foreground remains

in the data which can give rise to spurious signals. The same holds true for other systematics, e.g., the calibration of the data against ionospheric instabilities. Given that we now have a good idea about the parameter space which is favourable for a detection with a very high SNR, it will worth exploring in the future these systematic effects on our analysis.

Another possible avenue to extend this work would be the understand how to determine the properties of the source once the signal is detected. This is important as the nature of the first stars still remains one of the most fundamental questions in contemporary cosmology. In this sense, our present work should be taken as a first step outlining the possibility of detecting the signal, which would eventually be followed up by understanding the source properties in detail.

5. 21-CM SIGNATURE OF THE FIRST SOURCES IN THE UNIVERSE: PROSPECTS OF DETECTION WITH SKA

6 | Imaging the first sources during the Cosmic dawn with the SKA

The contents of this chapter are taken from Ghara et al. (2016b).

6.1 Introduction

Detection of the first sources of radiation in the universe which appeared during the cosmic dawn is at the forefront of modern observational astronomy. It is believed that these sources formed within the dark matter haloes sometime around redshifts $z \sim 15 - 20$ (Greif et al. 2010; Pawlik et al. 2011; Wise and Abel 2007; Wise et al. 2012). Observing these first sources will not only reveal their unknown properties but also help us in understanding their influence on the formation and evolution of astrophysical objects during later epochs. In recent times a large number of galaxies have been detected at redshift $z \gtrsim 6$ using the broad-band colour (Bouwens et al. 2015; Ellis et al. 2013) and the narrow-band Lyα emission (e.g., Hu et al. 2010; Kashikawa et al. 2011; Ouchi et al. 2010b). In addition, a significant number of bright quasars have been detected at high redshifts through various surveys (Fan et al. 2006a; Venemans et al. 2015). New space missions in the near future, e.g., the James Webb Space Telescope (JWST)[1], are expected to detect the most faint sources at even higher redshifts.

In addition to the above, 21-cm radiation from the neutral hydrogen (H I) in the intergalactic medium (IGM) can also be used as a probe to detect the very

[1] http://jwst.nasa.gov

early sources. Motivated by this fact, many of the present low-frequency radio telescopes like LOFAR, PAPER, MWA, GMRT etc have dedicated a large amount of their observing resources to detect the signal from the epoch of reionization (EoR). While most of these telescopes are still not able to probe the very early stages of the EoR as they lack the very low-frequency detectors, the future radio telescope like the SKA is expected to detect the signal even from the cosmic dawn. While the first generation telescopes are expected to detect the signal from the EoR statistically (e.g., in terms of the rms, power spectrum, skewness etc), the highly sensitive SKA1-low should be able to image the signal from cosmic H I (Mellema et al. 2015; Wyithe et al. 2015).

Recently, many studies have been done using analytical calculations (e.g., Furlanetto et al. 2004a; Paranjape and Choudhury 2014), semi-numerical simulations (Choudhury et al. 2009; Ghara et al. 2015a,b; Mesinger and Furlanetto 2007; Santos et al. 2008; Thomas et al. 2009; Zahn et al. 2007), and full numerical simulations involving radiative transfer (Baek et al. 2009; Iliev et al. 2006; McQuinn et al. 2007b; Mellema et al. 2006; Shin et al. 2008) to understand the behaviour of the redshifted 21-cm signal from the cosmic dawn and EoR for different source models. Though most of these studies have concentrated in detecting the signal using statistical quantities, it will be interesting to study the detectability using imaging techniques. Some recent attempts have been made to understand the detection possibility of large ionized bubbles with LOFAR, MWA, GMRT (Datta et al. 2007a, 2009, 2012a, 2008, 2012b; Geil and Wyithe 2008; Majumdar et al. 2011). In addition, Zaroubi et al. (2012) show that the redshifted 21-cm signal from the EoR can be detected in low-resolution images with LOFAR. Studies have also been done in the same context to detect the signal in post-reionization epochs with SKA1 (Villaescusa-Navarro et al. 2014). Chapter 5 of the thesis investigated the detectability of very early sources like metal-free Population III (PopIII) stars, galaxies containing Population II (PopII) stars, mini-QSOs and high-mass X-ray binaries (HMXBs) in the presence of system noise and astrophysical foregrounds using a visibility based techniques. The study showed that the SKA1-low should be able to detect the signal from the sources like the PopII stars, mini-QSOs and HMXBs with $\sim 9-\sigma$ confidence by integrating the visibilities signal over all baselines and frequency channels within $\sim$ 1000 hours of observation time.

Once the signal from the cosmic dawn is detected, the challenge would be to interpret it and understand the properties of the first sources and the surrounding IGM. One probably needs to use some sophisticated parameter estimation method like the Markov chain Monte Carlo (MCMC) to extract the relevant information. However, before getting involved in the complexities of the parameter estimation methods, one needs to set up appropriate observational strategies to detect the signal. Detection of the signal from the cosmic dawn is itself very challenging as it is very weak compared to the system noise and the astrophysical foregrounds. In general, one has to integrate the signal over a large observing time to reduce the noise and also use some efficient foreground subtraction method to recover the signal given that the foregrounds are 4-5 orders of magnitude stronger. In this chapter, we explore, in detail, the detection of the early sources during the cosmic dawn in H I 21-cm images in the presence of system noise and the foregrounds. Our analysis is based on realistic simulations of the signal, system noise, and the relevant astrophysical foregrounds, followed by predictions related to the detectability of the early sources using the SKA1-low. These predictions would be quite useful to plan for observational strategies for detecting the sources in 21-cm observations.

The chapter is organized in the following way. In Section 6.2, we describe the simulations used in this work. In particular, we describe the model for the sources used in this chapter in Section 6.2.1, while simulating the baseline distribution of the SKA1-low is described in Section 6.2.2. The methods to simulate the signal maps, system noise maps and foregrounds maps are described in Section 6.2.3, 6.2.4 and 6.2.5 respectively. The main results of the chapter are given in Section 6.3 before we conclude in Section 6.5. We choose the Cosmological parameters $\Omega_m = 0.32$, $\Omega_\Lambda = 0.68$, $\Omega_B = 0.049$, $h = 0.67$, $n_\mathrm{s} = 0.96$, and $\sigma_8 = 0.83$, which are consistent with the recent *Planck* mission results (Planck Collaboration et al. 2014a).

6.2 Simulation

The study of detectability of the first sources would require careful modelling of these sources, as well as that of the system noise and the astrophysical foregrounds. We discuss the methods for simulating each of these components in this

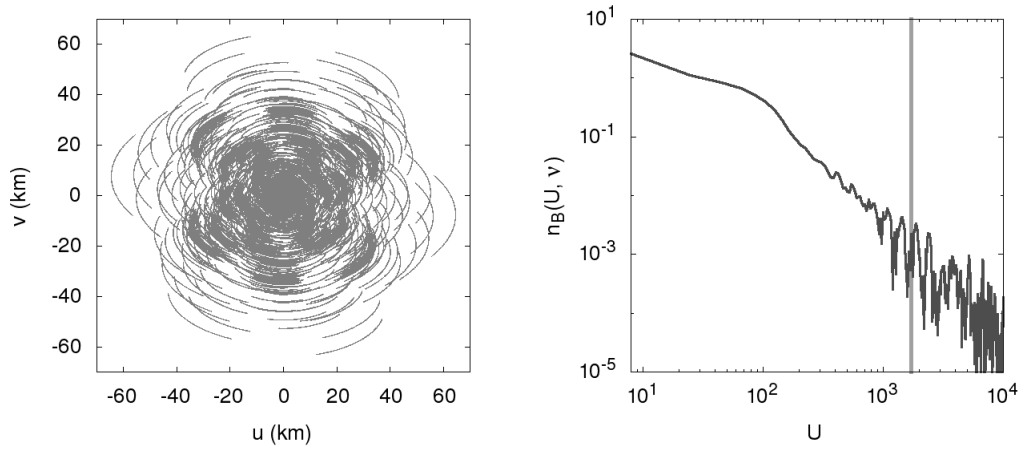

Figure 6.1: Left-hand panel: The baseline coverage of the SKA1-low for 4 h of observation at a declination $\delta_{\rm dec} = -30°$. The integration time taken in this study is 10 sec. Right-hand panel: The circularly averaged baseline distribution for the SKA1-low at frequency 90 MHz as a function of baseline U. The quantity $n_{\rm B}(U, \nu)$ denotes the number density of antenna pairs having baseline U at frequency ν. The vertical line in the right-hand panel represents the baseline corresponding to an angular resolution of $2^{'}$.

section.

6.2.1 Radiating sources

The physical conditions of the universe when the first sources formed are relatively poorly understood, and hence the properties of these sources are difficult to model. In this chapter, we consider different types of sources that could have existed in the early universe, i.e., the PopII stars in the primordial galaxies (O'Shea et al. 2015; Wise et al. 2014; Xu et al. 2016), the mini-QSOs (Alvarez et al. 2009; Bromm and Loeb 2003; Chuzhoy et al. 2006b; Tanaka et al. 2012; Thomas and Zaroubi 2008; Zaroubi et al. 2007) and the HMXBs (Fialkov et al. 2014; Kaaret 2014; Knevitt et al. 2014; Mirabel et al. 2011; Stacy et al. 2010). Besides these, the metal free PopIII stars are believed to be the another common source during the cosmic dawn. It is however expected that the individual PopIII stars may not be detected in the observations of the redshifted 21-cm signal even with advanced

telescopes like the SKA1-low because of the very small region of influence (see Chapter 5). Thus we have not considered them in this chapter. While we consider the PopII stars combined with the mini-QSOs in galaxies as our fiducial model source, we will briefly discuss the detectability of other sources too. The main properties of the sources used in this chapter and the details of their spectral energy distribution (SED) are given in Chapter 5. Here, we assume that our fiducial source model has stellar mass $M_\star = 10^7$ $M_\odot$, age $t_{\rm age} = 20$ Myr. We choose the escape fraction $f_{\rm esc} = 0.1$, spectral index $\alpha = 1.5$ (Laor et al. 1997; Vanden Berk et al. 2001; Vignali et al. 2003) and the ratio of the X-ray to UV luminosity $f_X = 0.05$ as the fiducial values.[1]

6.2.2 Baseline distribution of the SKA1-low

An important component for simulating radio maps similar to those ones would obtain in observations is the baseline distribution of the telescope. The only telescope considered in this work is the SKA1-low which holds the promise of imaging the high-redshift cosmological signal. As per the presently available design, the SKA1-low has a compact core of radius 350 m with closely packed 40 super-stations distributed in four concentric rings, while six closely packed antenna form a super-station. Rest of the 54 super-stations are distributed in a three-arm spiral from 350 m to 35 km radius, where the super-station density distribution follow a logarithmic relation[2]. The total number of antenna for the SKA1-low is $N_{\rm ant} = 564$. Table 6.1 shows the parameters related to the model-observation used in this study. The left-hand panel of Figure 6.1 shows the baseline uv coverage for 4 h of observation towards a region with declination $\delta_{\rm dec} = -30^\circ$ with the SKA1-low . The right-hand panel of Figure 6.1 shows the circularly averaged baseline distribution of the SKA1-low at frequency 90

[1]The fiducial stellar mass of the source corresponds to stellar content in a dark matter halo of mass $\sim 6\times10^8$ $M_\odot$ assuming $f_\star = 0.1$ where $f_\star$ is the fraction of baryons converted into stars. We set the fiducial value of the parameter as $f_X = 0.05$. This corresponds to an accreting BH to galaxy mass ratio of $\sim 10^{-3}$ which is consistent with observations e.g., Rix et al. 2004. The lifetime of the early sources is very uncertain, though the sources are expected to be short-lived (Meynet and Maeder 2005). Here we set the fiducial age to be $t_{\rm age} = 20$ Myr.

[2]The antennae positions for the SKA1-low is taken from http://astronomers.skatelescope.org/wp-content/uploads/2015/11/SKA1-Low-Configuration_V4a.pdf

MHz. The quantity plotted $n_{\rm B}(U,\nu)$ denotes the number density of antenna pairs having baseline U at frequency ν, and is normalized such that $\int n_{\rm B}(U,\nu)\ d^2U = N_{\rm ant} \times (N_{\rm ant}-1)/2$ is the total number of baselines for the SKA1-low. One can easily notice that the baseline distribution is more concentrated at low-baseline regions. Note that we have not actually used this circularly averaged baseline distribution in this study, rather we use the true baseline distribution as obtained from the antenna positions. The minimum and maximum baseline for the SKA1-low at redshift 15 turn out to be ~ 8.5 and ~ 19500 respectively.

The primary field of view (FOV), which depends on the diameter of the individual antenna and observing frequency, is $\sim 5.5^\circ$ for the SKA1-low at redshift $z = 15$. However, the maximum angular size ($\theta_{\rm ext}$) of the image which can be made depends on the minimum baseline considered for the analysis. For example, if the minimum baseline $U_{\rm min} \sim 8.5$, then the maximum angular extent $\theta_{\rm ext}$ will be 6.7° (which corresponds to a length scale of 1230 comoving Mpc at redshift 15). On the other hand, the angular resolution ($\Delta\theta$) of the image depends on the longest baseline considered for the analysis. For example, the SKA1-low should be able to produce images with highest resolution $0.175'$as its longest baseline is around $U_{\rm max} \sim 19500$ at redshift 15. However, the system noise will be much stronger compared to H I 21-cm signal if the image is made at this resolution. We, therefore, make images at coarser $2^{'}$ resolution in order to keep the noise contribution under control. In order to achieve the default images with $2^{'}$ resolution, we consider baselines only up to $U \sim 1720$ and discard larger baselines. We note that only a negligible fraction of the total baselines would be discarded in this process as most of the antennae for the SKA1-low are packed at the central region (see right-hand panel of Figure 6.1). Depending on the values of $\theta_{\rm ext}$ and $\Delta\theta$, we generate the signal, noise and foreground maps in a $N_{\rm pixel} \times N_{\rm pixel}$ grid, where $N_{\rm pixel} = \theta_{\rm ext}/\Delta\theta$. For example, for $\theta_{\rm ext} = 6.7$ degree and $\Delta\theta = 2'$ we obtain $N_{\rm pixel} = 200$.

6.2.3 Signal maps

Let us assume that there is an isolated source radiating photons in the neutral and cold IGM. Our first aim is to study the detectability of the 21-cm pattern around such a source. We later study a more complex and realistic model where

Parameters	Values
Redshift (z)	15
Central frequency (ν_c)	88.75 MHz
Band width (B_ν)	16 MHz
Frequency resolution ($\Delta\nu_c$)	100 kHz
Observational time ($t_{\rm obs}$)	2000 h
System temperature ($T_{\rm sys}$)	$60 \times (300\ {\rm MHz}/\nu_{\rm c})^{2.55}$ K
Number of antennae ($N_{\rm ant}$)	564
Effective collecting area ($A_{\rm eff}$)	962 m^2

Table 6.1: The parameters used in this chapter for a model-observation at redshift z with the SKA1-low.

multiple sources form within a cosmological volume. The main steps to simulate the H I signal maps around an isolated source are as follows:

- For a given source model, we generate one-dimensional $\delta T_{\rm b}$ profile around each source. The details of the method is described in Section 2.6 of Chapter 2 and Section 5.2.2 of Chapter 5.

- We use the one-dimensional $\delta T_{\rm b}$ profile to generate the spherically symmetric $\delta T_{\rm b}$ map in the simulation box. The comoving length and grid resolution of the simulation box in the angular directions are determined by $\theta_{\rm ext}$ and $\Delta\theta$ respectively. The same two quantities along the line of sight are determined by the frequency band width (B_ν) and frequency resolution ($\Delta\nu_c$) of the observation.

- We generate the two-dimensional baseline distribution (or uv coverage) $n_{\rm B}^{i,j}$ in a $N_{\rm pixel} \times N_{\rm pixel}$ grid for $t_{\rm obs}^{uv} = 4$ h of observation at a region with declination $\delta_{\rm dec} = -30^\circ$, while the integration time is taken as Δt_c =10 sec. To incorporate the effect of the empty pixels in the two-dimensional baseline distribution, we first obtain the visibilities of the signal at each uv grid point and then multiply the signal with the baseline (uv) sampling function, i.e., zero at uv grids which are empty and unity otherwise. We then obtain

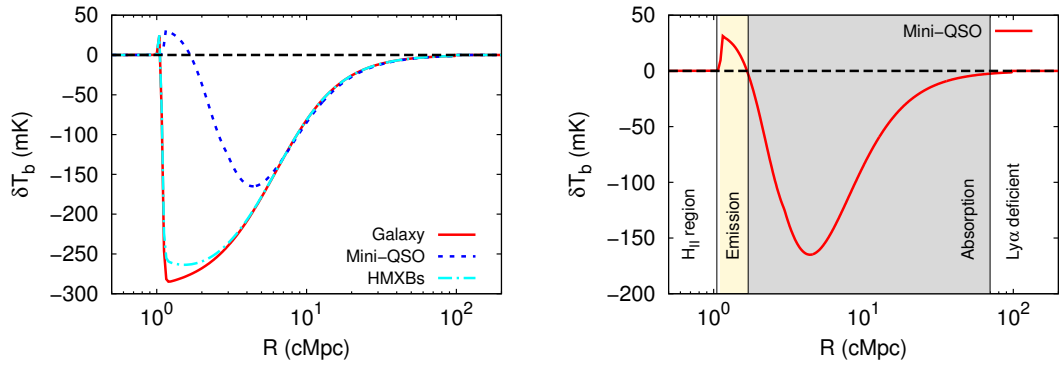

Figure 6.2: Left-hand Panel: The radial $\delta T_{\rm b}$ pattern as a function of the distance R from the centre of the model source for different source models. The stellar mass of the source is 10^7 $M_\odot$ for the three models. The ratio of X-ray to UV luminosity of the mini-QSO and HMXB models is 0.05, while the power law spectral index of the mini-QSO model is 1.5. Right-hand panel: Four different regions around the fiducial mini-QSO source model.

the final image (which is usually known as "dirty" image) of the signal by performing a two-dimensional inverse Fourier transform of the visibilities. We note that the H I signal in the "dirty" image is hardly distinguishable from the input H I signal. This is due to the fact that *uv* space is nearly filled and there are not many empty *uv* grids at small baselines where the H I signal is strong.

The left-hand panel of Figure 6.2 shows the $\delta T_{\rm b}$ distribution around the three types of sources considered in this work. One can easily identify that there exist four separate regions radially outward from the centre of the source (see the right-hand panel of Figure 6.2). These are (1) H II *region*: the signal is zero at the medium just adjacent the source as $x_{\rm HI} \sim 0$. (2) *emission region*: the H II region is followed by an emission region where $T_{\rm S} > T_\gamma$. (3) *absorption region*: the emission region is followed by a strong absorption region where $T_{\rm S} < T_\gamma$ and (4) Lyα *deficient region*: the signal vanishes at far away region as Lyα coupling is not strong enough and thus $T_{\rm S} = T_\gamma$. The lengths of different regions depend on the source properties. The strength, as well as the volume of the absorption signal, is much larger than the emission signal for the sources we consider. For

example, the minimum $\delta T_{\rm b}$ for the fiducial mini-QSO model is ~ -160 mK, which is much larger compared to the maximum $\delta T_{\rm b} \sim 30$ mK. Thus, one can expect that this region will be the easiest to be detected in radio images, while it may be difficult to identify the H II and emission regions because of the contamination of the weak signal by the system noise and foregrounds. One can also notice that the strength of the absorption signal is larger in the case of the models Galaxy and HMXB compared to the mini-QSO. In other words, one may expect higher detectability for the Galaxy and HMXB source models than the mini-QSO, assuming the sources to be isolated. This will be discussed in more detail in the later part of the chapter.

The one-dimensional $\delta T_{\rm b}$ profile around the fiducial mini-QSO source model is shown in the left-hand panel of Figure 6.3. The sky specific intensity can be related to $\delta T_{\rm b}$ as

$$I_\nu(\vec{\theta}) = \frac{2k_B\nu^2}{c^2}\delta T_{\rm b}(\vec{\theta},\nu), \tag{6.1}$$

where k_B is Boltzmann constant and c is the speed of light. The flux per synthesized beam can be obtained by,

$$S_\nu = I_\nu(\vec{\theta}) \times \Delta\Omega, \tag{6.2}$$

where $\Delta\Omega = (\Delta\theta)^2$ is the beam solid angle. The quantity S_ν thus gives the total flux within a single beam. The middle panel of Figure 6.3 shows S_ν distribution along the angular directions for our fiducial source for an angular resolution (or beam) $2'$ at the central frequency channel (which contains the centre of the source in this case). Although the angular extents of our original image are $6.7^\circ \times 6.7^\circ$, we show only a smaller $3.4^\circ \times 3.4^\circ$ image. The maximum amplitude of the signal S_ν in the map is ~ -13 μJy, with the negative sign signifying that the signal is in absorption.

6.2.4 Noise maps

The system noise $N(\vec{U},\nu)$ at different baselines and frequency channels are uncorrelated and expected to be Gaussian random variables with zero mean. The rms noise for each baseline and frequency channel of width $\Delta\nu_c$ and correlator

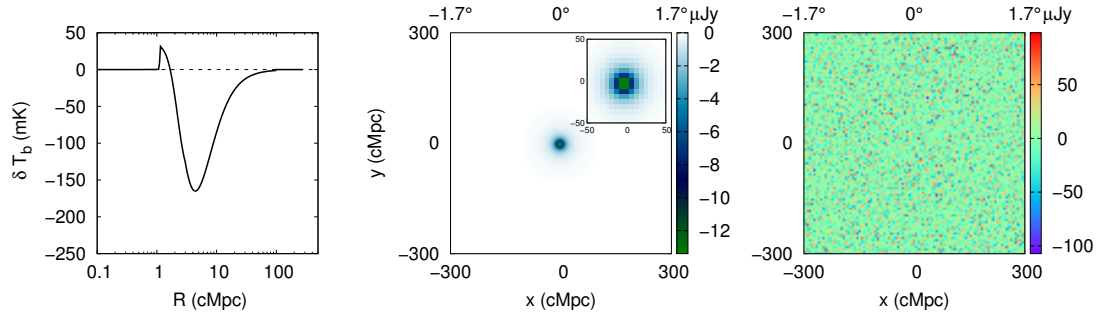

Figure 6.3: Left-hand panel: The $\delta T_{\rm b}$ profile of the fiducial source ($M_\star$= 10^7 $M_\odot$, $\delta = 0$, $\alpha = 1.5$, $f_X = 0.05$, $t_{\rm age} = 20$ Myr) as a function of the radial distance from the centre of the source at redshift 15. Middle panel: $3.4° \times 3.4°$ image of the signal (without noise) at the frequency channel that contains the centre of the source at redshift 15 for an angular resolution of $2'$. The inner panel represents the zoomed version of the same image. All the color palettes represent μJy per beam. Right-hand panel: The corresponding noise maps at the central frequency channel. The noise map corresponds to a frequency resolution of 100 kHz and 2000 h of observation time.

integration time Δt_c is given by (for single polarization),

$$\sqrt{\langle N^2 \rangle} = \frac{\sqrt{2} k_B T_{\rm sys}}{A_{\rm eff} \sqrt{\Delta \nu_c \ \Delta t_c}}, \tag{6.3}$$

where $A_{\rm eff}$ is the effective collecting area of each antenna and $T_{\rm sys}$ is the system temperature. Here we have chosen $\Delta t_c = 10$ sec. The steps to generate the noise maps are given below:

- First, we generate Gaussian random noise (both the real and imaginary parts) with zero mean and rms $\sqrt{\langle N^2 \rangle}$ in the $N_{\rm pixel} \times N_{\rm pixel}$ grid in the Fourier space.
- The presence of multiple baselines in a uv grid point can be used to decrease the noise in that pixel. We account for this by simply scaling the noise in (i, j)th pixel by a factor $1/\sqrt{n_{\rm B}^{i,j}}$.[1]

[1]In principle, the baseline distribution is dependent on the frequency of interest and thus, should be different for different frequency channels. In this study, we have ignored this fact and worked with only one baseline distribution which corresponds to the central frequency of the observation.

- By averaging over long observation time $t_{\rm obs}$, one can decrease the noise further by a factor of $\sqrt{t_{\rm obs}/t^{uv}_{\rm obs}}$, which is done in this work as well.
- As mentioned earlier, the presence of empty pixels in the two-dimensional baseline distribution is accounted for by including a mask which is zero at the empty pixels and unity otherwise.
- We obtain the real space noise map by doing two-dimensional inverse Fourier transform of the reduced noise in Fourier space at each frequency channel.

The right-hand panel of Figure 6.3 shows the simulated noise map at the central frequency channel for an angular resolution $2'$ for 2000 h of observation time and the parameters listed in Table 6.1. The rms noise per beam of the corresponding map is $\sim$ 19 μJy. The amplitude of the signal as shown in the middle panel of Figure 6.3 is significantly smaller the rms noise for 2000 h of observation, thus the signal is not detectable without further reducing the noise using some other techniques like "smoothing", which we will discuss later part of the chapter (in Section 6.3.1.2).

6.2.5 Foreground maps

The cosmological signal will be contaminated by other astrophysical foregrounds which have significantly larger amplitude (Ali et al. 2008; Ghosh et al. 2012). In this study, we consider the Galactic synchrotron radiation and emission from unresolved extragalactic point sources as the major contributors to these foregrounds. Among these two, the Galactic synchrotron radiation contributes $\sim$ 70% of the total foregrounds (Jelić et al. 2008; Wang et al. 2006). In addition to these, the Galactic free-free emission, supernova remnants, and extragalactic radio clusters may also provide a small contribution to the total foreground, which has been neglected in this study. The method of simulating the foregrounds is given below:

- *Galactic synchrotron radiation:* We have mainly followed Choudhuri et al. (2014) for simulating the Galactic synchrotron radiation. The fluctuations in the foregrounds are assumed to be Gaussian random fields with an angular power spectrum $C^{\rm syn}_{2\pi U}(\nu)$ that can be expressed as (see, e.g., Ghosh

et al. 2012),

$$C_l^{\rm syn}(\nu) = A_{150} \left(\frac{1000}{l}\right)^{\bar{\beta}} \left(\frac{\nu}{\nu_\star}\right)^{-2\bar{\alpha}_{\rm syn} - 2\Delta\bar{\alpha}_{\rm syn}\log(\frac{\nu}{\nu_\star})}, \tag{6.4}$$

where $\nu_\star = 150$ MHz, $A_{150} = 513$ mK^2, $\bar{\beta} = 2.34$, $\bar{\alpha}_{\rm syn} = 2.8$ and $\Delta\bar{\alpha}_{\rm syn} = 0.1$. The parameters for the Galactic synchrotron emission have been taken from Platania et al. (1998); Wang et al. (2006).

Given the angular power spectrum, we first generate the maps of the temperature fluctuations for the foregrounds in the Fourier space using the relation

$$\Delta T_{\rm syn}(U,\nu) = \sqrt{\frac{\Omega C_l^{\rm syn}(\nu)}{2}}\,[x(U) + iy(U)]\,, \tag{6.5}$$

where $l = 2\pi U$ and Ω is the total solid angle of the simulated area. The quantities $x(U)$ and $y(U)$ are two independent Gaussian random variables with zero mean and unit variance. We then carry out a two-dimensional inverse Fourier transform on the $\Delta T_{\rm syn}(U,\nu)$ distribution to obtain the real space distribution $\delta T_{\rm syn}(\vec{\theta},\nu)$ at each frequency channel. The specific intensity fluctuation can be simply obtained as $\delta I_{\rm syn}(\vec{\theta},\nu) = (2k_B/\lambda^2)\delta T_{\rm syn}(\vec{\theta},\nu)$. We multiply this with the beam solid angle to obtain the flux per synthesized beam for the Galactic synchrotron radiation maps.

- *Extragalactic point sources:* The method used to simulate the foregrounds from the extragalactic point sources is based on the observations of Ghosh et al. (2012) with GMRT at frequency $\nu_\star = 150$ MHz.[1] The differential source count is given by

$$\frac{dN}{dS} = \frac{10^{3.75}}{\rm Jy.Sr}\left(\frac{S}{\rm Jy}\right)^{-1.6}. \tag{6.6}$$

We assume that the point sources with flux larger than 5σ can be identified and removed from the pixel. In this work, we generate the map for

[1]The foreground contribution from the unresolved extragalactic point sources can be divided into two parts, (*i*) the Poisson contribution and (*ii*) the clustering contribution. The point source clustering part dominates over the Poisson part at large angular scales (Di Matteo et al. 2002). However, the diffuse synchrotron emission from our galaxy is expected to be much stronger than the point source clustering contribution at these large scales (Datta et al. 2007a; Di Matteo et al. 2002; Santos et al. 2005). We, therefore, do not consider the foreground contribution from the clustering part in this study.

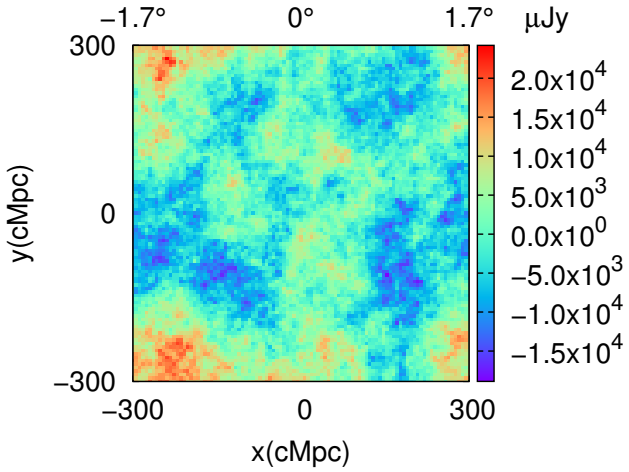

Figure 6.4: The foreground map at the central frequency channel $\nu_c = 88.75$ MHz. The angular resolution of the map is $2'$. The map includes the contributions from the Galactic synchrotron radiation and extragalactic radio emission from the unresolved point sources.

the unresolved extragalactic point sources within a flux range 10^{-4} to 0.1 mJy, while we assume that all source above $5\sigma \sim 0.1$ mJy will be resolved and removed. First, we divide the flux range into multiple flux bins and calculate the number of sources associated with each flux bins. We randomly distribute the sources in the two-dimensional map along the angular directions at the central frequency channel. The maps at other frequency channels are generated assuming the flux of the sources changes with frequency as,

$$S_\nu = S_{\nu_\star} \left(\frac{\nu}{\nu_\star}\right)^{-\alpha_{\rm ps}}, \tag{6.7}$$

where $\alpha_{\rm ps}$ is the spectral index of the foregrounds contribution from the point sources. We generate the index $\alpha_{\rm ps}$ for each point source from a uniform random distribution with values in the range of 0.7 to 0.8.

Figure 6.4 shows the $2'$ resolution map for the total foreground signal at the central frequency channel with the two-dimensional mean is subtracted out. The strength of the foreground signal is $\sim 3-4$ order of magnitude stronger than the

expected signal at this resolution as can be seen by comparing with Figure 6.3. Thus, it is obvious that the recovery of the signal in the presence of such a strong foregrounds is indeed a challenging task. We will discuss various techniques to subtract the foregrounds below the signal level at the later part of the chapter.

6.3 Results

In order to estimate the detectability of the first sources through imaging the high-redshift 21-cm signal, we choose our fiducial source model to be the mini-QSO. We first study in great detail the simplistic situation where there is a single isolated source in the FOV, and then consider a more realistic situation where there are multiple sources in the field.

6.3.1 Isolated source

We assume that the isolated source is completely isolated and situated at the centre of the FOV. The fiducial parameters of the mini-QSO model, as mentioned earlier, are taken to be $M_\star = 10^7$ $\mathrm{M}_\odot$, $f_{\rm esc} = 0.1$, $f_X = 0.05$, α =1.5 and age $t_{\rm age} = 20$ Myr. We assume the IGM density contrast $\delta = 0$. We choose the fiducial angular resolution for imaging as $2'$. The spatial length scale corresponding to this resolution is ~ 6 cMpc, which is similar to the radial distance to the strongest absorption signal around the fiducial source.

6.3.1.1 Signal and the system noise

First, let us consider a scenario where we can ignore the complexities arising from the foregrounds. Even in this simple case where we deal only with the signal and the system noise, we find that the noise is much larger than the cosmological signal as shown earlier in Figure 6.3.

One method of increasing the SNR is by smoothing the maps using some filter. We have seen in Chapter 5 that the signal exceeds the system noise only for baselines $U \lesssim 100$, which corresponds to angular scales $\gtrsim 10'$. In order to see similar effects in the image, we have used Gaussian filters of different widths (i.e., standard deviations) for smoothing the images at all the frequency channels. The effect of smoothing on the image maps is shown in Figure 6.5. The three panels

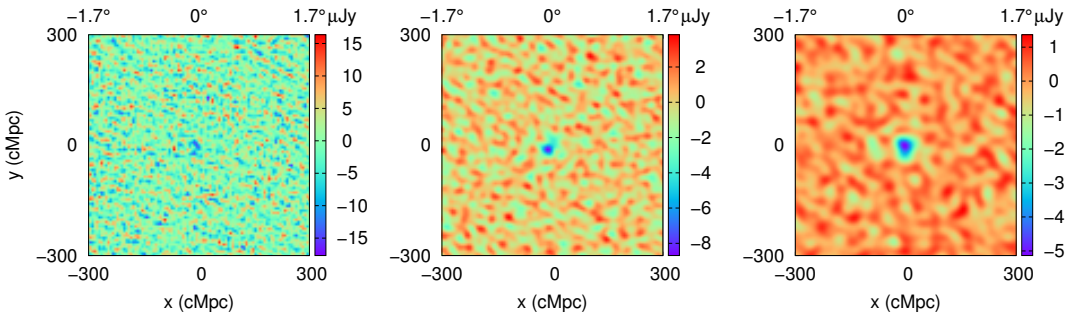

Figure 6.5: Left-hand to right-hand panels show the images smoothed with a Gaussian kernel of size $10'$, $20'$ and $30'$ respectively. The images contain the signal from the radiating source as well as the system noise. Our fiducial source parameters are $M_\star = 10^7$ $M_\odot$, $\alpha = 1.5$, $f_X = 0.05$, $t_{\rm age} = 20$ Myr at redshift 15. We have taken 100 kHz frequency resolution and 2000 h of observation time.

from the left-hand side show the effect of using a Gaussian smoothing kernel of width $10'$, $20'$ and $30'$ respectively. One can clearly see that the 21-cm pattern of the source becomes more prominent as we increase the width of the kernel. This is related to the fact that the noise amplitude decreases because of smoothing. For example, the rms noise of the map without smoothing (right-hand panel of Figure 6.3) is $\sim$19 μJy for 2000 h of observation and 100 kHz of frequency resolution, while the rms noise reduces to ~ 0.4 μJy for smoothing with the fiducial Gaussian filter of size $30'$ (right-hand panel of Figure 6.3).[1]

We define the SNR of the maps as the ratio of the largest absolute amplitude of the observed pixel (signal + noise in this case) in the image plane and the rms noise. We average over 10 independent realizations of the noise while calculating the SNR. The SNRs in the left-hand to right-hand panels of Figure 6.5 are 4, 7.5 and 11 respectively, while the corresponding rms noise are 4.4, 1.1 and 0.4 μJy respectively. It is clear that the SNR increases with the width of the Gaussian filter. Thus, it is possible to detect the signal by smoothing the maps with sufficiently wide filters like $30'$ within 400 (150) hours of observation with an SNR ~ 5 (~ 3).

[1] $30'$ corresponds to a spatial scale of $\sim$ 90 cMpc, which is typical size of the 21-cm region around the source after 20 Myr.

We use the Pearson-cross-correlation to quantify the similarity between two maps. For two maps having amplitudes x_i and y_i at the ith pixel, the Pearson-cross-correlation coefficient is defined as

$$\chi = \frac{\sum_i (x_i - \bar{x})(y_i - \bar{y})}{\sqrt{\sum_i (x_i - \bar{x})^2}\sqrt{\sum_i (y_i - \bar{y})^2}}, \tag{6.8}$$

where $\bar{x}$ and $\bar{y}$ are the mean of the maps x_i and y_i respectively. The value of χ for the 21-cm map around the isolated fiducial source smoothed by a Gaussian kernel of width $30'$ and a similar smoothed map which included the system noise is 0.56. The value of χ is relatively smaller in these case as the signal from the source is localized in the central part of the map, while most part of the image in the second case is dominated by the noise.

We have seen that the detectability of the signal from the fiducial source improves significantly when we smooth the image over some scale. However, this same smoothing can change the original profile of the $\delta T_{\rm b}$ distribution around the fiducial source. This may create additional difficulties in extracting the properties of the source from these maps. Thus, we must check whether these smoothed profiles can even be used for parameter estimation. The panels (a) - (h) in Figure 6.6 show the true $\delta T_{\rm b}$ profiles (solid lines) and the smoothed ones with a Gaussian filter of size $30'$(dashed lines) for different source parameters. In each of these panels, we keep all the parameters except one fixed to their fiducial values. One can easily notice that the smoothed profiles are quite sensitive to parameters like the stellar mass $M_\star$, over-density $(1 + \delta)$ and the UV escape fraction $f_{\rm esc}$, while the profiles are almost unaffected while changing the X-ray parameters f_X, α and the age of the source $t_{\rm age}$. We can thus infer that it should be possible to infer the values of the $M_\star, \delta$ and $f_{\rm esc}$ from the smoothed images, while other parameters may remain undetermined. The panel (g) in Figure 6.6 shows the smoothed $\delta T_{\rm b}$ profiles for different source models. It is interesting to note that the profiles look almost the same, thus implying that it would not be straightforward to infer the precise source model from the smoothed image maps. The panel (h) of Figure 6.6 shows the smoothed $\delta T_{\rm b}$ profile of the fiducial source for the Gaussian filters of width $10'$, $20'$ and $30'$. The error bars in the panel show the $1-\sigma$ error due to the system noise for 2000 h of observation and 100 kHz of frequency resolution when the filter width is taken to be $30'$. The errors have been obtained by averaging over pixels lying in circular annulus around the centre of the source. The system noise,

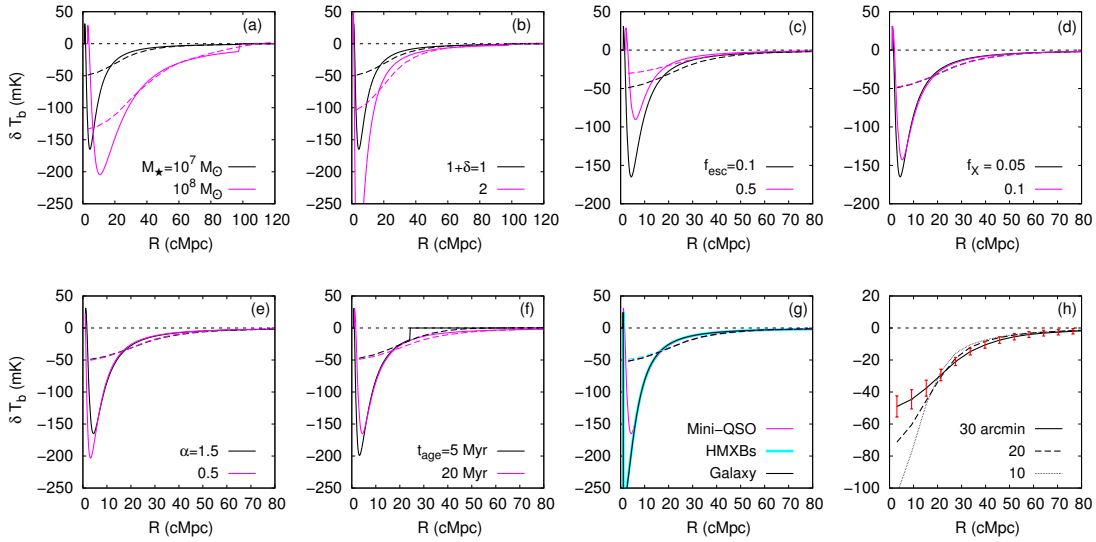

Figure 6.6: The radial brightness temperature profiles around an isolated source at $z = 15$. The panels (a) to (f) show the dependence of the profiles on the model parameters, namely, the stellar mass $M_\star$, the overdensity of the surrounding IGM $(1 + \delta)$, the UV escape fraction $f_{\rm esc}$, the ratio of X-ray to UV luminosity f_X, the X-ray spectral index α and the age of the source $t_{\rm age}$ respectively. The solid curves are for the case without any smoothing, while the corresponding dashed curves represent the corresponding smoothed $\delta T_{\rm b}$ profile, where the smoothing is done with a Gaussian filter of width $30'$. While varying one parameter, we have fixed the other parameters to their fiducial values for generating the $\delta T_{\rm b}$ profiles. Panel (g) shows the intrinsic and the smoothed $\delta T_{\rm b}$ profiles for the three different types of source models considered in this chapter. Panel (h) shows the smoothed $\delta T_{\rm b}$ profiles around the fiducial source for three different widths of Gaussian kernel, namely $30'$, $20'$ and $10'$. The error bars represent the 1σ rms of the system noise corresponding to a frequency resolution 100 kHz, 2000 h of observation time and $30'$ Gaussian filter.

when averaged circularly in a single slice, should drop like $R^{1/2}$ in a scenario when the noise in adjacent pixels in the image are uncorrelated. However, smoothing makes the noise at different pixels correlated and therefore a simple drop of the error like $R^{1/2}$ is not applicable in this case. We calculate the true error bars by making independent realizations of the noise map and smoothing it using the Gaussian filter. We then bin the image in the radial direction around the centre of the source and calculate the circularly averaged noise at each bin for each realization. The variation of this quantity across realizations gives the required rms. The error bars in panel (h) of Figure 6.6 represent the rms calculated using this method. By comparing with the panels (a) - (g), we find that the change in the profiles when we change the values of $M_\star, \delta$ and $f_{\rm esc}$ is larger than the sizes of the error bars. Thus one expects that a reasonably advanced parameter estimation method (e.g., MCMC) using the smoothed $\delta T_{\rm b}$ profile can put strong constraints on the three parameters $M_\star$, $(1 + \delta)$ and $f_{\rm esc}$, whereas the X-ray parameters and $t_{\rm age}$ may not be strongly constrained.

Now let us discuss the detectability of other source models in this foreground-free scenario. The SNRs for the Galaxy and HMXB source models for the fiducial parameter values are 11.3 and 11.2 respectively for the smoothed maps. Although the absorption signal in the expected $\delta T_{\rm b}$ profiles in Figure 6.2 is stronger for the Galaxy and HMXB source models compared to the mini-QSO, all the profiles look almost similar after smoothing which leads to similar SNRs (see panel (g) of Figure 6.6). The SNR is also quite sensitive to the redshift of observation. For example, if the source formation starts at a lower redshift, say, $z = 10$, the SNR of the fiducial mini-QSO model increases from $\sim$11 to $\sim$ 46 because of the decrease in the system noise. The SNRs for different values of the parameters are listed in Table 6.2.

Till now we have been considering the scenario where there is only one source in the FOV and the $\delta T_{\rm b}$ profile is calculated using the method given in Section 6.2.3. Since a small amount of Lyα radiation is sufficient to couple $T_{\rm S}$ to $T_{\rm K}$, it is possible that the IGM may rapidly attain a state where the Lyα coupling is very strong in every part of the IGM. This can arise, e.g., from the significant overlap between the individual Lyα bubbles of the very early sources. In such a scenario, we will have $T_{\rm S} = T_{\rm K}$ at all points in the IGM which we call the "Lyα coupled scenario" (same as model B in Chapter 5). In this case, a large fraction

Source	$M_\star$	$1+\delta$	$f_{\rm esc}$	$1+z$	Filter	SNR1	SNR2
Mini-QSO	$10^7 M_\odot$	1	0.1	16	$30^{'}$	11.1	9.1
Mini-QSO	$10^6 M_\odot$	1	0.1	16	$30^{'}$	3.6	3.4
Mini-QSO	$10^8 M_\odot$	1	0.1	16	$30^{'}$	25.9	20.2
Mini-QSO	$10^7 M_\odot$	2	0.1	16	$30^{'}$	20.4	17.5
Mini-QSO	$10^7 M_\odot$	1	0.5	16	$30^{'}$	5.2	4
Mini-QSO	$10^7 M_\odot$	1	0.1	11	$30^{'}$	46	38
Mini-QSO	$10^7 M_\odot$	1	0.1	16	$10^{'}$	4.2	4.0
Galaxy	$10^7 M_\odot$	1	0.1	16	$30^{'}$	11.3	9.4
HMXBs	$10^7 M_\odot$	1	0.1	16	$30^{'}$	11.2	9.2

Table 6.2: The SNRs for different scenarios considered in the chapter. These correspond to an observation time of 2000 h with the 564 antennae SKA1-low with a frequency resolution of 100 kHz. The quantities SNR1 and SNR2 represent the signal to noise ratios for the scenarios with and without foregrounds respectively.

of the IGM show strong absorption signal, however, the mean subtracted signal is expected to be very little in the emission and absorption regions. In order to achieve an SNR of ~ 5 for the fiducial source in this scenario, we require an observing time as large as 10,000 h when the smoothing is done with a Gaussian filter of size $30'$. Hence the detectability of the signal will be significantly more challenging when the Lyα coupling complete.

6.3.1.2 Signal + Noise + Foregrounds

Let us now investigate the detectability of the first sources in the presence of astrophysical foregrounds. As we have seen that the foregrounds are several orders larger than the signal as well as the system noise, it is in principle a very challenging task to recover the signal. However, the frequency dependence of the foregrounds is relatively smooth, while other components namely the signal and the noise behave differently. This property of the foregrounds can be used to subtract the foregrounds and recover the signal.

There are many approaches considered for removing the foregrounds, such as the polynomial fitting based method (Wang et al. 2006), Wp smoothing (Harker et al. 2010), independent component analysis (Chapman et al. 2013), continuous

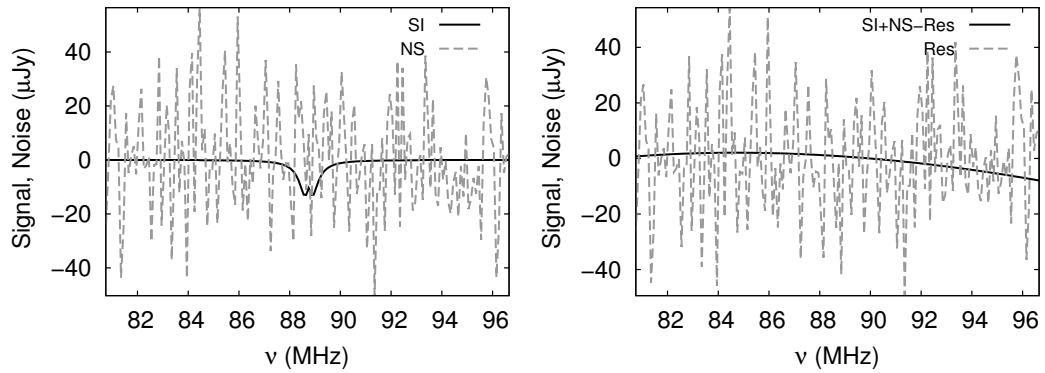

Figure 6.7: Left-hand panel: The real space signal (solid curve) and noise (dashed curve) as a function of the frequency channels along the line of sight to the centre of the source. Right-hand panel: The solid curve represents the difference between the signal + noise (before the foreground subtraction) and the residual signal + noise (after the foregrounds are subtracted) along the ν direction. The dashed curve represents the residual signal + noise along the frequency direction after the foregrounds are subtracted using a third order polynomial fitting method.

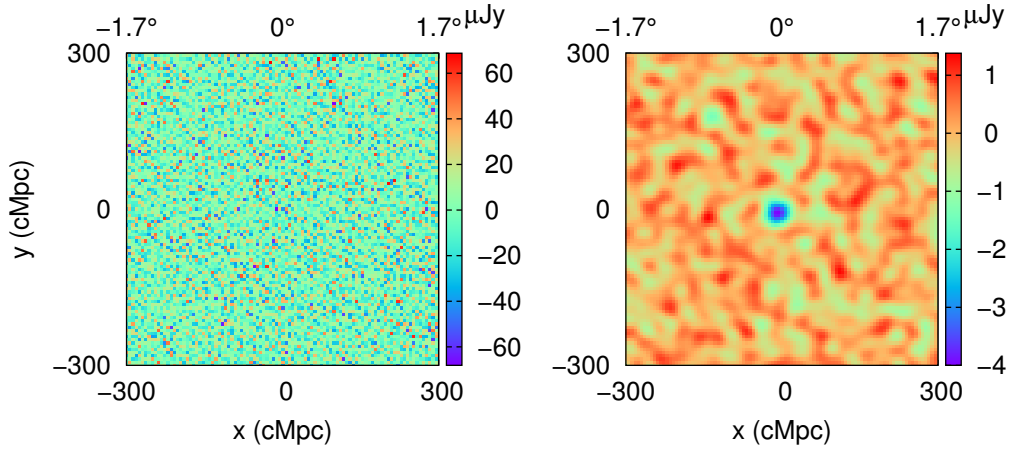

Figure 6.8: Left-hand panel : Map of the residual signal and noise after the foregrounds are subtracted (without smoothing). The angular resolution of the map is 2′. The noise corresponds to 2000 h of observation, 100 kHz of frequency resolution and baseline distribution of 564 antennae SKA1-low. Right-hand panel: Same as the left-hand panel but smoothed with a Gaussian filter of size 30′.

wavelet transform (Gu et al. 2013) and so on. In this work, we consider the polynomial fitting method which is relatively straightforward to implement among the existing ones. The steps we follow to generate the foregrounds subtracted smoothed images are:

- First, we calculate the total visibility $V(\vec{U},\nu)$ which can be written as,

$$V(\vec{U},\nu) = S(\vec{U},\nu) + N(\vec{U},\nu) + F(\vec{U},\nu), \tag{6.9}$$

  where $S(\vec{U},\nu)$, $N(\vec{U},\nu)$ and $F(\vec{U},\nu)$ are the contributions from the cosmological signal, system noise and foregrounds respectively.

- We choose the components of $V(\vec{U},\nu)$ along the frequency direction for each $\vec{U}$ and separately fit the real and imaginary part using a third order polynomial in logarithmic space. The form of the polynomial is given by

$$\log V(\vec{U},\nu) = \sum_{m=0}^{n} a_m \left(\log \nu\right)^m , \tag{6.10}$$

  where we choose $n = 3$ in this case. One thing to remember is that certain amount of signal and system noise is also removed during the foreground removal process. Thus fitting with a polynomial of a very high order may not be helpful.

- After the polynomial fitting, we subtract the fitted visibilities from the total visibilities to obtain the residual visibilities $V_{\rm res}(\vec{U},\nu)$. These residual visibilities contain the residual foregrounds, signal and noise.

- Finally we carry out the two-dimensional inverse Fourier transform of the $V_{\rm res}(\vec{U},\nu)$ at each frequency channel to get the real space maps that have the foregrounds subtracted.

- We smooth the image with a two-dimensional Gaussian filter to reduce the rms noise.

The left-hand panel of Figure 6.7 shows the real space 21-cm signal and system noise of the SKA1-low for 2000 h of observation as a function of the frequency channels along the line of sight which contains the centre of the source. One

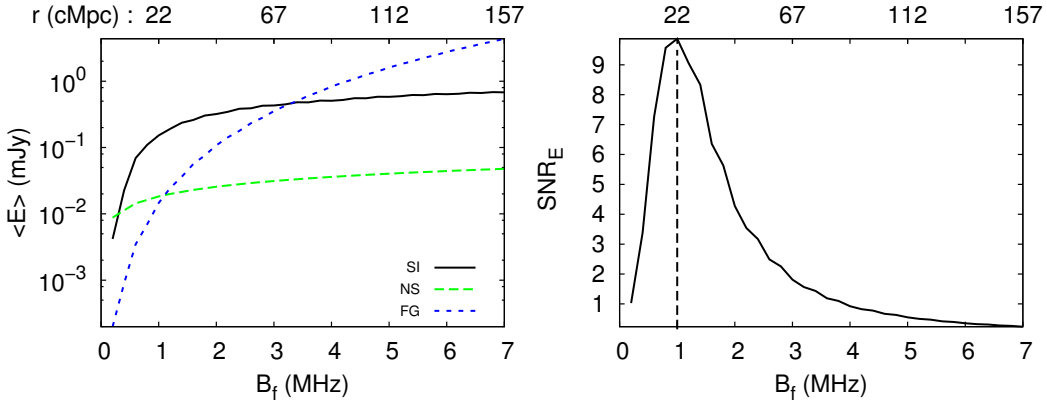

Figure 6.9: Left-hand panel: The estimator of the signal using the filter S_f and the corresponding error from the system noise and the foregrounds as a function of the parameter B_f. Right-hand panel: The signal to noise ratio as a function of the parameter B_f. The top labels of the panels show the spatial scales corresponds to B_f.

can see that the signal is contaminated by the system noise. The foregrounds along the same line of sight are several orders larger than the signal or the noise and hence is not shown in the figure. The right-hand panel shows the residual signal + noise after subtracting the foreground using the third order polynomial. Also shown is the difference between the original and the residual signal + noise. Clearly, the subtraction method is accurate enough to recover almost the original signal and noise. Figure 6.8 shows the foreground subtracted image without (left-hand panel) and with (right-hand panel) smoothing with the Gaussian filter of size $30'$. One can see that some amount of signal and noise also subtracted during the foregrounds removal process by comparing the images at the right-hand panel of Figure 6.8 and the right-hand panel of Figure 6.5. The value of χ for these two maps is 0.96. The SNR turns out to be ~ 9 for the same parameters for the foreground subtracted smoothed image, which is slightly smaller than the foreground-free image (the SNR turned out to be ~ 11 in that case).

6.4 Removing the foregrounds using a filter

In this section, we present a different approach to remove the foregrounds using a suitable filter rather than subtracting the foregrounds using some subtraction method as explained earlier. We showed in Chapter 5 that it is possible to detect the signal by summing up all the visibility contributions from different baselines and frequency channels in the foreground-free scenario. Even in the presence of the foregrounds, the signal is detectable using suitable filters which can decrease the foregrounds contributions below the signal. While the previous work was done using the analytical form of the signal from the source and for a somewhat idealized baseline distribution, here we repeat the calculation using the simulated signal and recently published baseline distribution of the SKA1-low.

The filter used introduced in Chapter 5 does not depend on any prior information on the signal and it only uses the fact that the foregrounds have smooth frequency dependence. The details of the method of subtracting foregrounds using filters can be found in previous works like Datta et al. (2007a); Ghara et al. (2016a). Here we briefly describe the method.

We define the estimator $\hat{E}$ as

$$\hat{E} = A_{\rm NS}(\Delta U)^2 \Delta\nu_c \sum_{a,b}\ V(\vec{U_a},\nu_b)\ S^{\star}_f(\vec{U_a},\nu_b)\ n_{\rm B}(\vec{U_a},\nu_b), \tag{6.11}$$

where ΔU is the grid resolution in the baseline distribution and the quantity $S_f(\vec{U},\nu)$ represents the filter. The sum is over all possible baselines a and frequency channels b. The normalization constant $A_{\rm NS}$ is given by

$$A^{-1}_{\rm NS} = (\Delta U)^2 \Delta\nu_c \sum_{a,b} n_{\rm B}(\vec{U_a},\nu_b) = N_{\rm B} B_\nu, \tag{6.12}$$

where $N_{\rm B}$ is the total number of baselines used in the study.

The system noise and the foregrounds are expected to be random numbers with zero mean. Thus, the expectation value of the estimator is expected to be,

$$\left\langle \hat{E} \right\rangle = A_{\rm NS}(\Delta U)^2 \Delta\nu_c \sum_{a,b}\ S(\vec{U_a},\nu_b)\ S^{\star}_f(\vec{U_a},\nu_b)\ n_{\rm B}(\vec{U_a},\nu_b). \tag{6.13}$$

The associated errors from the system noise can be written as (Datta et al. 2007a),

$$\begin{aligned}\left\langle (\Delta\hat{E})^2 \right\rangle_{\rm NS} &= \sigma_N^2 A_{\rm NS}(\Delta U)^2 \Delta\nu_c \\ &\times \sum_{a,b}\ |S_f(\vec{U_a},\nu_b)|^2\ n_{\rm B}(\vec{U_a},\nu_b),\end{aligned} \tag{6.14}$$

where the quantity σ_N is given by,

$$\sigma_N = \frac{\sqrt{2}\ k_B T_{\rm sys}}{A_{\rm eff}\ \sqrt{t_{\rm obs}\ B_\nu\ N_{\rm base}}}. \tag{6.15}$$

The error contribution from the foregrounds is

$$\begin{aligned}\left\langle (\Delta\hat{E})^2 \right\rangle_{\rm FG} = A_{\rm NS}^2 (\Delta U \Delta\nu_c)^2 \sum_{a,b,q} \left(\frac{2k_B}{c^2}\right)^2 (\nu_b \nu_q)^2 \\ \times\, n_{\rm B}(\vec{U_a}, \nu_b)\ n_{\rm B}(\vec{U_a}, \nu_q)\ C_{2\pi U_a}(\nu_b, \nu_q) \\ \times\, S_f^\star(\vec{U_a}, \nu_b) S_f(\vec{U_a}, \nu_q),\end{aligned} \tag{6.16}$$

where $C_l(\vec{U}, \nu_1, \nu_2)$ represent the multi-frequency angular power spectrum of the total foregrounds. The signal to noise ratio in this method is

$$\mathrm{SNR} = \frac{\left\langle \hat{E} \right\rangle}{\sqrt{\left\langle (\Delta\hat{E})^2 \right\rangle_{\rm NS} + \left\langle (\Delta\hat{E})^2 \right\rangle_{\rm FG}}}. \tag{6.17}$$

The form of the filter S_f, as defined in Chapter 5, is taken to be

$$\begin{aligned}S_f(\vec{U}, \nu) = \left(\frac{\nu}{\nu_c}\right)^2 \Bigg[S_T(\vec{U}, \nu, B_f) - \frac{\Theta(1 - |\nu - \nu_c|/B^{'})}{B^{'}} \\ \times \int_{\nu_c - B^{'}/2}^{\nu_c + B^{'}/2} S_T(\vec{U}, \nu^{'}, B_f)\ {\rm d}\nu^{'} \Bigg],\end{aligned} \tag{6.18}$$

where

$$\begin{aligned}S_T(\vec{U}, \nu, B_f) = 0 \text{ if } |\nu - \nu_c| > \frac{B_f}{2} \\ = -1 \text{ if } |\nu - \nu_c| \leq \frac{B_f}{2}.\end{aligned} \tag{6.19}$$

We choose $B^{'} = 2B_f$ if $B^{'} \leq B_\nu$, else $B^{'} = B_\nu$. The form of the filter S_f depends on the bandpass filter $S_T(\vec{U}, \nu, B_f)$ of width B_f. One can use other more sophisticated filters like the match filter (see, e.g., Datta et al. 2007a) to obtain higher SNR. However, for those filters, one usually requires some prior information about the expected signal.

The main result of the filtering method is shown in Figure 6.9. The left-hand panel shows the signal estimator and the corresponding errors from the system

noise and the foregrounds as a function of the bandpass width B_f. We find that it is possible to reduce the foregrounds contribution below the signal level using suitable bandpass width. The maximum SNR, as shown in the right-hand panel of Figure 6.9, is achieved for $B_f \sim 1$ MHz, and the peak SNR turns out to be ~ 10. The width of the filter that provides the maximum SNR, in fact, corresponds to the size of the absorption region around the source.

6.4.1 Realistic maps of the first sources

Till now we have been working under the assumption that there is only one source in the FOV. In reality, however, one expects to have multiple sources in the field, and depending on the separation between them there could be significant overlap in the 21-cm patterns. We study these effects using a full cosmological simulation. The steps to generate the realistic maps are briefly described below and one can find the details of the method in Ghara et al. (2015a,b) and in Chapter 2 of the thesis.

- We use the same dark matter simulation as used in Chapter 5 to generate the brightness temperature maps. We choose $f_\star = 0.07$ so that the reionization optical depth $\tau = 0.0584$ is consistent with the measurement of Planck Collaboration et al. (2015b). In this model, the reionization ends around $z \sim 6.3$.

- We generate δT_b maps in the simulation box following the method described in Chapter 2. We incorporate the effect of the peculiar velocities of the gas in the IGM using cell moving technique (see Chapter 3). Finally, we incorporate the light-cone effect, which is described in Chapter 4 in details.

- Finally, we re-grid the simulation box to get the desired angular resolution, frequency resolution and observational band width.

The left-hand panel of Figure 6.10 shows the $2.4^\circ \times 2.4^\circ$ image of the brightness temperature at the central frequency channel which corresponds to redshift $z = 15$. We show the angular positions of the sources by the '$\times$' marks within a band $\nu_c - 0.1$ to $\nu_c + 0.1$ MHz around the central frequency channel. One can clearly identify the absorption regions around the sources, however, there is substantial

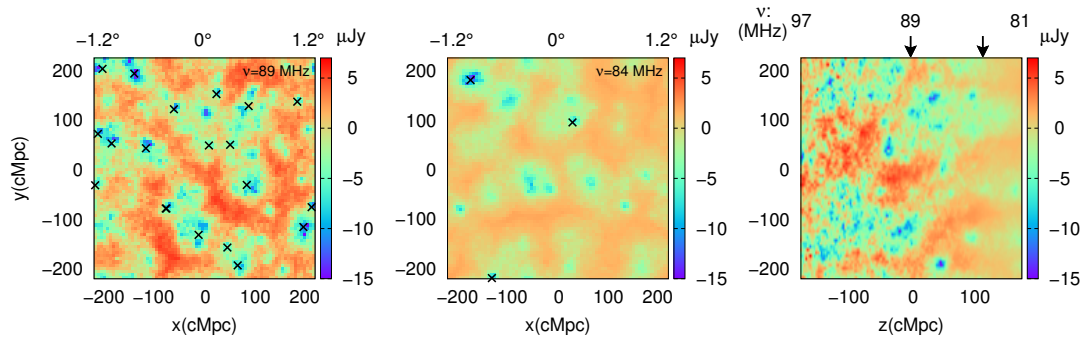

Figure 6.10: Left-hand panel: $2.4° \times 2.4°$ map of the 21-cm signal (without smoothing) at the frequency channel $\nu_c = 89$ MHz generated from the simulation using the N-body simulation and a one-dimensional radiative transfer code. The "$\times$" marks represent the angular positions of the sources between a band $\nu_c - 0.1$ to $\nu_c + 0.1$ MHz. Middle panel: Same as the left-hand panel, but at the frequency channel corresponding to $\nu = 84$ MHz. Right-hand panel: The light-cone map of $\delta T_{\rm b}$ distribution. The arrows in the top label of the panel show the frequency channels correspond to the maps at the left-hand and the middle panels. The maps include the effect of redshift-space distortion and the light-cone effect.

overlap between the individual patterns. The middle panel of Figure 6.10 shows the $\delta T_{\rm b}$ map at redshift 16. The number of sources drops quite drastically in this frequency channel as we are probing the initial stages of the cosmic dawn. The overlap between the individual patterns too is not that substantial. The decrease in the number of sources towards the lower frequency channels can be seen from the right-hand panel of Figure 6.10, where we show the light-cone from our simulation box. The signal at the higher frequency end of the box is essentially the strong absorption signal arising from the significant overlap between the Lyα photons from the sources. Note that we have subtracted the mean from each frequency channel while making the image and thus, the signal is a combination of emission and absorption regions. As the signal from the channels corresponding to redshifts 15 and 16 are dominated by the absorption regions, the mean of the expected signal is negative. The regions with positive values of the signal in the left-hand and middle panels of Figure 6.10 arise because of subtracting the mean signal from the maps. In reality, these are the Lyα deficient regions with almost no 21-cm signal.

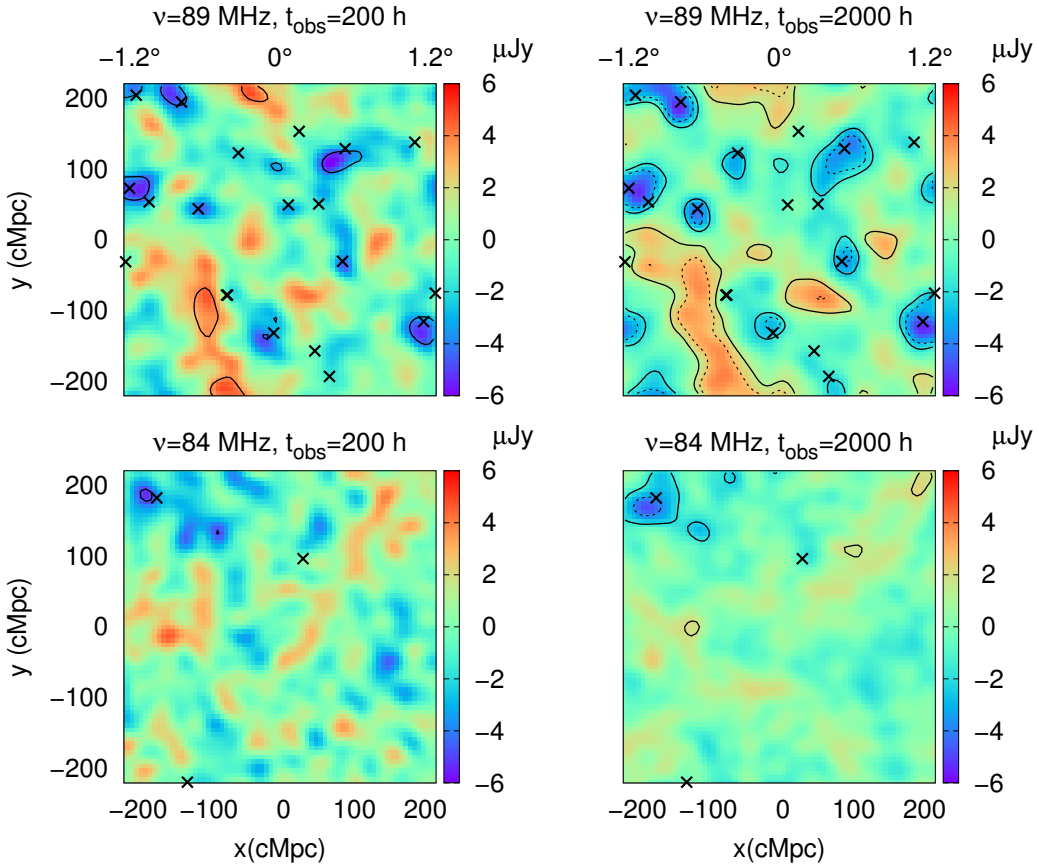

Figure 6.11: Top left-hand panel: Map of the residual signal and noise after foreground subtraction and smoothing with the Gaussian filter of size $30'$ at the central frequency channel $\nu_c = 89$ MHz. The signal is generated using the method described in Section 6.4.1. The noise corresponds to 200 h of observation, while the smoothing is done with a Gaussian filter of size $30'$. The "$\times$" marks show the angular positions of the sources present within a band $\nu_c - 0.1$ to $\nu_c + 0.1$ MHz. Top right-hand panel : Same as the top left-hand panel, but for 2000 h of observation. Bottom left-hand panel: Same as the top left-hand panel, but at a different frequency channel which corresponds to $\nu = 84$ MHz. Bottom right-hand panel: Same as the bottom left-hand panel, but for 2000 h of observation. The solid contours in all the panels correspond to $3-\sigma$ level, while the dotted curves correspond to $5-\sigma$ contours.

The top left-hand panel of Figure 6.11 shows the smoothed image of the residual signal and noise at the central frequency channel after subtracting the foregrounds using the polynomial method. The noise in the panel corresponds to 200 h of observation and the smoothing is done using the Gaussian filter of size $30'$. One can easily identify that even in the smoothed map, the signal is localized around the sources. The top right-hand panel of Figure 6.11 shows the same but for 2000 h of observation. The signal to noise ratios of these top left-hand and right-hand panels are 4.8 and 14.2 respectively. The bottom left-hand and right-hand panels are same as the top panels but at a different frequency channel corresponding to $\nu = 84$ MHz ($z = 16$). The corresponding SNRs in the bottom panels are 3.3 and 10.1 respectively. The Pearson cross-correlation coefficients χ, in this case, are given in Table 6.3. We find that the foreground subtraction method works effectively in this case as well leading to reasonably high values of χ.

We have also shown the $3-\sigma$ and $5-\sigma$ contours of the signal in Figure 6.11. One can see that it is possible to detect the signal at the $3-\sigma$ level within a modest 200 h of observations. The detection can be made more definite in an integration time of 2000 h where the signal is well above the $5-\sigma$ level. This can, in principle, help us in devising strategies for detecting the first sources. For definiteness, let us concentrate on the 84 MHz maps (bottom panels). One can see that, in the given field, one can identify a $3-\sigma$ region near the top-left corner of the map with a 200 h of observations (bottom left-hand panel). Once such a tentative detection of the signal happens in some field, one can attempt longer observation like 2000 h to identify the absorption regions with a larger SNR, as is shown in the bottom right-hand panel. As most of the absorption regions detected in the maps are situated around some sources, one can identify some isolated absorption region on the map to measure the smoothed $\delta T_{\rm b}$ profile around the corresponding isolated source. Once this smoothed $\delta T_{\rm b}$ profile is measured with error bars, it can be used to estimate the source parameters using some sophisticated methods like MCMC.

Redshift	$t_{\rm obs}$ (h)	χ
15	200	0.85
15	2000	0.8
16	200	0.89
16	2000	0.74

Table 6.3: The table shows the Pearson cross-correlation coefficients for different maps from the full cosmological simulation at different redshifts and for different observation time. The coefficient is calculated for the smoothed maps for the signal + noise and the residual signal + noise after foreground subtraction.

6.5 Summary and discussion

We have investigated the detectability of the first sources during the cosmic dawn using imaging techniques through future radio observations with the SKA1-low. Detecting the 21-cm signature of these sources is expected to reveal, at least to some extent, their properties and also the physical state of the surrounding IGM. However, their detection would be significantly challenging because the signal is much too weak compared to the system noise and the astrophysical foregrounds.

Our fiducial source model consists of stars within a galaxy along with a mini-QSO type X-ray source. The model for the sources can be parametrized by several unknown parameters, e.g., the stellar mass ($M_\star$), the escape fraction of the UV photons ($f_{\rm esc}$), the ratio of X-ray and UV luminosities (f_X), the X-ray spectral index (α), the age of the source ($t_{\rm age}$), and the redshift of observation (z). In addition, we also need to specify the overdensity of the surrounding IGM ($1+\delta$), assuming it to be uniform. The fiducial values of these parameters are taken to be $M_\star = 10^7$ M$_\odot$, $f_{\rm esc} = 0.1$, $f_X = 0.05$, $\alpha = 1.5$, $t_{\rm age} = 20$ Myr, $z = 15$ and $1+\delta = 1$.

We have considered a fiducial observation using the present antenna configuration of the SKA1-low. Assuming that we observe a region at declination $\delta = -30^\circ$, we have used the baseline distribution to obtain the "dirty" map. We have added the system noise as well as the astrophysical foregrounds (Galactic synchrotron and extragalactic point sources) to the images. Our main aim is to explore whether the images can be used for detecting the signal from the first

sources and if one can extract the properties of these sources from the maps.

Our main findings are listed below.

- If we assume the target source to be isolated, then in the situation where foregrounds can be perfectly subtracted out, it is possible to achieve a signal to noise ratio (SNR) ~ 11 for the fiducial source at a redshift of 15 for 2000 h of observation and a frequency resolution of 100 kHz. This SNR is achieved by smoothing the images with a Gaussian filter of size $30'$which helps in reducing the rms of the noise considerably. In general, the SNR increases with increasing width of the Gaussian filter.

- It is not possible to detect the signal in any reasonable observational time without smoothing the maps. Unfortunately, this smoothing alters the intrinsic brightness temperature profile around the sources which in turn makes it difficult to reliably extract their properties from the maps. We find that it is still possible to constrain the parameters $M_\star$, $f_{\rm esc}$ and $1+\delta$, while it will be difficult to extract any information on f_X, α and $t_{\rm age}$ from the smoothed $\delta T_{\rm b}$ profiles.

- Although the expected brightness temperature profiles around different types of sources are different, smoothing the maps makes it difficult to distinguish between these sources. In particular, we find that the smoothed profiles of the different X-ray sources, e.g., mini-QSOs and HMXBs, are similar to the case where there are no X-rays from the galaxy.

- The cosmological 21-cm signal is largely contaminated by the astrophysical foregrounds. In order to account for these, we model the Galactic synchrotron emission and extragalactic point sources (Choudhuri et al. 2014) and add them to our maps. We then use a third order polynomial fitting method to subtract the foregrounds. We are able to achieve an SNR ~ 9 for the fiducial source model which is only $\sim 20\%$ worse than the foreground-free scenario.

- Since the first galaxies are not expected to form in complete isolation, we generate more realistic signal maps from the output of a N-body simulation and using a one-dimensional radiative transfer code (see Chapter 2).

The reionization history is calibrated to recent Planck measurements of the electron scattering optical depth (Planck Collaboration et al. 2015b). We apply the same smoothing and foreground removal technique on these maps as discussed above. The SNR of the map at the redshift 15, after the foregrounds subtraction and smoothing with the fiducial filter, is ~ 14 (4) for 2000 (200) h of observations. The corresponding SNR value is 10 (3) at redshift 16. This suggests that a possible observation strategy for the SKA1-low could be to observe multiple fields for small observation time like 200 h. If one is able to detect a $3-\sigma$ signal in any of these fields (after smoothing with filters of widths $\sim 30'$), then one can perform a deeper observation of ~ 2000 h and possibly constrain properties of the first sources along with the surrounding IGM.

Finally, we discuss some of the aspects of the study which need to be addressed in more details. Although we have modelled the foregrounds in a fairly detailed manner, they can be more complex in the actual case. One probably needs to devise more sophisticated methods to disentangle the signal in that case. Our analysis ignores various other complications, e.g., those arising from instabilities in the ionosphere, calibration of the signal, man-made interference, and instrumental systematics. One possible extension of the present work could be to consider all these complexities and develop a complete pipeline to prepare mock data sets for analysis.

On the modelling aspect, one needs to work out the signal in different reionization scenarios accounting for the uncertainties in the galaxy formation processes at high redshifts. This could include studying the effects of, e.g., the small-mass sources of ionization and heating leading to a relatively early overlap of Lyα regions (see Chapter 2), alternate reionization scenarios driven by quasars (Khaire et al. 2016; Madau and Haardt 2015; Mitra et al. 2016). The smoothing filters used in this work have been constructed assuming that we do not have any prior idea of the signal. One could also explore devising more sophisticated filters which account for the nature of the signal to make a more efficient detection.

7 | Conclusions and Future outlook

The main aim of the thesis is to build a new framework to study various unknown processes during the cosmic dawn and the EoR. Observations of the high-redshifted H I 21-cm signal is a powerful probe of these epochs and is expected to provide us with an enormous amount of information about the properties of the primordial sources, the ionization and thermal state of the IGM etc. A number of experiments have been designed with the aim to detect the signal from the cosmic dawn and the EoR. However, the detection of the signal is a challenging task as the signal is very weak compared to the instrumental noise and astrophysical foregrounds. Detection of the signal requires a good understanding of the systematics of the instrument, accurate modeling of the astrophysical foregrounds and long observation time etc. Once the signal is detected, the interpretations will be pretty much model dependent. To understand the observational results we need to cover the huge parameter space of the cosmic dawn and EoR. With this aim, we have developed a method to generate the 21-cm signal self-consistently from the cosmic dawn and the EoR. This semi-numerical method is used to study the impact of various radiation backgrounds and effect of different physical processes like the redshift-space distortion and light-cone effect on the 21-cm signal. We also study the detectability of very early sources like the population III stars, primordial galaxies, mini-QSOs, HMXBs in 21-cm observations with existing and future telescopes. Now we will briefly summarize the outcomes and future prospects of the thesis.

7.1 Semi-numerical method

Modeling of the redshifted 21-cm signal from the cosmic dawn and EoR is very important to understand the observational results and design new observational strategies. A major effort of the thesis has been modeling the redshifted 21-cm signal from the cosmic dawn and EoR using semi-numerical simulations. In particular, we have developed a semi-numerical code for generating the brightness temperature distribution of the H I 21-cm signal using the output from $N-$body dark matter simulations and a 1D radiative transfer code. The algorithm is based on the methods of Thomas and Zaroubi (2008); Thomas et al. (2009). However, we have used slightly different method for generating the ionization and kinetic temperature maps. The main steps of the method are: (*i*) The density and velocity cubes at different redshifts are obtained using the $N-$body simulation code CUBEP^{3}M. (*ii*) We identify the dark matter haloes in the simulation box using spherical overdensity method. In case the mass resolution of the simulation is not high enough to identify dark matter haloes down to $M_{\rm halo} \sim 10^8\,{\rm M}_\odot$, we use a sub-grid recipe to identify the low-mass haloes. This sub-grid method uses the extended Press-Schechter model of Bond et al. (1991) and hybrid prescription of Barkana and Loeb (2004). (*iii*) We assume that the stellar mass of a galaxy is proportion to the hosting halo mass. Each source is associated with an SED, e.g., we generate the SED for the galaxies using a population synthesis code PEGASE2. (*iv*) The ionization and kinetic temperature maps are generated using a 1D radiative transfer code for isolated sources. The 1D radiative transfer code incorporates different ionization-recombination and heating-cooling processes for hydrogen and helium. It tracks the time evolution of the ionization fraction of different ionization states of hydrogen and helium and the kinetic temperature of gas in the IGM around individual sources. The overlap between UV, X-rays and Lyα photons in the simulation box have been accounted appropriately. The details of the method are described in Chapter 2 of the thesis.

Now we will state some of the future prospects of this semi-numerical method.

1. The semi-numerical method can be extended to build a framework incorporating the instrumental effects to test the observational pipelines (Ghara et al. 2015a). The framework can be used to generate H I intensity maps at post-reionization epoch and thus will be relevant for experiments like

MeerKAT, SKA, HERA etc. The simulation can be used to study the instrumental effects which will affect the observation, develop optimal estimators and design H I survey strategies. Using H I intensity mapping techniques, it is possible to probe the large-scale structure of the universe. In addition, this H I intensity-mapping technique can be used for many science cases like putting constraints on the nature of dark energy, the curvature of the Universe etc. Also, it can probe high-redshifts Baryon Acoustic Oscillations as well as ultra-large scales, which can be used to constrain effects such as primordial non-Gaussianity.

2. Our semi-numerical code is able to account for the spin temperature ($T_{\rm S}$) fluctuations arising from inhomogeneous X-ray heating and Lyα coupling during the cosmic dawn and EoR. The algorithm was validated by comparing with other existing results like Baek et al. (2010); Christian and Loeb (2013); Mesinger et al. (2011); Pritchard and Furlanetto (2007); Santos et al. (2008). While full radiative transfer codes can produce realistic results, these are computationally very expensive. On the other hand, various semi-numerical models are computationally much less expensive and thus, can be used to cover huge parameter space of the EoR. However, the approximations considered in these semi-numerical schemes may limit their ability to predict the redshifted 21-cm signal accurately. Thus comparing the semi-numerical methods, with each other and with the full radiative transfer schemes, are very important while predicting 21-cm signals from the Cosmic dawn and epoch of reionization. Thus, a more rigorous comparison of our method with many other semi-numerical models of reionization, e.g., Choudhury et al. (2009); Mesinger et al. (2011) and with the full radiative transfer schemes like Mellema et al. (2006) , are very important while predicting 21-cm signals from the Cosmic dawn and epoch of reionization.

7.2 Study different physical processes

One of the major goals of the thesis is to understand different physical processes on the H I 21-cm signal from the cosmic dawn. In this thesis, we have used the semi-numerical method to study the impact of various radiation backgrounds like

UV, X-rays and Lyα on the 21-cm signal from these epochs. In addition, the code is used to study the impact of the redshift-space distortion and light-cone effect on the signal. Here we summarize our finding from these studies.

- **Different radiation background**

  The nature of sources during the cosmic dawn and EoR is one of the uncertainties of reionization. The impact of different sources will be imprinted in the brightness temperature maps in term of the neutral fraction and the spin temperature fluctuation in the IGM. In principle, different sources will provide different signatures in the 21-cm signal. Thus, the observed signal can be used to extract the source information. In this thesis, we have studied the impact of different sources like the stars in galaxies and mini-QSOs on the expected spherically averaged power spectrum of the brightness temperature fluctuations. We assume that the SED of the galaxy is solely determined by the stellar population in the galaxy. We generate the galaxy SED using the publicly available population synthesis code PEGASE2 (see chapter 2 for details). For the mini-QSO source, we assume that there is an additional power law SED due to the accretion of the intermediate mass black hole at the centre of the galaxy.

  For the reionization models driven by stars, the size of the emission regions in the IGM is small throughout the EoR. However, in the presence of the mini-QSOs, there will be a mixture of emission and absorption regions in the IGM at cosmic dawn and the initial stage of reionization. The power spectrum in such model shows a "bump"-like feature during the cosmic dawn and its location measures the typical sizes of heated regions. The presence of inhomogeneous Lyα coupling, X-ray heating, and ionization produce separate peaks in the large-scale power spectrum while plotted as a function of redshift. In the case of stellar driven reionization models, the heating in the neutral region is not present and thus the second peak (heating peak) will be absent when the large-scale power spectrum is plotted as a function of redshift (Ghara et al. 2015a). This work is described in Chapter 3 of the thesis.

- **Effect of redshift-space distortion (RSD)**

The peculiar velocity has a significant impact on the reionization and pre-reionization H I 21-cm signal (Bharadwaj and Ali 2004). The coherent inflows of matter into overdense regions and the outflows of matter from underdense regions will produce an additional red or blue shift on top of the cosmological redshift. Thus, the over-density/under-density regions will appear to be more over-density/under-density region at large scales. In principle, this effect can make the 21-cm power spectrum anisotropic (Barkana and Loeb 2005a; Majumdar et al. 2013). Studies like Jensen et al. (2013); Mao et al. (2012) have shown that the peculiar velocity can boost the H I power spectrum by a factor of ~ 5 at large scales during the initial stages of reionization when $x_{\rm HII} \lesssim 0.2$. This also produces anisotropy in the power spectrum of the signal. Studies like Jensen et al. (2013) predicted that the anisotropy due to the RSD is detectable with LOFAR 2000 h of observations. However, all these studies are based on the assumption $T_{\rm S} >> T_{\gamma}$, thus making the signal independent of $T_{\rm S}$ fluctuation.

We have incorporated the redshift-space distortion using the particle movement method and cell movement method (see chapter 3 for details) in the presence of spin temperature fluctuation. Here we investigate how the above results change once the heating and Lyα coupling, and hence the spin temperature, are calculated self-consistently. We find that in the presence of inhomogeneous Lyα coupling and heating, the effect of RSD at large scales will be smaller than expected earlier, while the effect will be prominent at small scales. The effect of RSD, at large scales, will be significant at the trough regions in the power spectrum when plotted as a function of redshift. The effect of the RSD will be different for different source models, for example, the effect will be significant for most of the period for a reionization model driven by stars in galaxies, where inhomogeneous heating is not present. The details of this work are described in Chapter 3 of the thesis.

- **Light-cone effect**

  The "light-cone effect" is another important line of sight effect on the 21-cm signal from the cosmic dawn and EoR. As light takes a finite amount of time to reach from a distant point to an observer, the cosmological 21-cm signal coming from different cosmological redshifts essentially belongs to different

distances and thus correspond to different cosmological epochs. The effect basically incorporates the redshift evolution of the signal while generating the signal in the simulation box. Studies like Datta et al. (2014) assume $T_{\rm S} >> T_{\gamma}$ and showed that, depending on the observational bandwidth, the light-cone effect could enhance the large-scale power spectrum of the signal by a factor of up to $\sim$ 5 when reionization is $\sim$ 20% completed and suppress by a significant amount at the final stages of the EoR (with ionization fraction ~ 0.8).

In this thesis, we study the light-cone effect on the H I power spectrum in the presence of inhomogeneous heating and Lyα coupling for various source models and reionization histories. The main results of this study are: (*i*) It turns out that the effect is much stronger and dramatic in the presence of the $T_{\rm S}$ fluctuation of the IGM compared to the studies like Datta et al. (2014). In presence of light-cone effect, the spherically averaged power spectrum increase (decrease) up to a factor of 3 (0.6) at the large scales ($k \sim 0.05\,{\rm Mpc}^{-1}$). However, the effects are highly dependent on the reionization history and source model. (*ii*) The effect has a significant impact at various stages of reionization. In particular, the effect is significant near the peak and dip-like features seen in evolution the power spectrum as a function of redshift. The effect is the maximum when the spherical averaged power spectrum evolve non-linearly, in particular, near the peak and dip-like features seen in evolution the power spectrum as a function of redshift. The impact of the light-cone effect is minimum when the power spectrum evolve linearly as the linear evolution of the power spectrum gets canceled out to a large extent. (*iii*) Studies like Mesinger et al. (2014) suggested that the source properties can be extracted from the amplitude and position of the peaks in the evolution of large-scale power spectrum. However, for a large observational frequency band, the suppression of the power spectrum near the peaks and dips due to the light-cone effect smoothed out the three-peak nature of the evolution of the large-scale power spectrum to a large extent. Thus, it is necessary to incorporate the light-cone effect while extracting the source parameters from the observations of the peaks and dips of the power spectrum. We refer Ghara et al. (2015b) to the reader for details of the work. This work is presented in the Chapter 4 of the thesis.

Now we will state some future prospects of these studies.

1. In this thesis, we have mainly focused on the galaxy and mini-QSO type sources. It will be interesting to see the impact of other sources like HMXBs, QSOs etc on the 21-cm signal and cover the parameter spaces for different source parameters. Finally, we would like to combine our semi-numerical code with code like MCMC to make it useful for parameter estimation etc.

2. In addition to the redshift-space distortion and light-cone effect, the Alcock-Paczynski effect (Alcock and Paczynski 1979) (caused due to the non-Euclidean geometry of the space-time) is another line of sight effect which can have a significant impact on the 21-cm power spectrum and in principle, can also introduce anisotropy to the signal along the LoS. It will be interesting to find the relative impact of the redshift-space distortion, light-con effect and the Alcock-Paczynski effect on the power spectrum using realistic models of the 21-cm signal from the cosmic dawn and EoR.

3. In principle, the redshift-space distortion, the light-cone effect, and the Alcock-Paczynski effect can introduce a significant amount of anisotropy to the 21-cm signal. However, separation of the individual anisotropies will be a challenging task. Also, in reality, the effect of RSD and the light-cone effect will be different for different source models. Thus, it will be a nice project to check the effect for different sources and also to find the detectability of the RSD, light-cone effect and Alcock-Paczynski effect anisotropies in the presence of inhomogeneous Lyα coupling and X-ray heating using interferometers like LOFAR, SKA1-low, HERA etc.

7.3 Detectability of the early sources

Finding out the properties of the early sources, like the galaxies, mini-QSos or HMXBs etc, is one of the major goals of modern astronomy. It is believed that the redshift 21-cm signal is a promising probe to extract source information. However, the H I signal is very weak compared to the instrumental noise and astrophysical foregrounds. Especially, the level of contamination increases at low

frequencies. Thus, the first task would be to simply make a detection of the signatures of these early sources in low-frequency observations. Once the detection of the signal is confirmed, one can follow it up and make further progress by constraining various properties of these sources. In this thesis, we have modeled the 21-cm signal structure around the different sources. We have used a number of parameters to characterize the source properties and the properties of the surrounding medium. We have investigated the detectability of the early sources in radio observations like the SKA1-low using visibility based and imaging techniques. These studies would help in planning observations using the SKA1-low so as to make the detection of the signal around the first sources.

- **Using visibilities**

  Studies like Datta et al. (2007a); Geil and Wyithe (2008) have shown that the large ionized bubbles around individual sources can be detected in the presence of instrumental noise and foregrounds using telescopes like the GMRT, LOFAR, and the MWA within reasonable integration time around redshift ~ 8. In this thesis, we have considered different source models, i.e., the metal-free Population III (PopIII) stars, primordial galaxies consisting of Population II (PopII) stars, mini-QSOs and HMXBs and model the 21-cm signal pattern around the sources using the one-dimensional radiative transfer code. In our case, however, the situation is much more complex than that of Datta et al. (2007a) as we are interested in the very early stages of reionization (i.e., the cosmic dawn) where the IGM contains both emission and absorption regions.

  We investigate the detectability of these sources by comparing the 21-cm visibility signal with the system noise appropriate for a telescope like the SKA1-low. The main results of the study are: (i) The signal around sources like PopII galaxies, mini-QSOs and HMXBs at redshift 15 is detectable only at the low baseline, e.g., $U \lesssim 100$ for 1000 h of observation while source like pop III stars are unlikely to be detected as the 21-cm regions are very small. We integrate the visibility around a typical source over all baselines and over a frequency interval of 16 MHz to determine the signal to noise ratio. We find that it will be possible to make a $\sim 9-\sigma$ detection of the isolated sources like PopII galaxies, mini-QSOs and HMXBs at $z \sim 15$ with

the SKA1-low in 1000 hours (for a scenario where foregrounds are removed accurately without removing the signal and system noise). (*ii*) We have studies the exact value of SNR by varying different source parameters. We find that the SNR depend strongly on parameters like the mass and age of the source and the escape fraction of ionizing photons, while it weakly depends on X-ray source parameters like the power law spectral index and the ratio of the X-ray and UV luminosities. The SNR increases with the overdensity of the IGM and decreases at higher redshift. (*iii*) Even in the presence of astrophysical foregrounds, it is possible to achieve an SNR ~ 9 by subtracting out the frequency-independent component of the observed signal using suitable filters. The details on the method and the results are presented in Chapter 5 of the thesis.

- **Using imaging techniques**

  We have also studied the detectability of the first sources with the SKA1-low using image-based techniques in the presence of the system noise and astrophysical foregrounds. It is expected that the sources may not be detectable in very high-resolution images within observation time $\sim$ 2000 hours, mainly because the signal will be contaminated by the foregrounds and the system noise. These sources, however, can be detected in lower resolution images within reasonable observation time where the signal per beam is expected to be higher than the rms noise. We use the models we built earlier to calculate the signal expected from the early sources. In addition, we also model the astrophysical foregrounds to contaminate the signal similar to what is expected in observations. We find that, after subtracting the foreground sufficiently and suppressing the rms noise by smoothing using a Gaussian filter, the sources are detectable with $\sim 9-\sigma$ confidence level over 2000 hours of observation with the SKA1-low in images of resolution $2'$. Though the recovered brightness temperature profiles around the sources get modified because of the Gaussian smoothing, they can still be used to extract the source parameters. As the signal to noise ratio increases for low-resolution images, the first attempt of the low-frequency radio experiments should probably be to observe multiple fields and detect the signal in low-resolution images within short observation time like 200

hours. Once there is a detection of the signal in some field, one should attempt for longer observation in that particular field and try to recover the $\delta T_{\rm b}$ profiles around the isolated sources which can be used for parameter estimation. These calculations are presented in Chapter 6 of the thesis.

The main aim of these studies is to reveal the early source properties using the low-frequency radio observations. As it is expected that these sources will be detected in observation of the redshifted 21-cm signal from the cosmic dawn and epoch of reionization using interferometers like the SKA for reasonable observation time. Some possible future prospects of these studies are: (*i*) A possible extent of these studies is to find some optimum method to enhance the detectability of the H I 21-cm signal, e.g., one can use techniques like the match filtering to enhance the SNR. (*ii*) Once the $\delta T_{\rm b}$ profile or the visibility profile around an isolated source is measured with sufficient accuracy, it can be used for extracting the source parameters. However, there will be uncertainty in the accuracy of the extracted parameters. The 1D radiative transfer code and some sophisticated parameter estimation method like the MCMC method can be used to build an efficient framework for parameter estimation.

Bibliography

Abel, T., Bryan, G. L., and Norman, M. L. (2002). The Formation of the First Star in the Universe. *Science*, 295:93–98. 118

Adelberger, K. L. and Steidel, C. C. (2000). Multiwavelength Observations of Dusty Star Formation at Low and High Redshift. ApJ, 544:218–241. 11

Ahn, K., Xu, H., Norman, M. L., Alvarez, M. A., and Wise, J. H. (2015). Spatially Extended 21 cm Signal from Strongly Clustered Uv and X-Ray Sources in the Early Universe. ApJ, 802:8. 34, 56

Alcock, C. and Paczynski, B. (1979). An evolution free test for non-zero cosmological constant. Nature, 281:358. 93, 197

Ali, S. S., Bharadwaj, S., and Chengalur, J. N. (2008). Foregrounds for redshifted 21-cm studies of reionization: Giant Meter Wave Radio Telescope 153-MHz observations. MNRAS, 385:2166–2174. 169

Ali, S. S., Bharadwaj, S., and Pandey, B. (2005). What will anisotropies in the clustering pattern in redshifted 21-cm maps tell us? MNRAS, 363:251–258. 93

Ali, Z. S., Parsons, A. R., Zheng, H., Pober, J. C., Liu, A., Aguirre, J. E., Bradley, R. F., Bernardi, G., Carilli, C. L., Cheng, C., DeBoer, D. R., Dexter, M. R., Grobbelaar, J., Horrell, J., Jacobs, D. C., Klima, P., MacMahon, D. H. E., Maree, M., Moore, D. F., Razavi, N., Stefan, I. I., Walbrugh, W. P., and Walker, A. (2015). PAPER-64 Constraints on Reionization: The 21 cm Power Spectrum at z = 8.4. ApJ, 809:61. 26

Allison, A. C. and Dalgarno, A. (1969). Spin Change in Collisions of Hydrogen Atoms. ApJ, 158:423. 31

BIBLIOGRAPHY

Alonso, D., Bull, P., Ferreira, P. G., and Santos, M. G. (2015). Blind foreground subtraction for intensity mapping experiments. MNRAS, 447:400–416. 154

Alvarez, M. A., Pen, U.-L., and Chang, T.-C. (2010). Enhanced Detectability of Pre-reionization 21 cm Structure. ApJ, 723:L17–L21. 40, 48, 118

Alvarez, M. A., Wise, J. H., and Abel, T. (2009). Accretion onto the First Stellar-Mass Black Holes. ApJ, 701:L133–L137. 162

Baek, S., Di Matteo, P., Semelin, B., Combes, F., and Revaz, Y. (2009). The simulated 21 cm signal during the epoch of reionization: full modeling of the Ly-α pumping. A&A, 495:389–405. xiii, 3, 12, 21, 23, 56, 63, 64, 67, 118, 160

Baek, S., Semelin, B., Di Matteo, P., Revaz, Y., and Combes, F. (2010). Reionization by UV or X-ray sources. A&A, 523:A4. 32, 65, 86, 193

Barkana, R. (2006). Separating out the Alcock-Paczyński effect on 21-cm fluctuations. MNRAS, 372:259–264. 93

Barkana, R. and Loeb, A. (2001a). In the beginning: the first sources of light and the reionization of the universe. Phys. Rep., 349:125–238. 1

Barkana, R. and Loeb, A. (2001b). In the beginning: the first sources of light and the reionization of the universe. Phys. Rep., 349:125–238. 35

Barkana, R. and Loeb, A. (2004). Unusually Large Fluctuations in the Statistics of Galaxy Formation at High Redshift. ApJ, 609:474–481. xv, 34, 35, 94, 192

Barkana, R. and Loeb, A. (2005a). A Method for Separating the Physics from the Astrophysics of High-Redshift 21 Centimeter Fluctuations. ApJ, 624:L65–L68. xvi, 32, 57, 58, 195

Barkana, R. and Loeb, A. (2005b). Detecting the Earliest Galaxies through Two New Sources of 21 Centimeter Fluctuations. ApJ, 626:1–11. 56

Barkana, R. and Loeb, A. (2006). Light-cone anisotropy in 21-cm fluctuations during the epoch of reionization. MNRAS, 372:L43–L47. xviii, 91

Battaglia, N., Trac, H., Cen, R., and Loeb, A. (2013). Reionization on Large Scales. I. A Parametric Model Constructed from Radiation-hydrodynamic Simulations. ApJ, 776:81. xiii, 29, 32, 55

Becker, R. H., Fan, X., White, R. L., Strauss, M. A., Narayanan, V. K., Lupton, R. H., Gunn, J. E., Annis, J., Bahcall, N. A., Brinkmann, J., Connolly, A. J., Csabai, I., Czarapata, P. C., Doi, M., Heckman, T. M., Hennessy, G. S., Ivezić, Ž., Knapp, G. R., Lamb, D. Q., McKay, T. A., Munn, J. A., Nash, T., Nichol, R., Pier, J. R., Richards, G. T., Schneider, D. P., Stoughton, C., Szalay, A. S., Thakar, A. R., and York, D. G. (2001). Evidence for Reionization at z˜6: Detection of a Gunn-Peterson Trough in a z=6.28 Quasar. AJ, 122:2850–2857. xi, 1, 14, 15

Bernardi, G., de Bruyn, A. G., Brentjens, M. A., Ciardi, B., Harker, G., Jelić, V., Koopmans, L. V. E., Labropoulos, P., Offringa, A., Pandey, V. N., Schaye, J., Thomas, R. M., Yatawatta, S., and Zaroubi, S. (2009). Foregrounds for observations of the cosmological 21 cm line. I. First Westerbork measurements of Galactic emission at 150 MHz in a low latitude field. A&A, 500:965–979. 20

Bernardi, G., de Bruyn, A. G., Harker, G., Brentjens, M. A., Ciardi, B., Jelić, V., Koopmans, L. V. E., Labropoulos, P., Offringa, A., Pandey, V. N., Schaye, J., Thomas, R. M., Yatawatta, S., and Zaroubi, S. (2010). Foregrounds for observations of the cosmological 21 cm line. II. Westerbork observations of the fields around 3C 196 and the North Celestial Pole. A&A, 522:A67. 20

Bharadwaj, S. and Ali, S. S. (2004). The cosmic microwave background radiation fluctuations from HI perturbations prior to reionization. MNRAS, 352:142–146. xvi, 32, 57, 195

Bharadwaj, S. and Ali, S. S. (2005). On using visibility correlations to probe the HI distribution from the dark ages to the present epoch - I. Formalism and the expected signal. MNRAS, 356:1519–1528. 22, 58

Bittner, J. M. and Loeb, A. (2011). Measuring the redshift of reionization with a modest array of low-frequency dipoles. *JCAP*, 4:38. 76

Bolton, J. S. and Haehnelt, M. G. (2007). The observed ionization rate of the intergalactic medium and the ionizing emissivity at z >= 5: evidence for a photon-starved and extended epoch of reionization. MNRAS, 382:325–341. 62

Bolton, J. S., Haehnelt, M. G., Warren, S. J., Hewett, P. C., Mortlock, D. J., Venemans, B. P., McMahon, R. G., and Simpson, C. (2011). How neutral is the intergalactic medium surrounding the redshift z = 7.085 quasar ULAS J1120+0641? MNRAS, 416:L70–L74. 15

Bond, J. R., Cole, S., Efstathiou, G., and Kaiser, N. (1991). Excursion set mass functions for hierarchical Gaussian fluctuations. ApJ, 379:440–460. xv, 23, 34, 35, 94, 192

Bouwens, R. J., Illingworth, G. D., Oesch, P. A., Trenti, M., Labbé, I., Bradley, L., Carollo, M., van Dokkum, P. G., Gonzalez, V., Holwerda, B., Franx, M., Spitler, L., Smit, R., and Magee, D. (2015). UV Luminosity Functions at Redshifts z $\tilde{4}$ to z $\tilde{1}0$: 10,000 Galaxies from HST Legacy Fields. ApJ, 803:34. 17, 117, 159

Bowman, J. D., Cairns, I., Kaplan, D. L., Murphy, T., Oberoi, D., Staveley-Smith, L., Arcus, W., Barnes, D. G., Bernardi, G., Briggs, F. H., Brown, S., Bunton, J. D., Burgasser, A. J., Cappallo, R. J., Chatterjee, S., Corey, B. E., Coster, A., Deshpande, A., deSouza, L., Emrich, D., Erickson, P., Goeke, R. F., Gaensler, B. M., Greenhill, L. J., Harvey-Smith, L., Hazelton, B. J., Herne, D., Hewitt, J. N., Johnston-Hollitt, M., Kasper, J. C., Kincaid, B. B., Koenig, R., Kratzenberg, E., Lonsdale, C. J., Lynch, M. J., Matthews, L. D., McWhirter, S. R., Mitchell, D. A., Morales, M. F., Morgan, E. H., Ord, S. M., Pathikulangara, J., Prabu, T., Remillard, R. A., Robishaw, T., Rogers, A. E. E., Roshi, A. A., Salah, J. E., Sault, R. J., Shankar, N. U., Srivani, K. S., Stevens, J. B., Subrahmanyan, R., Tingay, S. J., Wayth, R. B., Waterson, M., Webster, R. L., Whitney, A. R., Williams, A. J., Williams, C. L., and Wyithe, J. S. B. (2013). Science with the Murchison Widefield Array. *Pub. Astro. Soc. Australia*, 30:e031. xii, 2

Bowman, J. D., Morales, M. F., and Hewitt, J. N. (2009). Foreground Contamination in Interferometric Measurements of the Redshifted 21 cm Power Spectrum. ApJ, 695:183–199. 154

Bowman, J. D. and Rogers, A. E. E. (2010). A lower limit of $\Delta z > 0.06$ for the duration of the reionization epoch. Nature, 468:796–798. 24, 25

Bromm, V., Ferrara, A., Coppi, P. S., and Larson, R. B. (2001a). The fragmentation of pre-enriched primordial objects. MNRAS, 328:969–976. 121

Bromm, V., Kudritzki, R. P., and Loeb, A. (2001b). Generic Spectrum and Ionization Efficiency of a Heavy Initial Mass Function for the First Stars. ApJ, 552:464–472. 120

Bromm, V. and Loeb, A. (2003). Formation of the First Supermassive Black Holes. ApJ, 596:34–46. 162

Bromm, V. and Loeb, A. (2006). High-Redshift Gamma-Ray Bursts from Population III Progenitors. ApJ, 642:382–388. 18

Bromm, V., Yoshida, N., Hernquist, L., and McKee, C. F. (2009). The formation of the first stars and galaxies. Nature, 459:49–54. 118

Bryan, G. L. and Norman, M. L. (1998). Statistical Properties of X-Ray Clusters: Analytic and Numerical Comparisons. ApJ, 495:80–99. 8

Chapman, E., Abdalla, F. B., Bobin, J., Starck, J.-L., Harker, G., Jelić, V., Labropoulos, P., Zaroubi, S., Brentjens, M. A., de Bruyn, A. G., and Koopmans, L. V. E. (2013). The scale of the problem: recovering images of reionization with Generalized Morphological Component Analysis. MNRAS, 429:165–176. 177

Chen, X. and Miralda-Escudé, J. (2008). The 21 cm Signature of the First Stars. ApJ, 684:18–33. 120

Choudhuri, S., Bharadwaj, S., Ghosh, A., and Ali, S. S. (2014). Visibility-based angular power spectrum estimation in low-frequency radio interferometric observations. MNRAS, 445:4351–4365. 20, 154, 169, 188

Choudhury, T. R. (2009). Analytical Models of the Intergalactic Medium and Reionization. *Current Science*, 97:841. 12

Choudhury, T. R. and Ferrara, A. (2006). Updating reionization scenarios after recent data. MNRAS, 371:L55–L59. xii, 2, 10, 16, 62, 117

Choudhury, T. R. and Ferrara, A. (2007). Searching for the reionization sources. MNRAS, 380:L6–L10. 120

Choudhury, T. R., Haehnelt, M. G., and Regan, J. (2009). Inside-out or outside-in: the topology of reionization in the photon-starved regime suggested by Lyα forest data. MNRAS, 394:960–977. xii, xiii, 3, 12, 21, 23, 29, 32, 55, 118, 160, 193

Choudhury, T. R., Puchwein, E., Haehnelt, M. G., and Bolton, J. S. (2015). Lyman α emitters gone missing: evidence for late reionization? MNRAS, 452:261–277. 18

Christian, P. and Loeb, A. (2013). Measuring the X-ray background in the reionization era with first generation 21 cm experiments. *JCAP*, 9:014. 56, 78, 86, 193

Chuzhoy, L., Alvarez, M. A., and Shapiro, P. R. (2006a). Recognizing the First Radiation Sources through Their 21 cm Signature. ApJ, 648:L1–L4. 31

Chuzhoy, L., Alvarez, M. A., and Shapiro, P. R. (2006b). Recognizing the First Radiation Sources through Their 21 cm Signature. ApJ, 648:L1–L4. 162

Chuzhoy, L. and Zheng, Z. (2007). Radiative Transfer Effect on Ultraviolet Pumping of the 21 cm Line in the High-Redshift Universe. ApJ, 670:912–918. 56

Cooke, J., Ryan-Weber, E. V., Garel, T., and Díaz, C. G. (2014). Lyman-continuum galaxies and the escape fraction of Lyman-break galaxies. MNRAS, 441:837–851. 11

Datta, A., Bowman, J. D., and Carilli, C. L. (2010). Bright Source Subtraction Requirements for Redshifted 21 cm Measurements. ApJ, 724:526–538. 20

Datta, K. K., Bharadwaj, S., and Choudhury, T. R. (2007a). Detecting ionized bubbles in redshifted 21-cm maps. MNRAS, 382:809–818. xix, 118, 119, 130, 133, 137, 138, 149, 150, 160, 170, 181, 182, 198

Datta, K. K., Bharadwaj, S., and Choudhury, T. R. (2009). The optimal redshift for detecting ionized bubbles in HI 21-cm maps. MNRAS, 399:L132–L136. 160

Datta, K. K., Choudhury, T. R., and Bharadwaj, S. (2007b). The multifrequency angular power spectrum of the epoch of reionization 21-cm signal. MNRAS, 378:119–128. 22

Datta, K. K., Friedrich, M. M., Mellema, G., Iliev, I. T., and Shapiro, P. R. (2012a). Prospects of observing a quasar H II region during the epoch of reionization with the redshifted 21-cm signal. MNRAS, 424:762–778. xiii, 29, 32, 55, 102, 115, 160

Datta, K. K., Jensen, H., Majumdar, S., Mellema, G., Iliev, I. T., Mao, Y., Shapiro, P. R., and Ahn, K. (2014). Light cone effect on the reionization 21-cm signal - II. Evolution, anisotropies and observational implications. MNRAS, 442:1491–1506. xviii, 88, 91, 97, 102, 103, 109, 111, 114, 196

Datta, K. K., Majumdar, S., Bharadwaj, S., and Choudhury, T. R. (2008). Simulating the impact of HI fluctuations on matched filter search for ionized bubbles in redshifted 21-cm maps. MNRAS, 391:1900–1912. 160

Datta, K. K., Mellema, G., Mao, Y., Iliev, I. T., Shapiro, P. R., and Ahn, K. (2012b). Light-cone effect on the reionization 21-cm power spectrum. MNRAS, 424:1877–1891. xviii, xix, xxi, 88, 91, 95, 97, 102, 103, 118, 119, 160

Davis, M., Efstathiou, G., Frenk, C. S., and White, S. D. M. (1985). The evolution of large-scale structure in a universe dominated by cold dark matter. ApJ, 292:371–394. 9

Dayal, P., Ferrara, A., and Saro, A. (2010). The cool side of Lyman alpha emitters. MNRAS, 402:1449–1457. 37

Dayal, P., Ferrara, A., Saro, A., Salvaterra, R., Borgani, S., and Tornatore, L. (2009). Lyman alpha emitter evolution in the reionization epoch. MNRAS, 400:2000–2011. 37

de Souza, R. S., Ishida, E. E. O., Johnson, J. L., Whalen, D. J., and Mesinger, A. (2013). Detectability of the first cosmic explosions. MNRAS, 436:1555–1563. 117

de Souza, R. S., Ishida, E. E. O., Whalen, D. J., Johnson, J. L., and Ferrara, A. (2014). Probing the stellar initial mass function with high-z supernovae. MNRAS, 442:1640–1655. 117

Dewdney, P. (2013). Document number SKA-TEL-SKO-DD-001 Revision 1. 131. 128

Di Matteo, T., Ciardi, B., and Miniati, F. (2004). The 21-cm emission from the reionization epoch: extended and point source foregrounds. MNRAS, 355:1053–1065. 20

Di Matteo, T., Perna, R., Abel, T., and Rees, M. J. (2002). Radio Foregrounds for the 21 Centimeter Tomography of the Neutral Intergalactic Medium at High Redshifts. ApJ, 564:576–580. 170

Dijkstra, M. (2014). Lyα Emitting Galaxies as a Probe of Reionisation. *Pub. Astro. Soc. Australia*, 31:e040. 142

Dijkstra, M., Haiman, Z., and Loeb, A. (2004). A Limit from the X-Ray Background on the Contribution of Quasars to Reionization. ApJ, 613:646–654. 18

Dijkstra, M., Mesinger, A., and Wyithe, J. S. B. (2011). The detectability of Lyα emission from galaxies during the epoch of reionization. MNRAS, 414:2139–2147. 18

Dillon, J. S., Liu, A., Williams, C. L., Hewitt, J. N., Tegmark, M., Morgan, E. H., Levine, A. M., Morales, M. F., Tingay, S. J., Bernardi, G., Bowman, J. D., Briggs, F. H., Cappallo, R. C., Emrich, D., Mitchell, D. A., Oberoi, D., Prabu, T., Wayth, R., and Webster, R. L. (2014). Overcoming real-world obstacles in 21 cm power spectrum estimation: A method demonstration and results from early Murchison Widefield Array data. Phys. Rev. D, 89(2):023002. 20, 26

Dove, J. B., Shull, J. M., and Ferrara, A. (2000). The Escape of Ionizing Photons from OB Associations in Disk Galaxies: Radiation Transfer through Superbubbles. ApJ, 531:846–860. 10

Einstein, A. (1916). Die Grundlage der allgemeinen Relativitätstheorie. *Annalen der Physik*, 354:769–822. 4

Ellis, R. S., McLure, R. J., Dunlop, J. S., Robertson, B. E., Ono, Y., Schenker, M. A., Koekemoer, A., Bowler, R. A. A., Ouchi, M., Rogers, A. B., Curtis-Lake, E., Schneider, E., Charlot, S., Stark, D. P., Furlanetto, S. R., and Cirasuolo, M. (2013). The Abundance of Star-forming Galaxies in the Redshift Range 8.5-12: New Results from the 2012 Hubble Ultra Deep Field Campaign. ApJ, 763:L7. 17, 117, 159

Elvis, M., Wilkes, B. J., McDowell, J. C., Green, R. F., Bechtold, J., Willner, S. P., Oey, M. S., Polomski, E., and Cutri, R. (1994). Atlas of quasar energy distributions. ApJS, 95:1–68. 37

Ewall-Wice, A., Dillon, J. S., Hewitt, J. N., Loeb, A., Mesinger, A., Neben, A. R., Offringa, A. R., Tegmark, M., Barry, N., Beardsley, A. P., Bernardi, G., Bowman, J. D., Briggs, F., Cappallo, R. J., Carroll, P., Corey, B. E., de Oliveira-Costa, A., Emrich, D., Feng, L., Gaensler, B. M., Goeke, R., Greenhill, L. J., Hazelton, B. J., Hurley-Walker, N., Johnston-Hollit, M., Jacobs, D. C., Kaplan, D. L., Kasper, J. C., Kim, H., Kratzenberg, E., Lenc, E., Line, J., Lonsdale, C. J., Lynch, M. J., McKinley, B., McWhirter, S. R., Mitchell, D. A., Morales, M. F., Morgan, E., Thyagarajan, N., Oberoi, D., Ord, S. M., Paul, S., Pindor, B., Pober, J. C., Prabu, T., Procopio, P., Riding, J., Rogers, A. E. E., Roshi, A., Udaya Shankar, N., Sethi, S. K., Srivani, K. S., Subrahmanyan, R., Sullivan, I. S., Tingay, S. J., Trott, C. M., Waterson, M., Wayth, R. B., Webster, R. L., Whitney, A. R., Williams, A., Williams, C. L., Wu, C., and Wyithe, J. S. B. (2016). First Limits on the 21 cm Power Spectrum during the Epoch of X-ray heating. *ArXiv e-prints*. 26

Fan, X., Strauss, M. A., Becker, R. H., White, R. L., Gunn, J. E., Knapp, G. R., Richards, G. T., Schneider, D. P., Brinkmann, J., and Fukugita, M. (2006a). Constraining the Evolution of the Ionizing Background and the Epoch of Reionization with z˜6 Quasars. II. A Sample of 19 Quasars. AJ, 132:117–136. 15, 117, 159

Fan, X., Strauss, M. A., Richards, G. T., Hennawi, J. F., Becker, R. H., White, R. L., Diamond-Stanic, A. M., Donley, J. L., Jiang, L., Kim, J. S., Vestergaard, M., Young, J. E., Gunn, J. E., Lupton, R. H., Knapp, G. R., Schneider, D. P., Brandt, W. N., Bahcall, N. A., Barentine, J. C., Brinkmann, J., Brewington,

H. J., Fukugita, M., Harvanek, M., Kleinman, S. J., Krzesinski, J., Long, D., Neilsen, Jr., E. H., Nitta, A., Snedden, S. A., and Voges, W. (2006b). A Survey of z>5.7 Quasars in the Sloan Digital Sky Survey. IV. Discovery of Seven Additional Quasars. AJ, 131:1203–1209. xi, xii, 1, 2, 10, 14, 16, 62, 117

Fan, X., Strauss, M. A., Schneider, D. P., Becker, R. H., White, R. L., Haiman, Z., Gregg, M., Pentericci, L., Grebel, E. K., Narayanan, V. K., Loh, Y.-S., Richards, G. T., Gunn, J. E., Lupton, R. H., Knapp, G. R., Ivezić, Ž., Brandt, W. N., Collinge, M., Hao, L., Harbeck, D., Prada, F., Schaye, J., Strateva, I., Zakamska, N., Anderson, S., Brinkmann, J., Bahcall, N. A., Lamb, D. Q., Okamura, S., Szalay, A., and York, D. G. (2003). A Survey of z>5.7 Quasars in the Sloan Digital Sky Survey. II. Discovery of Three Additional Quasars at z>6. AJ, 125:1649–1659. xii, 1, 14, 62

Ferrara, A. and Loeb, A. (2013). Escape fraction of the ionizing radiation from starburst galaxies at high redshifts. MNRAS, 431:2826–2833. 10, 11

Fialkov, A., Barkana, R., and Cohen, A. (2015). Reconstructing the Nature of the First Cosmic Sources from the Anisotropic 21-cm Signal. *Physical Review Letters*, 114(10):101303. 111

Fialkov, A., Barkana, R., and Visbal, E. (2014). The observable signature of late heating of the Universe during cosmic reionization. Nature, 506:197–199. 37, 56, 107, 115, 162

Field, G. B. (1958). Excitation of the Hydrogen 21-CM Line. *Proceedings of the IRE*, 46:240–250. 30, 31

Finkelstein, S. L., Rhoads, J. E., Malhotra, S., and Grogin, N. (2009). Lyman Alpha Galaxies: Primitive, Dusty, or Evolved? ApJ, 691:465–481. 36, 121

Fioc, M. and Rocca-Volmerange, B. (1997). PEGASE: a UV to NIR spectral evolution model of galaxies. Application to the calibration of bright galaxy counts. A&A, 326:950–962. 37, 86, 121

Fixsen, D. J. (2009). The Temperature of the Cosmic Microwave Background. ApJ, 707:916–920. 5

Fragos, T., Lehmer, B., Tremmel, M., Tzanavaris, P., Basu-Zych, A., Belczynski, K., Hornschemeier, A., Jenkins, L., Kalogera, V., Ptak, A., and Zezas, A. (2013a). X-Ray Binary Evolution Across Cosmic Time. ApJ, 764:41. 37, 122

Fragos, T., Lehmer, B. D., Naoz, S., Zezas, A., and Basu-Zych, A. (2013b). Energy Feedback from X-Ray Binaries in the Early Universe. ApJ, 776:L31. 37, 122

Friedmann, A. (1922). Über die Krümmung des Raumes. *Zeitschrift fur Physik*, 10:377–386. 5

Friedrich, M. M., Mellema, G., Alvarez, M. A., Shapiro, P. R., and Iliev, I. T. (2011). Topology and sizes of H II regions during cosmic reionization. MNRAS, 413:1353–1372. 67

Fryxell, B., Olson, K., Ricker, P., Timmes, F. X., Zingale, M., Lamb, D. Q., MacNeice, P., Rosner, R., Truran, J. W., and Tufo, H. (2000). FLASH: An Adaptive Mesh Hydrodynamics Code for Modeling Astrophysical Thermonuclear Flashes. ApJS, 131:273–334. 23

Fujita, A., Martin, C. L., Mac Low, M.-M., and Abel, T. (2003). The Influence of Supershells and Galactic Outflows on the Escape of Ionizing Radiation from Dwarf Starburst Galaxies. ApJ, 599:50–69. 10

Furlanetto, S. R. and Furlanetto, M. R. (2007). Spin-exchange rates in electron-hydrogen collisions. MNRAS, 374:547–555. 31

Furlanetto, S. R. and Oh, S. P. (2006). Redshifted 21 cm Emission from Minihalos before Reionization. ApJ, 652:849–856. 30, 120

Furlanetto, S. R., Oh, S. P., and Briggs, F. H. (2006). Cosmology at low frequencies: The 21 cm transition and the high-redshift Universe. Phys. Rep., 433:181–301. xii, xiv, 1, 2, 9, 18, 31, 43

Furlanetto, S. R., Zaldarriaga, M., and Hernquist, L. (2004a). Statistical Probes of Reionization with 21 Centimeter Tomography. ApJ, 613:16–22. xii, xiii, 3, 19, 21, 29, 32, 55, 118, 160

Furlanetto, S. R., Zaldarriaga, M., and Hernquist, L. (2004b). The Growth of H II Regions During Reionization. ApJ, 613:1–15. 22

Geil, P. M. and Wyithe, J. S. B. (2008). The impact of a percolating IGM on redshifted 21-cm observations of quasar HII regions. MNRAS, 386:1683–1694. xix, 12, 22, 118, 119, 160, 198

Ghara, R., Choudhury, T. R., and Datta, K. K. (2015a). 21 cm signal from cosmic dawn: imprints of spin temperature fluctuations and peculiar velocities. MNRAS, 447:1806–1825. xiii, xvii, 3, 12, 21, 24, 29, 55, 58, 118, 125, 145, 160, 183, 192, 194

Ghara, R., Choudhury, T. R., and Datta, K. K. (2016a). 21-cm signature of the first sources in the Universe: prospects of detection with SKA. MNRAS, 460:827–843. 117, 181

Ghara, R., Choudhury, T. R., Datta, K. K., and Choudhuri, S. (2016b). Imaging the redshifted 21-cm pattern around the first sources during the cosmic dawn using the SKA. MNRAS. 159

Ghara, R., Datta, K. K., and Choudhury, T. R. (2015b). 21 cm signal from cosmic dawn - II. Imprints of the light-cone effects. MNRAS, 453:3143–3156. xix, 58, 91, 118, 145, 147, 160, 183, 196

Ghosh, A., Koopmans, L. V. E., Chapman, E., and Jelić, V. (2015). A Bayesian analysis of redshifted 21-cm H I signal and foregrounds: simulations for LOFAR. MNRAS, 452:1587–1600. 19

Ghosh, A., Prasad, J., Bharadwaj, S., Ali, S. S., and Chengalur, J. N. (2012). Characterizing foreground for redshifted 21 cm radiation: 150 MHz Giant Metrewave Radio Telescope observations. MNRAS, 426:3295–3314. xii, 2, 19, 169, 170

Gleser, L., Nusser, A., and Benson, A. J. (2008). Decontamination of cosmological 21-cm maps. MNRAS, 391:383–398. 154

Gnedin, N. Y. and Abel, T. (2001). Multi-dimensional cosmological radiative transfer with a Variable Eddington Tensor formalism. *New Astronomy*, 6:437–455. 23

Goto, T., Utsumi, Y., Hattori, T., Miyazaki, S., and Yamauchi, C. (2011). A Gunn-Peterson test with a QSO at z = 6.4. MNRAS, 415:L1–L5. xii, 1, 2, 14, 117

Greenhill, L. J. and Bernardi, G. (2012). HI Epoch of Reionization Arrays. *ArXiv e-prints*. 25

Greif, T. H., Glover, S. C. O., Bromm, V., and Klessen, R. S. (2010). The First Galaxies: Chemical Enrichment, Mixing, and Star Formation. ApJ, 716:510–520. 159

Greig, B. and Mesinger, A. (2015). 21CMMC: an MCMC analysis tool enabling astrophysical parameter studies of the cosmic 21 cm signal. MNRAS, 449:4246–4263. 23

Gu, J., Xu, H., Wang, J., An, T., and Chen, W. (2013). The Application of Continuous Wavelet Transform Based Foreground Subtraction Method in 21 cm Sky Surveys. ApJ, 773:38. 154, 179

Gunn, J. E. and Peterson, B. A. (1965). On the Density of Neutral Hydrogen in Intergalactic Space. ApJ, 142:1633–1641. xii, 1, 14, 15, 62

Harker, G., Zaroubi, S., Bernardi, G., Brentjens, M. A., de Bruyn, A. G., Ciardi, B., Jelić, V., Koopmans, L. V. E., Labropoulos, P., Mellema, G., Offringa, A., Pandey, V. N., Pawlik, A. H., Schaye, J., Thomas, R. M., and Yatawatta, S. (2010). Power spectrum extraction for redshifted 21-cm Epoch of Reionization experiments: the LOFAR case. MNRAS, 405:2492–2504. 154, 177

Harnois-Déraps, J., Pen, U.-L., Iliev, I. T., Merz, H., Emberson, J. D., and Desjacques, V. (2013). High-performance P^3M N-body code: CUBEP^{3}M. MNRAS, 436:540–559. 33, 86, 94

Hasegawa, K. and Umemura, M. (2010). START: smoothed particle hydrodynamics with tree-based accelerated radiative transfer. MNRAS, 407:2632–2644. 23

Hassan, S., Davé, R., Finlator, K., and Santos, M. G. (2016). Simulating the 21 cm signal from reionization including non-linear ionizations and inhomogeneous recombinations. MNRAS, 457:1550–1567. 12

Hinshaw, G., Weiland, J. L., Hill, R. S., Odegard, N., Larson, D., Bennett, C. L., Dunkley, J., Gold, B., Greason, M. R., Jarosik, N., Komatsu, E., Nolta, M. R., Page, L., Spergel, D. N., Wollack, E., Halpern, M., Kogut, A., Limon, M., Meyer, S. S., Tucker, G. S., and Wright, E. L. (2009). Five-Year Wilkinson Microwave Anisotropy Probe Observations: Data Processing, Sky Maps, and Basic Results. ApJS, 180:225–245. 62

Hirata, C. M. (2006). Wouthuysen-Field coupling strength and application to high-redshift 21-cm radiation. MNRAS, 367:259–274. 31

Hirata, C. M. and Sigurdson, K. (2007). The spin-resolved atomic velocity distribution and 21-cm line profile of dark-age gas. MNRAS, 375:1241–1264. 31

Hu, E. M., Cowie, L. L., Barger, A. J., Capak, P., Kakazu, Y., and Trouille, L. (2010). An Atlas of z = 5.7 and z = 6.5 Lyα Emitters. ApJ, 725:394–423. 17, 117, 159

Hubble, E. and Humason, M. L. (1931). The Velocity-Distance Relation among Extra-Galactic Nebulae. ApJ, 74:43. 4, 5

Hui, L. and Haiman, Z. (2003). The Thermal Memory of Reionization History. ApJ, 596:9–18. 18

Iliev, I. T., Ciardi, B., Alvarez, M. A., Maselli, A., Ferrara, A., Gnedin, N. Y., Mellema, G., Nakamoto, T., Norman, M. L., Razoumov, A. O., Rijkhorst, E.-J., Ritzerveld, J., Shapiro, P. R., Susa, H., Umemura, M., and Whalen, D. J. (2006). Cosmological radiative transfer codes comparison project - I. The static density field tests. MNRAS, 371:1057–1086. xiii, 3, 21, 118, 160

Iliev, I. T., Mellema, G., Ahn, K., Shapiro, P. R., Mao, Y., and Pen, U.-L. (2014). Simulating cosmic reionization: how large a volume is large enough? MNRAS, 439:725–743. xiii, 29, 32, 55

Jelić, V., Zaroubi, S., Labropoulos, P., Bernardi, G., de Bruyn, A. G., and Koopmans, L. V. E. (2010). Realistic simulations of the Galactic polarized foreground: consequences for 21-cm reionization detection experiments. MNRAS, 409:1647–1659. 154

Jelić, V., Zaroubi, S., Labropoulos, P., Thomas, R. M., Bernardi, G., Brentjens, M. A., de Bruyn, A. G., Ciardi, B., Harker, G., Koopmans, L. V. E., Pandey, V. N., Schaye, J., and Yatawatta, S. (2008). Foreground simulations for the LOFAR-epoch of reionization experiment. MNRAS, 389:1319–1335. 76, 169

Jensen, H., Datta, K. K., Mellema, G., Chapman, E., Abdalla, F. B., Iliev, I. T., Mao, Y., Santos, M. G., Shapiro, P. R., Zaroubi, S., Bernardi, G., Brentjens, M. A., de Bruyn, A. G., Ciardi, B., Harker, G. J. A., Jelić, V., Kazemi, S., Koopmans, L. V. E., Labropoulos, P., Martinez, O., Offringa, A. R., Pandey, V. N., Schaye, J., Thomas, R. M., Veligatla, V., Vedantham, H., and Yatawatta, S. (2013). Probing reionization with LOFAR using 21-cm redshift space distortions. MNRAS, 435:460–474. xvi, 57, 58, 73, 74, 75, 82, 88, 92, 128, 195

Kaaret, P. (2014). X-ray luminous binaries, metallicity, and the early Universe. MNRAS, 440:L26–L30. 122, 162

Kashikawa, N., Shimasaku, K., Matsuda, Y., Egami, E., Jiang, L., Nagao, T., Ouchi, M., Malkan, M. A., Hattori, T., Ota, K., Taniguchi, Y., Okamura, S., Ly, C., Iye, M., Furusawa, H., Shioya, Y., Shibuya, T., Ishizaki, Y., and Toshikawa, J. (2011). Completing the Census of Lyα Emitters at the Reionization Epoch. ApJ, 734:119. 17, 117, 159

Khaire, V., Srianand, R., Choudhury, T. R., and Gaikwad, P. (2015). The redshift evolution of escape fraction of hydrogen ionizing photons from galaxies. *ArXiv e-prints*. 10

Khaire, V., Srianand, R., Choudhury, T. R., and Gaikwad, P. (2016). The redshift evolution of escape fraction of hydrogen ionizing photons from galaxies. MNRAS, 457:4051–4062. 189

Knevitt, G., Wynn, G. A., Power, C., and Bolton, J. S. (2014). Heating and ionization of the primordial intergalactic medium by high-mass X-ray binaries. MNRAS, 445:2034–2048. 162

Komatsu, E., Smith, K. M., Dunkley, J., Bennett, C. L., Gold, B., Hinshaw, G., Jarosik, N., Larson, D., Nolta, M. R., Page, L., Spergel, D. N., Halpern,

M., Hill, R. S., Kogut, A., Limon, M., Meyer, S. S., Odegard, N., Tucker, G. S., Weiland, J. L., Wollack, E., and Wright, E. L. (2011). Seven-year Wilkinson Microwave Anisotropy Probe (WMAP) Observations: Cosmological Interpretation. ApJS, 192:18. xii, 1, 15, 16

Kuhlen, M. and Madau, P. (2005). The first miniquasar. MNRAS, 363:1069–1082. 40

La Plante, P., Battaglia, N., Natarajan, A., Peterson, J. B., Trac, H., Cen, R., and Loeb, A. (2014). Reionization on Large Scales. IV. Predictions for the 21 cm Signal Incorporating the Light Cone Effect. ApJ, 789:31. xiii, xviii, 3, 88, 91, 97

Labropoulos, P., Koopmans, L. V. E., Jelic, V., Yatawatta, S., Thomas, R. M., Bernardi, G., Brentjens, M., de Bruyn, G., Ciardi, B., Harker, G., Offringa, A., Pandey, V. N., Schaye, J., and Zaroubi, S. (2009). The LOFAR EoR Data Model: (I) Effects of Noise and Instrumental Corruptions on the 21-cm Reionization Signal-Extraction Strategy. *ArXiv e-prints*. 20

Lacey, C. and Cole, S. (1994). Merger Rates in Hierarchical Models of Galaxy Formation - Part Two - Comparison with N-Body Simulations. MNRAS, 271:676. 9

Lai, K., Huang, J.-S., Fazio, G., Cowie, L. L., Hu, E. M., and Kakazu, Y. (2007). The Stellar Population of Lyα-emitting Galaxies at z ˜ 5.7. ApJ, 655:704–713. 36, 121

Laor, A., Fiore, F., Elvis, M., Wilkes, B. J., and McDowell, J. C. (1997). The Soft X-Ray Properties of a Complete Sample of Optically Selected Quasars. II. Final Results. ApJ, 477:93–113. 37, 122, 163

Lewis, A., Challinor, A., and Lasenby, A. (2000). Efficient Computation of Cosmic Microwave Background Anisotropies in Closed Friedmann-Robertson-Walker Models. ApJ, 538:473–476. 33, 94

Loeb, A. (2006). First Light. *ArXiv Astrophysics e-prints*. 1, 11

Madau, P. and Haardt, F. (2015). Cosmic Reionization after Planck: Could Quasars Do It All? ApJ, 813:L8. 189

Madau, P., Meiksin, A., and Rees, M. J. (1997). 21 Centimeter Tomography of the Intergalactic Medium at High Redshift. ApJ, 475:429–444. xiv, 31

Maio, U., Ciardi, B., Dolag, K., Tornatore, L., and Khochfar, S. (2010). The transition from population III to population II-I star formation. MNRAS, 407:1003–1015. 121

Majumdar, S., Bharadwaj, S., and Choudhury, T. R. (2012). Constrainingquasar and intergalactic medium properties through bubble detection in redshifted 21-cm maps. MNRAS, 426:3178–3194. 118

Majumdar, S., Bharadwaj, S., and Choudhury, T. R. (2013). The effect of peculiar velocities on the epoch of reionization 21-cm signal. MNRAS, 434:1978–1988. xvi, 57, 58, 74, 75, 82, 88, 92, 102, 195

Majumdar, S., Bharadwaj, S., Datta, K. K., and Choudhury, T. R. (2011). The impact of anisotropy from finite light traveltime on detecting ionized bubbles in redshifted 21-cm maps. MNRAS, 413:1409–1418. 160

Majumdar, S., Mellema, G., Datta, K. K., Jensen, H., Choudhury, T. R., Bharadwaj, S., and Friedrich, M. M. (2014). On the use of seminumerical simulations in predicting the 21-cm signal from the epoch of reionization. MNRAS, 443:2843–2861. 23, 88

Malhotra, S. and Rhoads, J. E. (2006). The Volume Fraction of Ionized Intergalactic Gas at Redshift z=6.5. ApJ, 647:L95–L98. 10, 16, 62

Mannucci, F., Cresci, G., Maiolino, R., Marconi, A., and Gnerucci, A. (2010). A fundamental relation between mass, star formation rate and metallicity in local and high-redshift galaxies. MNRAS, 408:2115–2127. 11

Mao, Y., Shapiro, P. R., Mellema, G., Iliev, I. T., Koda, J., and Ahn, K. (2012). Redshift-space distortion of the 21-cm background from the epoch of reionization - I. Methodology re-examined. MNRAS, 422:926–954. xvi, 57, 58, 60, 70, 73, 74, 82, 92, 195

Maselli, A., Ferrara, A., and Ciardi, B. (2003). CRASH: a radiative transfer scheme. MNRAS, 345:379–394. 23

Mather, J. C., Cheng, E. S., Eplee, Jr., R. E., Isaacman, R. B., Meyer, S. S., Shafer, R. A., Weiss, R., Wright, E. L., Bennett, C. L., Boggess, N. W., Dwek, E., Gulkis, S., Hauser, M. G., Janssen, M., Kelsall, T., Lubin, P. M., Moseley, Jr., S. H., Murdock, T. L., Silverberg, R. F., Smoot, G. F., and Wilkinson, D. T. (1990). A preliminary measurement of the cosmic microwave background spectrum by the Cosmic Background Explorer (COBE) satellite. ApJ, 354:L37–L40. 5

McGreer, I. D., Mesinger, A., and D'Odorico, V. (2015). Model-independent evidence in favour of an end to reionization by z $\sim$ 6. MNRAS, 447:499–505. 15

McQuinn, M. (2012). Constraints on X-ray emissions from the reionization era. MNRAS, 426:1349–1360. 56

McQuinn, M., Hernquist, L., Zaldarriaga, M., and Dutta, S. (2007a). Studying reionization with Lyα emitters. MNRAS, 381:75–96. 18

McQuinn, M., Lidz, A., Zahn, O., Dutta, S., Hernquist, L., and Zaldarriaga, M. (2007b). The morphology of HII regions during reionization. MNRAS, 377:1043–1063. xiii, 3, 12, 21, 23, 118, 160

McQuinn, M., Zahn, O., Zaldarriaga, M., Hernquist, L., and Furlanetto, S. R. (2006). Cosmological Parameter Estimation Using 21 cm Radiation from the Epoch of Reionization. ApJ, 653:815–834. xiii, 29, 32, 55

Mellema, G., Iliev, I. T., Pen, U.-L., and Shapiro, P. R. (2006). Simulating cosmic reionization at large scales - II. The 21-cm emission features and statistical signals. MNRAS, 372:679–692. xiii, 3, 12, 21, 23, 58, 76, 118, 160, 193

Mellema, G., Koopmans, L., Shukla, H., Datta, K. K., Mesinger, A., and Majumdar, S. (2015). HI tomographic imaging of the Cosmic Dawn and Epoch of Reionization with SKA. *Advancing Astrophysics with the Square Kilometre Array (AASKA14)*, page 10. 160

Merz, H., Pen, U.-L., and Trac, H. (2005). Towards optimal parallel PM N-body codes: PMFAST. *New Astronomy*, 10:393–407. 33

Mesinger, A., editor (2016). *Understanding the Epoch of Cosmic Reionization*, volume 423 of *Astrophysics and Space Science Library*. 1

Mesinger, A., Ewall-Wice, A., and Hewitt, J. (2014). Reionization and beyond: detecting the peaks of the cosmological 21 cm signal. MNRAS, 439:3262–3274. 19, 29, 109, 111, 115, 196

Mesinger, A., Ferrara, A., and Spiegel, D. S. (2013). Signatures of X-rays in the early Universe. MNRAS, 431:621–637. 64, 65

Mesinger, A. and Furlanetto, S. (2007). Efficient Simulations of Early Structure Formation and Reionization. ApJ, 669:663–675. xiii, 3, 12, 21, 22, 29, 32, 55, 118, 160

Mesinger, A., Furlanetto, S., and Cen, R. (2011). 21CMFAST: a fast, seminumerical simulation of the high-redshift 21-cm signal. MNRAS, 411:955–972. 86, 193

Meynet, G. and Maeder, A. (2005). Stellar evolution with rotation. XI. Wolf-Rayet star populations at different metallicities. A&A, 429:581–598. 36, 37, 123, 163

Mirabel, I. F., Dijkstra, M., Laurent, P., Loeb, A., and Pritchard, J. R. (2011). Stellar black holes at the dawn of the universe. A&A, 528:A149. 162

Mitra, S., Choudhury, T. R., and Ferrara, A. (2011). Reionization constraints using principal component analysis. MNRAS, 413:1569–1580. xii, 2, 10, 16, 117

Mitra, S., Choudhury, T. R., and Ferrara, A. (2012). Joint quasar-cosmic microwave background constraints on reionization history. MNRAS, 419:1480–1488. xii, 2, 10, 16, 117

Mitra, S., Choudhury, T. R., and Ferrara, A. (2015). Cosmic reionization after Planck. MNRAS, 454:L76–L80. xii, xxix, 2, 11, 13, 14, 17, 117, 132

Mitra, S., Choudhury, T. R., and Ferrara, A. (2016). Cosmic reionization after Planck II: contribution from quasars. *ArXiv e-prints*. 189

Mo, H., van den Bosch, F., and White, S. (2010). *Galaxy Formation and Evolution*. 4

Morales, M. F. and Wyithe, J. S. B. (2010). Reionization and Cosmology with 21-cm Fluctuations. ARA&A, 48:127–171. xii, 1, 2, 18, 29

Mortlock, D. J., Warren, S. J., Venemans, B. P., Patel, M., Hewett, P. C., McMahon, R. G., Simpson, C., Theuns, T., Gonzáles-Solares, E. A., Adamson, A., Dye, S., Hambly, N. C., Hirst, P., Irwin, M. J., Kuiper, E., Lawrence, A., and Röttgering, H. J. A. (2011a). A luminous quasar at a redshift of z = 7.085. Nature, 474:616–619. 15, 117

Mortlock, D. J., Warren, S. J., Venemans, B. P., Patel, M., Hewett, P. C., McMahon, R. G., Simpson, C., Theuns, T., Gonzáles-Solares, E. A., Adamson, A., Dye, S., Hambly, N. C., Hirst, P., Irwin, M. J., Kuiper, E., Lawrence, A., and Röttgering, H. J. A. (2011b). A luminous quasar at a redshift of z = 7.085. Nature, 474:616–619. 15

O'Shea, B. W. and Norman, M. L. (2007). Population III Star Formation in a ΛCDM Universe. I. The Effect of Formation Redshift and Environment on Protostellar Accretion Rate. ApJ, 654:66–92. 118

O'Shea, B. W., Wise, J. H., Xu, H., and Norman, M. L. (2015). Probing the Ultraviolet Luminosity Function of the Earliest Galaxies with the Renaissance Simulations. ApJ, 807:L12. 162

Ouchi, M., Shimasaku, K., Furusawa, H., Saito, T., Yoshida, M., Akiyama, M., Ono, Y., Yamada, T., Ota, K., Kashikawa, N., Iye, M., Kodama, T., Okamura, S., Simpson, C., and Yoshida, M. (2010a). Statistics of 207 Lyα Emitters at a Redshift Near 7: Constraints on Reionization and Galaxy Formation Models. ApJ, 723:869–894. 17

Ouchi, M., Shimasaku, K., Furusawa, H., Saito, T., Yoshida, M., Akiyama, M., Ono, Y., Yamada, T., Ota, K., Kashikawa, N., Iye, M., Kodama, T., Okamura, S., Simpson, C., and Yoshida, M. (2010b). Statistics of 207 Lyα Emitters at a Redshift Near 7: Constraints on Reionization and Galaxy Formation Models. ApJ, 723:869–894. 117, 159

Paardekooper, J.-P., Kruip, C. J. H., and Icke, V. (2010). SimpleX2: radiative transfer on an unstructured, dynamic grid. A&A, 515:A79. 23

Paciga, G., Albert, J. G., Bandura, K., Chang, T.-C., Gupta, Y., Hirata, C., Odegova, J., Pen, U.-L., Peterson, J. B., Roy, J., Shaw, J. R., Sigurdson, K., and Voytek, T. (2013). A simulation-calibrated limit on the H I power spectrum from the GMRT Epoch of Reionization experiment. MNRAS, 433:639–647. xii, 2, 25

Paciga, G., Chang, T.-C., Gupta, Y., Nityanada, R., Odegova, J., Pen, U.-L., Peterson, J. B., Roy, J., and Sigurdson, K. (2011). The GMRT Epoch of Reionization experiment: a new upper limit on the neutral hydrogen power spectrum at z $\tilde{8}$.6. MNRAS, 413:1174–1183. 21, 26

Pacucci, F., Mesinger, A., Mineo, S., and Ferrara, A. (2014). The X-ray spectra of the first galaxies: 21 cm signatures. MNRAS, 443:678–686. 37, 56, 122

Padmanabhan, T. (1993). *Structure Formation in the Universe*. 4, 7

Paranjape, A. and Choudhury, T. R. (2014). An improved model of H II bubbles during the epoch of reionization. MNRAS, 442:1470–1482. xii, 3, 21, 22, 118, 160

Parsons, A. R., Liu, A., Aguirre, J. E., Ali, Z. S., Bradley, R. F., Carilli, C. L., DeBoer, D. R., Dexter, M. R., Gugliucci, N. E., Jacobs, D. C., Klima, P., MacMahon, D. H. E., Manley, J. R., Moore, D. F., Pober, J. C., Stefan, I. I., and Walbrugh, W. P. (2013). New Limits on 21cm EoR From PAPER-32 Consistent with an X-Ray Heated IGM at z=7.7. *arXiv-1304.4991*. 26

Parsons, A. R., Liu, A., Aguirre, J. E., Ali, Z. S., Bradley, R. F., Carilli, C. L., DeBoer, D. R., Dexter, M. R., Gugliucci, N. E., Jacobs, D. C., Klima, P., MacMahon, D. H. E., Manley, J. R., Moore, D. F., Pober, J. C., Stefan, I. I., and Walbrugh, W. P. (2014). New Limits on 21 cm Epoch of Reionization from PAPER-32 Consistent with an X-Ray Heated Intergalactic Medium at z = 7.7. ApJ, 788:106. xii, 2

Patil, A. H., Zaroubi, S., Chapman, E., Jelić, V., Harker, G., Abdalla, F. B., Asad, K. M. B., Bernardi, G., Brentjens, M. A., de Bruyn, A. G., Bus, S.,

Ciardi, B., Daiboo, S., Fernandez, E. R., Ghosh, A., Jensen, H., Kazemi, S., Koopmans, L. V. E., Labropoulos, P., Mevius, M., Martinez, O., Mellema, G., Offringa, A. R., Pandey, V. N., Schaye, J., Thomas, R. M., Vedantham, H. K., Veligatla, V., Wijnholds, S. J., and Yatawatta, S. (2014a). Constraining the epoch of reionization with the variance statistic: simulations of the LOFAR case. MNRAS, 443:1113–1124. 19

Patil, A. H., Zaroubi, S., Chapman, E., Jelić, V., Harker, G., Abdalla, F. B., Asad, K. M. B., Bernardi, G., Brentjens, M. A., de Bruyn, A. G., Bus, S., Ciardi, B., Daiboo, S., Fernandez, E. R., Ghosh, A., Jensen, H., Kazemi, S., Koopmans, L. V. E., Labropoulos, P., Mevius, M., Martinez, O., Mellema, G., Offringa, A. R., Pandey, V. N., Schaye, J., Thomas, R. M., Vedantham, H. K., Veligatla, V., Wijnholds, S. J., and Yatawatta, S. (2014b). Constraining the epoch of reionization with the variance statistic: simulations of the LOFAR case. *arXiv-1401.4172*. 76, 86

Patra, N., Subrahmanyan, R., Sethi, S., Udaya Shankar, N., and Raghunathan, A. (2015). Saras Measurement of the Radio Background At Long Wavelengths. ApJ, 801:138. 24

Pawlik, A. H., Milosavljević, M., and Bromm, V. (2011). The First Galaxies: Assembly of Disks and Prospects for Direct Detection. ApJ, 731:54. 159

Pawlik, A. H. and Schaye, J. (2008). TRAPHIC - radiative transfer for smoothed particle hydrodynamics simulations. MNRAS, 389:651–677. 23

Peacock, J. A. (1999). *Cosmological Physics, Cambridge University Press (1999)* . 4, 7

Peebles, P. J. E. (1993). *Principles of Physical Cosmology*. 4

Planck Collaboration, Adam, R., Ade, P. A. R., Aghanim, N., Arnaud, M., Ashdown, M., Aumont, J., Baccigalupi, C., Banday, A. J., Barreiro, R. B., and et al. (2015a). Planck 2015 results. VIII. High Frequency Instrument data processing: Calibration and maps. *ArXiv e-prints*. 5

Planck Collaboration, Adam, R., Aghanim, N., Ashdown, M., Aumont, J., Baccigalupi, C., Ballardini, M., Banday, A. J., Barreiro, R. B., Bartolo, N., Basak, S.,

Battye, R., Benabed, K., Bernard, J.-P., Bersanelli, M., Bielewicz, P., Bock, J. J., Bonaldi, A., Bonavera, L., Bond, J. R., Borrill, J., Bouchet, F. R., Bucher, M., Burigana, C., Calabrese, E., Cardoso, J.-F., Carron, J., Chiang, H. C., Colombo, L. P. L., Combet, C., Comis, B., Coulais, A., Crill, B. P., Curto, A., Cuttaia, F., Davis, R. J., de Bernardis, P., de Rosa, A., de Zotti, G., Delabrouille, J., Di Valentino, E., Dickinson, C., Diego, J. M., Doré, O., Douspis, M., Ducout, A., Dupac, X., Elsner, F., Enßlin, T. A., Eriksen, H. K., Falgarone, E., Fantaye, Y., Finelli, F., Forastieri, F., Frailis, M., Fraisse, A. A., Franceschi, E., Frolov, A., Galeotta, S., Galli, S., Ganga, K., Génova-Santos, R. T., Gerbino, M., Ghosh, T., González-Nuevo, J., Górski, K. M., Gruppuso, A., Gudmundsson, J. E., Hansen, F. K., Helou, G., Henrot-Versillé, S., Herranz, D., Hivon, E., Huang, Z., Ili, S., Jaffe, A. H., Jones, W. C., Keihänen, E., Keskitalo, R., Kisner, T. S., Knox, L., Krachmalnicoff, N., Kunz, M., Kurki-Suonio, H., Lagache, G., Lähteenmäki, A., Lamarre, J.-M., Langer, M., Lasenby, A., Lattanzi, M., Lawrence, C. R., Le Jeune, M., Levrier, F., Lewis, A., Liguori, M., Lilje, P. B., López-Caniego, M., Ma, Y.-Z., Macías-Pérez, J. F., Maggio, G., Mangilli, A., Maris, M., Martin, P. G., Martínez-González, E., Matarrese, S., Mauri, N., McEwen, J. D., Meinhold, P. R., Melchiorri, A., Mennella, A., Migliaccio, M., Miville-Deschênes, M.-A., Molinari, D., Moneti, A., Montier, L., Morgante, G., Moss, A., Naselsky, P., Natoli, P., Oxborrow, C. A., Pagano, L., Paoletti, D., Partridge, B., Patanchon, G., Patrizii, L., Perdereau, O., Perotto, L., Pettorino, V., Piacentini, F., Plaszczynski, S., Polastri, L., Polenta, G., Puget, J.-L., Rachen, J. P., Racine, B., Reinecke, M., Remazeilles, M., Renzi, A., Rocha, G., Rossetti, M., Roudier, G., Rubiño-Martín, J. A., Ruiz-Granados, B., Salvati, L., Sandri, M., Savelainen, M., Scott, D., Sirri, G., Sunyaev, R., Suur-Uski, A.-S., Tauber, J. A., Tenti, M., Toffolatti, L., Tomasi, M., Tristram, M., Trombetti, T., Valiviita, J., Van Tent, F., Vielva, P., Villa, F., Vittorio, N., Wandelt, B. D., Wehus, I. K., White, M., Zacchei, A., and Zonca, A. (2016). Planck intermediate results. XLVII. Planck constraints on reionization history. *ArXiv e-prints*. xii, 1

Planck Collaboration, Ade, P. A. R., Aghanim, N., Armitage-Caplan, C., Arnaud, M., Ashdown, M., Atrio-Barandela, F., Aumont, J., Baccigalupi, C., Banday, A. J., and et al. (2014a). Planck 2013 results. XVI. Cosmological parameters.

A&A, 571:A16. xiv, 6, 15, 58, 92, 119, 161

Planck Collaboration, Ade, P. A. R., Aghanim, N., Armitage-Caplan, C., Arnaud, M., Ashdown, M., Atrio-Barandela, F., Aumont, J., Baccigalupi, C., Banday, A. J., and et al. (2014b). Planck 2013 results. XVII. Gravitational lensing by large-scale structure. A&A, 571:A17. 16

Planck Collaboration, Ade, P. A. R., Aghanim, N., Arnaud, M., Ashdown, M., Aumont, J., Baccigalupi, C., Banday, A. J., Barreiro, R. B., Bartlett, J. G., and et al. (2015b). Planck 2015 results. XIII. Cosmological parameters. *ArXiv e-prints*. 4, 6, 11, 16, 97, 132, 183, 189

Planck Collaboration, Ade, P. A. R., Aghanim, N., Arnaud, M., Ashdown, M., Aumont, J., Baccigalupi, C., Banday, A. J., Barreiro, R. B., Bartlett, J. G., and et al. (2015c). Planck 2015 results. XV. Gravitational lensing. *ArXiv e-prints*. 16

Platania, P., Bensadoun, M., Bersanelli, M., De Amici, G., Kogut, A., Levin, S., Maino, D., and Smoot, G. F. (1998). A Determination of the Spectral Index of Galactic Synchrotron Emission in the 1-10 GHz Range. ApJ, 505:473–483. 170

Pober, J. C., Ali, Z. S., Parsons, A. R., McQuinn, M., Aguirre, J. E., Bernardi, G., Bradley, R. F., Carilli, C. L., Cheng, C., DeBoer, D. R., Dexter, M. R., Furlanetto, S. R., Grobbelaar, J., Horrell, J., Jacobs, D. C., Klima, P. J., Kohn, S. A., Liu, A., MacMahon, D. H. E., Maree, M., Mesinger, A., Moore, D. F., Razavi-Ghods, N., Stefan, I. I., Walbrugh, W. P., Walker, A., and Zheng, H. (2015). PAPER-64 Constraints On Reionization. II. The Temperature of the z =8.4 Intergalactic Medium. ApJ, 809:62. 26

Pober, J. C., Liu, A., Dillon, J. S., Aguirre, J. E., Bowman, J. D., Bradley, R. F., Carilli, C. L., DeBoer, D. R., Hewitt, J. N., Jacobs, D. C., McQuinn, M., Morales, M. F., Parsons, A. R., Tegmark, M., and Werthimer, D. J. (2014). What Next-generation 21 cm Power Spectrum Measurements can Teach us About the Epoch of Reionization. ApJ, 782:66. xii, 2, 20

Presley, M. E., Liu, A., and Parsons, A. R. (2015). Measuring the Cosmological 21 cm Monopole with an Interferometer. ApJ, 809:18. 25

Press, W. H. and Schechter, P. (1974). Formation of Galaxies and Clusters of Galaxies by Self-Similar Gravitational Condensation. ApJ, 187:425–438. 9

Pritchard, J. R. and Furlanetto, S. R. (2006). Descending from on high: Lyman-series cascades and spin-kinetic temperature coupling in the 21-cm line. MNRAS, 367:1057–1066. xvi

Pritchard, J. R. and Furlanetto, S. R. (2007). 21-cm fluctuations from inhomogeneous X-ray heating before reionization. MNRAS, 376:1680–1694. 86, 193

Pritchard, J. R. and Loeb, A. (2012). 21 cm cosmology in the 21st century. *Reports on Progress in Physics*, 75(8):086901. xii, 1, 2, 18, 19, 29, 64

Raiter, A., Schaerer, D., and Fosbury, R. A. E. (2010). Predicted UV properties of very metal-poor starburst galaxies. A&A, 523:A64. 17

Raskutti, S., Bolton, J. S., Wyithe, J. S. B., and Becker, G. D. (2012). Thermal constraints on the reionization of hydrogen by Population II stellar sources. MNRAS, 421:1969–1981. 18

Razoumov, A. O. and Cardall, C. Y. (2005). Fully threaded transport engine: new method for multi-scale radiative transfer. MNRAS, 362:1413–1417. 23

Rix, H.-W., Barden, M., Beckwith, S. V. W., Bell, E. F., Borch, A., Caldwell, J. A. R., Häussler, B., Jahnke, K., Jogee, S., McIntosh, D. H., Meisenheimer, K., Peng, C. Y., Sanchez, S. F., Somerville, R. S., Wisotzki, L., and Wolf, C. (2004). GEMS: Galaxy Evolution from Morphologies and SEDs. ApJS, 152:163–173. 39, 123, 163

Robertson, B. E., Ellis, R. S., Dunlop, J. S., McLure, R. J., and Stark, D. P. (2010). Early star-forming galaxies and the reionization of the Universe. Nature, 468:49–55. xxix, 2

Roy, A., Nath, B. B., and Sharma, P. (2015). Narrow escape: how ionizing photons escape from disc galaxies. MNRAS, 451:1939–1954. 10

Santos, M. G., Amblard, A., Pritchard, J., Trac, H., Cen, R., and Cooray, A. (2008). Cosmic Reionization and the 21 cm Signal: Comparison between an

Analytical Model and a Simulation. ApJ, 689:1–16. xiii, 3, 12, 21, 32, 56, 64, 65, 86, 118, 160, 193

Santos, M. G., Cooray, A., Haiman, Z., Knox, L., and Ma, C.-P. (2003). Small-Scale Cosmic Microwave Background Temperature and Polarization Anisotropies Due to Patchy Reionization. ApJ, 598:756–766. 16

Santos, M. G., Cooray, A., and Knox, L. (2005). Multifrequency Analysis of 21 Centimeter Fluctuations from the Era of Reionization. ApJ, 625:575–587. 149, 170

Santos, M. G., Ferramacho, L., Silva, M. B., Amblard, A., and Cooray, A. (2010). Fast large volume simulations of the 21-cm signal from the reionization and pre-reionization epochs. MNRAS, 406:2421–2432. 12, 22

Semelin, B., Combes, F., and Baek, S. (2007). Lyman-alpha radiative transfer during the epoch of reionization: contribution to 21-cm signal fluctuations. A&A, 474:365–374. 56

Shapiro, P. R., Mao, Y., Iliev, I. T., Mellema, G., Datta, K. K., Ahn, K., and Koda, J. (2013). Will Nonlinear Peculiar Velocity and Inhomogeneous Reionization Spoil 21 cm Cosmology from the Epoch of Reionization? *Physical Review Letters*, 110(15):151301. 75

Shaver, P. A., Windhorst, R. A., Madau, P., and de Bruyn, A. G. (1999). Can the reionization epoch be detected as a global signature in the cosmic background? A&A, 345:380–390. 20

Sheth, R. K. and Tormen, G. (1999). Large-scale bias and the peak background split. MNRAS, 308:119–126. 35

Shin, M.-S., Trac, H., and Cen, R. (2008). Cosmological H II Bubble Growth during Reionization. ApJ, 681:756–770. xiii, 3, 12, 21, 118, 160

Shull, J. M. and van Steenberg, M. E. (1985). X-ray secondary heating and ionization in quasar emission-line clouds. ApJ, 298:268–274. 43, 44, 56, 122

Sobacchi, E. and Mesinger, A. (2014). Inhomogeneous recombinations during cosmic reionization. MNRAS, 440:1662–1673. 23

Sokolowski, M., Tremblay, S. E., Wayth, R. B., Tingay, S. J., Clarke, N., Roberts, P., Waterson, M., Ekers, R. D., Hall, P., Lewis, M., Mossammaparast, M., Padhi, S., Schlagenhaufer, F., Sutinjo, A., and Tickner, J. (2015a). BIGHORNS - Broadband Instrument for Global HydrOgen ReioNisation Signal. *Pub. Astro. Soc. Australia*, 32:e004. 25

Sokolowski, M., Wayth, R. B., Tremblay, S. E., Tingay, S. J., Waterson, M., Tickner, J., Emrich, D., Schlagenhaufer, F., Kenney, D., and Padhi, S. (2015b). The Impact of the Ionosphere on Ground-based Detection of the Global Epoch of Reionization Signal. ApJ, 813:18. 21

Stacy, A., Greif, T. H., and Bromm, V. (2010). The first stars: formation of binaries and small multiple systems. MNRAS, 403:45–60. 162

Tanaka, T., Perna, R., and Haiman, Z. (2012). X-ray emission from high-redshift miniquasars: self-regulating the population of massive black holes through global warming. MNRAS, 425:2974–2987. 162

Theuns, T., Zaroubi, S., Kim, T.-S., Tzanavaris, P., and Carswell, R. F. (2002). Temperature fluctuations in the intergalactic medium. MNRAS, 332:367–382. 18

Thomas, R. M. and Zaroubi, S. (2008). Time-evolution of ionization and heating around first stars and miniqsos. MNRAS, 384:1080–1096. xiv, 39, 40, 43, 48, 86, 117, 118, 162, 192

Thomas, R. M. and Zaroubi, S. (2011). On the spin-temperature evolution during the epoch of reionization. MNRAS, 410:1377–1390. xiv, 39, 53, 56, 64, 65

Thomas, R. M., Zaroubi, S., Ciardi, B., Pawlik, A. H., Labropoulos, P., Jelić, V., Bernardi, G., Brentjens, M. A., de Bruyn, A. G., Harker, G. J. A., Koopmans, L. V. E., Mellema, G., Pandey, V. N., Schaye, J., and Yatawatta, S. (2009). Fast large-scale reionization simulations. MNRAS, 393:32–48. xiii, xiv, 3, 12, 21, 24, 48, 49, 51, 86, 118, 160, 192

Thompson, A. R., Moran, J. M., and Swenson, Jr., G. W. (2001). *Interferometry and Synthesis in Radio Astronomy, 2nd Edition*. 128

Tingay, S. J., Goeke, R., Bowman, J. D., Emrich, D., Ord, S. M., Mitchell, D. A., Morales, M. F., Booler, T., Crosse, B., Wayth, R. B., Lonsdale, C. J., Tremblay, S., Pallot, D., Colegate, T., Wicenec, A., Kudryavtseva, N., Arcus, W., Barnes, D., Bernardi, G., Briggs, F., Burns, S., Bunton, J. D., Cappallo, R. J., Corey, B. E., Deshpande, A., Desouza, L., Gaensler, B. M., Greenhill, L. J., Hall, P. J., Hazelton, B. J., Herne, D., Hewitt, J. N., Johnston-Hollitt, M., Kaplan, D. L., Kasper, J. C., Kincaid, B. B., Koenig, R., Kratzenberg, E., Lynch, M. J., Mckinley, B., Mcwhirter, S. R., Morgan, E., Oberoi, D., Pathikulangara, J., Prabu, T., Remillard, R. A., Rogers, A. E. E., Roshi, A., Salah, J. E., Sault, R. J., Udaya-Shankar, N., Schlagenhaufer, F., Srivani, K. S., Stevens, J., Subrahmanyan, R., Waterson, M., Webster, R. L., Whitney, A. R., Williams, A., Williams, C. L., and Wyithe, J. S. B. (2013). The Murchison Widefield Array: The Square Kilometre Array Precursor at Low Radio Frequencies. *Publications of the Astronomical Society of Australia (PASA)*, 30:7. xii, 2

Trac, H. and Cen, R. (2007). Radiative Transfer Simulations of Cosmic Reionization. I. Methodology and Initial Results. ApJ, 671:1–13. 12, 23

Trott, C. M. (2016). Exploring the evolution of reionization using a wavelet transform and the light cone effect. MNRAS, 461:126–135. 111

Trott, C. M., Wayth, R. B., and Tingay, S. J. (2012). The Impact of Point-source Subtraction Residuals on 21 cm Epoch of Reionization Estimation. ApJ, 757:101. 20

van Haarlem, M. P., Wise, M. W., Gunst, A. W., Heald, G., McKean, J. P., Hessels, J. W. T., de Bruyn, A. G., Nijboer, R., Swinbank, J., Fallows, R., Brentjens, M., Nelles, A., Beck, R., Falcke, H., Fender, R., Hörandel, J., Koopmans, L. V. E., Mann, G., Miley, G., Röttgering, H., Stappers, B. W., Wijers, R. A. M. J., Zaroubi, S., van den Akker, M., Alexov, A., Anderson, J., Anderson, K., van Ardenne, A., Arts, M., Asgekar, A., Avruch, I. M., Batejat, F., Bähren, L., Bell, M. E., Bell, M. R., van Bemmel, I., Bennema, P., Bentum, M. J., Bernardi, G., Best, P., Bîrzan, L., Bonafede, A., Boonstra, A.-J., Braun, R., Bregman, J., Breitling, F., van de Brink, R. H., Broderick, J., Broekema, P. C., Brouw, W. N., Brüggen, M., Butcher, H. R., van Cappellen, W., Ciardi, B., Coenen, T., Conway, J., Coolen, A., Corstanje, A., Damstra, S., Davies,

O., Deller, A. T., Dettmar, R.-J., van Diepen, G., Dijkstra, K., Donker, P., Doorduin, A., Dromer, J., Drost, M., van Duin, A., Eislöffel, J., van Enst, J., Ferrari, C., Frieswijk, W., Gankema, H., Garrett, M. A., de Gasperin, F., Gerbers, M., de Geus, E., Grießmeier, J.-M., Grit, T., Gruppen, P., Hamaker, J. P., Hassall, T., Hoeft, M., Holties, H. A., Horneffer, A., van der Horst, A., van Houwelingen, A., Huijgen, A., Iacobelli, M., Intema, H., Jackson, N., Jelic, V., de Jong, A., Juette, E., Kant, D., Karastergiou, A., Koers, A., Kollen, H., Kondratiev, V. I., Kooistra, E., Koopman, Y., Koster, A., Kuniyoshi, M., Kramer, M., Kuper, G., Lambropoulos, P., Law, C., van Leeuwen, J., Lemaitre, J., Loose, M., Maat, P., Macario, G., Markoff, S., Masters, J., McFadden, R. A., McKay-Bukowski, D., Meijering, H., Meulman, H., Mevius, M., Middelberg, E., Millenaar, R., Miller-Jones, J. C. A., Mohan, R. N., Mol, J. D., Morawietz, J., Morganti, R., Mulcahy, D. D., Mulder, E., Munk, H., Nieuwenhuis, L., van Nieuwpoort, R., Noordam, J. E., Norden, M., Noutsos, A., Offringa, A. R., Olofsson, H., Omar, A., Orrú, E., Overeem, R., Paas, H., Pandey-Pommier, M., Pandey, V. N., Pizzo, R., Polatidis, A., Rafferty, D., Rawlings, S., Reich, W., de Reijer, J.-P., Reitsma, J., Renting, G. A., Riemers, P., Rol, E., Romein, J. W., Roosjen, J., Ruiter, M., Scaife, A., van der Schaaf, K., Scheers, B., Schellart, P., Schoenmakers, A., Schoonderbeek, G., Serylak, M., Shulevski, A., Sluman, J., Smirnov, O., Sobey, C., Spreeuw, H., Steinmetz, M., Sterks, C. G. M., Stiepel, H.-J., Stuurwold, K., Tagger, M., Tang, Y., Tasse, C., Thomas, I., Thoudam, S., Toribio, M. C., van der Tol, B., Usov, O., van Veelen, M., van der Veen, A.-J., ter Veen, S., Verbiest, J. P. W., Vermeulen, R., Vermaas, N., Vocks, C., Vogt, C., de Vos, M., van der Wal, E., van Weeren, R., Weggemans, H., Weltevrede, P., White, S., Wijnholds, S. J., Wilhelmsson, T., Wucknitz, O., Yatawatta, S., Zarka, P., Zensus, A., and van Zwieten, J. (2013). LOFAR: The LOw-Frequency ARray. A&A, 556:A2. xii, 2

Vanden Berk, D. E., Richards, G. T., Bauer, A., Strauss, M. A., Schneider, D. P., Heckman, T. M., York, D. G., Hall, P. B., Fan, X., Knapp, G. R., Anderson, S. F., Annis, J., Bahcall, N. A., Bernardi, M., Briggs, J. W., Brinkmann, J., Brunner, R., Burles, S., Carey, L., Castander, F. J., Connolly, A. J., Crocker, J. H., Csabai, I., Doi, M., Finkbeiner, D., Friedman, S., Frieman, J. A., Fukugita, M., Gunn, J. E., Hennessy, G. S., Ivezić, Ž., Kent, S., Kunszt,

P. Z., Lamb, D. Q., Leger, R. F., Long, D. C., Loveday, J., Lupton, R. H., Meiksin, A., Merelli, A., Munn, J. A., Newberg, H. J., Newcomb, M., Nichol, R. C., Owen, R., Pier, J. R., Pope, A., Rockosi, C. M., Schlegel, D. J., Siegmund, W. A., Smee, S., Snir, Y., Stoughton, C., Stubbs, C., SubbaRao, M., Szalay, A. S., Szokoly, G. P., Tremonti, C., Uomoto, A., Waddell, P., Yanny, B., and Zheng, W. (2001). Composite Quasar Spectra from the Sloan Digital Sky Survey. AJ, 122:549–564. 37, 121, 122, 163

Vedantham, H. K., Koopmans, L. V. E., de Bruyn, A. G., Wijnholds, S. J., Brentjens, M., Abdalla, F. B., Asad, K. M. B., Bernardi, G., Bus, S., Chapman, E., Ciardi, B., Daiboo, S., Fernandez, E. R., Ghosh, A., Harker, G., Jelic, V., Jensen, H., Kazemi, S., Lambropoulos, P., Martinez-Rubi, O., Mellema, G., Mevius, M., Offringa, A. R., Pandey, V. N., Patil, A. H., Thomas, R. M., Veligatla, V., Yatawatta, S., Zaroubi, S., Anderson, J., Asgekar, A., Bell, M. E., Bentum, M. J., Best, P., Bonafede, A., Breitling, F., Broderick, J., Brüggen, M., Butcher, H. R., Corstanje, A., de Gasperin, F., de Geus, E., Deller, A., Duscha, S., Eislöffel, J., Engels, D., Falcke, H., Fallows, R. A., Fender, R., Ferrari, C., Frieswijk, W., Garrett, M. A., Grießmeier, J., Gunst, A. W., Hassall, T. E., Heald, G., Hoeft, M., Hörandel, J., Iacobelli, M., Juette, E., Kondratiev, V. I., Kuniyoshi, M., Kuper, G., Mann, G., Markoff, S., McFadden, R., McKay-Bukowski, D., McKean, J. P., Mulcahy, D. D., Munk, H., Nelles, A., Norden, M. J., Orru, E., Pandey-Pommier, M., Pizzo, R., Polatidis, A. G., Reich, W., Renting, A., Röttgering, H., Schwarz, D., Shulevski, A., Smirnov, O., Stappers, B. W., Steinmetz, M., Swinbank, J., Tagger, M., Tang, Y., Tasse, C., ter Veen, S., Thoudam, S., Toribio, C., Vocks, C., Wise, M. W., Wucknitz, O., and Zarka, P. (2015). Lunar occultation of the diffuse radio sky: LOFAR measurements between 35 and 80 MHz. MNRAS, 450:2291–2305. 25

Venemans, B. P., Bañados, E., Decarli, R., Farina, E. P., Walter, F., Chambers, K. C., Fan, X., Rix, H.-W., Schlafly, E., McMahon, R. G., Simcoe, R., Stern, D., Burgett, W. S., Draper, P. W., Flewelling, H., Hodapp, K. W., Kaiser, N., Magnier, E. A., Metcalfe, N., Morgan, J. S., Price, P. A., Tonry, J. L., Waters, C., AlSayyad, Y., Banerji, M., Chen, S. S., González-Solares, E. A., Greiner, J., Mazzucchelli, C., McGreer, I., Miller, D. R., Reed, S., and Sullivan, P. W.

(2015). The Identification of Z-dropouts in Pan-STARRS1: Three Quasars at 6.5< z< 6.7. ApJ, 801:L11. 15, 117, 159

Verner, D. A., Ferland, G. J., Korista, K. T., and Yakovlev, D. G. (1996). Atomic Data for Astrophysics. II. New Analytic FITS for Photoionization Cross Sections of Atoms and Ions. ApJ, 465:487. 42

Vignali, C., Brandt, W. N., and Schneider, D. P. (2003). X-Ray Emission from Radio-Quiet Quasars in the Sloan Digital Sky Survey Early Data Release: The α_{ox} Dependence upon Ultraviolet Luminosity. AJ, 125:433–443. 37, 121, 122, 163

Villaescusa-Navarro, F., Viel, M., Datta, K. K., and Choudhury, T. R. (2014). Modeling the neutral hydrogen distribution in the post-reionization Universe: intensity mapping. *JCAP*, 9:050. xxi, 160

Voytek, T. C., Natarajan, A., Jáuregui García, J. M., Peterson, J. B., and López-Cruz, O. (2014). Probing the Dark Ages at z ˜ 20: The SCI-HI 21 cm All-sky Spectrum Experiment. ApJ, 782:L9. 25

Wang, X., Tegmark, M., Santos, M. G., and Knox, L. (2006). 21 cm Tomography with Foregrounds. ApJ, 650:529–537. 154, 169, 170, 177

Willott, C. J., Albert, L., Arzoumanian, D., Bergeron, J., Crampton, D., Delorme, P., Hutchings, J. B., Omont, A., Reylé, C., and Schade, D. (2010). Eddington-limited Accretion and the Black Hole Mass Function at Redshift 6. AJ, 140:546–560. 39, 123

Wise, J. H. and Abel, T. (2007). Resolving the Formation of Protogalaxies. I. Virialization. ApJ, 665:899–910. 159

Wise, J. H., Demchenko, V. G., Halicek, M. T., Norman, M. L., Turk, M. J., Abel, T., and Smith, B. D. (2014). The birth of a galaxy - III. Propelling reionization with the faintest galaxies. MNRAS, 442:2560–2579. 162

Wise, J. H., Turk, M. J., Norman, M. L., and Abel, T. (2012). The Birth of a Galaxy: Primordial Metal Enrichment and Stellar Populations. ApJ, 745:50. 118, 159

Wouthuysen, S. A. (1952). On the excitation mechanism of the 21-cm (radio-frequency) interstellar hydrogen emission line. AJ, 57:31–32. 31

Wyithe, J. S. B. and Loeb, A. (2003). Reionization of Hydrogen and Helium by Early Stars and Quasars. ApJ, 586:693–708. 120

Wyithe, S., Geil, P., and Kim, H. (2015). Imaging HII Regions from Galaxies and Quasars During Reionisation with SKA. *Advancing Astrophysics with the Square Kilometre Array (AASKA14)*, page 15. 160

Xu, H., Wise, J. H., Norman, M. L., Ahn, K., and O'Shea, B. W. (2016). Galaxy Properties and UV Escape Fractions During Epoch of Reionization: Results from the Renaissance Simulations. *ArXiv e-prints*. 162

Yajima, H. and Li, Y. (2014). Distinctive 21-cm structures of the first stars, galaxies and quasars. MNRAS, 445:3674–3684. 48, 117, 118, 138

Zackrisson, E., Rydberg, C.-E., Schaerer, D., Östlin, G., and Tuli, M. (2011). The Spectral Evolution of the First Galaxies. I. James Webb Space Telescope Detection Limits and Color Criteria for Population III Galaxies. ApJ, 740:13. 117, 148

Zahn, O., Lidz, A., McQuinn, M., Dutta, S., Hernquist, L., Zaldarriaga, M., and Furlanetto, S. R. (2007). Simulations and Analytic Calculations of Bubble Growth during Hydrogen Reionization. ApJ, 654:12–26. xiii, 3, 21, 23, 118, 160

Zaldarriaga, M. and Seljak, U. c. v. (1997). All-sky analysis of polarization in the microwave background. *Phys. Rev. D*, 55:1830–1840. 16

Zaroubi, S. (2013). The Epoch of Reionization. In Wiklind, T., Mobasher, B., and Bromm, V., editors, *The First Galaxies*, volume 396 of *Astrophysics and Space Science Library*, page 45. 1

Zaroubi, S., de Bruyn, A. G., Harker, G., Thomas, R. M., Labropolous, P., Jelić, V., Koopmans, L. V. E., Brentjens, M. A., Bernardi, G., Ciardi, B., Daiboo, S., Kazemi, S., Martinez-Rubi, O., Mellema, G., Offringa, A. R., Pandey, V. N., Schaye, J., Veligatla, V., Vedantham, H., and Yatawatta, S. (2012). Imaging

neutral hydrogen on large scales during the Epoch of Reionization with LOFAR. MNRAS, 425:2964–2973. xxi, 118, 160

Zaroubi, S., Thomas, R. M., Sugiyama, N., and Silk, J. (2007). Heating of the intergalactic medium by primordial miniquasars. MNRAS, 375:1269–1279. 162

Zawada, K., Semelin, B., Vonlanthen, P., Baek, S., and Revaz, Y. (2014). Light-cone anisotropy in the 21 cm signal from the epoch of reionization. MNRAS, 439:1615–1627. xviii, 88, 91, 92

Zygelman, B. (2005). Hyperfine Level-changing Collisions of Hydrogen Atoms and Tomography of the Dark Age Universe. ApJ, 622:1356–1362. 31